

Electrochemical Promotion of Catalytic Ethylene Oxidation on a Solid Ionic Conductor

Von der Naturwissenschaftlichen Fakultät
der Gottfried Wilhelm Leibniz Universität Hannover
zur Erlangung des Grades

Doktor der Naturwissenschaften

Dr. rer. nat.

genehmigte Dissertation

von

M. Sc. Arafat Ahmed Toghhan Ahmed

geboren am 18.03.1978 in Qena, Ägypten

2012

Referent: Univ.-Prof. Dr. Ronald Imbihl

Korreferent: Univ.-Prof. Dr. Jürgen Caro

Tag der Promotion: 08.11.2012

TO
THE MEMORY OF MY BROTHER ALI
MY PARENTS
MY WIFE
AND
MY CHILDREN

Preface

The results of this thesis were obtained since May 2008 during my Ph. D. study at the Institute of Physical Chemistry and Electrochemistry at the Gottfried Wilhelm Leibniz Universität Hannover under the supervision of Prof. Dr. Ronald Imbihl. In this period, I had a scholarship from the Egyptian government (Ministry of Higher Education, Egypt) for the first two years, after that I was a fellow of the DFG (German Research Foundation) research project for further support till now.

Eight chapters are presented this thesis as follows:

In the 1st chapter, *Introduction*, the motivations and objectives of this study are explained.

The 2nd chapter, *EPOC Basics*, gives an overview of the Electrochemical Promotion (EPOC) and solid electrolytes.

The 3rd chapter, *Experimental Techniques*, describes the experimental methods used in this work.

In the 4th chapter, *Experimental Setup*, a detailed description of the experimental setups is given.

In the 5th chapter, *Preparation and Characterization of Pt/YSZ Catalyst Electrodes*, the microstructure of the Pt/YSZ catalysts has been studied.

The 6th chapter is, *The Electrochemical Promotion of Ethylene Oxidation at Pt/YSZ Catalysts*. The goal of this chapter is to study the mechanism of the electrochemical promotion effect under UHV conditions and under high pressure XPS.

The 7th chapter is, *In Situ X-ray Photoelectron Spectroscopy during Electrochemical Promotion of Ethylene Oxidation over a Bimetallic Pt-Ag/YSZ Catalyst at High Pressure*. The goal of this chapter is to determine how a bimetallic system behaves in EPOC experiments, and to study the mechanism of the electrochemical promotion effect over Pt-Ag catalyst at high pressure using XPS measurements.

In the 8th chapter, *Summary*, the conclusions from the results in this thesis are drawn.

Acknowledgement

First of all I am greatly indebted in my work to our merciful "ALLAH"

This Ph. D. thesis was completed with the dedications of many people. Here, I would like to express my gratitude to all those who gave me the possibility to complete this thesis.

First of all I would like to express the deepest gratitude to my supervisor Prof. Dr. Ronald Imbihl for giving me the opportunity to do my Ph.D. work in his group. His scientific insights, supports, encouragement, guidance and his numerous discussions on the project and my thesis writing are especially valuable for the implement of this work. I am deeply impressed by his hard-working attitude and his dedication to science. I thank him for his constant assistance of my scientific work. I also thank him for his enthusiasm in assisting me when I met problems in my daily life.

The author is furthermore indebted to Prof. Dr. Jürgen Caro and Prof. Dr. Harald Behrens for being the co-referees of this thesis.

I am deeply indebted to my former supervisor Prof. Dr. Mahmoud Khodari, currently working as vice president for graduate studies and research, South Valley University, Egypt for his help, advices, stimulating suggestions, continuously support, and encouragement helped me in all the time of my work.

I would like to thank all my current and some former colleagues in the working group of Prof. Imbihl, not only for their help, scientific support, and valuable hints, but also for the fun we had together. I am very happy with the nice atmosphere in Prof. Imbihl's group. I am much obliged to Mrs. Liz Rösken, Dr. Florian Lovis, Dr. Matias Rafti, Dr. Hong Liu, Mr. Tim Smolnisky and Mr. Martin Hesse.

I would also like to extend my gratitude to other colleagues at the institute: Prof. Dr. Armin Feldhoff, Dr. Konstantin Efimov, Dr. Victor Yarovy and Mr. Frank Steinbach for their kind help on the electron microscopy. Exceptional thanks go to Mr. Frank Steinbach for his valuable cooperation on SEM and TEM measurements and also for his friendship. I appreciate the great job done by the mechanical and electrical workshop, my special thanks to Mr. Bieder, Mr. Egly, Mr. Becker, Mr. Rogge, and Mr. Ribbe. A special thank goes to Mrs. Yvonne Gabbey-Uebe and Mrs. Kerstin Battermann, the secretaries of the institute.

I would also like to thank all my friends in Hannover University, Dr. Heqing Jiang, Mr. Zhengwen Cao and Dr. Huixia Luo, for their support and friendship. Especial

thanks to my dear friend Dr. Heqing Jiang, currently working in Max-Planck-Institut für Kohlenforschung in Mülheim an der Ruhr for his help, stimulating suggestions and numerous discussions. Especially, His always-ready-to-help attitude facilitated my work very much.

I would like to employ this opportunity to thank Prof. Dr. Carla Vogt and all members of her group in the Institute of Inorganic Chemistry, Hannover University, for providing the sputtering-coating instrument used for sample preparation.

I wish to convey my warmest thanks to Prof. Dr. Robert Schlögl, Dr. Axel Knop-Gericke, Dr. Michael Hävecker, Dr. Rosa Arrigo, Dr. Mark Greiner at the Fritz-Haber-Institut der Max-Planck Gesellschaft, Berlin, for their valuable cooperation of the DFG project and the full support of our beamtime at BESSY, they gave me a lot of help on the XPS studies.

A special acknowledgement again flies back Egypt to my former supervisors Prof. Dr. Mortga Abou-Krishna and Prof. Dr. Fawzi Assaf at the Chemistry Department, Faculty of Science, South Valley University, Egypt whose introduced me to step into the door of science, and whose inculcation is of great benefit to my research work. I also want to sincerely thank Prof. Dr. Hesham Rageh for welcoming me in his lab during my master study and for his advices, support and encouragement right now.

I am very grateful to my dear friend Dr. Adel Ismail, assistant professure in the Central Metallurgical R&D Institute (CMRDI), Egypt for his support, advices, nice discussions, and encouragement.

As for the financial support, I appreciate the Egyptian Ministry of Higher Education fellowship which supported me from May 2008 – April 2010 and the DFG (German Research Foundation) for the further support from Juli 2010 – till now. I wish to express my thanks to my home university (South Valley University, Qena, Egypt) for allowing me to do my docoral study in Germany.

Last but not least, I would like to express my special thanks and regards to my dear parents, who taught me the value of hard work by their own example. I would like to share this moment of happiness with my parents, brothers and sisters. They rendered me enormous support during the whole tenure of my research. Particularly, I am grateful to my wife Maha Abdel-Twab for the comfortable work environment and moral support she provided throughout my research work. Without her patient love and understanding I would never have completed my present work. I also would like to thank my lovely children for being the sunshine and joy of my life.

Abstract

The catalytic activity and selectivity of metals (e.g. platinum) can be altered dramatically and reversibly by interfacing the metal with an ion conducting solid electrolyte. As solid electrolyte the O^{2-} conducting yttrium stabilized zirconia (YSZ) was applied here which supplies O^{2-} ions onto the catalyst surface by polarization of the catalyst/solid electrolyte interface. For reactions catalyzed by the metal electrode the phenomenon of so-called electrochemical promotion of catalysis (EPOC), also known as non-Faradaic electrochemical modification of catalytic activity (NEMCA), is observed. The induced change in the catalytic rate is some times several orders of magnitude higher than the rate increase predicted from the ion supply. The effect of electrochemical promotion appears to apply to all heterogeneously catalyzed reactions, but it is particularly pronounced for platinum.

The electrochemical promotion of catalytic C_2H_4 oxidation has been investigated under low pressure conditions ($p \approx 10^{-6} - 10^{-4}$ mbar) and high pressure up to ≈ 1 mbar with a Pt films on yttrium stabilized zirconia (YSZ) as catalyst. All low pressure measurements were conducted with a UHV system with a differentially pumped quadruple mass spectrometer (QMS) for rate measurements and a photoelectron emission microscope (PEEM) for spatially resolved measurements. A pronounced rate hysteresis upon cyclic variation of $p(C_2H_4)$ was observed under open circuit conditions. XPS studies at BESSY in Berlin, conducted under high pressure, up to 1 mbar showed that, the hysteresis is caused by the build-up of a carbonaceous CH_x layer inhibiting O_2 adsorption and hence poisoning the reaction. Application of a positive potential causes a partial removal of the inhibiting CH_x adlayer by spillover oxygen thus triggering a transition from thus poisoned state of the surface to an active state with reduced carbon coverage. The ignition effect and therefore also the electrochemical promotion effect are linked to the presence of a carbon adlayer on the surface. The non – Faradaicity which is observed in this reaction system is explained as an ignition effect.

The basic idea of the “ignition concept” is to explain the huge non-Faradaic effect found in the electrochemical promotion of catalytic ethylene oxidation and many other reaction systems exhibiting an EPOC effect without having to invoke the special oxygen spillover species postulated by Vayenas et al. In their “sacrificial promoter” mechanism besides regular chemisorbed oxygen a special oxygen spillover species should exist on

Pt/YSZ with particular properties which differ from the properties of regular chemisorbed oxygen on Pt.

The pressure gap in the ethylene oxidation over Pt-Ag/YSZ catalyst has been bridged by systematically increasing the pressure and utilizing the *in situ* techniques to monitor the state of the surface. In a high-pressure reaction cell the electrochemical promotion of the $C_2H_4 + O_2$ reaction over a bimetallic Pt/Ag catalyst (Pt:Ag ratio ≈ 1.5) interfaced to yttrium stabilized zirconia (YSZ) has been studied at 0.25 mbar and $T = 650$ K using X-ray photoelectron spectroscopy as *in situ* method. Applying a positive potential of 2V causes a relative rate increase in the CO_2 production up to 120%; the electrocatalytic promotion effect is non-Faradaic ($\Lambda \approx 2$). An electrochemical promotion is found to occur only at high enough $p(C_2H_4)$ when a carbonaceous CH_x layers builds up inhibiting O_2 adsorption. The CH_x film is estimated to be about 5-6 layers thick. Only at low $p(C_2H_4)$ the application of an electric potential causes a decrease in the carbon signal associated with a growth of the O1s signal at 529.3 eV. The latter species can be assigned to an electrochemically generated oxygen spillover species at Ag sites.

Keywords: Electrochemical Promotion of Catalysis, EPOC, Solid Electrolytes, Yttrium Stabilized Zirconia (YSZ), Platinum, Silver, Spillover, Ethylene Oxidation, Hysteresis, Rate Oscillations, PEEM, XPS, Ultra High Vacuum (UHV), Pressure Gap, SEM, TEM, XRD

Kurzzusammenfassung

Die katalytische Aktivität und Selektivität von Metallen (z. B. Platin) kann drastisch und reversibel dadurch geändert werden, indem das Metall als Elektrode eines ionenleitenden Festelektrolyten eingesetzt wird. Als Festelektrolyt wurde hier mit Yttrium stabilisiertes Zirkondioxid (YSZ) verwandt, das O^{2-} -ionenleitend ist und nach elektrochemischer Polarisation der Grenzschicht Katalysator/ Festelektrolyt atomaren Sauerstoff auf die Oberfläche des Metalls wandern läßt. Man beobachtet dann an Reaktionen, die an der Metall-Elektrode katalysiert werden, beim Anlegen eines elektrischen Potentials einen Ratenanstieg. Dieses Phänomen der sogenannten elektrochemischen Promotion der katalytischen Reaktion (engl. EPOC = electrochemical promotion of catalysis) ist auch unter der Bezeichnung NEMCA (non-Faradic electrochemical modification of catalytic activity) bekannt. Die elektrochemisch induzierte Änderung der katalytischen Rate ist manchmal um mehrere Größenordnungen höher als die Rate, die aus dem transportierten Ionenstrom auf Grund der Faraday'schen Gesetze vorhergesagt wird. Eine elektrochemische Promotion scheint bei allen heterogen katalysierten Reaktionen möglich zu sein, sie ist aber bei bestimmten Metallen wie z. B. Platin besonders ausgeprägt.

Die elektrochemische Promotion der katalytischen Oxidation von C_2H_4 ist hier zum einen unter Niederdruckbedingungen ($p \approx 10^{-6} - 10^{-4}$ mbar) und zum anderen unter hohem Druck bei etwa 1 mbar untersucht worden. Als Katalysator wurden Pt-Filme auf Yttrium stabilisiertem Zirkondioxid (YSZ) verwandt. Alle Niederdruck-Messungen wurden an einem UHV-System durchgeführt, das mit einem differentiell gepumpten Quadrupolmassenspektrometer (QMS) für Raten-Messungen und und einem Photoelektronen-Emissions-Mikroskop (PEEM) für ortsaufgelöste Messungen ausgerüstet war. Bei zyklischer Variation von $p(C_2H_4)$ wurden ohne angelegtes elektrisches Potential ausgeprägte Raten-Hysteresen beobachtet. XPS Untersuchungen bei BESSY in Berlin, die unter hohem Druck bis zu 1 mbar durchgeführt wurden, zeigten, dass die Hysterese durch den Aufbau einer kohlenstoffhaltigen CH_x -Schicht verursacht wurden. Das Anlegen eines positiven Potentials bewirkt eine teilweise Entfernung des inhibierenden CH_x durch reaktiven Sauerstoff der von YSZ auf die Metallelektrodenoberfläche übertritt (spillover oxygen). Durch einen Lochfraßmechanismus wird ein Übergang ausgelöst, der von einem vergifteten Zustand

der Oberfläche zu einem aktiven Zustand mit reduzierter C-Bedeckung führt. Der Zündeffekt und damit auch der elektrochemische Promotionseffekt sind an die Gegenwart einer inhibierenden Kohlenstoffschicht auf der Oberfläche geknüpft. Das nicht-Faraday'sche Verhalten, das in diesem Reaktionssystem beobachtet wird, ist eine Folge des Zündeffekts.

Über das "Zündungs-Konzept" ist es möglich, die riesigen nicht-Faraday'schen Effekte, die in der elektrochemischen Promotion der katalytischen Ethylenoxidation und vielen anderen Reaktionssystemen gefunden wurden, ohne die von Vayenas et al. postulierte spezielle Sauerstoff-Spillover-Spezies zu erklären. Die postulierte spezielle Spillover-Spezies sollte neben dem gewöhnlichen chemisorbierten Sauerstoff auftreten und durch ihre besonderen Eigenschaften wie hohes Dipolmoment und verringerte Reaktivität eine Art Promotor-Wirkung erzeugen.

Um die Drucklücke zwischen UHV-Bedingungen und der sogenannten Realkatalyse zu überbrücken, wurde die Ethylenoxidation über einem bimetallic Pt-Ag/YSZ Katalysator (Pt:Ag-Verhältnis $\approx 1,5$) mittels eines differentiell gepumpten XPS bei BESSY bei Drücken um 0.25 mbar und einer Temperatur von 650 K *in situ* untersucht. Das Anlegen eines positiven Potentials von 2V bewirkt eine relative Zunahme der CO₂-Produktion um bis zu 120%. Die elektrochemisch induzierte Ratenerhöhung war nicht-Faradayisch ($\Lambda \approx 2$). Die elektrochemische Promotion trat nur bei ausreichend hohem $p(\text{C}_2\text{H}_4)$ auf, wenn durch die Zersetzung des Ethylens sich ein Kohlenstofffilm auf der Metalloberfläche aufbaut. Die Dicke des CH_x-Films wurde auf etwa 5-6 Schichten geschätzt. Im Gegensatz zu einer reinen Platinelektrode bildet sich auf der Pt/Ag-Elektrode bereits bei kleinem $p(\text{C}_2\text{H}_4)$, das heißt bei Sauerstoffüberschuß, eine Kohlenstoffschicht aus. Unter diesen Bedingungen findet man, dass das Anlegen eines elektrischen Potentials zu einer Abnahme des Kohlenstoff-Signals führt verbunden mit einem Wachstum des O1s-Signals bei 529,3 eV. Die letztere Spezies wird elektrochemisch erzeugten Spillover-Sauerstoff über Ag-Adsorptionsplätzen zugewiesen.

Schlüsselwörter: Elektrochemische Promotion katalytischer Reaktionen, EPOC, Festkörperelektrolyte, Yttrium stabilisiertes Zirkonoxid (YSZ), Platin, Silber, Spillover, Ethylenoxidation, Hysteresen, kinetische Oszillationen, PEEM, XPS, Ultrahochvakuum (UHV), Drucklücke, SEM, TEM, XRD

Table of content

1.	Introduction	1
1.1	Introduction	2
1.2	Motivations and objectives	3
1.3	References	5
2.	EPOC Basics	7
2.1	Electrochemical promotion	8
	2.1.1 Phenomenology and basic definitions	8
	2.1.2 Concept of a special spillover species ($O^{\delta-}$ with $\delta \approx 2$)	13
	2.1.3 Basic empirical relations	16
2.2	Solid Electrolytes (SE's)	23
	2.2.1 Zirconia (ZrO_2)	24
	2.2.2 Yttrium stabilized zirconia (YSZ)	25
2.3	References	31
3.	Experimental Techniques	35
3.1	Photoemission Electron Microscopy (PEEM)	36
	3.1.1 Introduction	36
	3.1.2 Instrumentation	37
3.2	X-ray Photoelectron Spectroscopy (XPS)	39
	3.2.1 Introduction	39
	3.2.2 XPS process	39
	3.2.3 Instrumentation	40
3.3	The Quadrupole Mass Spectrometer (QMS)	41
3.4	References	42
4.	Experimental Setup	43
4.1	Low pressure experiment for PEEM	44
	4.1.1 Sample preparation	44

4.1.2	Electrochemical setup	44
4.1.3	Reaction experiments and sample holder	45
4.1.4	Ultra high vacuum chamber	48
4.1.5	Gas calibration in UHV	48
4.1.6	Rate measurement	50
4.1.7	Calculation of the Faradaic efficiency (Λ -Factor)	52
4.2	High pressure XPS	53
4.2.1	Sample preparation and electrochemical set-up	53
4.2.2	Reaction experiments	54
4.2.3	Gas calibration	56
4.2.4	Rate measurement	57
4.2.5	XPS and data analysis	58
4.3	References	60
5.	Preparation and Characterization of Pt/YSZ Catalyst Electrodes	61
5.1	Introduction	62
5.2	Electrode preparation	63
5.3	Sample characterizations	64
5.3.1	Scanning Electron Microscopy (SEM) and XRD	65
5.3.2	Transmission Electron Microscopy (TEM)	73
5.4	Conclusions	76
5.5	References	77
6.	The Electrochemical Promotion of Ethylene Oxidation at Pt/YSZ Catalysts	78
6.1	Introduction	79
6.2	Reaction kinetics	82
6.2.1	Bistable kinetics under open circuit conditions	82
6.2.2	Effect of electrochemical pumping ($V_{WR} = 1$ V)	87
6.3	Dependence of the promotion effect on reaction conditions	90
6.3.1	Effect of applying potential starting from lower rate branch	90
6.3.2	Effect of applying potential starting from upper rate branch	95

6.4	Catalyst potential variation (V_{WR})	100
	6.4.1 Dependence on temperature	100
	6.4.2 Dependence on ethylene partial pressure	104
6.5	Formation of bright spots in PEEM	104
6.6	High pressure XPS	107
6.7	Discussion	109
6.8	Conclusions	111
6.9	References	112
7.	In Situ X-ray Photoelectron Spectroscopy during Electrochemical Promotion of Ethylene Oxidation over a Bimetallic Pt-Ag/YSZ Catalyst at High Pressure	114
7.1	Introduction	115
7.2	Sample characterization	116
	7.2.1 Surface morphology	116
	7.2.2 XPS characterizations	117
7.3	Reaction kinetics	121
	7.3.1 Stationary kinetics	121
	7.3.2 Kinetic instabilities	123
7.4	Variation of the surface composition during EPOC	127
7.5	Discussion	142
7.6	Conclusions	147
7.7	References	147
8.	Summary	150

Abbreviations and symbols

AC	Alternative current
AES	Auger electron spectroscopy
a_0	Activity of atomic oxygen
AFM	Atomic force microscopy
BE	Binding energy
CB	Conduction band
CE	Counter electrode
CV	Cyclic voltammetry
CF	Calibration factor
CPD	Contact potential difference
D	Diffusion coefficient
DC	Direct current
D_O	Oxygen self-diffusivity
E	Energy
EPOC	Electrochemical promotion of catalytic reactions
e.m.f	Electromotive force
EDX	Energy-dispersive X-ray analysis
ESCA	Electron spectroscopy for chemical analysis
Eq.	Equation
E_F	Fermi level
E_g	Band gap
E_a	Activation energy
F	Faraday constant
FOV	Fields of view
FWHM	Full width at half maximum
fcc	Face centered cubic
h	Hour
h	Planck's constant
$h\nu$	Photon energy
I	Electric current
I_0	Exchange current

$J(O_2)$	Oxygen flux
K	Boltzmann's constant
KE	Kinetic energy
KP	Kelvin probe
ℓ_{tpb}	Length of the tpb
M	Metal
MCP	Microchannel plate
MFC	Mass flow controllers
m/e	Mass-to-charge ratio
NEMCA	Non-Faradaic electrochemical modification of catalytic activity
n	Number of moles
nm	Nanometer
N_{part}	Number of particles in the gas phase
N_A	Avogadro constant
OC	Open-circuit
OCP	Open circuit potential
O_{ad}	Adsorbed atomic oxygen
O_{tpb}	Oxygen at the tpb
p	Partial pressure
PEEM	Photoemission electron microscopy
P-EPOC	Permanent EPOC
QMS	Quadrupole mass spectrometer
R	Ideal, or universal, gas constant
RE	Reference electrode
r	Electropromoted catalytic rate i.e. rate under potential application
r_0	Open-circuit catalytic rate
Δr	Rate difference
r_{per}	Permanent rate under open-circuit conditions
r_F	Faradaic rate
r_z	Reaction zone
S	Pumping speed
s	Second
S_{reac}	Reactive sticking coefficient
SE	Solid electrolyte

SCCM	Standard cubic centimeters per minute
SOFC	Solid oxide fuel
SAED	Selected area electron diffraction
SEM	Scanning electron microscopy
STM	Scanning tunneling microscopy
STEM	Scanning transmission electron microscopy
tpb	Three-phase-boundary (solid electrolyte/metal/gas)
T	Temperature
t	Time
TMP	Turbomolecular pump
TEM	Transmission electron microscopy
TPD	Temperature programmed desorption
UHV	Ultra high vacuum
UV	Ultraviolet
UPS	Ultra violet photoelectron spectroscopy
V_{WR}	Applied potential to the WE with respect to RE
V_{WR}^0	Open circuit potential
V	Volte
VB	Valence band
VBM	Valence bands maximum
$V_{\text{O}}^{\cdot\cdot}$	Oxygen vacancies
WE	Working electrode
XRD	X-ray diffraction
XPS	X-ray photoelectron spectroscopy
YSZ	Yttrium stabilized zirconia
Z	Atomic number
Λ	Faradaic efficiency
ρ	Rate enhancement ratio
τ	NEMCA time constant
Φ	Work function
Φ_{sp}	Work function of the spectrometer
γ	Permanent rate enhancement
α_a	Anodic transfer coefficient

α_c	Cathodic transfer coefficient
η	Overpotential
η_{ohmic}	Ohmic overpotential
η_{ac}	Activation overpotential
η_{conc}	Concentration overpotential
$\mu(O_2, WE)$	Chemical potentials of oxygen adsorbed on the WE
$\mu(O_2, RE)$	Chemical potentials of oxygen adsorbed on the RE
μ°	Standard chemical potential
μm	Micrometer
σ	Electrical conductivity
σ_a	Ambipolar conductivity

Chapter 1

Introduction

The following chapter describes the Motivations and objectives of this study.

1.1 Introduction

Catalysis plays an important role in chemical industry. The first time a catalyst was used in chemical industry was in 1746 by J. Roebuck and S. Gardner in the manufacture of sulfuric acid in a lead chamber [1]. Nowadays heterogeneous catalysts are involved in at least one step in about 80% of the chemicals produced in chemical industry [2,3]. In addition, catalysts play a great importance in environmental chemistry, i.e. in removing pollutants by chemical reactions, e.g. by removing CO, NO and CH_x emissions in automotive exhaust gas. For improving catalysts it is important that researchers from different fields work together.

One of these fields is *surface science*. In surface science with a well defined surface structure and chemical composition of a model catalyst and of elementary steps like adsorption, desorption, and diffusion are studied under UHV (ultra high vacuum) conditions employing typically single crystals. The conditions and the samples in surface science are thus quite far away from the conditions of so-called real catalysis. This difference constitutes the famous “pressure gap” and “material gap” problem [4]. The pressure gap arises because surface model studies are usually conducted under low pressure conditions ($p < 10^{-6}$ mbar), while industrial catalysis is performed at atmospheric or even higher pressure ($p \approx 1-100$ bar). Indeed, low pressure conditions provide a couple of advantages: a high level of purity can be realized, experiments are strictly isothermal due to low conversion rates, and, most of all, surface analytical techniques based on free electrons are available to characterize the catalyst surfaces [5]. Since the 1980s, many researchers have devoted their efforts to surface science studies in order to efficiently use the results to explain or even predict the catalytic activity of certain systems [6,7].

The interfacing of electrochemistry and catalysis offers some exciting theoretical and technological possibilities. A dramatic improvement in the catalytic activity and selectivity of a composite catalyst metal/solid electrolyte has been achieved simply by polarization of the interface by application of an electrical current/potential. A solid electrolyte is highly efficient in order to improve the catalytic performance. The first time the use of solid electrolytes was proposed to control the chemical potential of a surface species was in 1970 by C. Wagner [8]. However, it was not until C. Vayenas found an efficient realization by depositing porous metal electrodes onto a solid electrolyte that EPOC was investigated systematically on a large scale. Pioneered by Vayenas and his group in Patras the EPOC effect has been demonstrated with about 100

reaction systems and with different types of solid electrolytes [9,10]. Rate enhancements up to a factor 200 have been reported. It is worth to mention that EPOC has not been found to be limited to any particular electrolyte, e.g. cationic or anionic, any conducting catalyst, e.g. metal or metal oxide, or any particular type of catalytic reaction [10]. Solid electrolytes are used primarily in solid oxide fuel cells (SOFC) and in gas sensors [11,12].

On one hand, the content of this PhD thesis work is part of the effort to bridge the pressure and material gap in ethylene oxidation over pure Pt and bimetallic Pt/Ag electrodes interfaced to a solid ionic conductor (e.g. yttrium stabilized zirconia, YSZ). On the other hand, it is also an aim of this investigation is to study the connection between electrochemistry and catalytic activity via application of a constant current/potential to a metal catalyst which also serves as working electrode for an electrochemical cell. Indeed, a dramatic enhancement of the catalytic activity of a conducting catalyst supported on a solid electrolyte during the application of a constant current/potential step is seen. This phenomenon is known under electrochemical promotion of catalytic reactions (EPOC). EPOC is a challenging interdisciplinary phenomenon connecting the fields of catalysis, surface science, and solid state electrochemistry.

Irrespective of the many EPOC studies which have been conducted [10], only a few groups study the catalytic promotion effect using *in situ* surface science techniques. The group of J. Janek in Giessen, Germany and of R. Lambert in Cambridge, England the former group investigating the O^{2-} conducting YSZ and the latter group studying the Na^+ conducting β'' - Al_2O_3 [13-17]. General concepts and mechanistic schemes were proposed for the EPOC effect but these concepts and schemes are largely speculative in nature [10]. Applying surface analytical tools to EPOC systems the proposed mechanistic schemes can be verified or invalidated [18]. In this thesis, for the first time the EPOC experiments were extended up to 1 mbar using *in situ* techniques in order to clarify the mechanistic understanding of the catalytic promotion effect.

1.2 Motivations and objectives

The central motivation of this thesis is the elucidation of the mechanism of the electrochemical promotion of catalysis (EPOC) for ethylene oxidation with O_2 on a Pt/YSZ catalyst under different pressure conditions. The reason for the choice of this

reaction system is the huge Λ -factor of 3×10^5 of this system, reported by Vayenas et al. in 1989, and the paradigmatic role of this system therefore had in EPOC and in numerous review papers and monographs on the EPOC effect [9,10,19-22].

Toward these objectives, the following investigations have been performed:

1. **Low pressure experiments:** An experimental study of the $C_2H_4 + O_2$ reaction on Pt/YSZ in an UHV environment (low pressure $\approx 10^{-6}$ - 10^{-4} mbar). Of the large number of EPOC systems studied at high pressure only catalytic CO oxidation and some alkali promoted systems have so far been investigated under UHV conditions. As will be shown in chapter 6, based on the results of this study different conclusions were reached about the origin of the non-Faradaicity of this reaction than the concept proposed by Vayenas and co-workers.
2. **High pressure experiments:** Most of the difficulties in coming to a clear mechanistic picture of the EPOC effect can be traced back to the well known pressure and material gap in heterogeneous catalysis. Nearly all of the EPOC studies have been conducted in the mbar to atmospheric pressure range with structurally and chemically badly defined catalysts [9,10,19-22]. A small number of surface science type studies have been conducted but what is completely missing are high pressure studies characterizing the state of the catalyst with *in situ* techniques [13-18]. For this reason a differentially pumped X-ray photoelectron spectrometer was used with which *in situ* XPS experiments are feasible up to ≈ 1 mbar. The reaction system investigated is catalytic ethylene oxidation on a Pt/YSZ catalyst.
3. **Catalyst characterization:** In order to know more about the morphologies, microstructures and interfaces of Pt/YSZ, the electrodes were characterized by scanning electron microscopy (SEM), transmission electron microscopy (TEM), selected area electron diffraction (SAED), X-ray diffraction (XRD), energy-dispersive X-ray analysis (EDX) and by surface profilometry as discussed in detail in chapters 5.
4. **Bimetallic Pt-Ag/YSZ catalyst:** For both separate systems, Pt/YSZ and Ag/YSZ the electrochemically induced oxygen spillover has been characterized by XPS under low pressure conditions [14,23,24]. The question addressed here is whether the presence of two metals leads to new unexpected results with respect to spillover and electrochemical promotion of ethylene oxidation or whether the two metals just act independent of each other so that the resulting behavior is just

a superposition of the known behavior of each of the two metals. As will be shown in chapter 7, the two metals largely retain their individual properties in this electrochemical experiment.

1.3 References

- [1] L. Lloyd, *Handbook of Industrial Catalysts (Fundamental and Applied Catalysis)*, Springer, New York, USA, 2011.
- [2] G. Ertl, *Reactions at Surfaces: From Atoms to Complexity (Nobel Lecture)*, *Angew. Chem.Int. Ed.* 47 (2008) 3524.
- [3] I. Chorkendorff, J. W. Niemantsverdriet, *Concepts of Modern Catalysis and Kinetics*, Wiley-VCH, Weinheim, 2003.
- [4] R. Imbihl, R. J. Behm, R. Schlögl, *Bridging the pressure and material gap in heterogeneous catalysis*, *Phys. Chem. Chem. Phys.* 9 (2007) 3459.
- [5] G. Ertl, J. Küppers, *Low Energy Electrons and Surface Chemistry*, VCH, Weinheim 1985.
- [6] V. I. Bukhtiyarov, *Kinet. Catal.* 44 (2003) 420.
- [7] J. A. Rodriguez, D. W. Goodman, *Surf. Sci. Rep.* 14 (1991) 1.
- [8] C. Wagner, *Adsorbed Atomic Species as Intermediates in Heterogeneous Catalysis*, *Adv. Catal.* 21 (1970) 323.
- [9] C. G. Vayenas, S. Bebelis, S. Ladas, *Nature* 343 (1990) 625.
- [10] C. G. Vayenas, S. Bebelis, C. Pliangos, S. Brosda, D. Tsiplakides, *Electrochemical Activation of Catalysis: Promotion, Electrochemical Promotion, and Metal-Support Interactions*, Kluwer Academic / Plenum Publishers, New York, 2001.
- [11] S. Park, J. M. Vohs, R. J. Gorte, *Nature* 404 (2000) 265.
- [12] A. Mandelis, C. Christofides, *Solid State Gas Sensor Devices*, John Wiley & Sons, New York 1993.
- [13] E. Mutoro, B. Luerssen, S. Guenther, J. Janek, *Solid State Ion.* 180 (2009)1019.
- [14] B. Luerßen, E. Mutoro, H. Fischer, S. Günther, R. Imbihl, J. Janek, *Angew. Chem. Int. Ed.* 45 (2006) 1473.
- [15] I. V. Yentekakis, A. Palermo, N. C. Filkin, M. S. Tikhov, R. M. Lambert, *J. Phys. Chem. B* 101 (1997) 3759.
- [16] R. M. Lambert, F. Williams, A. Palermo, M. S. Tikhov, *Topics in Catalysis* 13 (2000) 91.
- [17] O. A. Marina, I. V. Yentekakis, C. G. Vayenas, A. Palermo, R. M. Lambert, *J. Catal.* 166 (1997) 218.
- [18] R. Imbihl, *Prog. Surf. Sci.* 85 (2010) 240.
- [19] S. Bebelis, C.G. Vayenas, *J. Catal.* 118 (1989) 125.

- [20] C.G. Vayenas, M.M. Jaksic, S.I. Bebelis, S.G. Neophytides, *The Electrochemical Activation of Catalytic Reactions*, in: J.O.M. Bockris et al. (Eds.), *Modern Aspects of Electrochemistry*, 29, Plenum Press, New York, 1995, p. 57.
- [21] C.G.Vayenas, S.G. Neophytides, *Electrochemical Activation of Catalysis*, in: *Catalysis*, Vol. 12, The Royal Society of Chemistry, Cambridge, 1996, p. 195.
- [22] C. G. Vayenas, S. Bebelis, I. V. Yentekakis, H. G. Lintz, *Non-Faradaic Electrochemical Modification of Catalytic Activity: A Status Report*, *Catal. Today* 11 (1992) 303.
- [23] B. Luerßen, S. Günther, H. Marbach, M. Kiskinova, J. Janek, R. Imbihl, *Chem. Phys. Lett.* 316 (2000) 331.
- [24] W. Zipprich, H. D. Wiemhöfer, U. Vöhrer, W. Göpel, *Ber. Bunsen.-Ges. Phys. Chem.* 99 (1995) 1406.

Chapter 2

EPOC Basics

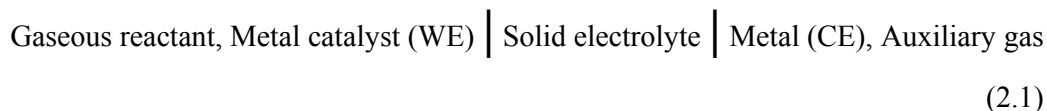
The following chapter describes the basic phenomenology of the electrochemical promotion of catalysis (EPOC) or non-faradaic electrochemical modification of catalytic activity (NEMCA) effect. In addition the general characters of the solid electrolytes have been explained as well.

2.1 Electrochemical promotion

The electrochemical promotion of catalysis (EPOC), also known as non-Faradaic electrochemical modification of catalytic activity (NEMCA), is a rather general phenomenon observed in about 30 years ago for the first time [1-5]. The phenomenon has a strong impact on modern electrochemistry, heterogeneous catalysis and surface science.

2.1.1 Phenomenology and basic definitions

Solid electrolytes interfaced with noble metal electrodes allow an EPOC effect simply by varying the electrode potential. The principle possibility of using solid electrolytes to control the chemical potential of a surface species has already been recognized by C. Wagner in 1970 [1]. He proposed the use of solid electrolyte potentiometry (SEP) for the measurement of oxygen activity simultaneously with reaction rate measurements during oxidation reactions. Vayenas and Saltsburg were the first to follow reaction rates and oxygen activities during the oxidation of SO₂ on platinum, gold and silver [2]. In their pioneering work in the early 1980s Vayenas et al. reported the control of catalytic reactions via electrochemical polarization of the metal/solid electrolyte interface [3-5]. They found that the catalytic activity of a porous metal catalyst films could be dramatically increased in a controlled manner by polarization of the catalyst/solid electrolyte interface in an electrochemical cells of the type [6,7]:



where the metal catalyst film is the working electrode (WE) and a typically catalytically inert metal is the counter electrode (CE). The auxiliary gas can be ambient air when using the “fuel cell” type design [8-11] (Fig. 2.1a) or the reactive gas mixture itself in the, so called, single pellet design [11-13] (Fig. 2.1b). This effect is so-called electrochemical promotion of catalysis (EPOC) or non-Faradaic electrochemical modification of catalytic activity (NEMCA).

In further studies, pioneered by Vayenas et al. the EPOC effect has been demonstrated for about 100 reaction systems utilizing a number of different solid electrolytes the most important ones being O²⁻ conducting yttrium stabilized zirconia

(YSZ) and Na^+ conducting $\beta''\text{-Al}_2\text{O}_3$ [11,14-16]. Nearly all of these studies have been conducted in the 10^{-2} mbar to atmospheric pressure range with structurally and chemically ill-defined metal electrodes prepared, for example, by depositing Pt paste with a brush onto YSZ followed by calcination. Based on a large body of experimental data empirical relations and theoretical concepts were proposed but due to the lack of data from *in situ* measurements with surface analytical methods these concepts were mostly speculative in nature.

Surface science type studies of the EPOC effect were started about 15 years ago [17-24]. As was demonstrated with photoelectron spectroscopy and other methods, the physical basis of the EPOC effect is the electrochemically induced spillover of the transported ionic species onto the surface of the metal electrode after discharge at the three-phase-boundary (tpb), gas/metal/solid electrolyte.

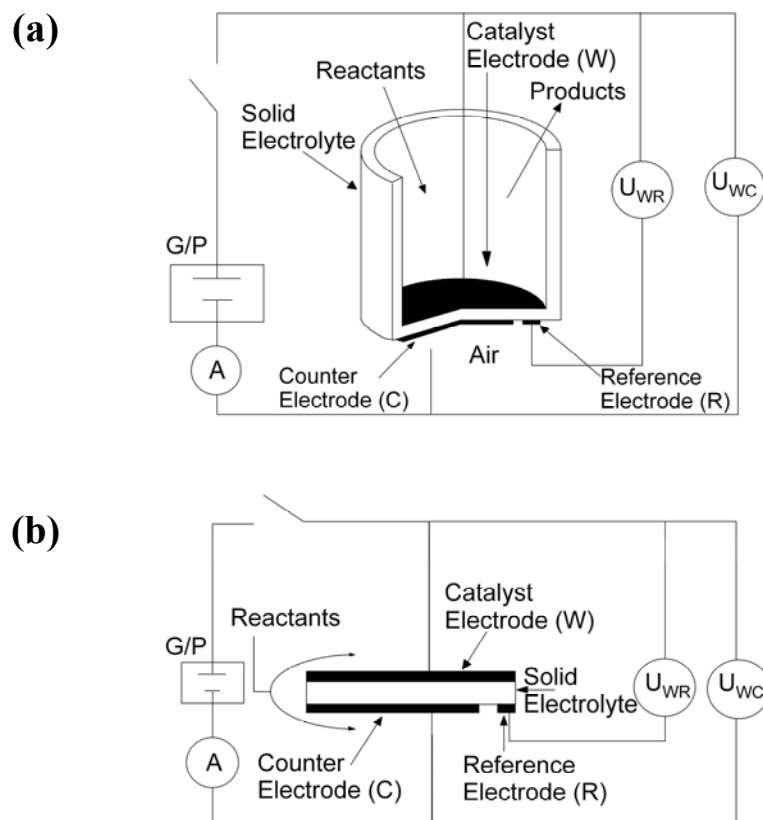
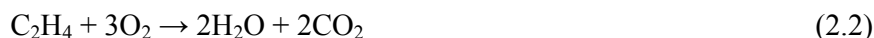


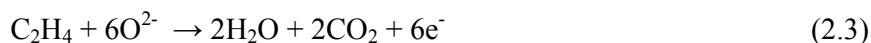
Figure 2.1: Typical experimental set-up for EPOC experiments using the fuel-cell type (a) and single-pellet type (b) configurations; G/P. galvanostat / potentiostat controls the electric current / the electric potential [16]. Using a half-closed YSZ tube a reactor the reactants are fed inside the tube where they react at the surface of the Pt working electrode (WE) whereas the reference electrode (RE) outside the tube is held in ambient air thus fixing the potential of the RE.

The basic experimental setup used to observe the EPOC effect or the NEMCA effect on O^{2-} -conducting solid electrolytes is shown in Fig. 2.1a with a half-closed YSZ tube as catalytic reactor using the fuel-cell type. For the electrochemical measurements a standard three-electrode set-up displayed in Fig. 2.1b is used.

In a typical NEMCA experiment, for example in the combustion of ethylene, the catalytic reaction takes place on the catalyst surface of a conductive porous Pt film of roughly 1-10 μm thickness [16] the Pt film also serves, at the same time, as the working electrode (WE) in a solid electrolytic cell: Gaseous reactant (e.g. $C_2H_4 + O_2$), Pt catalyst (WE) | Yttrium stabilized zirconia (YSZ) | Pt (CE), auxiliary gas (e.g. air). The porous Pt electrodes are prepared by simply depositing a Pt paste with a brush followed by calcination and sintering. Figure 2.2 shows a typical galvanostatic NEMCA experiment carried out in the setup of Fig. 2.1a [8]. The experiments are carried out with the partial pressures of the feed gases being in the 10^{-2} to mbar range but with He as carrier gas so that the total pressure is around 1 bar. Mass flow controllers are used to adjust the feed of the reactants. Under open-circuit (OC) conditions ($I = 0$, no electrochemical rate contribution) the catalytic (no net charge-transfer) reaction is given by the catalytic reaction:



For the non-electrochemist it is worth reminding that “a galvanostatic process” always fixes the current, I_{WC} , between the working electrode (WE) and the counter electrode (CE) at a desired constant value. Whereas “a potentiostatic process” always fixes the potential, V_{WR} , between the WE and the reference electrode (RE) at a certain constant value. Application of a constant electrical currents, I_{WC} , between the catalyst WE and the CE (galvanostatic operation) or a constant potentials, V_{WR} , between the catalyst WE and RE (potentiostatic operation) gives rise to very pronounced, non-Faradaic changes (i.e. $\Delta r \gg I/2F$) in the catalytic rate, r , and quite often in product selectivity [11,15,16]. The difference between Faradaic and non-Faradaic rate increase is explained as follows. The electrocatalytic reaction taking place at the three-phase-boundaries (tpb) (solid electrolyte/metal electrode/gas phase), where the O^{2-} ions are discharged as follows:



Supposing a current efficiency of 100%, the maximum possible electrochemical reaction rate, r_F , (mol O/ s), is calculated with Faraday's law:

$$r_F = I/nF \quad (2.4)$$

with I represent the applied electric current, n the charge number of the transported ions (for O^{2-} , $n = 2$), and F the Faraday constant. If open-circuit and Faradaic reactions would be additive, Eq. 2.4 would give the maximum expected increase in reaction rate due to polarization.

Figure 2.2 shows the evolution of the experimentally observed reaction rate, r , in a stepwise anodic polarization cycle, i.e. before, during, and after galvanostatic polarization of the catalyst/YSZ interface in the combustion of ethylene over a Pt/YSZ at 643 K, ($p(O_2)=4.6 \times 10^{-2}$ mbar and $p(C_2H_4)=3.6 \times 10^{-3}$ mbar), reported by Vayenas et al. [8].

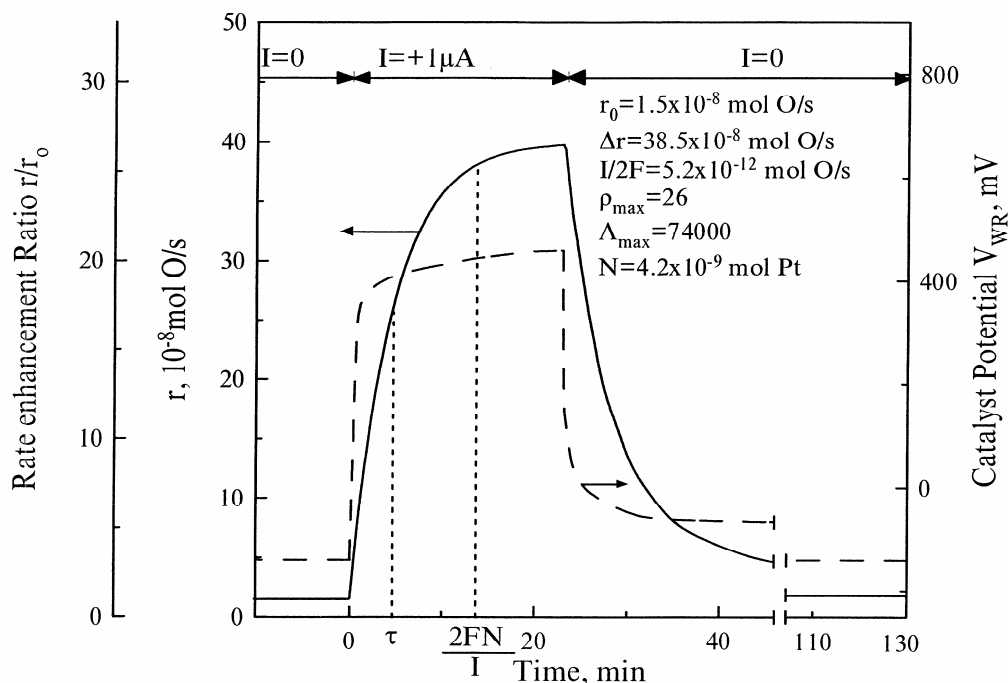


Figure 2.2: A typical galvanostatic NEMCA experiment of ethylene oxidation at a Pt/YSZ catalyst. The experimental (τ) and computed ($2FN/I$) rate relaxation time constants are indicated on the figure. The parameter ($2FN/I$) is the number of active sites of the Pt catalyst (N is the Pt/gas interface surface area in mol Pt). The dashed line represents the catalyst WE electrode potential, V_{WR} , response with respect to the reference electrode. Experimental conditions: $T=643$ K, $p(O_2)=4.6 \times 10^{-2}$ mbar, $p(C_2H_4)=3.6 \times 10^{-3}$ mbar, adopted from Vayenas et al. [8]. Not the experiment carried out in the setup of Fig. 2.1a.

As indicated by Fig. 2.2 under open-circuit (OC) conditions ($I = 0$, no electrochemical rate contribution) the catalytic reaction rate is equal, $r_0 = 1.5 \times 10^{-8}$ mol O/s. We now apply a positive constant current ($I_{WE} = 1 \mu\text{A}$) between the Pt WE catalyst and the counter electrode. In this way oxygen ions, O^{2-} , are supplied to the catalyst at a rate $I/2F = 5.2 \times 10^{-12}$ mol O/s, according to Faraday's law. The catalytic rate starts increasing and within 25 min gradually reaches a value $r = 4 \times 10^{-7}$ mol O/s which is 26 times larger than the initial value r_0 . Since a positive current or potential causes O^{2-} ions to be drawn to the WE, the measured increase in catalytic C_2H_4 combustion seems simply to be caused by the additional oxygen supply. Unexpectedly, the rate increase is strongly non-Faradaic by a factor of 74000! This means the increase in the catalytic rate is 74000 times larger than the Faradaic rate $I/2F$. Thus each O^{2-} ions supplied to the Pt catalyst causes at steady-state 74000 oxygen atoms, chemisorbed on the Pt surface, to react with C_2H_4 and to form CO_2 and H_2O .

Vayenas et al. introduced the term Faradaic efficiency or Λ -factor which is the electrochemically induced rate increase divided by the Faradaic rate. In Fig. 2.2 Λ has a value of 74000. The highest Λ -factor is reported with $\Lambda = 3 \times 10^5$ for the same reaction (i.e. ethylene oxidation over Pt/YSZ), but under application of a constant potential $V_{WR} = +1$ V to the Pt WE with respect to the RE, meaning that each transported O^{2-} ion catalyzes the oxidation of about 1×10^5 C_2H_4 molecules to CO_2 [8]. Also Λ -values are possible to be negative values depending on whether a positive or negative applied electric potential or current causes a promotion effect (i.e. depend on the polarity of the WE). A Λ -factor = 1 means Faradaic reaction. If Λ is smaller than 1, then instead of promotion are has a poisoning effect. The measured Λ -values range from 3×10^5 down to -5×10^4 [11,15,16].

In EPOC experiments two parameters are commonly used to quantify the magnitude of the phenomenon, defined as [11,15,16]:

(a) The faradaic efficiency, Λ , is defined as the ratio of the observed rate increase to the highest possible electrochemical rate:

$$\Lambda = \Delta r / I/2F \quad (2.5)$$

where $\Delta r = r - r_0$ is the change in the catalytic rate caused by the current or potential application and $I/2F$ is the rate of supply ($I > 0$) or removal ($I < 0$) of O^{2-} to or from the catalyst. The applied current is given as I and F is the Faraday's constant. When $|\Lambda| > 1$ the changes in the catalytic rate are non-Faradaic and the reaction exhibits NEMCA

behavior. When $\Lambda > 1$ the reaction is termed electrophobic and when $\Lambda < -1$ the reaction is termed electrophilic. Pure electrocatalysis dominates when $\Lambda = 1$ and the reaction then exhibits regular Faradaic behavior, i.e. the increase in the reaction rate, Δr , equals the rate of ion transport through the electrolyte $I/2F$.

(b) The rate enhancement ratio, ρ , defined as:

$$\rho = r / r_0 \quad (2.6)$$

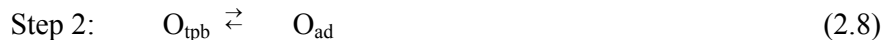
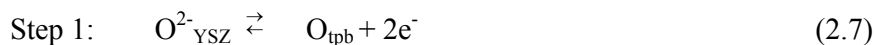
where r is the electropromoted catalytic rate observed under polarization by an applied current or potential and r_0 is the regular (i.e. open-circuit) catalytic rate. For the experiment of Fig. 2.2, the maximum ρ value is 26 [8]; ρ values up to 150 [25] or even higher [26] and down to 0 [9, 27] have been obtained.

2.1.2 Concept of a special spillover species ($O^{\delta-}$ with $\delta \approx 2$)

In order to explain the measured non-Faradaicity of such a reaction system, e.g. the huge Λ -factor of 3×10^5 in case of the ethylene oxidation reaction on Pt/YSZ [8]. Vayenas and co-workers proposed a hypothetical mechanism. The mechanism of the EPOC effect developed for the O^{2-} conducting Pt/YSZ system was based on the existence of two different oxygen species, regular chemisorbed oxygen and a special spillover species which acts as “sacrificial promoter”. This “sacrificial promoter” mechanism which involves two oxygen species has been advocated in numerous papers, reviews and monographs by Vayenas et al. [11,12,15,16]. They proposed an oxygen spillover species which (i) should be strongly polar, i. e. have a charge $O^{\delta-}$ with δ being close to two and (ii) should be bonded more strongly to platinum than chemisorbed oxygen, and (iii) should have a reduced reactivity as compared to chemisorbed oxygen. Owing to the high polarity of the spillover adsorbate complex the spillover oxygen should modify the binding strength of coadsorbed species thus causing a variation of the activation barriers of surface reactions. Since this special spillover species is less reactive than chemisorbed oxygen it can influence the surface reaction of many coadsorbed molecules while being very slowly consumed itself. This special spillover species thus acts very similar to a classic electronic promoter with the non-Faradaicity being a natural consequence of the reduced reactivity.

Comparing this consistent but largely hypothetical concept with the experimental results of the study in this thesis together with the results of earlier investigations one arrives at the following conclusions:

Identity of the oxygen spillover species: Using a microstructured Pt/YSZ sample XPS (X-ray photoelectron spectroscopy) showed that the spillover species is identical to chemisorbed oxygen from the gas phase [28]. The regular chemisorbed oxygen has a binding energy (BE) with an O1s of 530.4 eV. This result is in agreement with physical intuition because oxygen spilling over from the tpb onto the the surface of the metal electrode the oxygen should lose its memory of where it came from originally. The electrochemically induced spillover of oxygen ions onto the surface of the metal electrode is shown in Fig. 2.3. The oxygen ions which are transported through the YSZ solid electrolyte are discharged at the tpb and then the discharged oxygen generated at the tpb (O_{tpb}) spills over the electrode surface forming a layer of chemisorbed oxygen (O_{ad}). One can thus formulate the following steps:



Therefore the net charge transfer (electrocatalytic) reaction at the tpb is:

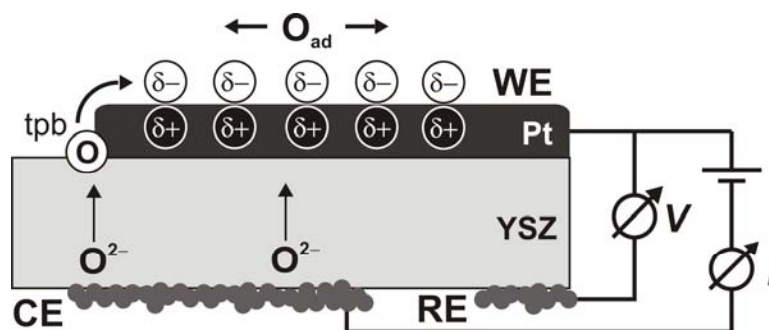


Figure 2.3: Scheme showing the electrochemically induced spillover of oxygen ions onto the surface of the metal electrode, adopted from ref. [29,30]. Oxygen ions are transported through the YSZ solid electrolyte during the anodic (positive) polarization of the metal catalyst (working electrode) and are discharged at the tpb and the discharged oxygen species then migrate onto the surface of the Pt electrode.

In old single XPS measurement done by Vayenas et al. suggested that the special spillover oxygen species has binding energy (BE) with an O1s of 528.8 eV [31]. However, the O1s BE at 528.8 eV often cited as evidence for $O^{\delta-}$ with ($\delta \approx 2$) stems from oxygen of YSZ which floats with the applied potential due to not all parts of the metal catalyst WE electrode may be in electrical contact with each other [32,33] with the consequence that instead of being grounded they will be floating with the potential of the solid electrolyte. Both, the oxygen from the YSZ electrolyte (i.e. O^{2-}) as well as chemisorbed oxygen (O_{ad}) on non-grounded Pt parts will therefore experience a downward shift of roughly 1.2 eV. With these artifacts which are difficult to quantify it is practically impossible to conclude the existence of a new state from the data. In addition, the O1s of 528.8 eV which is cited in all review papers and monographs has been measured in 1993 and since then never been checked again [31].

The proposal of a special oxygen spillover species in Pt/YSZ was not only based on XPS alone but also on the appearance of an additional peak in CV (cyclic voltammetry) and in TPD (temperature-programmed desorption) [11,16,34-37]. All these experiments which are discussed below have been conducted with porous Pt electrodes prepared in the usual way by depositing Pt paste with a brush onto YSZ. CV of the system Pt/YSZ gives rise to a number of peaks reflecting the oxidation or reduction of the oxygen species in this system [34,35,38]. The peak assigned in cyclic voltammetry (CV) by Vayenas et al. [34,35] to the special spillover species was shown to be caused by Si contamination, for other detailed investigations by Janek et al. [38]. In TPD after prolonged electrochemical pumping via positive current or potential application causes significant oxygen spillover from the solid electrolyte YSZ to the catalyst surface and causes oxygen to adsorb in two distinct adsorption states, a strongly bonded “special spillover” ionic oxygen and a weakly bonded atomic oxygen state with a temperature of 50 K lower than that of normally chemisorbed oxygen [35-37]. In fact here have been isotopic O^{16}/O^{18} exchange experiments with Pt/YSZ conducted by Sobyenin et al. demonstrated that an electrochemical polarization of the Pt/YSZ interface does not lead to an enhanced binding strength of oxygen on Pt [39]. These experiments which were conducted in the mbar range also ruled out the existence of a special oxygen spillover species with a binding strength different from that of regular chemisorbed oxygen.

Open question: Strictly speaking, the absence of a valid proof does not mean that this species does not exist. One should therefore leave the possibility open that in the

future some further experiments will be able to demonstrate that at high coverage/high pressure such a special spillover species exists. In any case, up to now no such proof exists. There is insofar agreement as the identity of chemisorbed oxygen and the spillover species at low coverage/low pressure is accepted by Vayenas, i. e. under these conditions only one oxygen species exists [28-30].

2.1.3 Basic empirical relations

I. Open circuit potential (OCP)

In aqueous electrochemistry, electrochemical (charge transfer) reactions take place over the entire metal/electrolyte interface. In contrast, in solid state electrochemistry, electrochemical (charge transfer) reactions take place primarily at the three-phase boundaries (tpb) metal/electrolyte/gas, e.g.:



where O^{2-} represents lattice oxygen in the solid electrolyte YSZ and e^- represents an electron associated with the metal (M) electrode. Generally, the oxygen partial pressure can be determined electrochemically by measuring the potential difference between the two electrodes of an electrochemical cell consisting of a solid electrolyte membranes (e.g. YSZ) onto which two porous electrodes (anode and cathode) are deposited. Consequently, the measured open circuit potential (OCP) V_{WR}^0 or the e.m.f (electromotive force) of the cell that relates the oxygen partial pressures on both sides of the membrane can be calculated by the Nernst equation [16,30,40-44]:

$$V_{\text{WR}}^0 = RT/4F \ln p(\text{O}_2, \text{WE})/p(\text{O}_2, \text{RE}) \quad (2.11)$$

The Nernst equation (2.11) relies on the assumption that oxygen at the electrode surfaces is in equilibrium with gas phase oxygen, i.e. there is equilibrium between gaseous oxygen and oxygen, O_{tpb} , adsorbed at the tpb. In this case an electrochemical equilibrium exist (i.e. $E_{\text{cell}} = 0$). It also required that the net charge transfer (electrocatalytic) reaction at the tpb is given by Eq. 2.9.

As mentioned before C. Wagner [1] who first proposed the used of galvanic cells in heterogeneous catalysis to measure the thermodynamic activity of adsorbed oxygen, O_{ad} , on metal catalyst electrodes interfaced with solid electrolytes during oxidation reactions. This led to a technique called solid electrolyte potentiometry (SEP) as shown in Fig. 2.4. The open circuit potential, V_{WR}^0 , is equal the difference in chemical potential

of gaseous oxygen, $\mu(\text{O}_2)$, between the inside and the outside of the tube in Fig. 2.1a, i.e. between the WE and the RE, respectively.

$$V_{\text{WR}}^{\circ} = 1/4F [\mu(\text{O}_2, \text{WE}) - \mu(\text{O}_2, \text{RE})] \quad (2.12)$$

where $\mu(\text{O}_2, \text{WE})$ and $\mu(\text{O}_2, \text{RE})$ are the chemical potentials of oxygen adsorbed on the WE and the RE, respectively, given by:

$$\mu(\text{O}_2, \text{WE}) = \mu^{\circ}(\text{O}_2, \text{WE}) + RT \ln a_{\text{O}}^2(\text{tpb}, \text{WE}) \quad (2.13)$$

$$\mu(\text{O}_2, \text{RE}) = \mu^{\circ}(\text{O}_2, \text{RE}) + RT \ln a_{\text{O}}^2(\text{tpb}, \text{RE}) \quad (2.14)$$

with μ° is the standard chemical potential of gaseous oxygen at the temperature of the interest. Based on Eq. 2.9 an equilibrium exist at the tpb, i.e. thermodynamic equilibrium is established between gaseous and adsorbed oxygen, the measured open circuit potential, V_{WR}° , is related to the activity of atomic oxygen, a_{O} , at the tpb [16]. Thereby, combining Eqs. 2.12, 2.13 and 2.14 on obtains:

$$V_{\text{WR}}^{\circ} = RT/4F \ln a_{\text{O}}^2(\text{tpb}, \text{WE})/p(\text{O}_2, \text{RE}) \quad (2.15)$$

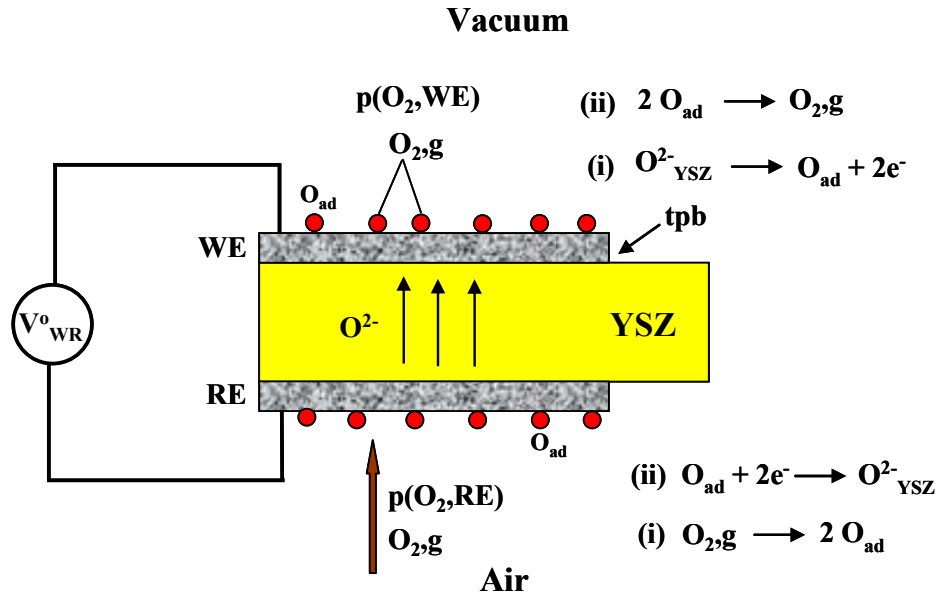


Figure 2.4: Schematic drawing for SEP technique explains the permeation of oxygen species to the working electrode under open circuit conditions at elevated temperature (because the conductivity of YSZ solid electrolyte increase at elevated temperature i.e. $T \approx 650$, see section 2.2), due to transport of oxygen ions (ionic conductivity) that enables oxygen O^{2-} transport from the atmospheric side to the vacuum side.

The RE is exposed to air, thereby $p(\text{O}_2, \text{RE}) = 0.21$ bar (note: dry air contains roughly, by volume, 78% nitrogen, 21% oxygen, 0.93% argon, 0.04% carbon dioxide, and small amounts of other gases [45]). Consequently by measuring V_{WR}^0 and T one can calculate the oxygen activity, $a_{\text{O}}^2(\text{tpb}, \text{WE})$, at the catalyst WE surface.

II. NEMCA time constant (τ)

Setting the potential V_{WR} back to zero in an EPOC experiment, such as the one depicted in Fig. 2.2, the rate returns to its initial value within a few minutes (i.e. in this case EPOC is reversible reaction). As indicated by Fig. 2.2, τ is of the order of $2FN/I$ and this turns out to be a general observation in NEMCA studies with O^{2-} conductors is that the magnitude of τ can be predicted by [11,15,16]:

$$\tau \approx 2FN/I \quad (2.16)$$

with N (mol) represents the number of adsorption sites on the electrode surface and I is the ionic current. The parameter $2FN/I$ denotes the time, τ , required to form a monolayer of O_{ad} on the metal surface i.e. to fill the electrode surface with ions discharged at the tpb. This necessarily requires the spillover of ions discharged at the tpb onto the surface of the metal electrode.

III. Catalyst/solid electrolyte exchange current (I_0)

As mentioned before, the electrocatalytic reactions taking place at the tpb. This means the catalyst/electrode should be also characterized from the electrochemical viewpoint. Strictly speaking the exchange current I_0 is a measure of the electrocatalytic activity of the tpb for a given electrocatalytic reaction. Thus I_0 is a measure of how fast ions are discharged at the interface catalyst/solid electrolyte. In addition it has been shown that the exchange current I_0 is proportional to the length, ℓ_{tpb} , of the tpb [34]. The measurements of I_0 described formally in the Butler–Volmer equation [16,30]:

$$I = I_0 [\exp(\alpha_a F \eta / RT) - \exp(\alpha_c F \eta / RT)] \quad (2.17)$$

where α_a and α_c denote the anodic and cathodic transfer coefficient (usually in the order of unity). I_0 is obtained by plotting the current I versus the overpotential η in a so-called Tafel plot. The electrochemical cell overpotential η_{WR} (between the WE and RE) is given by:

$$\eta_{\text{WR}} = \Delta E = V_{\text{WR}} - V_{\text{WR}}^0 \quad (2.18)$$

where V_{WR}^0 and V_{WR} are the potentials of the WE with respect to the RE under equilibrium conditions (open-circuit, $I = 0$) and when an electric current is flowing

between the WE and CE (closed-circuit, I), respectively. The cell overpotential η_{WR} is the sum of three terms:

$$\eta_{WR} = \eta_W + \eta_R + \eta_{\text{ohmic, WR}} \quad (2.19)$$

where η_W , η_R are the WE and RE overpotentials, respectively. $\eta_{\text{ohmic, WR}}$ is the ohmic overpotential due to the resistance of the solid electrolyte between the WE and the RE.

The current in both galvanostatic and potentiostatic operations is flowing between the WE and the CE. In principle no current at all passes through the RE in ideal case, therefore it should be $\eta_R = 0$ and $\eta_{\text{ohmic, WR}} = 0$. In practice a very small current is passing through the RE, thereby the ohmic drop between the WE and RE, $\eta_{\text{ohmic, WR}}$, is not negligible [11,16]. In aqueous electrochemistry the RE is necessary to be placed as close to the WE as possible in order to minimize the ohmic drop overpotential between the WE and RE, $\eta_{\text{ohmic, WR}}$.

In general the overpotential, η , of an electrode, e.g. WE, is given by:

$$\eta_W = \eta_{\text{ac,W}} + \eta_{\text{conc,W}} + \eta_{\text{ohmic,W}} \quad (2.20)$$

with $\eta_{\text{ac,W}}$, $\eta_{\text{conc,W}}$ and $\eta_{\text{ohmic,W}}$ are the activation, concentration and ohmic drop overpotentials, respectively. The activation overpotential at the WE, $\eta_{\text{ac,W}}$, is due to slow charge transfer reactions (e.g. spillover, adsorption, desorption) at the metal/electrolyte interface. The concentration overpotential, $\eta_{\text{conc,W}}$, is due to slow mass transfer of reactants and /or products involved in the charge transfer reactions. In solid electrolyte cells mass transfer in the gas phase is fast, thereby, gaseous concentration overpotential is negligible i.e. $\eta_{\text{conc,W}} = 0$, in contrast in liquid electrochemistry, the concentration overpotential is very important due to low diffusion of reactants and /or products in liquid phase. In our case the metal catalyst (WE) is a conductive film, therefore the ohmic overpotential, $\eta_{\text{ohmic,W}}$, is negligible. Finally, in solid electrolyte cells the overpotential of the WE is given by:

$$\eta_W = \eta_{\text{ac,W}} \quad (2.21)$$

Now, we can rewrite Butler–Volmer (Eq. 2.17) used for measurements the catalyst/electrolyte exchange current I_0 as follow [16]:

$$I = I_0 [\exp(\alpha_a F \eta_{\text{ac}}/RT) - \exp(\alpha_c F \eta_{\text{ac}}/RT)] \quad (2.22)$$

Where η_{ac} represents the activation overpotential of the electrode.

IV. Catalyst work function (Φ)

Definition: Work function, Φ , is defined as the minimum energy (eV) needed to remove an electron from a solid at a distance of few μm to a point immediately outside the solid

surface, i.e. the energy needed to escape an electron from the Fermi level, E_F , of the solid into vacuum. Figure 2.5 shows a schematic energy diagram of metals and semiconductors. In metals, the valence bands (VB) are filled with electrons up to the Fermi level. As indicated by Fig. 2.5a, in metals the work function and ionization energy (energy difference between valence bands maximum, VBM, and vacuum level) are the same [46]. In semiconductor the VB and conduction bands (CB) are separated by the band gap (E_g), thereby the Fermi level is located within the band gap. This means, in semiconductors the work function is different than the ionization energy (Fig. 2.5b).

Following the literature clean metal surfaces have work function, Φ_0 , values which vary between roughly ≈ 2 eV for alkali metals and $\approx 5-6$ eV for noble transition metals such as Pt [47]. It is important to notice that the work function of a given solid surface is strongly affected by the condition of the surface i.e. it changes significantly during chemisorption. Thus oxygen adsorption on transition metal surfaces such as Pt causes increases in the Φ up to ≈ 1 eV (see chapter 6). *In general electronegative (electron acceptor, e.g. oxygen) adsorbates on solid surfaces cause an increase in the Φ , while electropositive (electron donor, e.g. Na) adsorbates on solid surfaces cause a decrease in the Φ [16].*

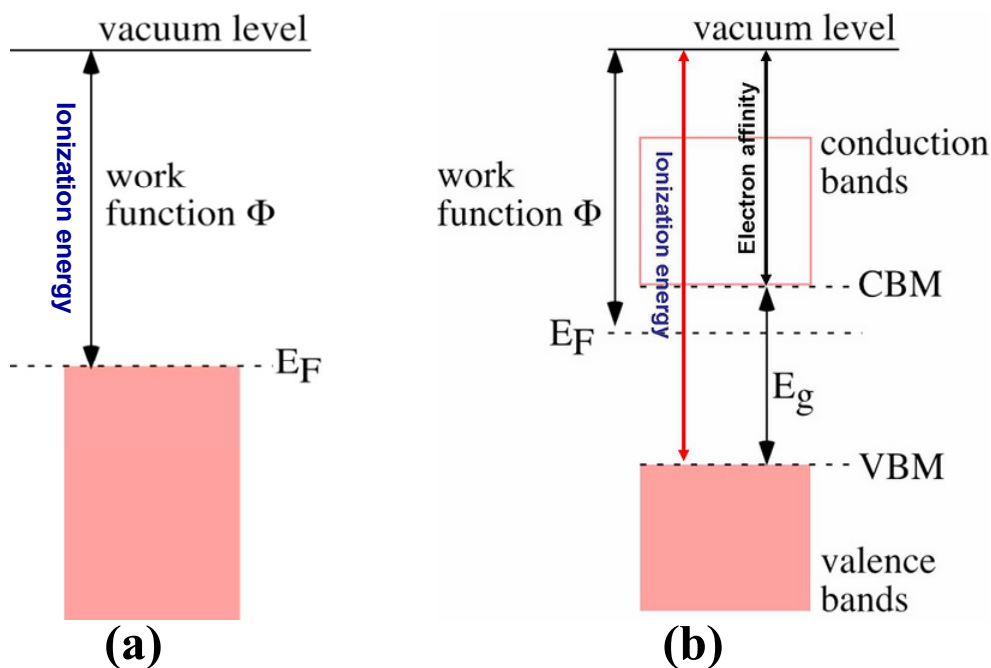


Figure 2.5: Schematic energy diagram of: (a) a metal, and (b) a semiconductor. Adapted and modified from ref. [48].

Measurements: Three techniques are commonly used for work function measurements: Kelvin probe (KP), UPS (ultra violet photoelectron spectroscopy) and PEEM (photoelectron emission microscopy). UPS allows the measurement of the absolute work function while KP gives only the contact potential difference (CPD) between the actual probe of a flat Au element with known work function ≈ 5 eV and the sample surface. Calibration with UPS allows turning KP results into absolute values [48].

Work function changes during EPOC experiments: Changes in the catalyst work function under reaction conditions (e.g. EPOC experiments) can be measured relatively easy with a Kelvin probe. Electrochemical promotion induced, by application of an electrical potential difference between the working-catalyst electrode and the reference, V_{WR} , causes a changes in the catalyst work function, $\Delta\Phi$.

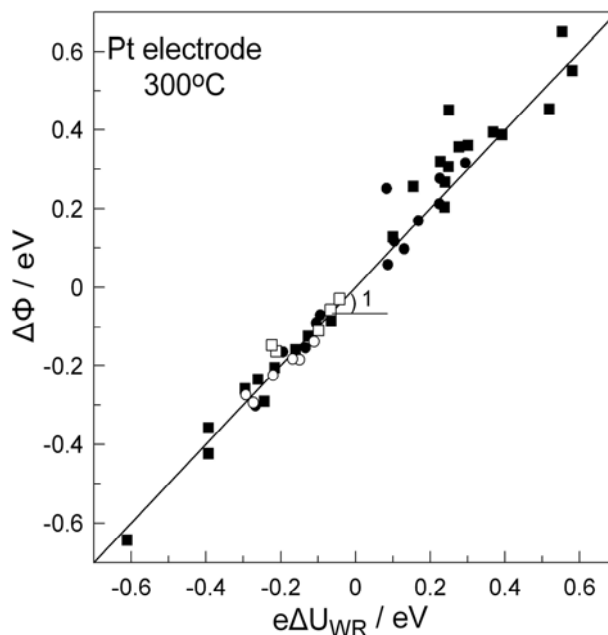


Figure 2.6: One-to-one relationship between variation of the applied potential, V_{WR} , and the work function changes, $\Delta\Phi$, of the Pt catalyst electrode using different solid electrolytes under open (open symbols) and closed circuit conditions (filled symbols). Squares: YSZ, $T = 573$ K and Circles: $\beta''\text{-Al}_2\text{O}_3$, $T = 513$ K, From ref. [14].

As shown by Fig. 2.6 catalyst work function measurements performed by Vayenas et al. using the Kelvin probe technique over Pt catalyst interfaced to O^{2-} conducting YSZ and Na^+ conducting $\beta''\text{-Al}_2\text{O}_3$, revealed that the changes in the work function, $\Delta\Phi$, vary with the applied potential with a one-to-one relation [14,49]:

$$\Delta\Phi = V_{WR} \quad (2.23)$$

The proposed equality between applied potential, V_{WR} , and the $\Delta\Phi$ changes of the catalyst has always occupied a central place on the EPOC effect because it was seen as the essential connection between electrochemistry and catalysis in the EPOC [11,12,14-16,49,50]. This relation also shows that the surface of the catalyst is modified, i.e. changes in the catalyst's work function modify the binding strength of the chemisorbed reactants and intermediates, thus giving rise to changes in the catalytic activity. Experimentally, the above relation was shown to hold only for part of the systems and only over a limited range of V_{WR} of roughly 1 eV as shown by Fig. 2.6. Despite the fact that the proposed equality only holds in a limited number of cases over a certain potential range, this strikingly simple relationship has stimulated efforts to derive it on a theoretical basis [30, 51-55].

V. Catalytic rate dependence on the applied potential (V_{WR})

It has been proposed that the catalytic rate depends exponentially on the applied catalyst potential as follows [16]:

$$\ln(r/r_0) = \alpha(V_{WR} - V_{WR}^*)/kT \quad (2.24)$$

where k is Boltzmann's constant; α and V_{WR}^* are adjustable parameters specific for each reaction system. With Eq. 2.23 the above equation can be written as:

$$\ln(r/r_0) = \alpha(\Phi - \Phi^*)/kT \quad (2.25)$$

The NEMCA coefficient, α , is positive when the rate increases with rising Φ of the catalyst (electrophobic reactions) and negative when the rate decreases with rising Φ of the catalyst (electrophilic reactions), typically α takes values between -1 and 1 [11,15,16].

VI. Permanent EPOC (P-EPOC)

Electrochemical promotion is called "permanent" if the reaction rate under open-circuit conditions after current or potential interruption remains different from the value before current or potential application. As shown in Fig. 2.7 the EPOC effect is generally completely reversible, whereas irreversible "permanent" EPOC has been observed under certain conditions. Experimentally, the first observation of P-EPOC made by Cominellis et al. for C_2H_4 oxidation on IrO_2 as an electrode on a YSZ solid electrolyte cell [56]. An electrochemical promotion leading to an enhanced activity which persist after switching off the electric potential and has been summarized under "permanent EPOC" or "permanent NEMCA effect" [56-61]. The activation of the catalyst is

explained through the formation of a higher oxide, $\text{IrO}_{2+\delta}$. In the light of the experiments with ethylene oxidation over Pt/YSZ (see chapter 6), it is very likely that often a restructuring of the catalyst is behind this so-called "permanent EPOC" effect.

In order to quantify the irreversible character of the promotion a "permanent" rate enhancement ratio, γ , Comninellis and co-workers used [56-61]:

$$\gamma = r_{\text{per}}/r_0 \quad (2.26)$$

where r_0 and r_{per} denote the open-circuit catalytic rate before and after the polarization pulse, respectively.

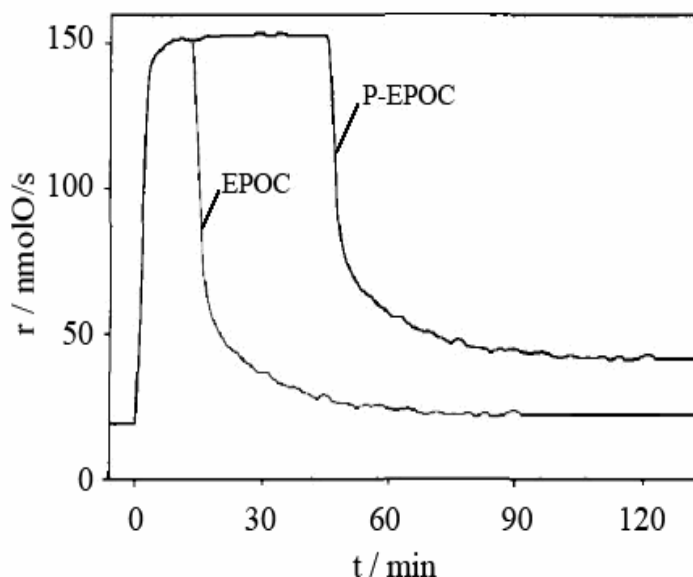


Figure 2.7: A typical galvanostatic NEMCA experiment of ethylene oxidation at IrO_2/YSZ catalyst due to current application ($300 \mu\text{A}$) for two different polarization times: (a) short polarization to give reversible EPOC and (b) long polarization to give P-EPOC. Experimental conditions: $T = 380 \text{ }^\circ\text{C}$, $p(\text{O}_2) = 17 \text{ kPa}$, $p(\text{C}_2\text{H}_4) = 140 \text{ Pa}$, reproduced from ref. [61].

2.2 Solid electrolytes (SE's)

In solid-state ionic, solid electrolytes, also known as fast ion conductors, are materials that act as solid state ion conductors and are used primarily in solid oxide fuel cells (SOFC). They conduct electrically not due to the transport of electrons, but via the movement of ions through vacancies (voids, or empty crystallographic positions) in their crystal structure. One component of the structure, the cation or anion, is essentially free to move throughout the structure, acting as charge carrier. SE's should have high ionic conductivity and low electronic conductivity.

SE's are intermediate in nature between crystalline solids which possess a regular structure with immobile ions, and liquid electrolytes which have no regular structure and fully mobile ions. The preparation, properties, and some applications of SE's have been discussed in a number of books [62-64] and reviews [65,66]. The major commercial application of SE's is in gas sensors [67,68] and SOFC [69,70]. SE's play an increasingly important role in heterogeneous catalysis, both as nanodispersed catalyst carriers and as supports of thick or thin, electrochemically promoted films [11,16,30,71-74]. Solid electrolytes can be made from organic or inorganic materials, good examples of SE's are:

- Yttrium stabilized zirconia (YSZ), an O^{2-} conductor at temperature higher than 250 °C.
- β'' - Al_2O_3 , which is conductive for Na^+ ion at temperature between 180 and 300 °C.
- $CsHSO_4$, and Nafion, which are proton conductors at temperatures about 150 and 25 °C, respectively.
- CaF_2 , conductive for F^- ions at temperature between 550 and 700 °C.
- Mixed ionic-electronic conductors such as TiO_2 and CeO_2 .

The most often used SE in EPOC experiments is yttrium stabilized zirconia (YSZ). Therefore, in the next section, a short description is provided of some important properties of YSZ.

2.2.1 Zirconia (ZrO_2)

Pure Zirconia (ZrO_2) has three well-defined crystal structures that are stable depending on temperature and pressure, namely, the monoclinic, tetragonal, and cubic structures. The monoclinic crystal structure is stable from room temperature up to ≈ 1100 °C, where it transforms over a 100 °C temperature range to the tetragonal phase; at temperature greater than 2370 °C the compound adopts the cubic fluorite structure [75-77]. The cubic fluorite crystal structure (face centered cubic, fcc) of ZrO_2 is shown in Fig. 2.8 [78]. Changes in crystal structure from one phase to another result in a volume change of the lattice. The volume expansion caused by the transformation for cubic to tetragonal to monoclinic induces large stresses, and these stresses cause ZrO_2 to crack upon cooling from high temperatures.

In order to alleviate this phase instability problem and improve ionic conductivity through the creation of more oxygen vacancies, pure ZrO_2 is typically doped with a second lower-valent oxide (i.e. lower-valence cation), such as magnesia (MgO), yttria (Y_2O_3), calcia (CaO), and ceria (Ce_2O_3) [77]. The dopant is introduced as a solid solution that acts to stabilize the zirconia in a particular crystal structure from room temperature to the operational temperature.

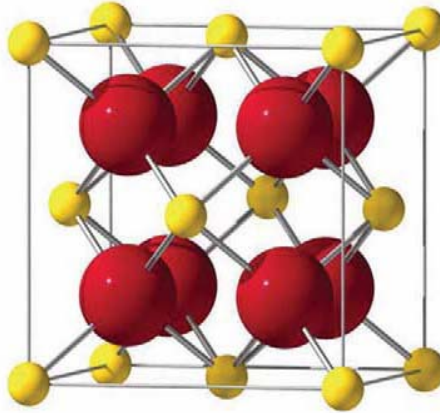


Figure 2.8: Cubic fluorite crystal structure of stabilized zirconia (ZrO_2), with O ions shown in red and the smaller Zr ions shown in yellow, from ref. [78]. The cubic fluorite structure has a face-centered cubic (fcc) zirconia lattice and a cubic oxygen lattice placed in the fcc lattice. The Zr^{4+} cations occupy the tetrahedral sites and the O^{2-} anions occupy the octahedral sites. The remaining octahedral sites are occupied by the Zr^{4+} cations.

2.2.2 Yttrium stabilized zirconia (YSZ)

- **Composition**

Yttrium stabilized zirconia (YSZ) is a zirconium-oxide based ceramic, in which the particular crystal structure of zirconium oxide stabilized at room temperature by the addition of yttrium oxide. These oxides are commonly called "zirconia" (ZrO_2) and "yttria" (Y_2O_3). The addition of yttria to pure zirconia replaces some of the Zr^{4+} ions in the zirconia lattice with Y^{3+} ions. This produces oxygen vacancies to maintain charge neutrality in the lattice, as three O^{2-} ions replace four O^{2-} ions as shown in Fig. 2.9 [79]. The oxygen vacancies make it possible for oxygen ions to move through the electrolyte by hopping from vacancy to vacancy in the lattice. It also permits yttrium stabilized zirconia to conduct O^{2-} ions (and thus conduct an electrical current), provided there is

sufficient vacancy site mobility, a property that increases with temperature. This ability to conduct O^{2-} ions makes YSZ well suited to use in solid oxide fuel cells (SOFC), although it requires that they are operated at high enough temperature.

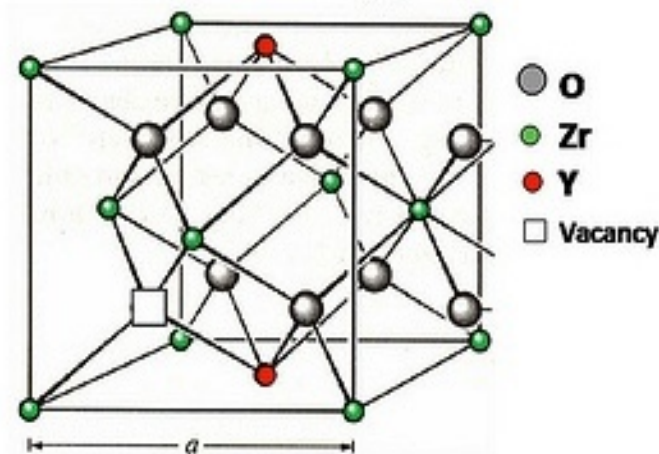


Figure 9: Yttrium stabilized zirconia (YSZ) cubic fluorite type structure, adopted from ref. [79].

To conclude, the addition of Y_2O_3 stabilizes the zirconia cubic fluorite structure to room temperature and changes the non-conducting zirconia into an ion conducting material (i.e. YSZ, an O^{2-} conductor). The defect chemical reaction resulted from the doping or incorporation of Y_2O_3 into ZrO_2 can be expressed by Kröger-Vink notation [80,81]:



The oxygen vacancies are mobile at high temperatures and give rise to high ionic oxygen conductivity. More than 99% of the current through YSZ is carried by oxide ions. The oxygen vacancies experience two types of interactions in the lattice, the repulsion between the oxygen vacancies themselves and with other positively charged carriers, and the attraction between oxygen vacancies and the acceptor cations [82].

- **Effect of composition on the ionic conductivity**

The maximum ionic conductivity lies around 8-10 mol% Y_2O_3 doping. In earlier considerations [83], it is stipulated that, at low dopant content, i.e., less than 8 mol% Y_2O_3 , the introduction of Y creates oxygen vacancies and acceptor centers. One half of dopants can form the acceptor-oxygen vacancy associations, also called the dipoles

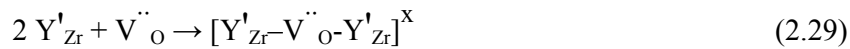
$[Y'_{Zr}-V''_O]$ complex, while the other will be present as Y'_{Zr} species [82,84]. Hence, the main defect associates present in the lattice are the dipoles $[Y'_{Zr}-V''_O]$ complex. In the dipoles, the oxygen vacancies, however, are only bonded to one cation each and the resulting defect associates are not electrostatically neutral but have a positive effective charge. The oxygen vacancy is only partially hindered in its mobility [82]:



In this case electrostatic interactions among charged defects take place, which results in an increase of the activation energy. Therefore, an increase of the ionic conductivity at low dopant Y_2O_3 content takes place [84].

By increasing the dopant content, the amount of dopant cations and vacancies increases. At $\approx 8-10$ mol% Y_2O_3 , there is equilibrium between the increase of oxygen vacancies and the increase of electrostatic interactions between the created defects, i.e. the vacancies and the substituted dopant cations. Therefore, a maximum in conductivity will be observed for a specimen with 8-10 mol% Y_2O_3 [84].

At higher doping the attraction between the oxygen vacancies and the yttria will result in the formation of complexes and decrease the mobility of the oxygen vacancies. A further increase of the Y_2O_3 concentration, and thereby of the vacancy concentration, gives more complex associations, which can form clusters. In these clusters the oxygen vacancy is bonded to two cations, decreasing the oxygen vacancies' mobility further. This complex is electrostatically neutral [82,84]:



In this case the interaction among the defects becomes the dominating factor giving rise to a gradual decrease in the electrolyte ionic conductivity, because the mobility of the oxygen ions is hindered [82,84,85].

In fact, those two defects also lead to local lattice distortions, wherein the oxygen vacancies are not free anymore but "blocked" with one dopant cation forming dipoles $[Y'_{Zr}-V''_O]$, or between two dopant cations, forming triplets $[Y'_{Zr}-V''_O-Y'_{Zr}]^X$. Consequently, the formation or the presence of both defect associates seems to determine the phase structure and the ionic conductivity.

A recently conducted experimental study has shown that the ionic conductivity of YSZ increases with increasing dopant Y_2O_3 concentration due to an increase in the ionic charge carrier (oxygen vacancy) concentration as shown in Fig. 2.10a [86].

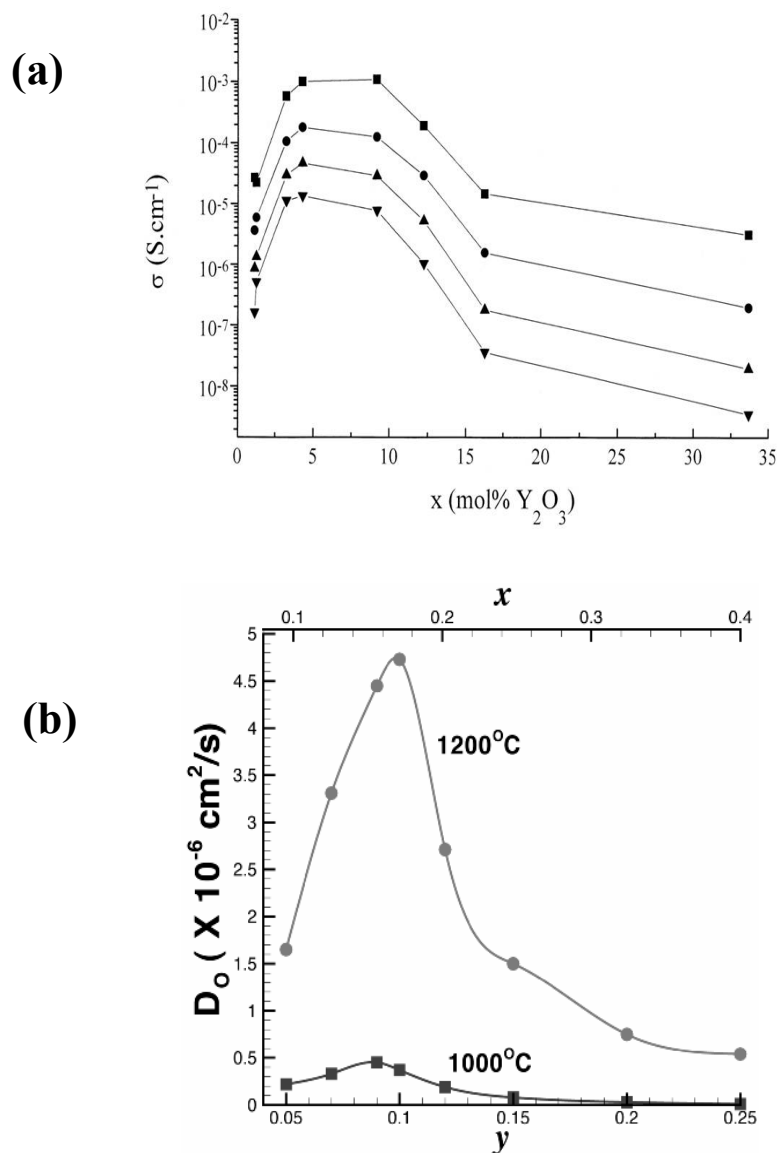


Figure 2.10: The effect of the dopant yttria concentration on the characteristics of YSZ solid electrolyte at different temperatures. (a) On the ionic conductivity of YSZ: (\blacktriangledown) 320 °C, (\blacktriangle) 360 °C, (\bullet) 422 °C and (\blacksquare) 503 °C [86]. (b) On the oxygen self-diffusivity (D_0) as a function of Y_2O_3 mole fraction in YSZ solid electrolyte, adopted from Krishnamurthy et al. [87].

However, the conductivity does not increase monotonically; it decreases after reaching the maximum at a certain dopant concentration. The maximum conductivity is obtained at ≈ 8 -10 mol% Y_2O_3 . This observed decrease in conductivity is probably attributable to the decrease of free oxygen vacancy concentration as displayed in Fig. 2.10b [87]. In general, several hypotheses related to the conductivity decrease behavior observed in zirconia have been suggested [82- 88].

- **Ionic conductivity calculation**

Basic equation: The conductivity of a sample can be calculated when the resistance is measured and the geometry is known [89]:

$$\sigma = d/RA \quad (2.30)$$

where R is the resistance (Ω), d is the distance between the electrodes (m) and A is the electrode surface area (m^2) and σ is the conductivity ($S m^{-1}$).

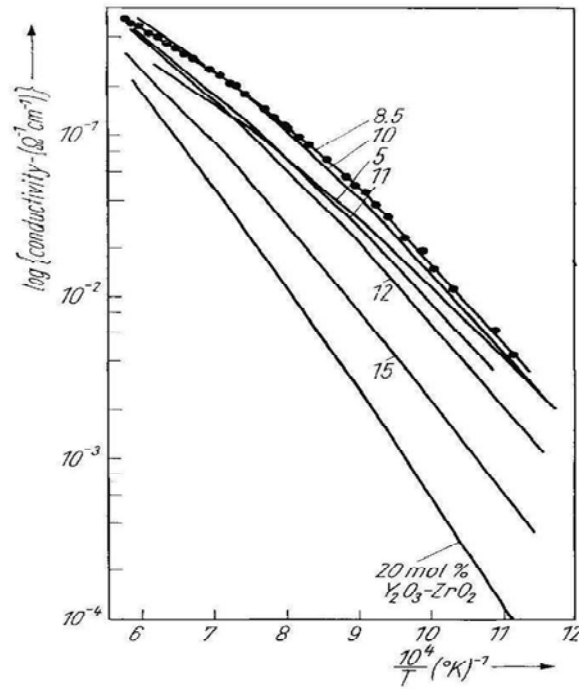


Figure 2.11: Logarithm of bulk conductivity in yttrium stabilized zirconia (YSZ) as function of the reciprocal of absolute temperature obtained in pure oxygen for a range of molar yttria (Y_2O_3) compositions, reproduced from ref. [90].

According to previous studies it was usually assumed that the temperature dependence of ionic conductivity of YSZ solid electrolyte is given by an Arrhenius equation [16,83,85,90-92]:

$$\sigma = \sigma_0 \exp^{-E_a/KT} \quad (2.31)$$

where σ and σ_0 are the ionic conductivity and pre-exponential factor respectively. E_a , K and T are the activation energy, Boltzman's constant and absolute temperature, respectively. The pre-exponential factor, σ_0 , contains all the remaining factors, i.e. other than the activation energy, that influence the ionic conductivity.

It is useful to linearise the Arrhenius equation to make the calculations easier:

$$\ln \sigma = \ln \sigma_0 - (E_a/K) \cdot 1/T \quad (2.32)$$

The above equation gives a straight line between $\ln \sigma$ and $1/T$, the slope of which is equal $(-E_a/K)$. Therefore, the activation energy, E_a , may be deduced easily from the slope. A typical plot between logarithmic conductivity and temperature of the YSZ pellets is shown in Fig. 2.11.

The ionic conductivity is also related to the diffusion coefficient of oxygen anions as given by the Nernst–Einstein expression [80,93]:

$$\sigma = n q^2 D_O/KT \quad (2.33)$$

where n is the number of anion sites per unit volume (i.e. per unit cm^3), q is its charge and D_O the self-diffusion coefficient of oxygen ions.

- **Oxygen transport**

Transport of oxygen through YSZ can be described with the Wagner theory [94]:

$$J(\text{O}_2) = \frac{RT}{4^2F^2L} \sigma_a \ln \frac{P(\text{O}_2)\text{I}}{P(\text{O}_2)\text{II}} \quad (2.34)$$

$$J(\text{O}_2) = \frac{RT}{16F^2L} \sigma_a \ln \frac{P(\text{O}_2)\text{I}}{P(\text{O}_2)\text{II}} \quad (2.35)$$

where $J(\text{O}_2)$ is the oxygen flux ($\text{mol m}^{-2} \text{s}^{-1}$), R is the gas constant, T the absolute temperature, F the Faraday constant, L the thickness of the solid electrolyte (m) and $P(\text{O}_2)\text{I}$ and $P(\text{O}_2)\text{II}$ are the oxygen partial pressures at both sides of the electrolyte (see Fig. 2.4). It is assumed that the oxygen flux is not limited by the surface exchange reaction, only by bulk diffusion. σ_a is the ambipolar conductivity given by:

$$\sigma_a = \frac{\sigma_i \cdot \sigma_e}{\sigma_i + \sigma_e} \quad (2.36)$$

where σ_i is the ionic conductivity and σ_e is the electronic conductivity.

2.3 References

- [1] C. Wagner, *Adsorbed Atomic Species as Intermediates in Heterogeneous Catalysis*, Adv. Catal. 21 (1970) 323.
- [2] C.G. Vayenas, H.M. Saltsburg, J. Catal. 57 (1979) 296.
- [3] M. Stoukides, C. C. Vayenas, J. catal. 70 (1981) 137.
- [4] M. Stoukides, C. C. Vayenas, *Catalysis under Transient Conditions*, ACS Symposium Series 178 (1982) 181.
- [5] M. Stoukides, C. C. Vayenas, J. Electrochem. Soc. 131(4) (1984) 839.
- [6] C. A. Cavalca, G. Larsen, C. C. Vayenas, G. L. Haller, J. Phys. Chem. 97 (1993) 6115.
- [7] S. Bebelis, M. Makri, A. Buekenhoudt, J. Luyten, S. Brosda, P. Petrolekas, C. Pliangos, C.G. Vayenas, Solid State Ionics 129 (2000) 33.
- [8] S. Bebelis, C.G. Vayenas, J. Catal. 118 (1989) 125.
- [9] C.G. Vayenas, S. Bebelis, M. Despotopoulou, J. Catal. 128 (1991) 415.
- [10] C.G. Vayenas, Costas G. Koutsodontis, J. Chem. Phys. 128 (2008) 182506.
- [11] C.G. Vayenas, M.M. Jaksic, S.I. Bebelis, S.G. Nephytides, *The Electrochemical Activation of Catalytic Reactions*, in: J.O.M. Bockris et al. (Eds.), *Modern Aspects of Electrochemistry*, 29, Plenum Press, New York, 1995, p. 57.
- [12] C.G. Vayenas, S.G. Neophytides, *Electrochemical Activation of Catalysis*, in: *Catalysis*, Vol. 12, The Royal Society of Chemistry, Cambridge, 1996, p. 195.
- [13] I.V. Yentekakis, S. Bebelis, J. Catal. 137 (1992) 278.
- [14] C.G. Vayenas, S. Bebelis, S. Ladas, Nature 343 (1990) 625.
- [15] C. G. Vayenas, S. Bebelis, I. V. Yentekakis, H. G. Lintz, *Non-Faradaic Electrochemical Modification of Catalytic Activity: A Status Report*, Catal. Today 11 (1992) 303.
- [16] C.G. Vayenas, S. Bebelis, C. Pliangos, S. Brosda, D. Tsiplakides, *Electrochemical Activation of Catalysis: Promotion, Electrochemical Promotion, and Metal-Support Interactions*, Kluwer Academic / Plenum Publishers, New York, 2001.
- [17] E. Mutoro, N. Baumann, J. Janek, J. Phys. Chem. Lett. 1 (2010) 2322.
- [18] J. Poppe, S. Völkening, A. Schaak, E. Schütz, J. Janek, R. Imbihl, Phys. Chem. Chem. Phys. 1 (1999) 5241.
- [19] B. Luerßen, S. Günther, H. Marbach, M. Kiskinova, J. Janek, R. Imbihl, Chem. Phys. Lett. 316 (2000) 331.
- [20] B. Luerßen, E. Mutoro, H. Fischer, S. Günther, R. Imbihl, J. Janek, Angew. Chem. Int. Ed. 45 (2006) 1473.
- [21] E. Mutoro, S. Günther, B. Luerßen, I. Valov, J. Janek, Solid State Ionics 179 (2008) 1835.
- [22] M. Makri, C. G. Vayenas, S. Bebelis, K. H. Besocke, C. Cavalca, Surf. Sci. 369 (1996) 351.
- [23] I. R. Harkness, C. Hardacre, R. M. Lambert, I. V. Yentekakis, C. G. Vayenas, J. Catal. 160 (1996) 19.
- [24] I. V. Yentekakis, A. Palermo, N. C. Filkin, M. S. Tikhov, R. M. Lambert, J. Phys. Chem. B 101 (1997) 3759.
- [25] C. Pliangos, C. Raptis, T. Badas and C.G. Vayenas, Solid State Ionics 136-137 (2000) 767.

- [26] I. Harkness, R.M. Lambert, J. Catal. 152 (1995) 211.
- [27] C. Karavassilis, S.Bebelis, C.G. Vayenas, J. Catal. 160 (1996) 205.
- [28] B. Luerßen, S. Günther, H. Marbach,, M. Kiskinova, J. Janek, R. Imbihl, Chem. Phys. Lett. 316 (2000) 331.
- [29] B. Luerßen, E. Mutoro, H. Fischer, S. Günther, R. Imbihl, J. Janek, Angew. Chem. Int. Ed., 45 (2006) 1473.
- [30] R. Imbihl, Prog. Surf. Sci. 85 (2010) 240.
- [31] S. Ladas, S. Kennou, S. Bebelis, C. G. Vayenas, J. Phys. Chem. 97 (1993) 8845.
- [32] See Section 6.5 in chapter 6.
- [33] T. Neubrand, S. Günther, A. Fenske, R. Imbihl, Phys. Chem. Chem. Phys. 6 (2004) 3569.
- [34] C.G. Vayenas, A. Ioannides, S. Bebelis, J. Catal. 129 (1991) 67.
- [35] S. G. Neophytides, C. G. Vayenas, J. Phys. Chem. 99 (1995) 17063.
- [36] S. G. Neophytides, D. Tsiplakides, C. G. Vayenas, J. Catal. 178 (1998) 414.
- [37] D. Tsiplakides, S. G. Neophytides, C. G. Vayenas, Ionics 3 (1997) 201.
- [38] E. Mutoro, B. Luerssen, S. Guenther, J. Janek, Solid State Ionics 180 (2009) 1019.
- [39] V.A. Sobyenin, V. I. Sobolev, V.D. Belyaev, O. A. Marina, Catal. Lett. 18 (1993) 153.
- [40] W C Maskell, J. Phys. E: Sci. Instrum. 20 (1987) 1156.
- [41] A.-M. Azad, S.A. Akbar, S.G. Mhaisalkar, L.D. Birkefeld, K.S. Goto, J. Electrochem. Soc. 139 (1992) 3690.
- [42] J. W. Bae, J. Y. Park, S. W. Hwang, G. Y. Yeom, K. D. Kim, Y. A. Cho, J. S. Jeon, D. Choi, J. Electrochem. Soc. 147(6) (2000) 2380.
- [43] R. Moos, K. Sahner, M. Fleischer, U. Guth, N. Barsan, U. Weimar, Sensors 9 (2009) 4323.
- [44] D. Bartha, M. Sahibzadab, D. Mantzavinoseb, I. S. Metcalfe, Solid State Ionics 136 (2000) 621.
- [45] http://www.geo.mtu.edu/~scarn/teaching/GE4250/atmosphere_lecture.pdf
- [46] C. Kittel, *Introduction to solid state physics*, Wiley publishers, Edition 7.
- [47] H. L. Skriver, N. M. Rosengaard, Phys. Rev. B 45 (1992) 9410.
- [48] <http://rsl.eng.usf.edu/Documents/Tutorials/TutorialsWorkFunction.pdf>
- [49] S. Ladas, S. Bebelis, C. G. Vayenas, Surf. Sci. 251/252 (1991) 1062.
- [50] F. J. Williams, A. Palermo, M. S. Tikhov, R. M. Lambert, Surf. Sci. 482-485 (2001) 177.
- [51] I. S. Metcalfe, J. Catal. 199 (2001) 247.
- [52] I. S. Metcalfe, J. Catal.199 (2001) 259.
- [53] I. Riess, C. G. Vayenas, Solid State Ionics 159 (2003) 313.
- [54] E. P. M. Leiva, C. G. Sanchez, J. Solid State Electrochem. 7 (2003) 588.
- [55] J. Fleig, J. Jamnik, J. Electrochem. Soc. 152 (2005) E138.
- [56] J. Nicole, D. T. Tsiplakides, S. Wodiunig, C. Comninellis, J. Electrochem. Soc. 144 (1997) L312.
- [57] J. Nicole, C. Comninellis, J. Appl. Electrochem. 28 (1998) 223.
- [58] D. Tsiplakides, J. Nicole, C. G. Vayenas, C. Comninellis, J. Electrochem. Soc. 145 (1998) 905.
- [59] G. Foti, O. Lavanchy, C. Comninellis, J. Appl. Electrochem. 30 (2000) 1223.
- [60] J. Nicole, C. Comninellis, Solid State Ionics 136–137 (2000) 687.
- [61] C. Falgairrette, A. Jaccoud, G. Foti, and C. Comninellis, J. Appl. Electrochem. 38 (2008) 1075.

- [62] V. N. Chebotin and M. V. Perfilov, *Electrochemistry of solid electrolytes*, Khimiia Publ. House, Moscow, 1978.
- [63] C. Deportes, M. Duclot, P. Fabry, J. Fouletier, A. Hammou, M. Kleitz, E. Siebert, J.-L. Souquet, *Electrochimie des solides*, Press Universitair de Grenoble, Grenoble, 1994.
- [64] H. Rickert, in *Electrochemistry of Solids*, Springer-Verlag, Berlin, 1982.
- [65] E. C. Subbarao, H. S. Maiti, *Solid State Ionics* 11 (1984) 317.
- [66] P. J. Gellings, H. J. M. Bouwmeester, *Catal. Today* 12 (1992) 1.
- [67] W. Göpel, *Sensor and Actuators B*, 18-19 (1994) 1.
- [68] A. Mandelis, C. Christofides, *Solid State Gas Sensor Devices*, John Wiley & Sons, New York 1993.
- [69] P. J. Gellings, H. J. M. Bouwmeester, *The CRC handbook of solid state electrochemistry*, CRC Press, Boca Raton, 1997.
- [70] W. Vielstich, H. A. Gasteiger, A. Lamm, *Handbook of Fuel Cells - Fundamentals, Technology and Applications*, John Wiley & Sons, Ltd, 2003.
- [71] C. G. Vayenas, S. Bebelis, C. Pliangos, S. G. Neophytides, *The electrochemical activation of catalysis*, Kluwer Academic/Plenum Publishers, New York, 1996.
- [72] G. Fóti, I. Bolzonella, C. Comninellis, in *Modern Aspects of electrochemistry*, Vol. 36 C. G. Vayenas, B. E. Conway, R. E. White, and M. E. Gamboa-Adelco, eds., Kluwer Academic / Plenum Publisher, New York, Boston, Dordrecht, London, Moscow, 2003, p. 310.
- [73] R. M. Lambert, F. Williams, A. Palermo, M. S. Tikhov, *Topics in Catalysis*, 13 (2000) 91.
- [74] X. E. Verykios, in *Catalysis and Electrocatalysis at nanoparticle surface*, A. Wieckowski, E. R. Savinova, and C. G. Vayenas, Eds., Marcel Dekker, Inc., New York - Basel, 2003, p. 745.
- [75] E. C. Subbarao, *Zirconia: An overview*, in *Advance in Ceramics*, vol. 3, A. H. Heuer and L. W. Hobbs, Eds.: American Ceramic Society, 1981.
- [76] Z. Ji, J. M. Rigsbee, *Growth of Tetragonal Zirconia Coatings by Reactive Sputter Deposition*, *J. Am. Ceram. Soc.* 48 (2001) 2841.
- [77] *High Temperature Solid Oxide Fuel Cells-Fundamentals, Design and Applications*, Oxford, UK, 2003.
- [78] D. R. Clarke, S. R. Phillpot, *Thermal Barrier Coating Materials*, *Mater. Today*, 2005, p. 22.
- [79] <http://electronicstructure.wikidot.com/predicting-the-ionic-conductivity-of-ysz-from-ab-initio-calc>.
- [80] P.S. Manning, J.D. Sirman, R.A. De Souza, J.A. Kilner, *Solid State Ionics* 100 (1997) 1.
- [81] P. Abelard, J. F. Baumard, *Pure Appl. Chem.* 67 (1995) 1891.
- [82] I. Kosacki, V. Petrovsky, H.U. Anderson, *J. Electroceram.* 4:1 (2000) 243.
- [83] A.I. Ioffe, D.S. Rutman, S.V. Karpachov, *Electrochim. Acta* 23 (1978) 141.
- [84] C. Haering, A. Roosena, H. Schichl, *Solid State Ionics* 176 (2005) 253.
- [85] A. Nakamura, J.B. Wagner Jr., *J. Electrochem. Soc.* 127 (11) (1980) 2325.
- [86] M. Hartmanova, J. Schneider, V. Navratil, F. Kundracik, H. Schulz, E.E. Lomonova, *Solid State Ionics* 136–137 (2000) 107.
- [87] R. Krishnamurthy, Y.-G. Yoon, D. J. Srolovitz, R. Car, *J. Am. Ceram. Soc.* 87 (10) (2004) 182.

- [88] J.A. Kilner, R.J. Brook, *Solid State Ionics* 6 (1982) 237.
- [89] H. J. Avila-Paredes, J. Zhao, S. Wang, M. Pietrowski, R. A. De Souza, A. Reinholdt, Z. A. Munir, M. Martinb, S. Kim, *J. Mater. Chem.* 20 (2010) 990.
- [90] R. E. W. Casselton, *Phys. Stat. Sol.* 2 (1970) 571.
- [91] K. Muthukkumaran¹, P. Kuppasami, E. Mohandas, V.S. Raghunathan, S. Selladurai, *International Symposium on Materials Science and Engineering*, Dec. 20–22, Chennai, India, 2004.
- [92] L. Ying, G. Jiang-Hong, T. Zi-Long, X. Yu-Sheng, Z. Zhong-Tia, *Acta Phys. Chim. Sin.* 17(9) (2001) 792.
- [93] P. P. Kumar, S. Yashonath, *J. Chem. Sci.* 118 (2006) 135.
- [94] P. J. Gellings, H. J. M. Bouwmeester, *The CRC handbook of solid state electrochemistry*, CRC Press, Inc, Florida, 1996.

Chapter 3

Experimental Techniques

The following chapter describes the experimental methods used in this work. As shown below several techniques were used to study the reaction mechanism of ethylene oxidation over a pure Pt and a bimetallic Pt-Ag catalyst electrode interfaced to yttrium stabilized zirconium (YSZ) solid electrolyte.

3.1 Photoemission Electron Microscopy (PEEM)

3.1.1 Introduction

PEEM is a surface-sensitive variant of an electron microscope that images the photoelectrons emitted from a surface upon absorption of photons. The basic idea is to use the work function (Φ), which is very sensitive to the surface chemical composition, to monitor surface concentrations *in situ*, in real time and spatially resolved [1]. For this purpose the sample was illuminated by ultraviolet (UV) radiation. The UV light generates photoelectrons whose intensity strongly depends on the work function and thus indirectly on the chemical composition and on the topography of the surface. The photoelectrons are accelerated into the microscope column, pass through a combination of magnifying lenses, and are projected after amplification with a channel plate onto a phosphorous screen, converting the electron image into a visible image. The visible image displays the strongly magnified distribution of photoelectrons emitted from the surface. This image can be recorded at video rate using a CCD camera, allowing fast changes occurring on the surface to be recorded.

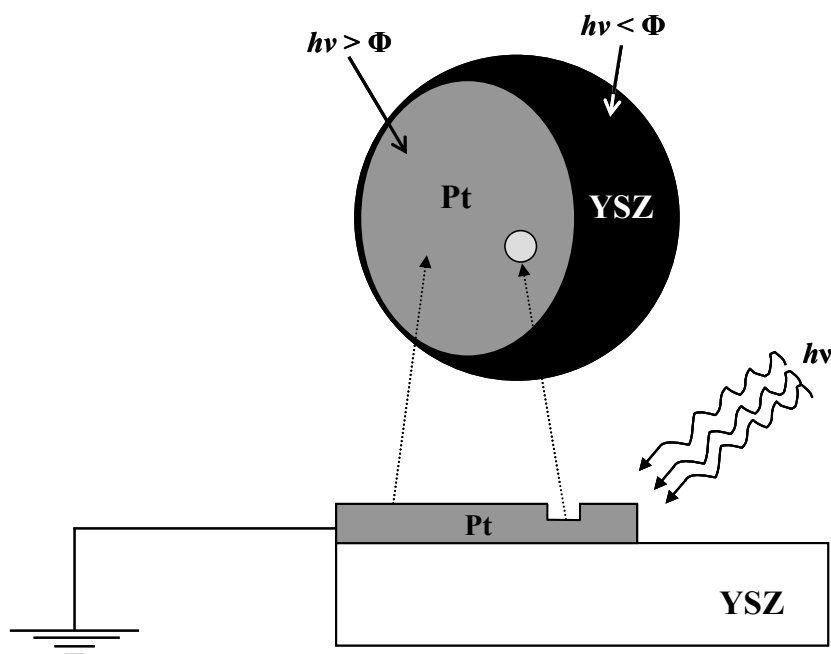


Figure 3.1: Schematic drawing showing a contrast due to different work functions of materials and a so-called topographical contrast mechanism in PEEM present of rough Pt samples. In the image, elevated parts of the Pt sample appear darker than valleys [2]. YSZ= yttrium stabilized zirconia

The contrast of the PEEM images during the reaction arises from the surface topography for [2] and differences in the local changes of the work function caused by the laterally varying adsorbate concentrations.

For low-energy photons (E several eV) generated for example by a laser, a mercury lamp or a deuterium lamp, a chemical contrast can be obtained if elements with different work functions are present at the sample surface. According to Fowler's theory, the change on the work function contrast depends on the photoelectron current (and thus the PEEM intensity) as the following Eq. [3]:

$$I \propto (h\nu - \Phi)^2 \quad (3.1)$$

where I is the photoelectron yield which is proportional to the local intensity of the PEEM image, $h\nu$ is the photon energy ($E = h\nu$), and Φ is the work function. It is possible to determine the absolute Φ of the surface, clean or adsorbate covered, to an accuracy of several meV, by plotting the square root of the total photoelectrons yield versus the photon energy when the $h\nu$ is varied from value ≈ 0.5 eV below the Φ to value ≈ 1 eV above the threshold. In our case, a deuterium discharge lamp (D 200 F, Heraeus Noblelight) is used as light source, which does not emit an isolated UV line, but a continuous spectrum (maximum intensity at 6.2 eV), this leads to more photons with $h\nu > \Phi$ at lower Φ , since both effects add up to produce high intensity at a low work function. Also in this case small changes of Φ strongly affect the PEEM intensity. Regions with high Φ imaged as dark and regions with low Φ are imaged as bright in PEEM as shown in Fig. 3.1. One can *in situ* study the surface Φ changes during the reaction simply by plotting the PEEM intensities versus time or versus temperature.

3.1.2 Instrumentation

A sketch of the microscope is displayed in Fig. 3.2 [4]. As indicated there, the main body is biased to a high positive potential (for this work instead of 20 kV just 12 – 14 kV were used to prevent discharges at high pressures), so the electrons are accelerated into the microscope. Three-lens optics (objective (cathode), intermediate- and projector lens) produce a magnified image, and then the electrons are slowed down in the drift tube to hit the detector with an appropriate energy. A microchannel plate (operated with 1 kV) multiplies the electrons, which are then accelerated again to 5 keV onto a luminescent phosphor screen, producing the visible image. The lateral resolution

of the instrument is $\approx 1 \mu\text{m}$, fields of view (FOV) between 100 and 500 μm can be adjusted.

As shown in Fig. 3.2 from the schematic drawing of the lens system PEEM is a parallel imaging instrument, which uses the complete distribution of the emitted photoelectrons to image the surface region. Therefore the viewed area of the sample must be illuminated homogeneously with appropriate UV light. For investigation surface reactions with PEEM, the channel plate is restricting the operating total pressure below 10^{-6} mbar. Therefore PEEM is differentially pumped (see chapter 4), allowing operation at total pressures up to 10^{-3} mbar. In order to maintain three orders of magnitude pressure difference, an aperture of 300 μm diameter has to be incorporated at the focus of the objective lens. Since there is no direct connection between the microscope and the specimen (5 – 10 mm distance), high sample temperatures can be handled.

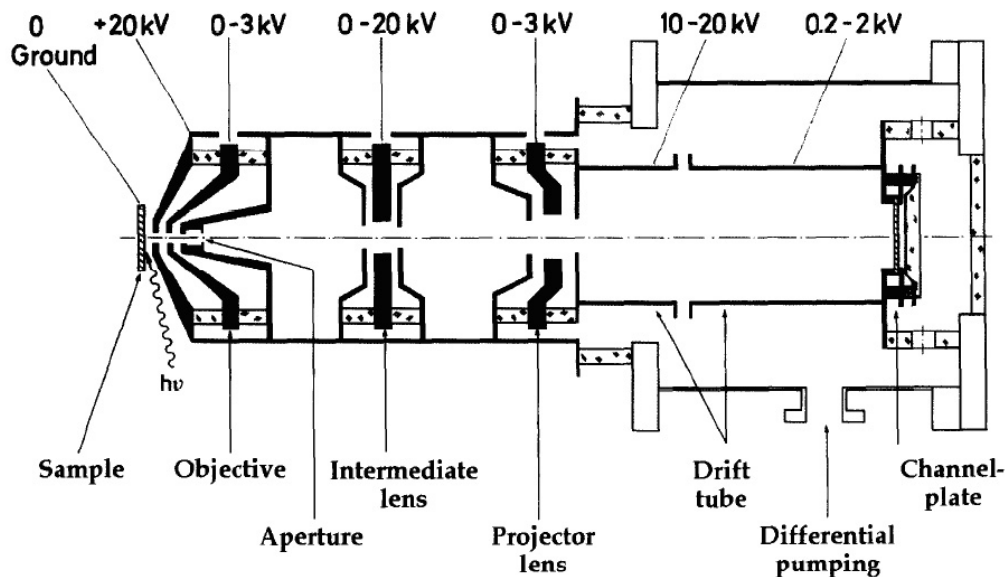


Figure 3.2: Scheme of the photoemission electron microscope (PEEM) designed by Engel [4].

In PEEM, the image on the phosphorous screen was captured by a CCD camera connected to the TV-adaptor of a video recorder. For evaluation and presentation, images or movies were processed with *VirtualDub* [5] or *Giotto* [6]; usually several frames were averaged for noise reduction, and the contrast was optimized.

3.2 X-ray Photoelectron Spectroscopy (XPS)

3.2.1 Introduction

XPS, also known as ESCA (Electron Spectroscopy for Chemical Analysis), is a surface analytical technique that can be used to analyze the surface chemistry of a material. XPS is a qualitative and quantitative spectroscopic technique that measures the chemical state, and electronic state of the elements in surface region of the sample.

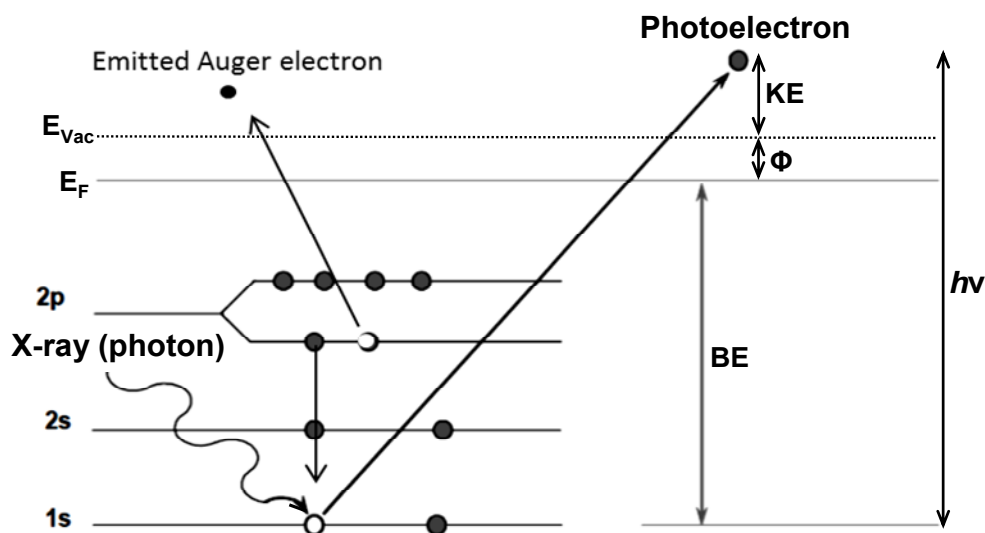


Figure 3.3: Schematic representation of the X-ray photoelectron spectroscopy (XPS) process, modified from [7].

3.2.2 XPS process

XPS involves a single electron process which is based on the photoelectron effect: X-radiation is focused on the sample, either from an X-ray tube or a synchrotron light source. Excitation occurs to all electronic levels energetically accessible to the primary beam. In more detail, an electron is ejected from an atomic energy level by an X-ray photon, mostly from an either monochromatic Al- K_α or non-monochromatic Mg- K_α primary source. Relaxation of the hole can occur through X-ray fluorescence or through an Auger process. An electron from a higher energy level fills the hole left behind and the energy is used to eject an Auger electron. Thus, XPS emits both photoelectrons and Auger electrons which can be seen in the spectrum. The electrons

ejected are analyzed in the XPS detector by measuring the electrons kinetic energy which provides the information to identify the elements present in the sample. The XPS process is schematically represented in Fig. 3.3 for the emission of an electron from the 1s shell of an atom.

The process of photo-ionization (photoemission) can be considered in several ways: one way is to look at the overall process as follows [8]:



The conservation of energy then requires that:

$$E(A) + h\nu = E(A^+) + E(e^-) \quad (3.3)$$

Since the electron's energy is present solely as kinetic energy, KE, this can be rearranged to give the following expression for the KE of the photoelectron:

$$KE = h\nu - (E(A^+) - E(A)) \quad (3.4)$$

The final term in brackets, representing the difference in energy between the ionized and neutral atoms, is generally called the binding energy, BE, of the electron - this then leads to the following commonly quoted Eq.:

$$KE = h\nu - BE \quad (3.5)$$

with h being Planck's constant (6.62×10^{-34} J.s) and ν the photon frequency (Hz) of the radiation. As in Eq. (3.5) the KE of these emitted photoelectrons is determined by the photon energy of the X-ray radiation, $h\nu$, and the BE of the electron. Not that the binding energies, BE, of energy levels in solids are conventionally measured with respect to the Fermi-level of the solid, rather than the vacuum level. This involves a small correction to the equation given above in order to account for the work function of the spectrometer (Φ_{sp}),

$$KE = h\nu - (BE + \Phi_{sp}) \quad (3-6)$$

3.2.3 Instrumentation

XPS instruments consist of an X-ray source, an energy analyzer for the photoelectrons, and an electron detector (see chapter 4). The analysis and detection of photoelectrons requires that the sample be placed in a high-vacuum chamber. Since the photoelectron energy depends on the X-ray energy, the excitation source must be monochromatic. The energy of the photoelectrons is analyzed by an electrostatic analyzer and the photoelectrons are detected by an electron multiplier tube or a multichannel detector such as a microchannel plate.

3.3 The Quadrupole Mass Spectrometer (QMS)

A diagram of a single quadrupole mass spectrometer is shown in Fig. 3.4. In general a mass spectrometer consists of an ion source (bombardment by electrons from a hot filament), a quadrupole mass analyzer and an ion detector.

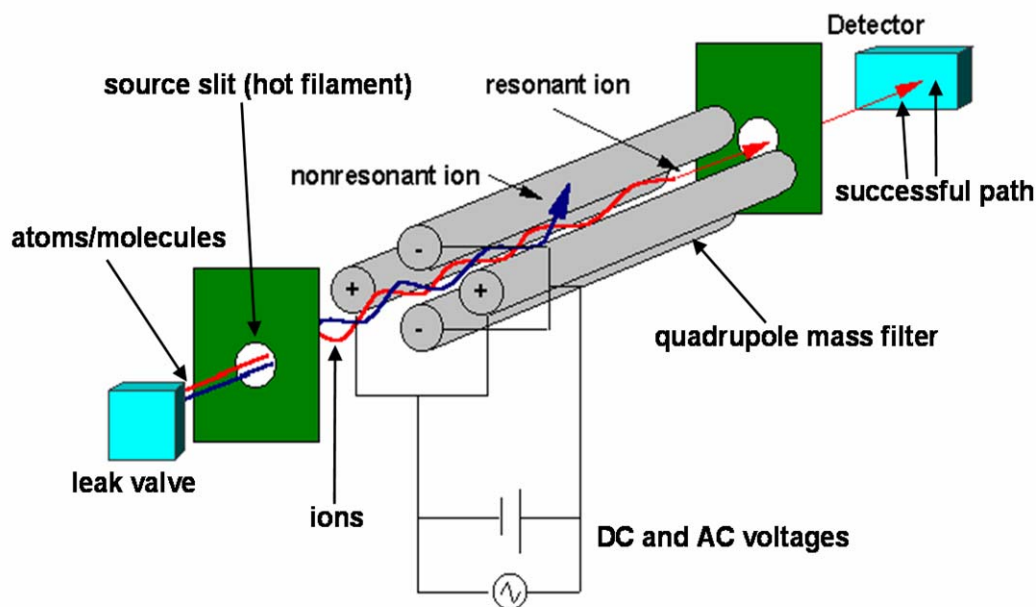


Figure 3.4: Schematic of a Quadrupole Mass Spectrometer (QMS), modified from [9].

A quadrupole mass analyzer consists of 4 circular rods of hyperbolic surfaces. A fixed DC voltage is applied to 2 rods and an AC voltage of radio frequency (RF) is applied to the other 2 rods. These rods generate an electric field through which the ions can move. Firstly the atoms or molecules will be ionized in the source of the instrument and can possibly split into charged fragments with a certain mass-to-charge ratio (m/e). These ions are then focused and passed along the middle of the quadrupoles. The applied voltages affect the trajectory of ions traveling down the flight path centered between the four rods. For given DC and AC voltages, only ions of a certain mass-to-charge ratio pass through the quadrupole filter and all other ions are thrown out of their original path. A mass spectrum is obtained by monitoring the ions passing through the quadrupole filter as the voltages on the rods are varied. Therefore mass spectrometers

use the difference in mass-to-charge ratio (m/e) of ionized atoms or molecules to separate them from each other. Mass spectrometry is therefore useful for quantitation of atoms or molecules and also for determining chemical and structural information about molecules. Molecules have distinctive fragmentation patterns that provide structural information to identify structural components.

3.4 References

- [1] K. Christmann, *Introduction to Surface Physical Chemistry*, Steinkopf/Springer, Darmstadt/Berlin 1991.
- [2] J. Stöhr, S. Anders, *IBM J. Res. Develop.* 44 (2000) 535.
- [3] R. H. Fowler, *The Analysis of Photoelectric Sensitivity Curves for Clean Metals at various Temperatures*, *Phys. Rev.* 38 (1931) 45.
- [4] W. Engel, M. E. Kordesch, H. H. Rotermund, S. Kubala, A. von Oertzen, *A UHV-compatible photoelectron emission microscope for applications in surface science*, *Ultramicroscopy* 36 (1991) 148.
- [5] A. Lee, *VirtualDub* 1.9.7 (2009).
- [6] Dittelssoft, *Giotto* 2.1.2 (2007).
- [7] http://webh01.ua.ac.be/mitac4/micro_xpsaes.pdf
- [8] http://www.chem.qmul.ac.uk/surfaces/scc/scat5_3.htm
- [9] <http://www.files.chem.vt.edu/chem-ed/ms/quadrupo.html>

Chapter 4

Experimental Setup

In this chapter, a detailed description of the experimental setups are given, some of the important operation methods of the instruments and experiments are presented as well.

4.1 Low pressure experiment for PEEM

4.1.1 Sample preparation

Electrode preparation and characterization will be explained in detail in chapter 5. Here only a short summary. The electrical connection of the three-electrodes has been done in two steps: a small Pt mesh was pressed into the edge of each electrode using platinum paste followed by sintering in air at 1123 K for 2 h in order to get a good contact as shown by Fig. 4.1. Secondly, platinum wires (0.1 mm thick, 99.95% purity, hard, supplier: Goodfellow GmbH, Germany) were spot-welded to the Pt mesh to connect the centre of the electrodes to an electrical circuit. The oxygen transfer flux from the cathode to the anode across the YSZ substrate is controlled by changing the applied voltage.

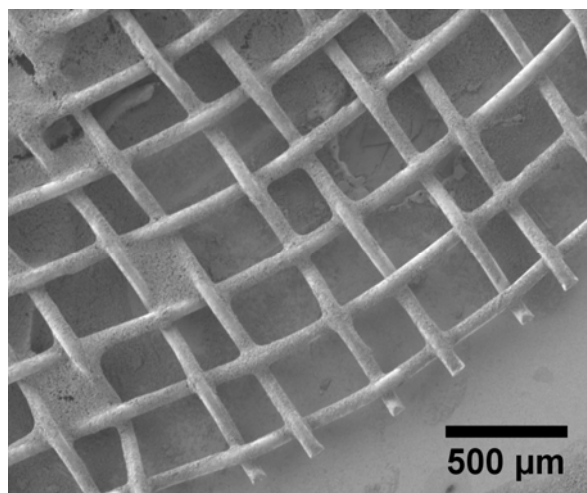


Figure 4.1: SEM micrograph of a platinum mesh prepared on a Pt/YSZ electrode after sintering for 2h in air at 1123 K.

4.1.2 Electrochemical setup

For the electrochemical measurements a standard three-electrode setup was used with EG&G Potentiostat/Galvanostat Model 273A controlled by a PC using 352 corrosion software controlling the potential of the WE with respect to a reference electrode as displayed in Fig. 4.2. Since no gas reference electrode was used the potential of the reference electrode is not fixed but may shift due to zirconia reduction at the interface YSZ/Pt of the reference electrode. In order to minimize this effect the sample was exposed to prolonged O₂ treatments after each set of experiments.

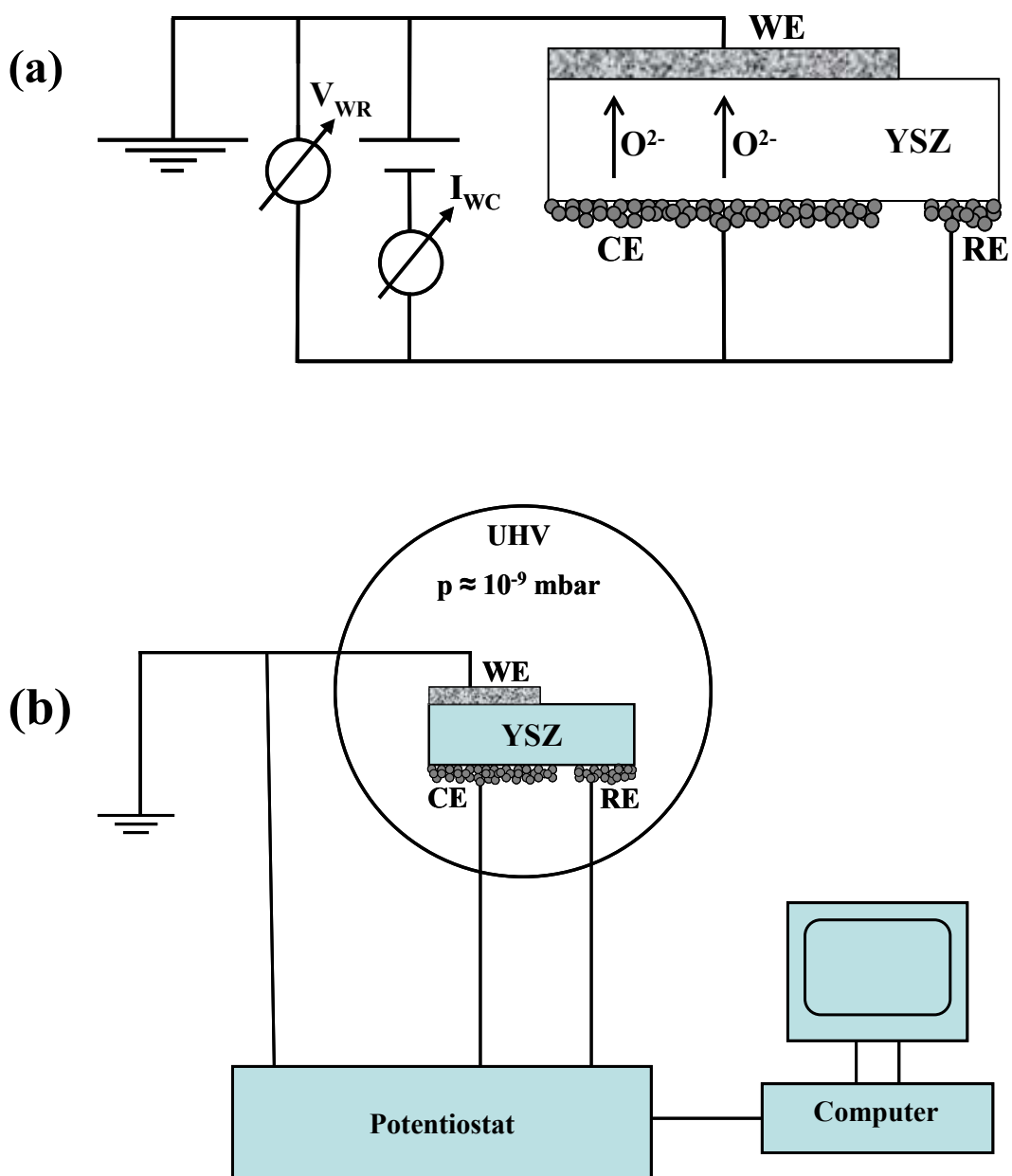


Figure 4.2: Schematic drawing of the electrochemical experimental setup. YSZ= yttrium stabilized zirconia, WE= working electrode, CE= counter electrode, RE= reference electrode.

4.1.3 Reaction experiments and sample holder

The experiments were conducted in a standard 100 L UHV system (Varian) equipped with PEEM for spatially resolving measurements and a differentially pumped QMS for rate measurements.

In PEEM the sample was illuminated with photons from a D₂ discharge lamp (photon energy $\approx 5 - 6$ eV) focused the photons into a small spot of the sample (≈ 2 mm²). The instrument itself was differentially pumped by a turbomolecular pump (Pfeiffer TMU 261 P, 230 L s⁻¹) to allow working pressures up to 10⁻³ mbar as shown by Fig. 4.3. The emitted photoelectrons were collected by an electrostatic three-lens system, amplified by a channel plate and then imaged onto a phosphorus screen. The images were then recorded with a CCD camera and digitalized. In this way the local work function can be imaged with a spatial resolution of roughly 1 μ m and the temporal resolution of video images (20 ms).

A highly precision UHV specimen manipulator (OMNIAX) supports the sample movements in the chamber in all directions (x, y, z), rotation in 360° and tilt. Utilizing these options, the face of the sample can be adjusted to the surrounding instruments for surface preparation and analysis. A standard ion gun (Leybold-Heraeus IQE 10/35) is used for the sample cleaning via ion bombardment at 0.5 to 5 keV.

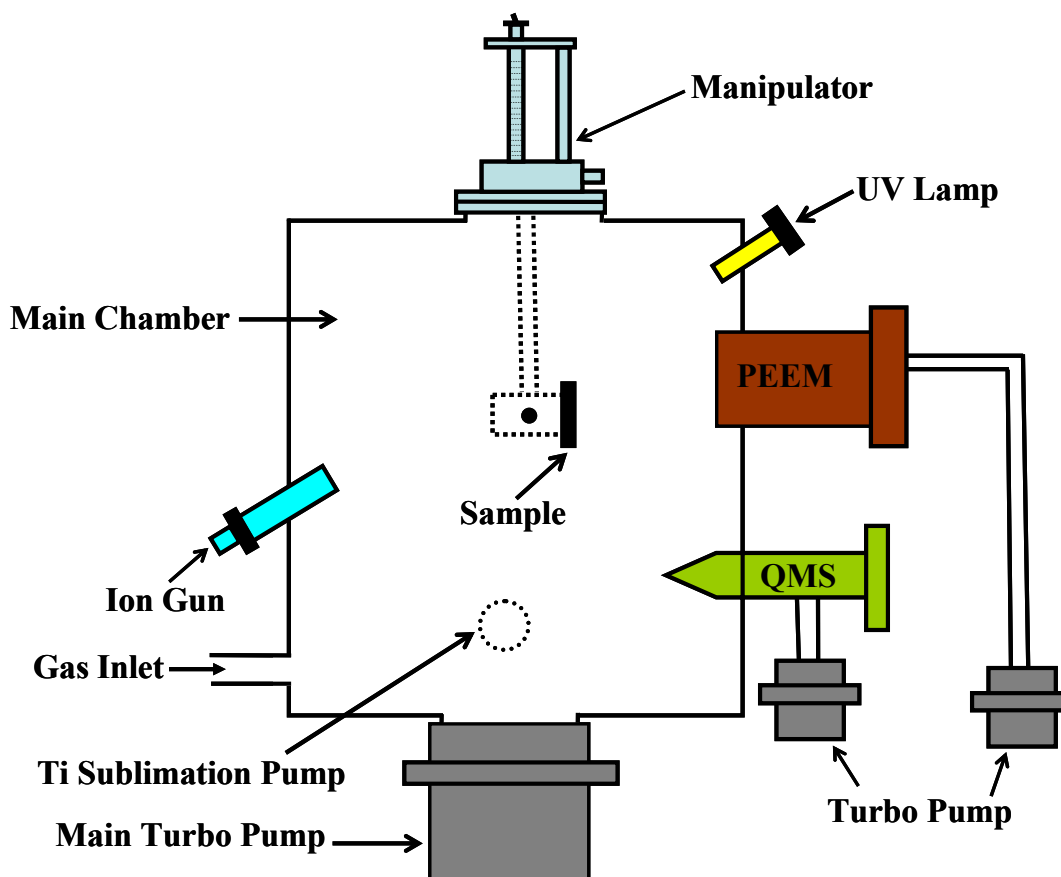


Figure 4.3: Schematic drawing of the UHV system equipped with PEEM and QMS.

Figure 4.4 shows a photograph of the mounted sample. The cell system composed of Pt/YSZ/Pt was mounted in Mo-sample holder into the UHV system. The YSZ sample was radiatively heated from the backside by a commercial slide projector lamp (Halogen photo optic lamp, XENOPHOT OSRAM, 24 V, 250 W). Sample temperatures were monitored by a K-type Ni/NiCr thermocouple spot-welded into the front of the sample.

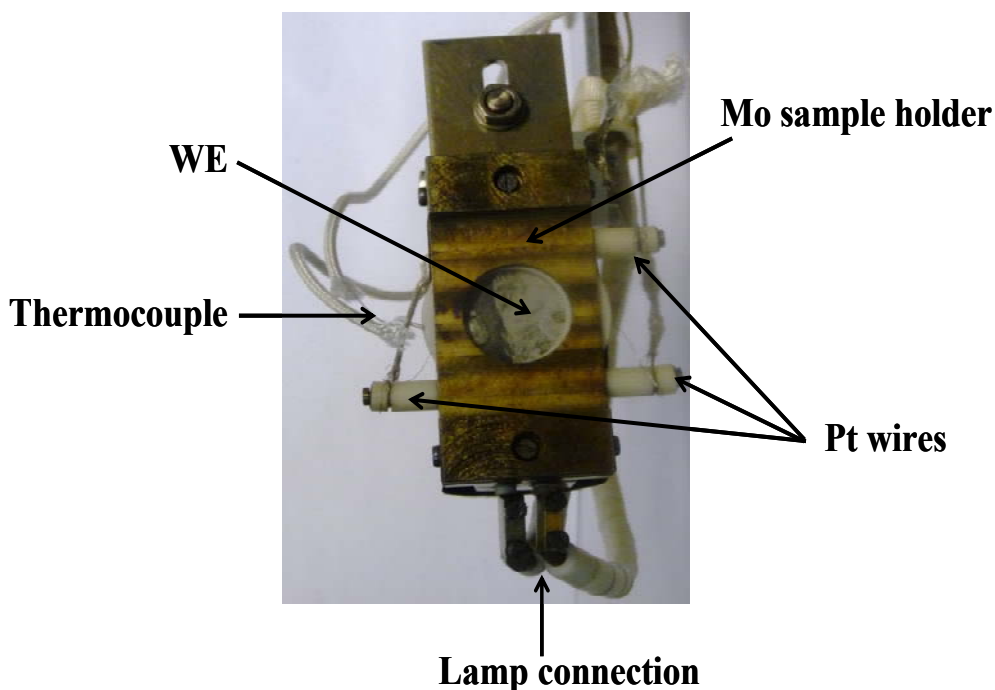


Figure 4.4: The home built Mo-sample holder for UHV EPOC experiments. Platinum wires used for electrical connections of WE, CE and RE in the electrochemical cell (Fig. 4.2).

The reaction studied during the kinetic experiments was ethylene oxidation under low pressure condition ($p \approx 10^{-6}$ - 10^{-4} mbar) with a Pt film on YSZ as catalyst. The operating temperature for the kinetic experiments was restricted to values between 570 K –720 K for two reasons: on the one hand, on the low T-side, the temperature was limited in order to obtain a good conductivity of the solid electrolyte YSZ as well as the necessary oxygen flux to supply the promoter onto the catalyst. On the other hand, on the high T-side the temperature was limited also up to 720 K, in order to observe a promotion effect since promotion does not occur at much higher temperatures [1].

4.1.4 Ultra High Vacuum chamber

Virtually all surface studies are carried out under UHV conditions - the question is why? Ultra high vacuum is required for surface science experiments for two principal reasons:

- To enable preparation of atomically clean surfaces. Such surfaces need to be maintained in a contamination-free state for the duration of the experiment.
- To permit the use of electron and ion-based experimental techniques without interference from gas phase scattering

As shown by Fig. 4.3 the UHV system is equipped with several kinds of pumps: roughing pump, a turbomolecular pump (Leybold-Heraeus Turbovac 360 L s⁻¹) and titanium sublimation pump (Varian). In order to achieve a UHV environment, i.e. low pressure conditions (10⁻¹⁰ -10⁻⁹ mbar), some special procedures are needed. Initially, the vacuum chamber will be pumped down to 10⁻² mbar using a rotary (roughing) pump. Then the chamber will be pumped down to about 10⁻⁶ mbar using a turbomolecular pump. The main vacuum chamber is enclosed in heat resistant boards (known as oven), process called “bake-out” to a temperature of about 150 -180 °C (tubes above turbo pumps at 120 -150 °C and gas inlet system at 100 -120 °C). After ≈ 10-20 h of baking, the chamber has a pressure in the UHV region.

After bake-out, all filaments were degassed to clean them from the impurities while the chamber is still hot. The titanium sublimation pump consists of a titanium filament through which a high current (typically around 40 A) is passed periodically. This current causes the filament to reach the sublimation temperature of titanium, and hence the surrounding chamber walls become coated with a thin film of clean titanium. Since clean titanium is very reactive, components of the residual gas in the chamber which collide with the chamber wall are likely to react and to form a stable, solid product. Thus the gas pressure in the chamber is reduced [2].

4.1.5 Gas Calibration in UHV

The gasses were supplied via a gas line connected to the UHV chamber. Reaction products were monitored with a differentially pumped QMS. All gases were introduced to the main chamber via sapphire-sealed variable leak valves (Varian) by manual operation. Gases of purity 5.0 for Ar, 4.5 for O₂, 5.0 for H₂ and 2.8 for C₂H₄ were used.

Calibration gas for O₂ was applied in order to relate the measured ionic current QMS signal to real partial pressures in the chamber as shown in Fig. 4.5. One can calculate the calibration factor (CF) using the data in Fig. 4.5 as the following:

The partial pressure of oxygen $p(\text{O}_2) = 5 \times 10^{-5}$ mbar as measured with an ionization gauge is compared with the corresponding ionic current QMS signal $I_{\text{QMS}} = 3.43 \times 10^{-7}$ A.

A calibration factor is calculated as: $\text{CF} = 146 \text{ mbar A}^{-1}$ (4.1)

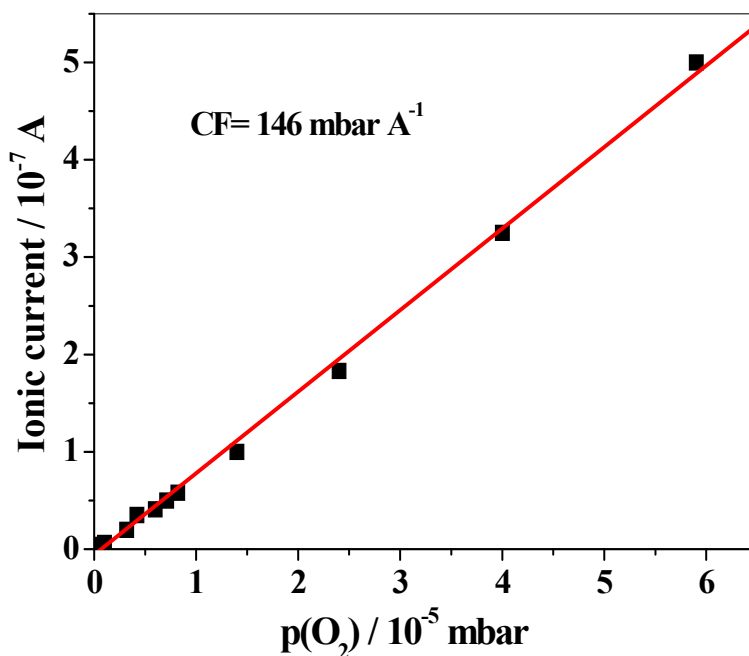


Figure 4.5: Calibration of $p(\text{O}_2)$ in order to relate the measured ionic current QMS signal to the partial pressure of oxygen as measured with an ionization gauge in the UHV chamber. Base pressure in UHV $\approx 10^{-9}$ mbar at 300 K.

From the detected QMS signal of the main product of complete oxidation of ethylene CO₂ ($m/e = 44$), the partial pressure of CO₂ can be calculated with the following Eq.:

$$p_{\text{real}} = I_{\text{QMS}} \cdot \text{CF} \quad (4.2)$$

where p_{real} is the real partial pressure of CO₂, I_{QMS} is the detected mass intensity of CO₂ by ionic current QMS signal and CF is the calibration factor. Accordingly,

$$p_{\text{real}}(\text{CO}_2) = (I_{\text{QMS}} \times 146) \text{ mbar} \quad (4.3)$$

4.1.6 Rate measurement

(i) Pumping speed calculation

The pumping speed can be calculated according to the following Eq.:

$$p = p_0 e^{(-S/V)t} \quad (4.4)$$

describing the pumping down of a chamber filled with gas. p_0 is the initial partial pressure of the gas at time t , p is the pressure of the gas, S is the pumping speed, V the volume of the chamber in litres and t is the pumping time. Now it is useful to linearise Eq. 4.4 to make the calculations easier:

$$\ln p/p_0 = (-S/V)t \quad (4.5)$$

If one plots the $\ln p/p_0$ values versus t one obtains the graph displayed in Fig. 4.6 in which the slope $(-S/V)$ will be equal ≈ -1 . The volume, V , of the UHV chamber is ≈ 100 L, accordingly, the pumping speed is:

$$S \approx 100 \text{ L s}^{-1} \quad (4.6)$$

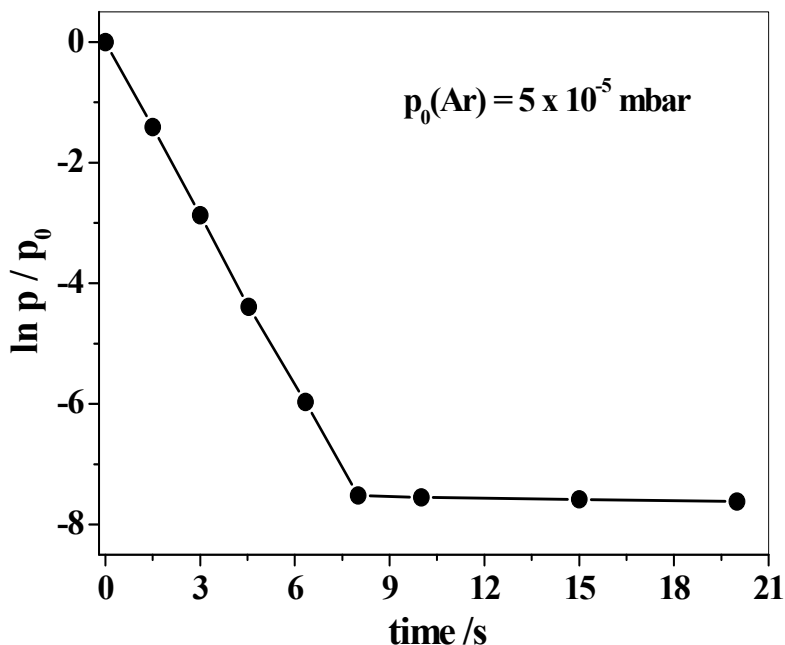


Figure 4.6: Pumping speed determination in a UHV chamber with volume of ≈ 100 L. The background pressure in UHV is $\approx 10^{-9}$ mbar at 300 K. An initial partial pressure p_0 , i.e. $p_0(\text{Ar}) = 5 \times 10^{-5}$ mbar has been adjusted. The amount of gas dosed to the UHV chamber at once by opening the leak valve in a faster way accompanied by recording the pressure of the gas, $p(\text{Ar})$, as a function of time per second.

(ii) Calibration of the reaction rate

According to the ideal gas Eq.:

$$pV = nRT \quad (4.7)$$

where p is the pressure of the gas, V is the volume of the gas, n is the amount of gas (number of moles), T is the absolute temperature of the gas and R is the universal gas constant.

$$R = N_A k \quad (4.8)$$

$$pV = n N_A kT \quad (4.9)$$

where N_A is the Avogadro constant; k is Boltzmann's constant, $N_A = N_{\text{part}}/n$. Accordingly,

$$N_{\text{part}} = n N_A \quad (4.10)$$

where N_{part} is the number of particles in the gas phase. Applying the data of Eq. 4.10 in Eq. 4.9 we got:

$$pV = N_{\text{part}} kT \quad (4.11)$$

The pressure increase due to thermal desorption, dp_{des}/dt , is described as:

$$dp_{\text{des}}/dt = (kT/V)dN_{\text{part}}/dt \quad (4.12)$$

The pressure changes attributed to pumping, dp_{pump}/dt , is given by:

$$dp_{\text{pump}}/dt = Sp/V \quad (4.13)$$

where S is the pumping speed of the chamber; p is the partial pressure of the gas. Under stationary conditions $dp/dt = dp_{\text{des}}/dt - dp_{\text{pump}}/dt = 0$, accordingly,

$$(kT/V) dN_{\text{part}}/dt = Sp/V \quad (4.14)$$

Assume the rate, $r (= dN_{\text{part}}/d t)$. Then the reaction rate of a certain product should be:

$$r = Sp_{\text{real}}/ kT \quad (4.15)$$

where $k = 1.38 \cdot 10^{-23} \text{ J K}^{-1}$, $T = 300 \text{ K}$ and p is the real pressure of the product in mbar.

According to Eqs. 4.3 and 4.6, the reaction rate is given by:

$$r = Sp_{\text{real}}/ kT = [100 \text{ L s}^{-1} \times (I_{\text{QMS}} \times 146) \text{ mbar}] / [1.38 \times 10^{-23} \text{ J K}^{-1} \times 300 \text{ K}] \quad (4.16)$$

Putting $S = 100 \times 10^{-3} \text{ m}^3 \text{ s}^{-1}$, $p_{\text{real}} = (I_{\text{QMS}} \times 146) \times 10^2 \text{ Kg s}^{-2} \text{ m}^{-1}$ and $k = 1.38 \times 10^{-23} \text{ m}^2 \text{ Kg s}^{-2} \text{ K}^{-1}$; in Eq. 4.16, one obtains:

$$r = [I_{\text{QMS}} \times 3.5 \times 10^{23}] \text{ molecules s}^{-1} \quad (4.17)$$

where r is the calibrated reaction rate CO_2 in molecules s^{-1} and I_{QMS} is the ionic current QMS signal of CO_2 .

4.1.7 Calculation of the Faradaic efficiency (Λ -Factor)

(i) Faradaic case

Catalytic ethylene oxidation reaction leads almost exclusively to the products CO_2 and H_2O according to Eqs. 2.2 and 2.3 in chapter 2.

The calculated Faradaic CO_2 production rate, r_{F} , is given by,

$$r_{\text{F}} = I/[2F \times 3] = I/6F \quad (4.18)$$

The factor 3 results from the stoichiometry of the combustion reaction, where I is the electric current in A and F representing Faraday constant ($F = 9.648 \times 10^4$ coulombs mol^{-1} or 9.648×10^4 A s mol^{-1}).

(ii) EPOC effect

Assuming under open-circuit (OC) conditions ($I = 0$, no electrochemical rate contribution) the catalytic CO_2 production rate is equal, r_0 . We now apply a fixed positive potential between the Pt WE catalyst and the RE electrode (see chapter 6 and 7). The catalytic CO_2 production rate will be increase reaches a value, r , larger than the initial value r_0 . The change in the catalytic CO_2 production rate caused by the potential application is given by,

$$\Delta r = r - r_0 \quad (4.19)$$

(iii) Λ -Factor calculation

Now if one compares the measured increase in CO_2 production Δr (Eq. 4.19), with the calculated Faradaic case, r_{F} , in Eq. 4.18, it turns out that the so-called Λ -factor or Faradaic efficiency [3]:

$$\Lambda = \Delta r / r_{\text{F}} \quad (4.20)$$

4.2 High pressure XPS

4.2.1 Sample preparation and electrochemical set-up

For the preparation of the sample a square-shaped (111) oriented YSZ single crystals (13 mol% yttrium, MaTeck GmbH, Germany) was used with a thickness of 1.5 mm and of the dimensions 16 x 16 mm² as shown in Fig. 4.7. Only one side was polished with a surface roughness < 0.5 nm. The counter (CE) and the reference electrodes (RE) were prepared with Pt paste on the unpolished side of the YSZ substrates followed by calcination at 1120 K in air for several hours (≈ 9 h) in order to remove the organic compounds.

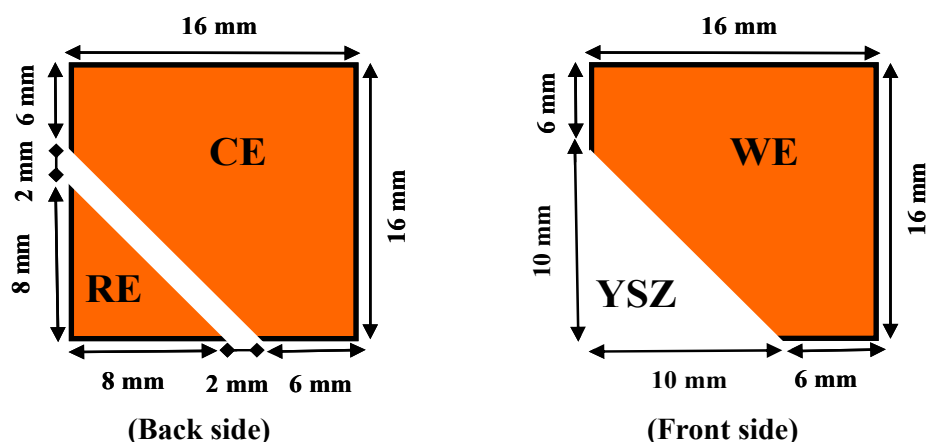


Figure 4.7: The actual dimensions of the sample and of the electrodes used for XPS studies. YSZ= yttrium stabilized zirconia, WE= working electrode, CE= counter electrode, RE= reference electrode.

The working electrode (WE) was prepared on the polished side of single crystal YSZ (111) in two stages. Firstly, Pt and Ag were codeposited by sputtering onto YSZ substrate in an inert atmosphere ($p(\text{Ar}) = 2 \times 10^{-2}$ mbar) at 300 K. The sputter deposition was followed by annealing in air at 1120 K for 3 h. In order to obtain a metal film with high enough electric conductivity, in a second step a thin coating of Pt paste (A1118 Demetron) was deposited with a brush followed by annealing in air at 1120 K for 3 h. As shown by XPS, the Ag segregates to the surface of the Pt film forming a Pt/Ag alloy (see chapter 7). The Pt-Ag film with a thickness in the order of few μm was characterized by SEM, XRD and surface profilometry (chapter 7).

For the electrochemical measurements a standard three-electrode set-up was used (see Fig. 4.2a) with a standard potentiostat (Wenking Model ST 88) controlling the potential of the working electrode (WE) with respect to a reference electrode. Under high

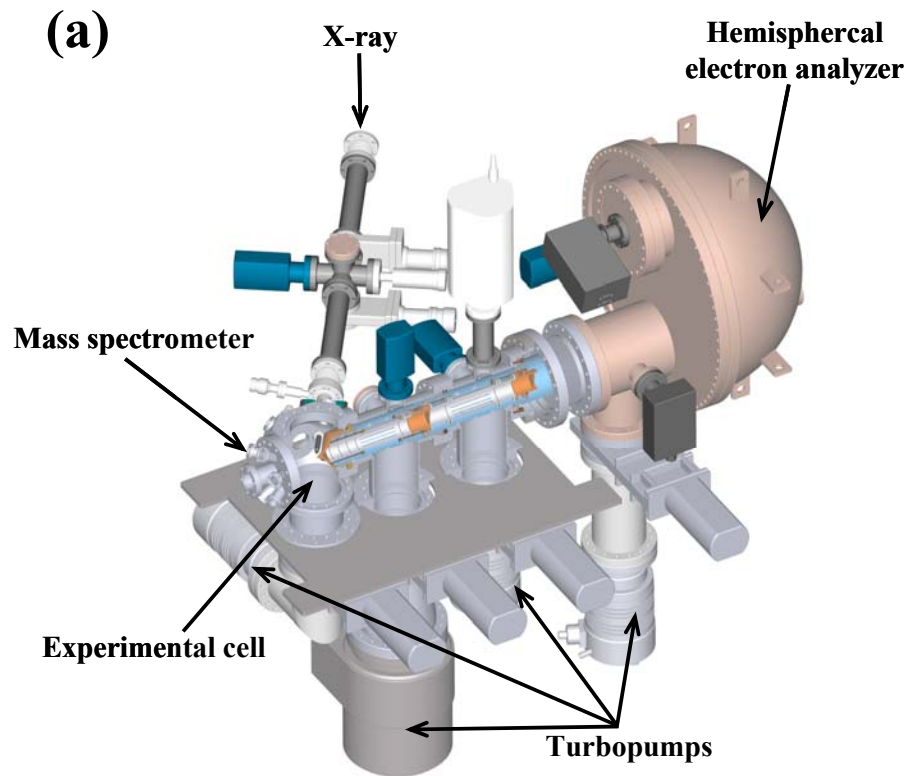
pressure conditions (0.1 – 1 mbar) there is practically no difference between the potentials of the CE and the RE versus the WE; at low pressure and, in particular under UHV conditions, the difference can reach up to several Volt. Since no gas reference electrode was used the potential of the reference electrode is not fixed but may shift due to zirconia reduction at the interface YSZ/Pt reference electrode. As discussed in detail in ref. [4] the measured potentials depend also on the cell geometry i. e. upon dimensions and lay-out of the electrodes because these geometric factors will control the current distribution. In our case, we do not explicitly calculate the error which is potentially introduced by the geometry because the main uncertainty in the measured potentials is caused by not working with a gas reference electrode with fixed potential.

4.2.2 Reaction experiments

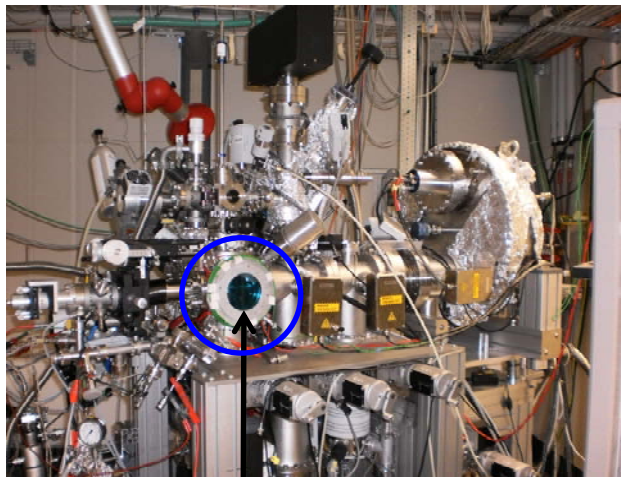
Under reaction conditions, the cell was operated as a continuous flow reactor. Gases were introduced via mass flow controllers. Reaction products were monitored with a differentially pumped QMS coupled to the spectroscopic characterization by XPS.

A sketch of the set-up and a close-up of the experimental cell and the differentially pumped electrostatic lens system are shown in Fig. 4.8. The sample was mounted on a transferable sapphire holder as shown in Fig. 4.9. Briefly, the Pt-Ag/YSZ sample is positioned inside a high pressure reaction cell approximately 2 mm in front of the 1st aperture of a differentially pumped electrostatic lens system as shown in Fig. 4.8c. A homebuilt electron lens serves as the input system for a (modified) commercial hemispherical electron analyzer (PHOIBOS 150, Specs-GmbH). The YSZ sample was heated from the backside through a 100-nm-thick SiC window with an infrared laser, heating is provided by a NIR laser at the rear of the sample and monitored by a K-type Ni/NiCr thermocouple spot-welded to the edge of WE side on the front of the sample.

Prior to the experiments the Pt-Ag film was cleaned by repeated cycles of mild Ar^+ ion bombardment ($t = 20$ min, $E = 1.5$ keV, $p(\text{Ar}) = 1 \times 10^{-4}$ mbar). The reaction system was investigated at 650 K keeping the total pressure fixed at 0.25 mbar and varying the ratio of the gases in the $\text{C}_2\text{H}_4/\text{O}_2$ mixture. The spectral regions of Pt4f, Ag3d, O1s and C1s were recorded under reaction condition. Blank experiments without the catalyst showed no catalytic contribution from SiC.



(b)



Experimental cell

(c)

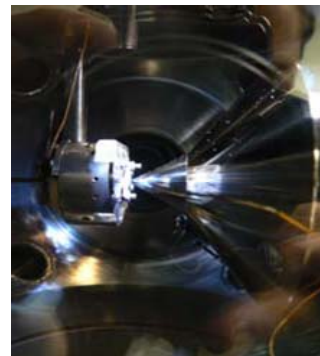


Figure 4.8: (a) Schematic layout demonstrating the main components of high pressure XPS set-up [5]. (b) Arrangement of the high pressure XPS set-up at BEESY, and (c) enlarging of the encircled position on the photograph presented in (b) shows sample position: Sample (left) in front of the cone of the differentially pumped lens system.

For background subtraction of the reaction rate the experiments with the Pt-Ag/YSZ sample were repeated at room temperature. The background production of CO_2 at 300 K is less than 1% of the CO_2 production rate at 650 K. All experiments were conducted at $T = 650$ K. The choice of this temperature was motivated by two limiting cases. At a temperature below 600 K the ionic conductivity of YSZ becomes too low to generate spillover oxygen and beyond 650 K no electrochemical promotion effect was observed in the YSZ/Pt/ $\text{C}_2\text{H}_4 + \text{O}_2$ system [6].

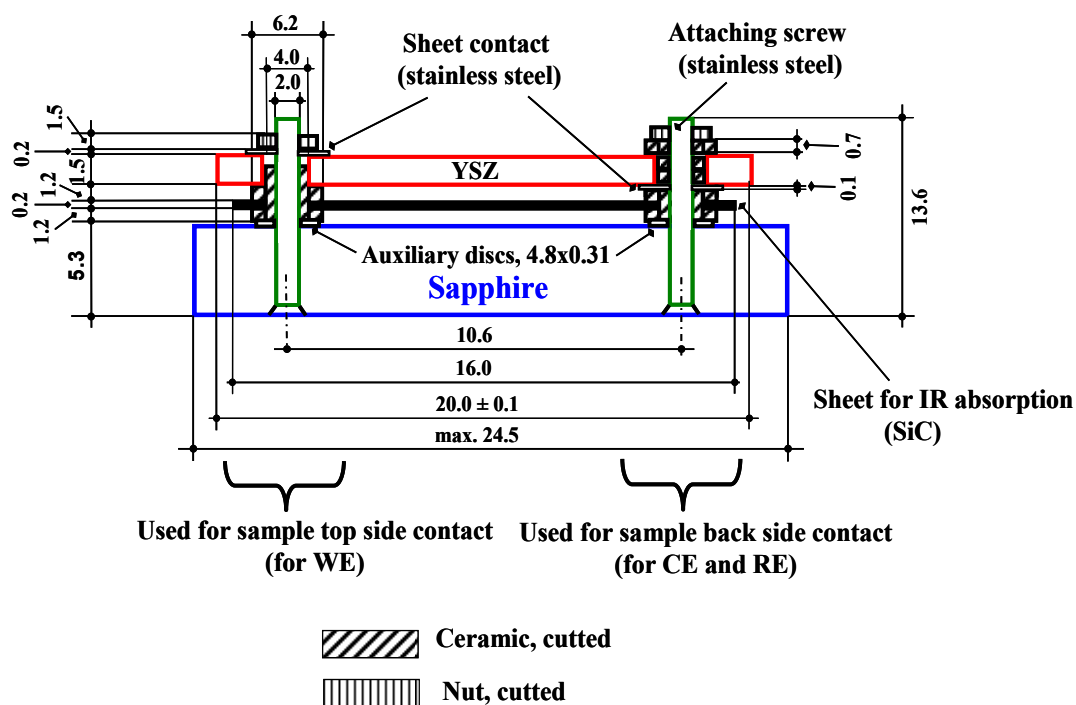


Figure 4.9: Schematic drawing for the sample holder used onto the XPS experiments.

4.2.3 Gas calibration

The gasses were supplied via a gas line connected to the UHV chamber. Gases were introduced to the main chamber in two different ways; the first is by using simple metal-leak valves via manual operation. Gases were introduced via mass flow controllers as a second facility. Gases of purity 5.0 for Ar, 4.5 for O_2 , 5.0 for H_2 and 2.8 for C_2H_4 were used.

A calibration of O_2 was conducted in order to relate the measured ionic current QMS signal to real partial pressures in the chamber as shown in Fig. 4.10.

$$CF = 2.17 \times 10^8 \text{ mbar A}^{-1} \quad (4.21)$$

Accordingly, the real partial pressure of CO_2 should be:

$$p_{\text{real}} = (I_{\text{QMS}} \times 2.17 \times 10^8) \text{ mbar} \quad (4.22)$$

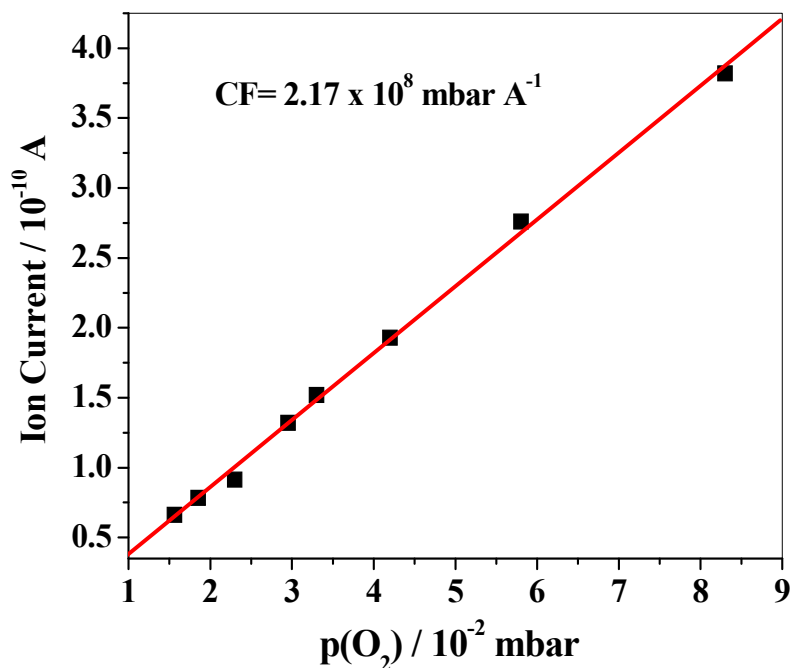


Figure 4.10: Calibration of $p(O_2)$ in order to relate the measured ionic current QMS signal to partial pressures of oxygen as measured with an ionization gauge in the XPS chamber.

4.2.4 Rate measurement

(1) Pumping rate calculation

A fixed pressure $p(\text{total}) = 0.25 \text{ mbar}$ for all experiments was used. The total inflow is therefore equal the total outflow (see Fig. 4.11). In the high pressure XPS a constant chamber pressure of 0.25 mbar is maintained by regulating the pumping speed with a feedback controlled valve while the ratio of the reactants is chosen by mass flow controllers (MFC).

The total inflow of the gases depends on the ratio, $p(\text{C}_2\text{H}_4)/p(\text{O}_2)$. For a ratio 10:1, the total inflow is 6.6 SCCM (standard cubic centimeters per minute) ($1 \text{ SCCM} = 10^{-3} \text{ L}$). The inflow of O_2 is 0.6 and the inflow of C_2H_4 is 6 SCCM.

Under stationary conditions the amount pumped away, has to be equal the total inflow at $T= 300 \text{ K}$ and $p= 1 \text{ bar}$ (10^3 mbar). Accordingly via $S = [(6.6 \cdot 10^{-3}) \text{ L}/60 \text{ s}] \times [10^3 \text{ mbar}/0.25 \text{ mbar}]$, one obtains:

$$S = 0.44 \text{ L s}^{-1} \quad (4.23)$$

where S is the pumping speed.

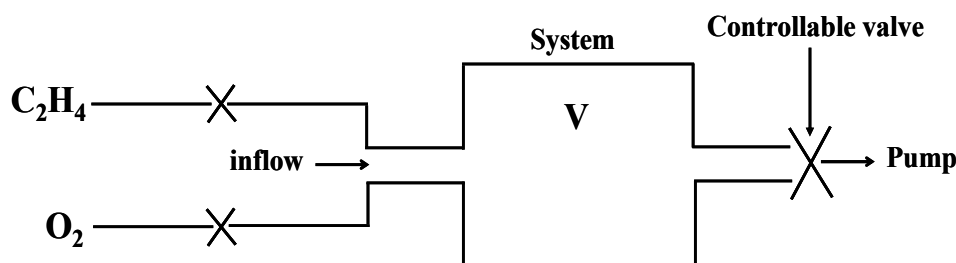


Figure 4.11: Simple schematic drawing for calculation the pumping speed of the high pressure XPS system.

(2) Calculation of the reaction rate

Using for the reaction rate in UHV in section 4.1.4, Eqs. 4.21 and 4.22, one calculates the reaction rate of a certain product, r , as:

$$r = Sp/kT = [0.44 \text{ L s}^{-1} \times (I_{\text{QMS}} \times 2.17 \times 10^8) \text{ mbar}] / [1.38 \times 10^{-23} \text{ J} \cdot \text{K}^{-1} \times 300 \text{ K}]$$

$$r = [I_{\text{QMS}} \times 0.2306 \times 10^{28}] \text{ molecules s}^{-1} \quad (4.24)$$

where r is the calibrated CO_2 reaction rate in molecules s^{-1} and I_{QMS} is the detected mass intensity of CO_2 by ionic current QMS signal in A .

4.2.5 XPS and data analysis

The XPS experiments were performed using the monochromatized radiation of the ISSIS (Innovative Station for In Situ Spectroscopy) beam-line as a tunable X-ray source at the synchrotron facility BESSY II (Berliner Elektronenspeicherringesellschaft für Synchrotronstrahlung) of the HZB in Berlin. A specially designed differentially pumped XPS system was used [7]. Details of the reaction cell and the differentially

electrostatic lens system are described elsewhere [8]. X-rays were admitted to the experimental cell through a 50-nm-thick Si₃N₄ window. The photoelectrons, emitted under normal emission, entered a differentially pumped electrostatic lens system and were focused on the entrance slit of a standard electron energy analyzer, where high vacuum conditions were maintained by an additional pumping stage. This setup allowed a variation of the total pressure in the reaction cell between 10⁻⁷ and 0.5 mbar.

As indicated in Fig.4.2a, the working electrode is at ground potential and all binding energies are therefore referenced to the Fermi level of the working electrode. The excitation (photon energy) for Pt4f, C1s, Ag3d and O1s core level spectra were 220, 435, 518 and 680 eV, respectively, resulting in the same high surface sensitivity with an inelastic mean free path (IMFP) of the photoelectrons of about 0.86 nm in carbon and 0.4 nm in platinum [9]. The Pt4f, Ag3d, C1s and O1s envelopes were fitted using Casa XPS software after subtraction of a Shirley background [10,11]. The fitting of the spectra was done with Gaussian-Lorentzian functions fixing the peak position within ± 0.1 eV.

The spectra have been normalized to the impinging photon flux that has been determined by a cleaned Au foil and corrected for the fraction of higher order of the monochromator and the electron current in the storage ring. Quantitative XPS data analysis was performed assuming homogeneous model distribution of the elements using theoretical cross sections according to the following equation [12]:

$$I_A^* = I_A / (\sigma r n_\gamma) \quad (4.25)$$

where I_A is the measured intensity and I_A^* the normalized intensity of species A; σ is the theoretical cross section, r is the ring current in mA and n_γ is the number of photons per mA ring current (photon flux). Correcting for the different photoionization cross sections one calculates a Pt:Ag ratio of 1.5 assuming a homogeneous mixture of the two components in the alloy. The abundance C_X was obtained as:

$$C_X = \frac{I_X^*}{\sum_{allY} I_Y^*} \cdot 100 \quad (4.26)$$

where I_X^* is the concentration of the element and I_Y^* is the total elements concentrations. The abundance calculated in this way is a rough approximation because one assumes a homogeneous mixing of the elements (Pt, Ag, C, O and Si) in the probed surface region (≈10 layers) which typically is not the case. The thickness of the carbon overlayer was determined by applying the exponential attenuation by overlayer model according to the following equation [13]:

$$I_C^*/I_S^* = (1 - e^{-t/\lambda_C})/e^{-t/\lambda_S} \quad (4.27)$$

where t is the overlayer thickness, I_C^* is the normalized intensity of the carbon overlayer and I_S^* is the normalized intensity of the Pt substrate. The inelastic mean free paths (IMFP) for C1s and Pt4f at 150 eV kinetic energy are denoted as λ_C and λ_S , respectively. For expressing the thickness in number of monolayers the interplanar spacing of graphite of 0.34 nm was taken [14].

4.3 References

- [1] C. G. Vayenas, S. Bebelis, C. Pliangos, S. Brosda, D. Tsiplakides, *Electrochemical Activation of Catalysis: Promotion, Electrochemical Promotion, and Metal-Support Interactions*, Kluwer Academic / Plenum Publishers, New York, 2001.
- [2] VG Scienta, retrieved 08 April 2009.
- [3] C. G. Vayenas, S. Bebelis, I. V. Yentekakis, H. G. Lintz, *Non-Faradaic Electrochemical Modification of Catalytic Activity: A Status Report*, *Catal. Today* 11 (1992) 303.
- [4] J. Winkler, P. V. Hendriksen, N. Bonanos, M. Mogensen, *J. Electrochem. Soc.* 145 (1998) 1184.
- [5] E. M. Vass, M. Hävecker, S. Zafeiratos, D. Teschner, A. Knop-Gericke, R. Schlögl, *J. Phys.: Condens. Matter.* 20 (2008) 184016.
- [6] D. Poulidi, M. E. Rivas, I. S. Metcalfe, *J. Catal.* 281 (2011) 188.
- [7] D. F. Ogletree, H. Bluhm, G. Lebedev, C. S. Fadley, Z. Hussain, M. Salmeron, *Rev. Sci. Instrum.* 73 (2002) 3872.
- [8] A. Knop-Gericke, E. Kleimenov, M. Hävecker, R. Blume, D. Teschner, S. Zafeiratos, R. Schlögl, V. I. Bukhtiyarov, V. V. Kaichev, I. P. Prosvirin, A. I. Nizovskii, H. Bluhm, A. Barinov, P. Dudin, M. Kiskinova, *Adv. Catal.* 52 (2009) 213.
- [9] *The IMFP of electrons at 150 eV were calculated using Quases-Tougard TPP2M software.*
- [10] D. A. Shirley, *Phys. Rev. B* 5 (1972) 4709.
- [11] N. Fairley, A. Carrick, *The Casa Cookbook – Part 1: Recipes for XPS Data Processing*, *Acolyte Science*, Kinderton Close, High Legh, Knutsford, Cheshire, WA16 6LZ U.K., 2005.
- [12] J. J. Yeh, I. Lindau, *Atom. Data Nucl. Data Tables* 32 (1985) 1.
- [13] J. E. Fulghum, R. W. Linton, *Surf. Interface Anal.* 13 (1988) 186.
- [14] M. Eizenberg, M. Blekely, *Surf. Sci.* 82 (1979) 228.

Chapter 5

Preparation and Characterization of Pt/YSZ Catalyst Electrodes

The aim of the present chapter is to study the microstructure of Pt/YSZ catalysts prepared by sputter deposition followed by annealing. The parameters varied were the sputtering time (5-20 min), the annealing temperature (1123 K – 1373 K) and the annealing time (1-6 h). It is shown that annealing at elevated temperatures cause a partial dewetting of the Pt film and the formation of (111) oriented single crystalline Pt grains. Large morphological changes are the consequence of these transformations.

5.1 Introduction

The interface Pt/YSZ is of considerable interest due to its technological importance in solid oxide fuel cells and sensors and due to the decisive role it plays in the electrochemical promotion of heterogeneously catalyzed reactions at Pt/YSZ catalysts [1-9]. Platinum is often applied due to both its inert character as a noble metal and its catalytic properties for the electrode reaction of oxygen. The stability of an oxide/metal interface is usually discussed in thermodynamic terms, i. e. by considering the relevant interfacial energies. Whether a metal can grow epitaxially on an oxide is primarily determined by the mismatch between the two lattice constants and by the difference in the thermal expansion coefficients [10]. In addition, segregation of impurities and also dynamic restructuring effects caused by electrochemical processes or by catalytic etching modifying the morphology of the Pt electrode will play an important role [11-13].

In the EPOC effect the structure of the interface Pt/YSZ is of decisive importance because the spillover of discharged oxygen ions onto the surface of the metal electrode takes place at the tpb (solid electrolyte/metal/gas phase) [8]. The efficiency of Pt/YSZ catalysts is thus determined by the length of the tpb and by the porous structure of the Pt electrode generating a large catalytic area and allowing gas molecules to access this area [7]. By depositing Pt paste on top of a YSZ substrate followed by calcination at high temperature Vayenas et al. found a very efficient realization of such an electrochemical promotion [5-7]. This experimental realization, which although so-called NEMCA effect was pioneered by Vayenas and co-workers, has up to now been demonstrated for roughly over 100 reactions employing different types of solid electrolytes and a variety of different metal catalysts. Mechanistically, the promotion effect has been attributed to a spillover species which migrates from the solid electrolyte via the tpb and then diffuses over the metal surface, thereby modifying its catalytic activity and inducing a work function (WF) change on the metal surface. These catalysts were, however, structurally and chemically not well defined. Alternative preparation methods by using optical lithography and sputter deposition were employed too [11-17]. By applying pulsed laser deposition followed by annealing at elevated temperatures Janek et al. were able to produce dense (111) oriented Pt films on YSZ with a high degree of structural perfection [11-13]. These dense films contained no pores - a property which gave rise to instability.

As a voltage is applied to the electrodes O₂ bubbles form underneath the anode whose mechanical pressure causes the Pt films to break.

5.2 Electrodes preparation

Polished (111) oriented YSZ single crystals (13 mol% Y₂O₃, supplier: MATECK) of circular shape with 1.5 mm thickness and 20 mm diameter were used for the preparation of all samples (see Fig. 5.1). No difference was found whether no cleaning steps were applied prior to the Pt deposition or whether the samples were cleaned with acetone in an ultrasonic bath followed by rinsing with 2-propanol.

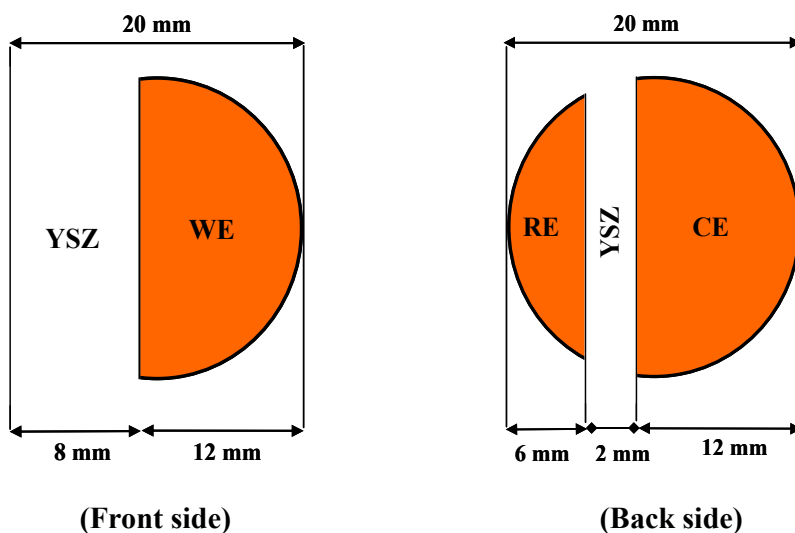


Figure 5.1: The actual dimensions of the samples and of the electrodes used for UHV studies. YSZ= yttrium stabilized zirconia, WE= working electrode, CE= counter electrode, RE= reference electrode.

The CE and RE electrodes were prepared firstly on the unpolished side of the YSZ samples using thin coatings of Pt paste (Demetron A1118) followed by calcinations at 1270 K for several hours (> 5 h) to remove organic compounds. The WE was brought onto the polished side of the samples using two different ways of preparation: The first type of WE's was prepared by depositing Pt paste (Demetron A1118) with a brush followed by heating (5 K min⁻¹) to 1123 K, and sintering at this temperature for 3 h in air.

The second type of WE's was prepared by sputtering Pt (Pt-target 99.99%, 57 mm x 0.1 mm, EleKtronen-Optik-Service GmbH, Germany) onto the polished side of the samples using a magnetron sputter technique (Elektronen-Optik-Service GmbH, Cressington 108auto, Germany) in an inert atmosphere ($p(\text{Ar}) = 2 \times 10^{-2}$ mbar) at 300 K. The samples were then heated up to 1123 K and 1373 K with a heating rate of 5 K min^{-1} and annealed in air for 3 h at constant temperature. This temperature range for annealing (1123-1373 K) was chosen high compared to the temperature range applied for EPOC experiments (546-763 K) (see chapter 6). The samples were then heated up to 1123 K and 1373 K (5 K min^{-1}) and annealed in air for one to three hours at constant temperature.

The area of the RE was kept as small as possible to minimize the internal resistance the working and counter electrodes were located in a symmetrical face-to-face arrangement on the opposite sides of the YSZ pellet. This geometry ensured a symmetrical current and potential distribution in the cell as shown by Fig. 5.1.

5.3 Sample characterizations

The morphology of the WE's before and after sintering were investigated by scanning electron microscopy (SEM, JEOL JSM-6700F) at an acceleration voltage of 2 kV and transmission electron microscopy (TEM, JEOL JEM-2100F-UHR). TEM studies were performed at 200 kV on Pt/YSZ cross-sections prepared by Ar ion thinning of the samples. The microscopes were equipped with an energy dispersive X-ray spectrometer (EDX). Structure and orientation of the Pt films was studied by X-ray diffraction (XRD, $2\theta = 10^\circ - 90^\circ$, Bragg-Brentano diffraction geometry, Cu-K α radiation, $V = 40 \text{ kV}$, $I = 40 \text{ mA}$). The thickness of the Pt films was determined by surface profilometry (Veeco Dektak 6M stylus) and by atomic force microscopy (AFM, Nanosurf easyscan 2).

The thickness values of the Pt electrodes prepared from Pt paste was around $8 \mu\text{m}$; for the sputtered Pt electrodes (20 min) the electrodes had a thickness of $\approx 1 \mu\text{m}$ after annealing to 1123 K which reduced to 800 nm after annealing to 1373 K. An overview of the samples used in our experiments is given in Table 4.1.

Nr	Preparation method	Sputtering time (minute)	Annealing temperature (K)	Annealing time (hour)	Film thickness (μm)	SEM Figure
1	past		1123	3	8	4.2a
2	sputtering	20	1123	3	1	4.7b
3	sputtering	20	1373	3	0.8	4.8
4	sputtering	15	1123	6	0.6	4.9
5	sputtering	10	1123	1	0.2	4.10

Table 5.1: Overview of the samples used in the experiments. SEM= Scanning electron microscopy.

5.3.1 Scanning Electron Microscopy (SEM) and XRD

The morphology and surface properties of the Pt/YSZ catalysts have been studied by SEM. The structure and orientation of the Pt films were studied by XRD.

I. Past platinum electrode

Figure 5.2a displays the SEM image (sample 1) of the platinum electrode prepared by depositing Pt paste (Demetron A1118) followed by sintering in air for 3 h at 1123 K.

In agreement with previous studies a three dimensional porous network film with a thickness in the order of a few μm is obtained [5-7]. The XRD of this electrode in Fig. 5.2b shows nearly the intensity distribution of a powder sample with statistical orientation of the grains.

II. Sputtered platinum electrodes

In the following we exclusively consider Pt films prepared by sputter deposition at room temperature varying the annealing temperature. The sputter deposition time was varied between 5 and 20 minutes; two different annealing temperatures of 1123 K and 1373 K, respectively, were chosen varying the annealing time between 1 and 6 h.

SEM images of the as-sputtered (freshly sputtered) platinum film catalysts on YSZ substrate i.e. without any subsequent heat treatment are displayed in Figs. 5.3a and b. The image show seemingly compact amorphous film which exhibits no porosity within the resolution of the images. The Pt film covers uniformly the substrate but on top of this compact film some small isolated particles of a diameter around 1 μm can be seen whose origin could not be clarified. EDX shows that these particles are pure Pt without any indication of oxide formation as demonstrated in Fig. 5.3c. After annealing these particles disappeared.

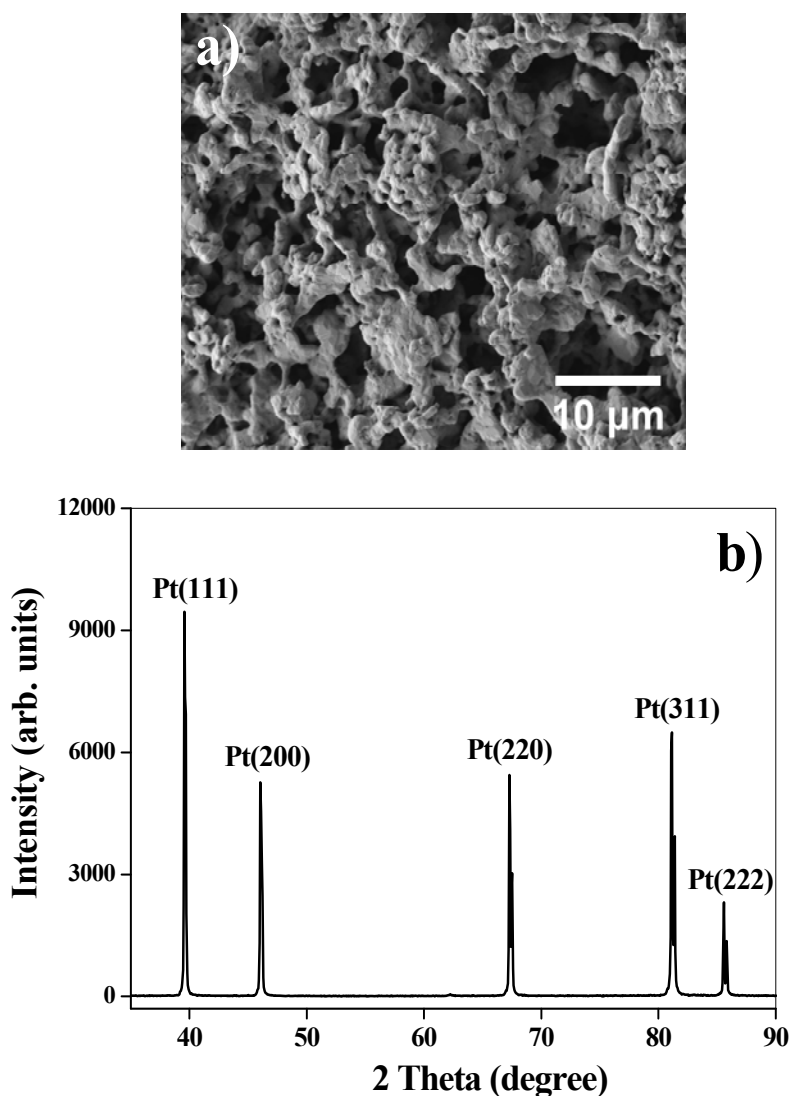


Figure 5.2: (a) SEM micrograph (sample 1) of a platinum electrode prepared sintering Pt paste on a YSZ single crystal for 3 h in air at 1123 K. (b) X-ray diffraction pattern corresponding to the electrode displayed in (a).

SEM micrographs of the sputtered electrode after annealing for 1-3 h at 1123 K are reproduced in Figs. 5.4 and 5.5. As demonstrated by Fig. 5.4a already after one hour annealing, holes of 1-2 μm diameters have developed in the compact Pt film through which the underlying YSZ substrate is visible as dark grey area. Prolonging the annealing time to 2 hours leads to the agglomeration of holes as demonstrated by Fig. 5.4b. Inside the large hole elongated Pt islands with an average width of 1-2 μm are present. These Pt stripes exhibit a reduced roughness as compared to the surrounding compact Pt film. After three hours annealing time the initially compact Pt film is completely transformed into a network of thin Pt stripes as shown by Fig. 5.5a. Evidently a dewetting process has occurred. An XRD of this structure displayed in Fig. 5.5b looks very similar to the XRD of the pasted Pt electrode in Fig. 5.2b. Evidently the Pt in the stripe structure is still predominantly polycrystalline.

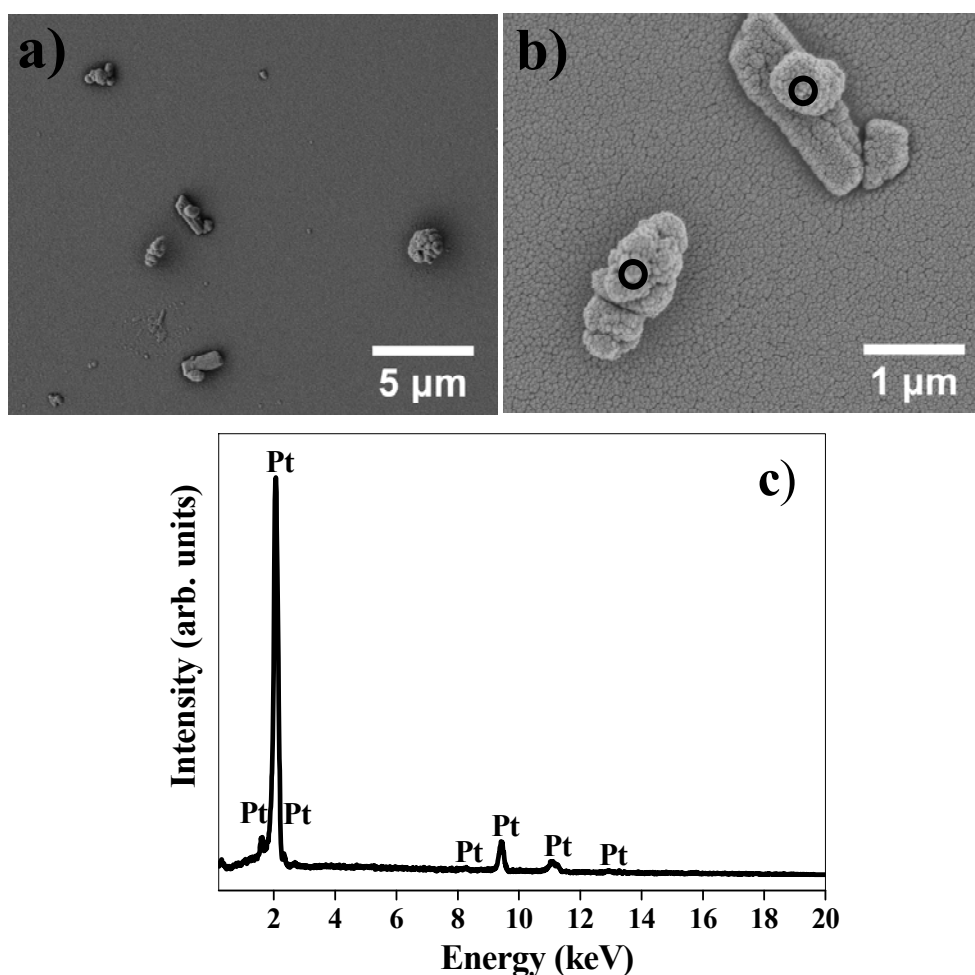


Figure 5.3: (a) SEM image of the as-sputtered platinum electrode on a YSZ (111) single crystal as substrate after sputtering time of 5 minutes at room temperature, and (b) enlarging of (a). (c) EDX analysis for the encircled positions on the sample presented in (b)

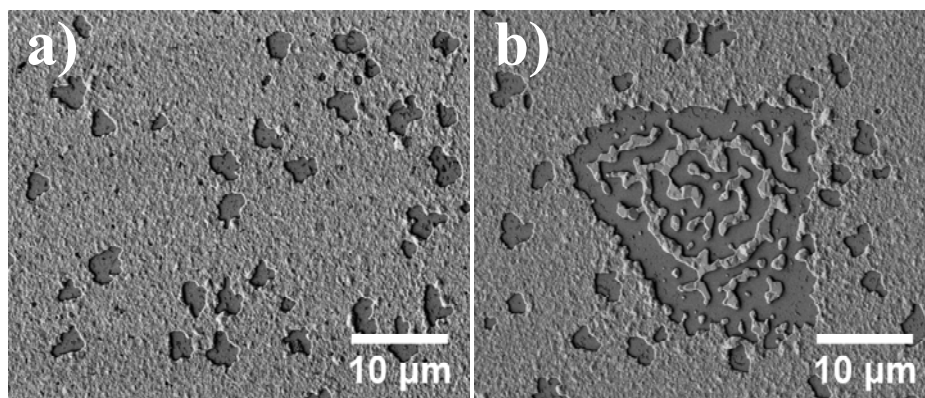


Figure 5.4: SEM images of a Pt electrode prepared by sputtering for 5 minutes followed by annealing at 1123 K with varying times: (a) after 1 h and (b) after 2 h.

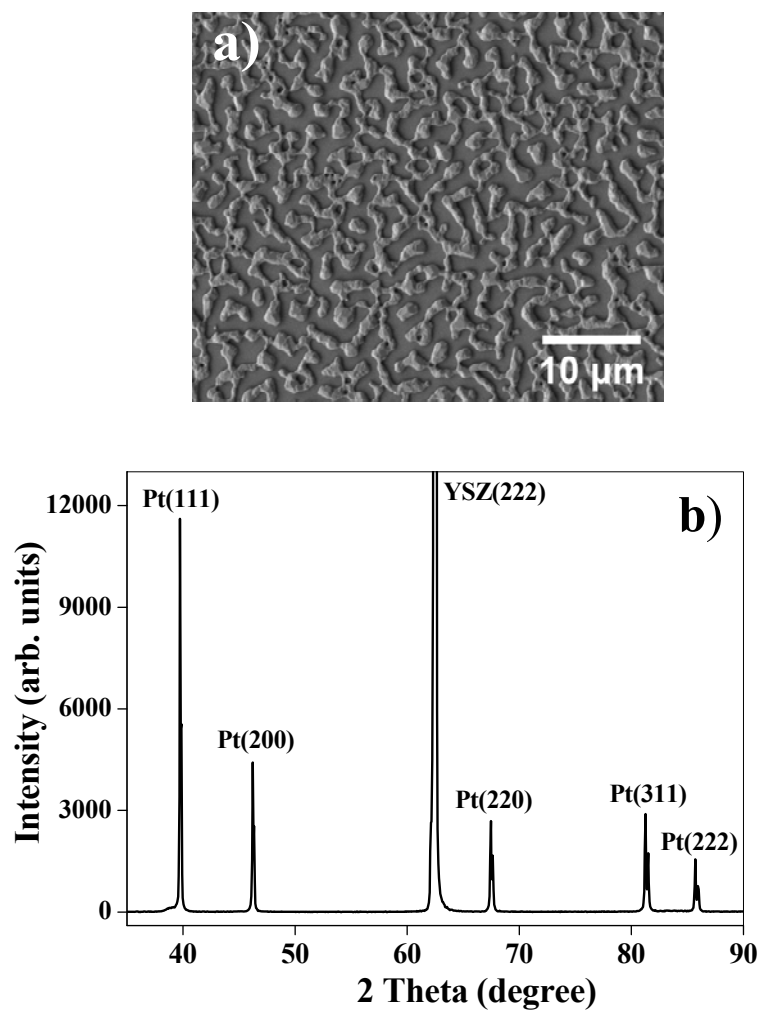


Figure 5.5: (a) SEM image of a Pt electrode prepared by sputtering for 5 minutes followed by annealing at 1123 K for 3 h. (b) X-ray diffraction pattern of the Pt/YSZ electrode presented in (a).

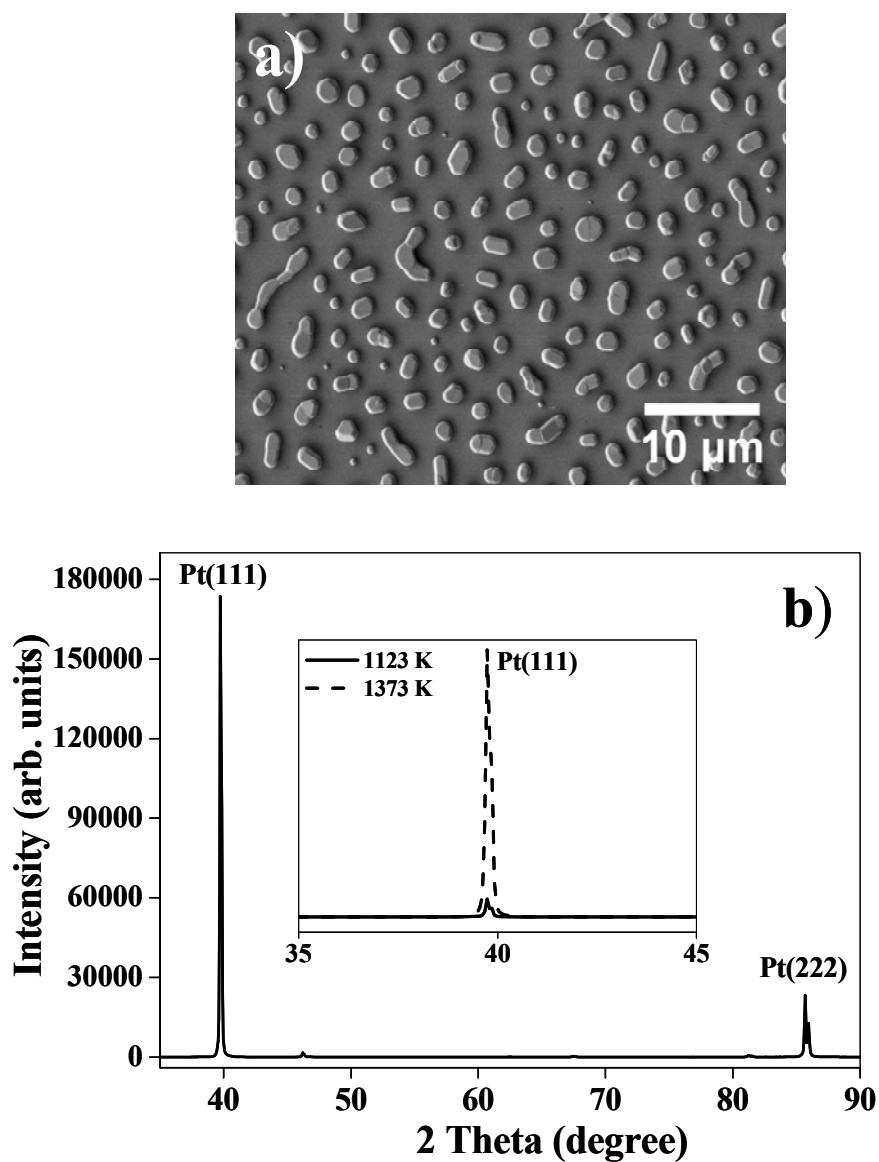


Figure 5.6: (a) SEM image of platinum film on YSZ (111) prepared by 5 minutes sputtering followed by annealing in air for 3 h at 1373 K. (b) XRD patterns of the electrode presented in (a). The inset shows a comparison of the Pt(111) peak in XRD of the sputtered electrode after annealing at two different temperatures for 3h in air. The full lines represent the peak behavior after annealing at 1123 K and the dashed lines after 1373 K.

Raising the annealing temperature by 250 K from 1123 K to 1373 K leads to drastic morphological changes film as demonstrated by Fig. 5.6a. Isolated Pt islands have developed often exhibiting the shape of a distorted hexagon. As clearly evidenced by the XRD in Fig. 5.6b these Pt particles are single crystalline exhibiting a (111)

orientation with respect to the substrate surface. In addition, the Pt film becomes more textured on the (111) plane as the annealing temperature is increased from 1123 K to 1373 K as illustrated in the inset of Fig. 5.6b. However, no change on the ratio of the peak intensities Pt(111) / Pt(222) has been seen, as the annealing temperature is raised from 1123 K to 1373 K, which indicates that no change in the texture occurred. However, the reflected intensity after annealing at 1373 K increases by a factor of 15 showing that the ordering is substantially improved. Since the individual Pt particles displayed in the last figures are electrically disconnected the structure cannot be used as an electrode. Therefore the sample is subjected to an additional Pt deposition with 15 minutes sputtering time. The sample surface directly after this additional deposition is displayed in Fig. 5.7a. Apparently the additional Pt did not lead to the nucleation of new Pt islands but the deposited Pt became attached to the already existing Pt islands. Annealing at 1373 K for 3 h enlarges the pores and smoothens the Pt surface with a thickness of 800 nm as demonstrated by Fig. 5.7b. Only small pores are left through which the YSZ substrate is still visible. Simple resistance measurements with two metal tips on the Pt surface in air at 300 K shows a very good conductivity with only a few ohms ($<1 \Omega$) over a distance of a few millimeters. In this case the sample is conducting on a macroscale which qualifies it for use as WE [18].

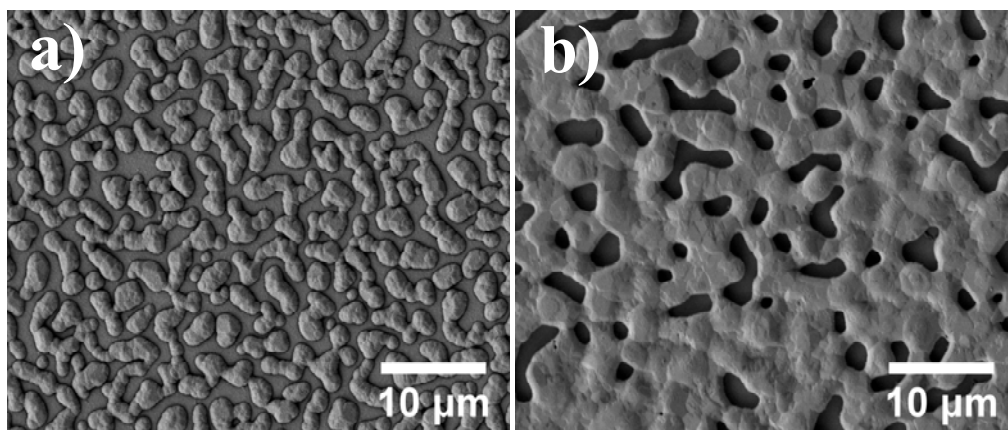


Figure 5.7: SEM micrographs of the sputtered Pt electrode in Fig. 5.6a after additional Pt deposition by 15 minutes sputtering. (a) as-deposited, (b) after annealing at 1373 K for 3 h in air (sample 3). Thickness of sample is ≈ 800 nm.

Another sample was prepared by 20 minutes sputter-deposition of Pt followed by heating to 1123 K and 3 h annealing in air with a thickness of 1 μm as shown in Fig. 5.8. XRD yields nearly the same diagram as in Fig. 5.5b showing that the Pt film is still polycrystalline. Annealing at higher temperature, at 1373 K, is required to transform the polycrystalline film with random orientation into single crystalline grains with preferential (111) orientation. This is revealed by XRD which is practically identical to the one displayed in Fig. 5.6b.

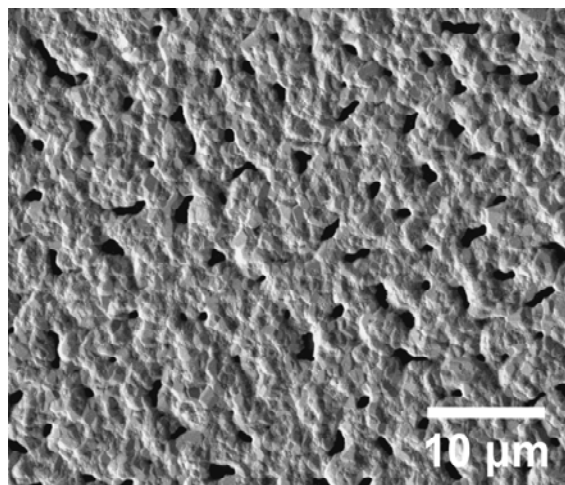


Figure 5.8: SEM micrographs (sample 2) of the sputtered Pt electrode prepared for comparison, a fresh sample prepared by 20 minutes Pt sputtering followed by annealing at 1123 K for 3 h in air. Thickness of sample is $\approx 1\mu\text{m}$.

A fourth sample was prepared by sputtering for 5 min then annealed at 1123 K for 3h in air. SEM image yield nearly the same diagram as in Fig. 5.5a showing that the Pt film is completely transformed into a network of thin Pt stripes. Re-sputtered of the sample surface with additional 10 minutes sputtering time. Annealing at 1123 K for 6h in air enlarges the pores and smoothens the Pt surface with a thickness of 600 nm as demonstrated by Fig. 5.9. In addition electrically isolated Pt particles start to develop from the dewetting process due to the longer time of annealing as shown in Fig. 5.9. XRD of this sample is quit similar to the one shown in Fig. 5.5b. It should be added that no indication of the existence of an additional phase (e.g. Pt oxides) or of impurities were found in any XRD and EDX measurements.

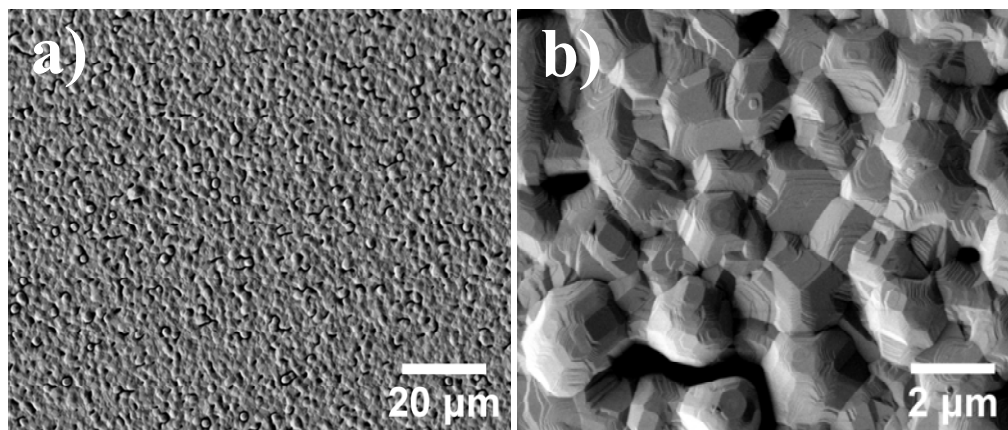


Figure 5.9: (a) SEM micrograph (sample 4) of a Pt electrode on YSZ prepared by sputtering for 20 minutes followed by annealing at 1123 K for 3 h in air, and (b) enlarging of (a). Thickness of sample is ≈ 600 nm.

Smoother sample numbered 5 with thickness of ≈ 200 nm has been prepared by sputtering more or less for 10 min followed by annealing at 1123 K for 1h in air. As indicated from SEM micrographs showed in Fig. 5.10 an incomplete dewetting of the Pt surface during annealing for a shorter time. In addition the surface is strongly inhomogeneous; only part of the Pt film has been dewetted (see Fig. 5.10a). Not the Pt films displayed in Figs. 5.2a, 5.7b, 5.8, 5.9 and 5.10 are the ones used later on in EPOC experiments (see chapter 6).

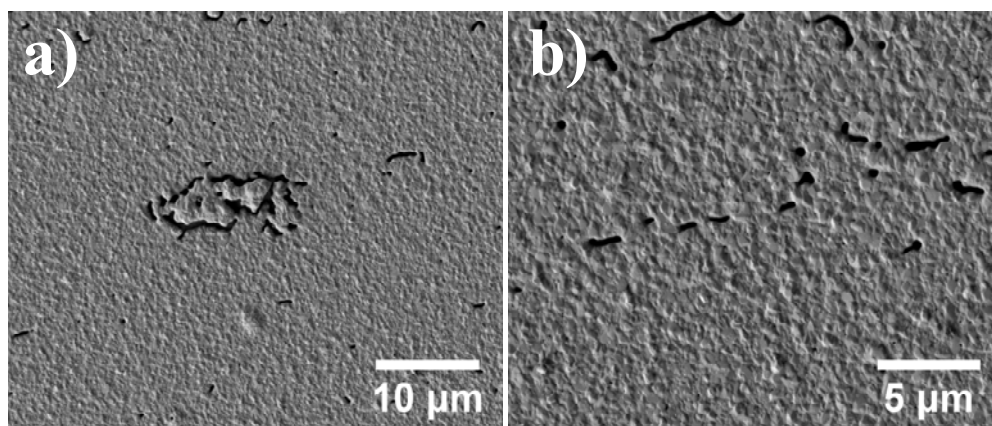


Figure 5.10: (a) SEM images (sample 5) of a Pt electrode on YSZ prepared by sputtering for 10 minutes followed by annealing at 1123 K for 1 h in air, and (b) enlarging of (a). Thickness of sample is ≈ 200 nm.

5.3.2 Transmission Electron Microscopy (TEM)

In order to know more about the Pt/YSZ interface TEM experiments were performed on cross-sections of Pt/YSZ electrodes. After 20 minutes sputter-deposition of Pt the samples were heated to 1123 K (Fig. 5.8) and 1373 K (Fig. 5.7b), respectively, and annealed during 3 h in air. A dark field image of the Pt/YSZ interface after annealing to 1123 K is displayed in Fig. 5.11. As demonstrated from Fig. 5.11 is clear after annealing at 1123 K for 3h the Pt film is in direct contact with the YSZ substrate with voids formation in the Pt/YSZ interface.

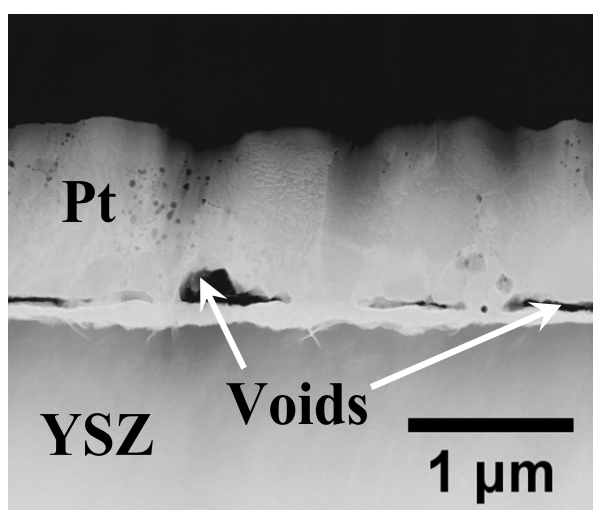


Figure 5.11: Dark field scanning transmission electron microscopy (STEM) of cross sections of the Pt/YSZ interface of sputtered Pt electrodes (sample 2) demonstrating the microstructure for varying annealing temperature. The sputtering deposition time was 20 minutes, annealing was conducted for 3h in air at 1123 K.

The Pt film is not always in direct contact with the YSZ substrate. Gaps and pores at the interface are clearly visible. Annealing to 1373 K enlarges the gaps and pores leading to the formation of bridge-like structures and large voids at the Pt/YSZ interface. In addition, hexagonal pores within the Pt film itself develop, as shown by Fig. 5.12. While the Pt film after annealing at 1123 K is still polycrystalline with random orientation annealing to 1373 K transforms the film into single crystalline grains with preferential (111) orientation thus generating a kind of mosaic structure.

A comparison of the structures obtained at 1123 K and 1373 K annealing is displayed in Figs. 5.13 and 5.15, respectively. Selected area diffraction shows that the bridge visible in Fig. 5.14b consists of large oriented single crystalline grains.

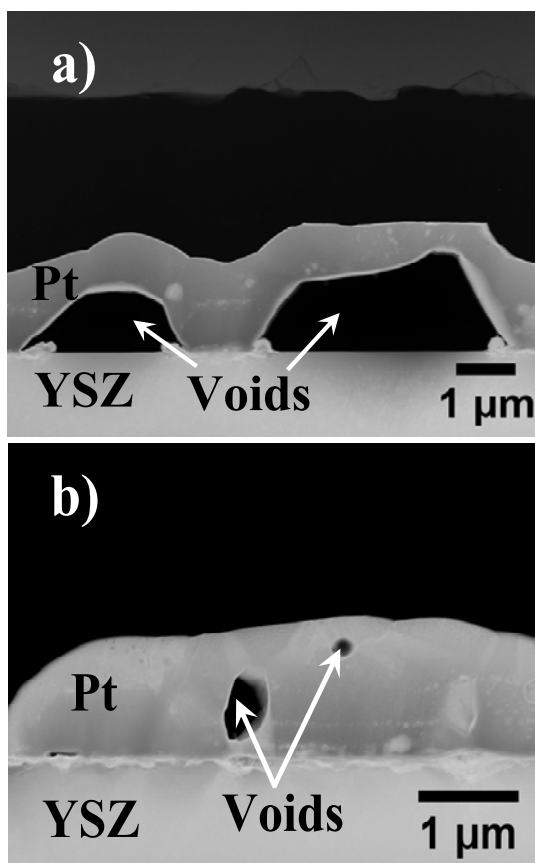


Figure 5.12: Dark field scanning transmission electron microscopy (STEM) of cross sections of the Pt/YSZ interface of sputtered Pt electrodes (sample 3) after annealing at 1373 K for 3h in air. The sputtering deposition time was 20 minutes.

A dark and bright field image of the bridge structure is reproduced in Fig. 5.13. Similar voids at the interface resulting from partial dewetting have been observed with thin Au films deposited on YSZ [19]. Also there the formation of voids occurred at grain boundaries as predicted by theory [20].

In order to follow the transformation of the Pt film into oriented single crystals more closely TEM was also performed after annealing to 1123 K. The results are displayed in Fig. 5.15. The bright field image in Fig. 5.15a reveals small gaps and voids at the Pt/YSZ interface similar to Fig. 5.11. The corresponding dark field image in Figs. 5.15b and c demonstrates that already at 1123 K annealing temperature parts of the Pt film are transformed into oriented single crystalline grains. The single crystalline grains nucleate simultaneously at different locations on the Pt film.

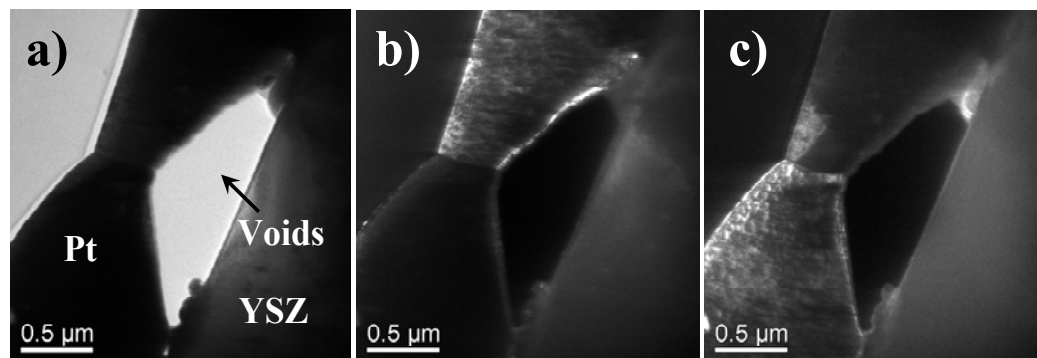


Figure 5.13: TEM images of cross sections of sputtered Pt electrodes demonstrating the formation of oriented single crystalline grains of Pt film after annealing at 1373 K 3h in air. The sputtering deposition time was 20 minutes. (a) Bright field. (b) and (c) dark field 1 and 2.

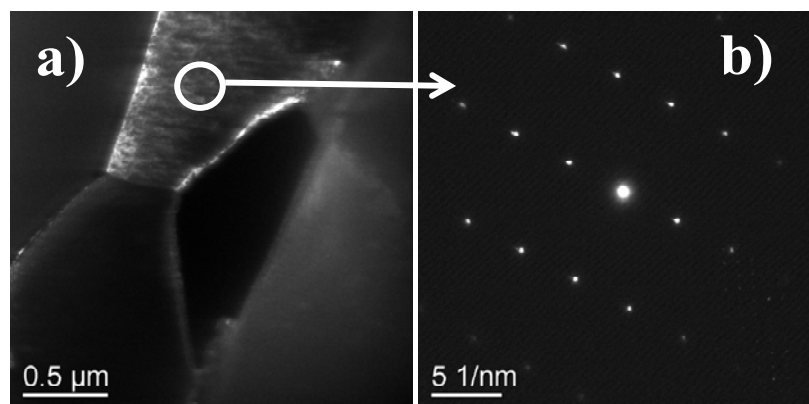


Figure 5.14: (a) Dark field image for annealing at 1373 K. (b) selected area electron diffraction pattern (SAED) of the region indicated in (a).

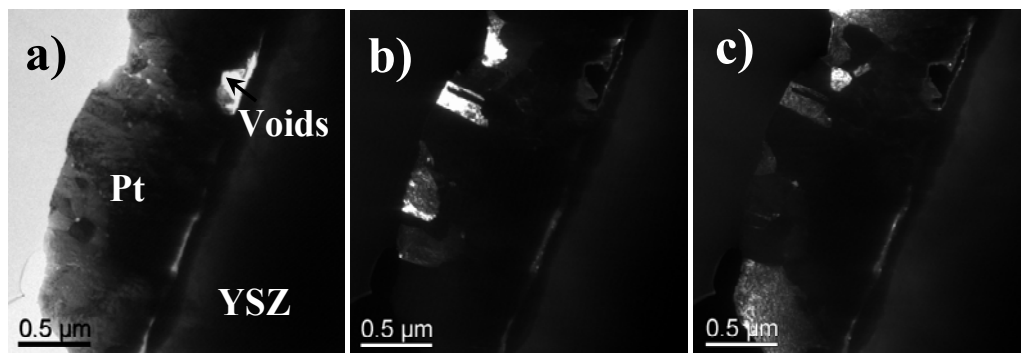


Figure 5.15: TEM images of cross sections of sputtered Pt electrodes showing the formation of polycrystalline Pt film after annealing at 1123 K 3h in air. The sputtering deposition time was 20 minutes. (a) Bright field. (b) and (c) dark field 1 and 2.

5.4 Conclusions

The morphology of Pt films on YSZ depends strongly on the preparation method and on the annealing temperature. Pt films prepared from calcinating Pt paste are highly rough and very porous. Sputtered Pt films are initially quite compact but annealing transforms the films very strongly leading to dewetting and severe morphological changes. A dewetting can already be observed at 1123 K annealing temperature but the Pt film remains predominantly polycrystalline with the grains exhibiting random orientation. A nearly complete transformation into (111) oriented single crystals is seen at 1373 K annealing temperature. The Pt/YSZ interface at this annealing temperature is characterized by large voids and bridge-like structures leaving only a relatively small contact area between Pt and YSZ. A connected network of Pt islands can be regenerated by depositing additional Pt followed by annealing. With respect to potential applications in EPOC one of the main questions to be solved in the future is that after the connection between certain morphological properties of the Pt/YSZ interface and the electrocatalytic properties of the Pt/YSZ catalyst. A second but more difficult question is that of how the morphology is modified as the Pt/YSZ catalyst is under operation in an EPOC experiment.

5.5 References

- [1] S. Adler, Chem. Phys. 104 (2004) 4791.
- [2] R. O'Hayre, S. Cha, W. Colella, F. B. Prinz, Fuel Cell Fundamentals, Wiley & Sons, New York, 2006.
- [3] C. Schwand, W. Weppner, J. Electrochem. Soc. 11 (1997) 3728.
- [4] S. Koch, M. Mogensen, P. V. Hendriksen, N. Dekker, B. Rietveld, Fuel Cell 6 (2006)117.
- [5] C. G. Vayenas, S. Bebelis, S. Ladas, Nature 343 (1990) 625.
- [6] C. G. Vayenas, M. M. Jaksic, S. I. Bebelis, S. G. Nephytides, in: J. O. M. Bockris et al. (Ed.), *Modern Aspects of Electrochemistry*, vol. 29, Plenum Press, New York, 1996, p. 57.
- [7] C. G. Vayenas, S. Bebelis, C. Pliangos, S. Brosda, D. Tsiplakides, *Electrochemical Activation of Catalysis: Promotion, Electrochemical Promotion, and Metal-Support Interactions*, Kluwer Academic / Plenum Publishers, New York, 2001.
- [8] B. Luerßen, E. Mutoro, H. Fischer, S. Günther, R. Imbihl, J. Janek, Angew. Chem. Int. Ed. 45 (2006) 1473.
- [9] R. Imbihl, Prog. Surf. Sci. 85 (2010) 240.
- [10] M. Rühle, A. G. Evans, Mater. Sci.. Eng. A 107 (1989) 87.
- [11] E. Mutoro, B. Luerssen, S. Günther, J. Janek, Solid State Ionics 179 (2008) 1214.
- [12] E. Mutoro, B. Luerssen, S. Günther, J. Janek, Solid State Ionics 180 (2009) 1019.
- [13] G. Beck, H. Fischer, E. Mutoro, V. Srot, K. Petrikowski, E. Tchernychova, M. Wuttig, M. Rühle, B. Luerßen, J. Janek, J. Solid State Ionics 178 (2007) 337.
- [14] B. Luerssen, S. Günther, H. Marbach, M. Kiskinova, J. Janek, R. Imbihl, Chem. Phys. Lett. 316 (2000) 331.
- [15] F. J. Williams, A. Palermo, S. Tracey, M. S. Tikhov, R. M. Lambert, J. Phys. Chem. B 106 (2002) 5668.
- [16] H. Galinski, T. Ryll, P. Elser, J. L. M. Rupp, A. Bieberle-Hütter, L. J. Gauckler, Phys. Rev. B 82 (2010) 235415.
- [17] T. Ryll, H. Galinski, L. Schlagenhauf, P. Elser, J. L. M. Rupp, A. Bieberle-Hutter, L. J. Gauckler, Adv. Funct. Mater. 21 (2011) 565.
- [18] T. Neubrand, S. Günther, A. Fenske, R. Imbihl, Phys. Chem. Chem. Phys. 6 (2004) 3569.
- [19] E. Shaffir, I. Riess, W. D. Kaplan, Acta Mater. 57 (2009) 248.
- [20] C. M. Kenefick, R. Raj, Acta Metall. 37 (1989) 2947.

Chapter 6

The Electrochemical Promotion of Ethylene Oxidation at Pt/YSZ Catalysts

The following chapter describes, the electrochemical promotion of catalytic ethylene oxidation under low pressure conditions ($p \approx 10^{-6} - 10^{-4}$ mbar) and high pressure up to 1 mbar with a Pt films on YSZ as catalyst. Since ethylene oxidation on Pt/YSZ due to its large Λ -factor at high pressure ($p \geq 10^{-2}$ mbar) played a kind of paradigmatic role in the EPOC effect for the first time this reaction system in an UHV environment was studied.

6. 1 Introduction

Solid electrolytes interfaced with noble metal electrodes allow an EPOC effect [1]. Pioneered by Vayenas and his group in Patras the EPOC effect has been demonstrated with about 100 reaction systems and with different types of solid electrolytes [2–6]. Rate enhancements up to a factor 200 have been reported.

The physical basis of EPOC was shown to be the electrochemically induced spillover of the transported ionic species onto the surface of the metal electrode. This has been demonstrated in surface science type studies for the O^{2-} conducting YSZ as well as for the Na^+ conducting $\beta''\text{-Al}_2O_3$ [6-11]. Setting the platinum electrode of the oxygen ion conducting electrolyte YSZ to a positive potential will not only cause a transport of the O^{2-} ions to the anode followed by a discharge at the tpb (solid electrolyte/metal/gas) but some of the discharged oxygen species will also spillover onto the surface of the metal electrode modifying the catalytic activity there.

Right from the beginning one unexpected property of the EPOC effect has been put in the center of the attention which is that the EPOC effect is typically strongly non-Faradaic [2-5]. Originally, this property even earned the phenomenon the name NEMCA-effect but later on the more general description of EPOC effect was chosen. In catalytic CO on Pt/YSZ each transported O^{2-} ion can oxidize one CO molecule to CO_2 but if one compares the measured increase in CO_2 production Δr , with the electric current I , it turns out that the electrochemically generated rate increase is much larger than the increase predicted by Faraday's law. In order to quantify this so-called Λ -factor or "Faradaic efficiency" (Vayenas) was introduced. For YSZ one has, $\Lambda = \Delta r / (I/2F)$ with F representing the Faraday constant. The Faradaic case is given by $\Lambda = 1$, a value larger than 1 means a promotion effect, for values smaller than 1 a "poisoning" [4, 5]. Ethylene oxidation over Pt/YSZ, this factor even reached 3×10^5 . Vastly differing values of 188, 975, 15000 and 3×10^5 were reported for the same reaction system but, different samples [12-15]. In the case of $\Lambda = 3 \times 10^5$ this means that each transported O^{2-} ion catalyzes the oxidation of about 1×10^5 C_2H_4 molecules to CO_2 [13]. The explanation for the non-Faradaicity in EPOC by Vayenas is similar to the concept of electronic promoters in heterogeneous catalysis [4-6, 12-15]. For the O^{2-} -conducting system Pt/YSZ the existence of a special oxygen spillover species, $O^{\delta-}$, is proposed with δ supposedly being close to two. This species differs from well known chemisorbed oxygen by a much higher dipole

moment of the adsorbate complex, higher adsorption energy, and a reduced reactivity. The non-Faradaicity in this picture results from the reduced reactivity of the spillover species because through electrostatic interactions this species can affect the reactivity of many coadsorbed molecules by its mere presence before being finally consumed by the reaction itself. An alternative concept was proposed by Sobyenin et al. who suggested that a chain reaction mechanism involving an electrochemically generated charged oxygen surface species could explain the non-Faradaicity in catalytic CO-oxidation on Pt/YSZ [16-18]. The main objective of this study was to investigate the mechanism of the ethylene oxidation over Pt/YSZ and to clarify the origin of the non-Faradaic behavior of the electrochemical promotion.

The experiments are conducted in Hannover in a standard stainless steel UHV system equipped with a differentially pumped QMS for rate measurements and PEEM for work function measurements. In PEEM the sample is illuminated with photons from a D₂ discharge lamp (5 – 6 eV) and the ejected photoelectrons are projected onto a phosphorus screen [19]. In this way the local work function can be imaged with a spatial resolution of roughly 1 μm and the temporal resolution of video images (20 ms). Under reaction conditions the UHV system is continuously pumped with a rate of about 100 L s⁻¹, i. e. we operate the UHV chamber as a continuous flow reactor (see chapter 4).

Altogether 5 different Pt/YSZ samples were studied differing in the preparation method, sputtering time, annealing time, annealing temperature range (1120 - 1370 K) and thickness of the Pt WE. One sample prepared from Pt past with thickness of the order of few μm (≈ 8-10 μm) and four samples from sputtering with thickness range (200 nm – 1 μm). With respect to catalytic activity all samples showed more or less the same behavior but in PEEM some differences were visible. Accordingly, only the results of two samples with thicknesses of 200 nm (sample 5) and 600 nm (sample 4) were shown, respectively. The electrodes preparation and characterization have been explained in details in chapter 5.

The YSZ sample was radiatively heated from the backside by a commercial slide projector lamp. Gases of purity 5.0 for Ar, 4.5 for O₂, 5.0 for H₂ and 2.8 for C₂H₄ were used. The Pt WE surfaces were cleaned by repeated cycles of mild Ar⁺ ion bombardment (T≈ 630 K, p(Ar)= 5 x 10⁻⁵ mbar and E= 1 keV). Prior to the experiments, the starting point was a Pt surface freshly prepared in several oxidation/reduction cycles with O₂/H₂

($T \approx 670$ K, $p(\text{O}_2) = 2 \times 10^{-5}$ mbar, $p(\text{H}_2) = 1 \times 10^{-6}$ mbar). A contribution from reaction at the backside of the sample cannot be excluded but since the backside was not cleaned by Ar^+ ion sputtering this contribution is presumably quite small.

The background in the rate hystereses was determined by cycling $p(\text{C}_2\text{H}_4)$ with the sample being at room temperature and $p(\text{O}_2)$ being kept fixed. The partial pressures in this report represent directly the ionization gauge readings (uncorrected).

For the electrochemical measurements a standard three-electrode set-up was used (see Fig. 4.2 in chapter 4) with a potentiostat controlling the potential of the working electrode with respect to a reference electrode. Since no gas reference electrode was used the potential of the reference electrode is not fixed but may shift due to zirconia reduction at the interface YSZ/Pt of the reference electrode. In order to minimize this effect the sample was exposed to prolonged O_2 treatments after each set of experiments.

In order to qualify and quantify the species formed on the Pt surface during the $\text{C}_2\text{H}_4 + \text{O}_2$ reaction *in situ* XPS have been studied under UHV and high pressure (≈ 1 mbar) conditions. The experiments were performed at the beamline U49/2-PGM1 at the synchrotron radiation facility BESSY in Berlin in a specially designed differentially pumped XPS system. The sample used for these measurements is sample number 2 (chapter 5). Under reaction conditions, the cell was operated as a continuous flow reactor. The gasses were supplied via a gas line connected to the UHV chamber. Reaction products were monitored with a differentially pumped QMS coupled to the spectroscopic characterization by XPS. For low pressure experiments all gases were introduced to the main chamber via sapphire-sealed variable leak valves (Varian) by manual operation. Gases were introduced via mass flow controllers for high pressure experiments. Gases of purity 5.0 for Ar, 4.5 for O_2 and 2.8 for C_2H_4 were used. A sketch of the set-up of the experimental cell, electrode configuration and differentially pumped electrostatic lens system are shown in section 4.2 in chapter 4. The YSZ sample was heated from the backside through a 100-nm-thick SiC window with an infrared laser, heating is provided by a NIR laser at the rear of the sample and monitored by a K-type Ni/NiCr thermocouple spot-welded to the edge of WE side on the front of the sample. Prior to the experiments the Pt film was cleaned by repeated cycles of mild Ar^+ ion bombardment ($t = 20$ min, $E = 1.5$ keV, $p(\text{Ar}) = 1 \times 10^{-4}$ mbar). The reaction system was investigated at 680 K keeping the $p(\text{C}_2\text{H}_4)$ fixed at 1×10^{-6} mbar and varying the $p(\text{O}_2)$.

For high-p experiments the reaction system was investigated at 650 K keeping the total pressure fixed at 0.2 mbar and varying the ratio of the gases in the C₂H₄/O₂ mixture.

6. 2 Reaction kinetics

6. 2.1 Bistable kinetics under open circuit conditions

Figure 6.1 displays the steady state behavior of ethylene oxidation to CO₂ upon cyclic variation of p(C₂H₄) under open circuit conditions (OC) i.e. without any applied potential, for five different temperatures, 546 K, 573 K, 623 K, 673 K and 763 K. All curves exhibit the same qualitative behavior. At low p(C₂H₄) the CO₂ production rises linearly with p(C₂H₄) but beyond the rate maximum the rate decreases monotonically with increasing p(C₂H₄). As was demonstrated in Fig. 6.2 by *in-situ* XPS measurements the rate decrease is due to the build-up of a carbonaceous layer inhibiting O₂ adsorption and hence poisoning the reaction [20-22]. Right the rate maximum, i.e. in an excess of ethylene pressure the surface is covered by a layer of carbonaceous CH_x species, while no carbon is detected left of the rate maximum, i.e. in an excess of oxygen pressure as shown by Fig. 6.2.

Similar rate curves as the ones shown here were obtained by Vayenas and co-workers but interpreted differently i.e. the formation of a carbonaceous layer and its inhibiting effect on O₂ adsorption were not taken into account [12-14, 23]. The term carbonaceous layer refers to the fact that in XPS the C1s signal deviates from the signal of a graphite layer thus indicating an incomplete C₂H₄ decomposition with CH_x groups still being present [24].

As indicated by Fig. 6.1 the rate curves exhibit a pronounced hysteresis which shrinks with rising temperature. Tentatively, one can assign the two kinetic branches of the hysteresis to different amounts of carbon poisoning the surface reaction i.e. different carbon coverages and hence different degrees of inhibition. Remarkably, the rate maximum shifts with rising temperature to lower p(C₂H₄). We can explain this relation assuming that higher temperatures facilitate the decomposition of ethylene thus allowing the faster build-up of a carbonaceous layer.

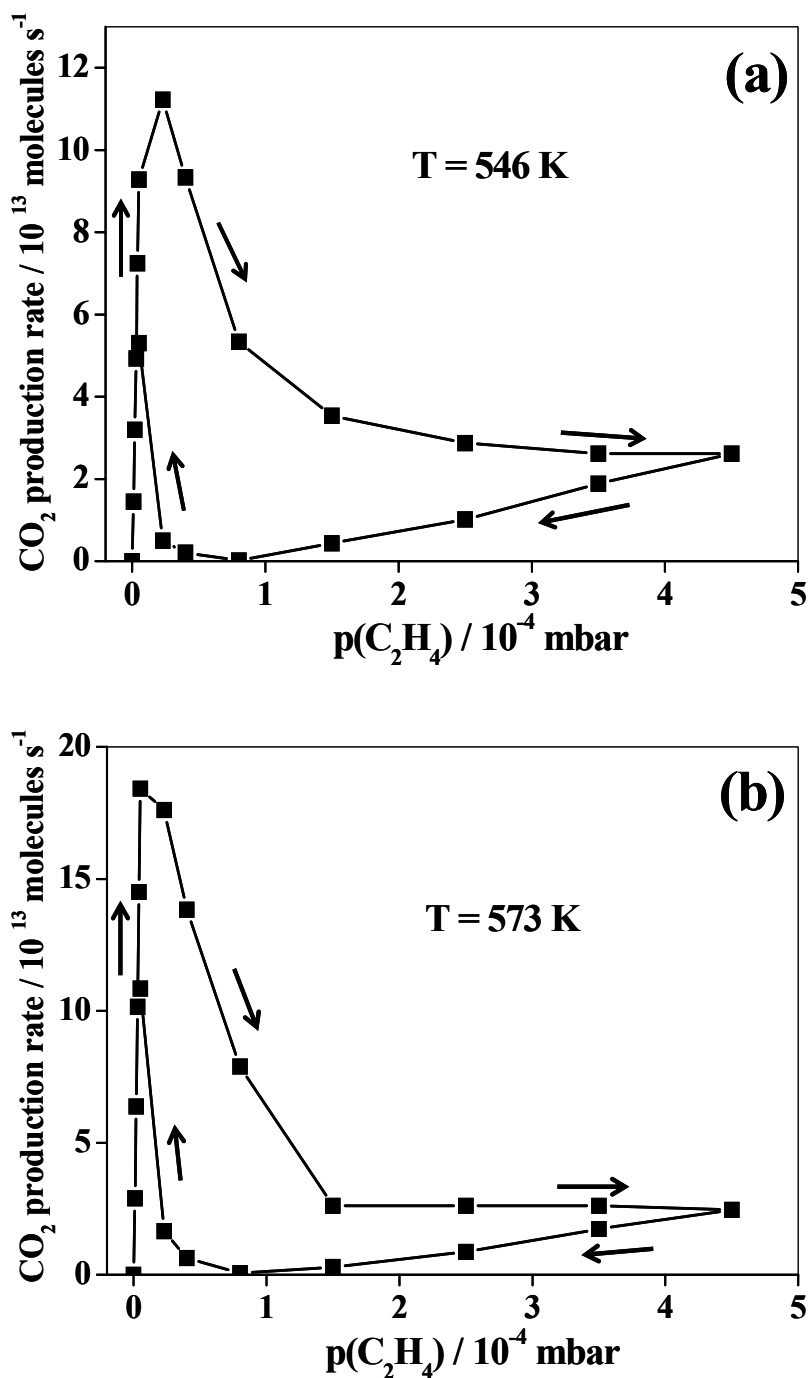


Figure 6.1.1: Hystereses in the CO₂ production rate upon cycling p(C₂H₄) at fixed p(O₂) = 5 × 10⁻⁵ mbar and varying temperatures: (a) 546 K and (b) 573 K. The starting point for each cycle was a Pt surface freshly prepared in several oxidation/reduction cycles with O₂/H₂ at 670 K. The partial pressure in this and all subsequent hystereses measurements was varied stepwise with a waiting period of about 2 min. for each data point.

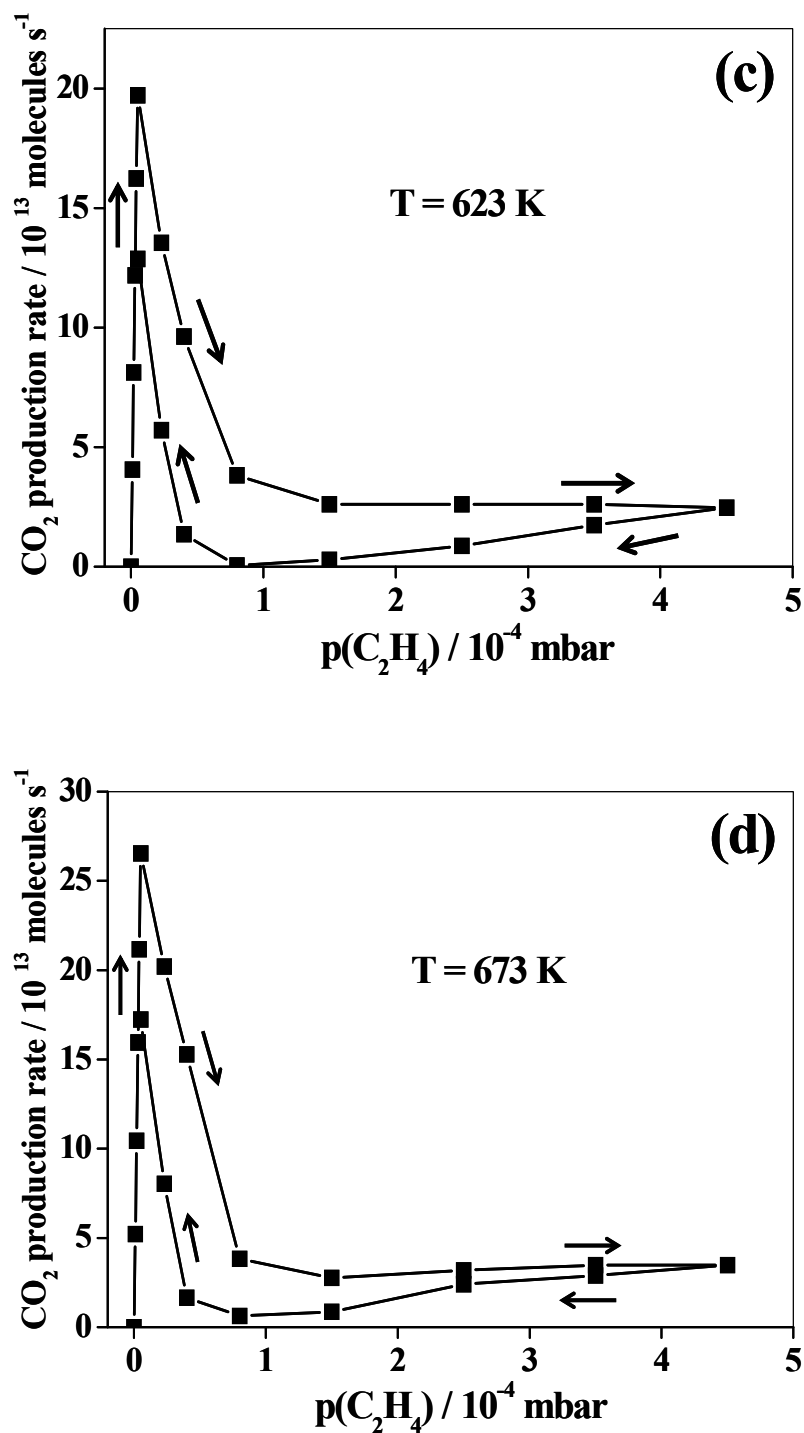


Figure 6.1.2: Hystereses in the CO₂ production rate upon cycling p(C₂H₄) at fixed p(O₂) = 5 × 10⁻⁵ mbar and varying temperatures: (c) 623 K and (d) 673 K. The starting point for each cycle was a Pt surface freshly prepared in several oxidation/reduction cycles with O₂/H₂ at 670 K. The partial pressure in this and all subsequent hystereses measurements was varied stepwise with a waiting period of about 2 min. for each data point.

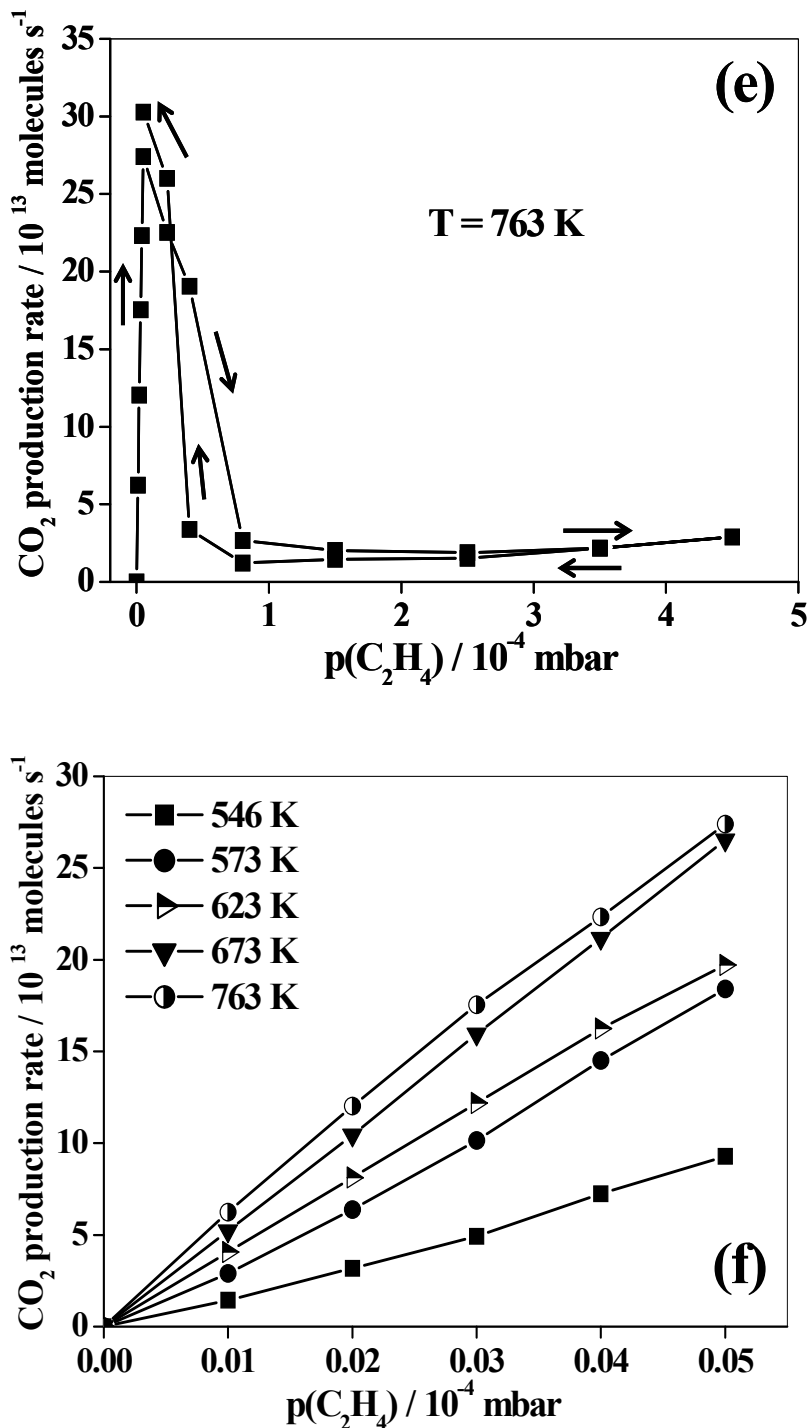


Figure 6.1.3: (e) Hystereses in the CO₂ production rate upon cycling p(C₂H₄) at 763 K and fixed p(O₂) = 5 × 10⁻⁵ mbar. The starting point for each cycle was a Pt surface freshly prepared in several oxidation/reduction cycles with O₂/H₂ at 670 K. The partial pressure in this and all subsequent hystereses measurements was varied stepwise with a waiting period of about 2 min. for each data point. (f) Linear dependence of the CO₂ production rate on p(C₂H₄) under open circuit conditions with oxygen being in excess. The drawing represents an enlarged section of (a-e) showing the behavior of the rate from zero up to the rate maximum with varying temperatures.

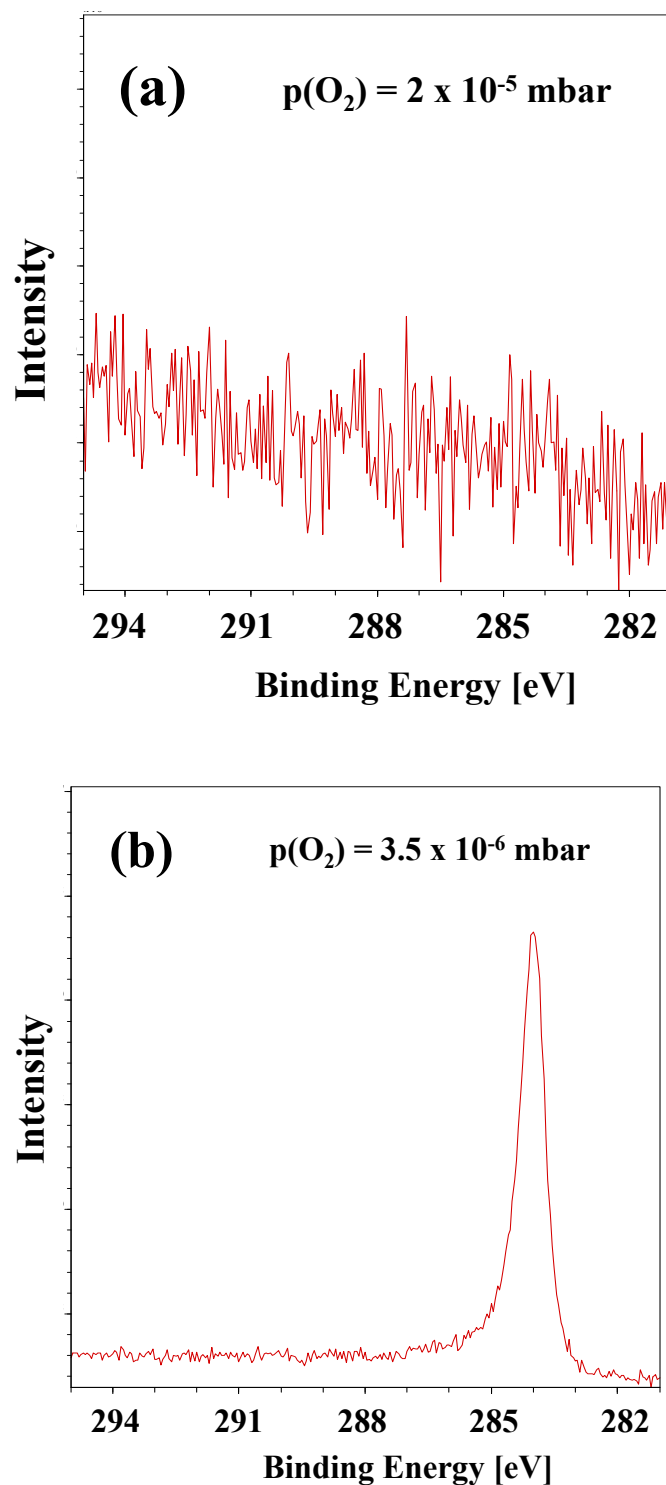


Figure 6.2: C1s photoelectron spectra showing the carbon formation with an increase of $p(\text{C}_2\text{H}_4)$ under OC conditions. (a) Spectrum taken left of the rate maximum in Fig. 6.1, i.e. in an excess of oxygen pressure, $p(\text{O}_2) = 2 \times 10^{-5}$ mbar. (b) C1s spectrum recorded right of the rate maximum in Fig. 6.1, i.e. in an excess of ethylene pressure, $p(\text{O}_2) = 3.5 \times 10^{-6}$ mbar. Experimental conditions: $T = 680$ K and at constant $p(\text{C}_2\text{H}_4) = 1 \times 10^{-6}$ mbar. Note that the sample used here is prepared by sputtering (sample 2 in chapter 5).

6.2.2 Effect of electrochemical pumping ($V_{WR}=1$ V)

Figure 6.3a shows the effect of a positive potential of 1 V, pumping oxygen onto the Pt surface. As indicated by the arrow the rate increases until a rate branch is reached which lies above the active branch of the unpromoted system. Remarkably, on this branch no hysteresis is seen upon cycling $p(\text{C}_2\text{H}_4)$ and with the potential still on.

The variation of the integral PEEM intensity during cycling $p(\text{C}_2\text{H}_4)$ is displayed in Fig. 6.3b. In PEEM, a homogeneous darkening upon applying a positive pumping potential was observed. The reduction in PEEM intensity is in agreement with the idea that the oxygen coverage grows thus causing an increase in work function. The large plateau in which the intensity only slightly increases with rising $p(\text{C}_2\text{H}_4)$ can be attributed to a carbon covered surface [20]. This assignment was also confirmed by *in-situ* XPS measurements showing a large carbon signal attributed to a carbonaceous layer and very low oxygen coverage beyond the rate maximum (see Figs. 6.2 and 6.17). The very pronounced hysteresis we see in the rate curves is hardly discernible in the PEEM intensities.

As indicated by Fig. 6.3b applying a positive potential $V_{WR}=1$ V shifts the whole intensity curve to a lower value. The homogeneity of this transition depends on the sample preparation. As will be shown below with other sample with a rougher surface topography (thickness= 200 nm) PEEM showed the formation of macroscopic dark islands upon pumping while the majority of the surface remained bright (see Fig. 6.7).

Furthermore, the PEEM data in Fig. 6.3b demonstrate that the magnitude of the shift during application of a positive potential of 1 V remains nearly constant over the whole range over which $p(\text{C}_2\text{H}_4)$ is varied. Tentatively, one can explain this observation assuming that electrochemical pumping generates a high oxygen coverage only locally around pores. The supply of oxygen spillover in these local areas is apparently high enough that these spots remain oxygen covered during the reaction, irrespective of $p(\text{C}_2\text{H}_4)$.

An electrochemical promotion is only observed beyond the rate maximum but not in the region before where the rate rises linearly with $p(\text{C}_2\text{H}_4)$. This was also confirmed by *in situ* XPS experiments meaning that the electrochemical promotion effect is linked to the presence of a carbon adlayer (see Figs. 6.2 and 6.17 below).

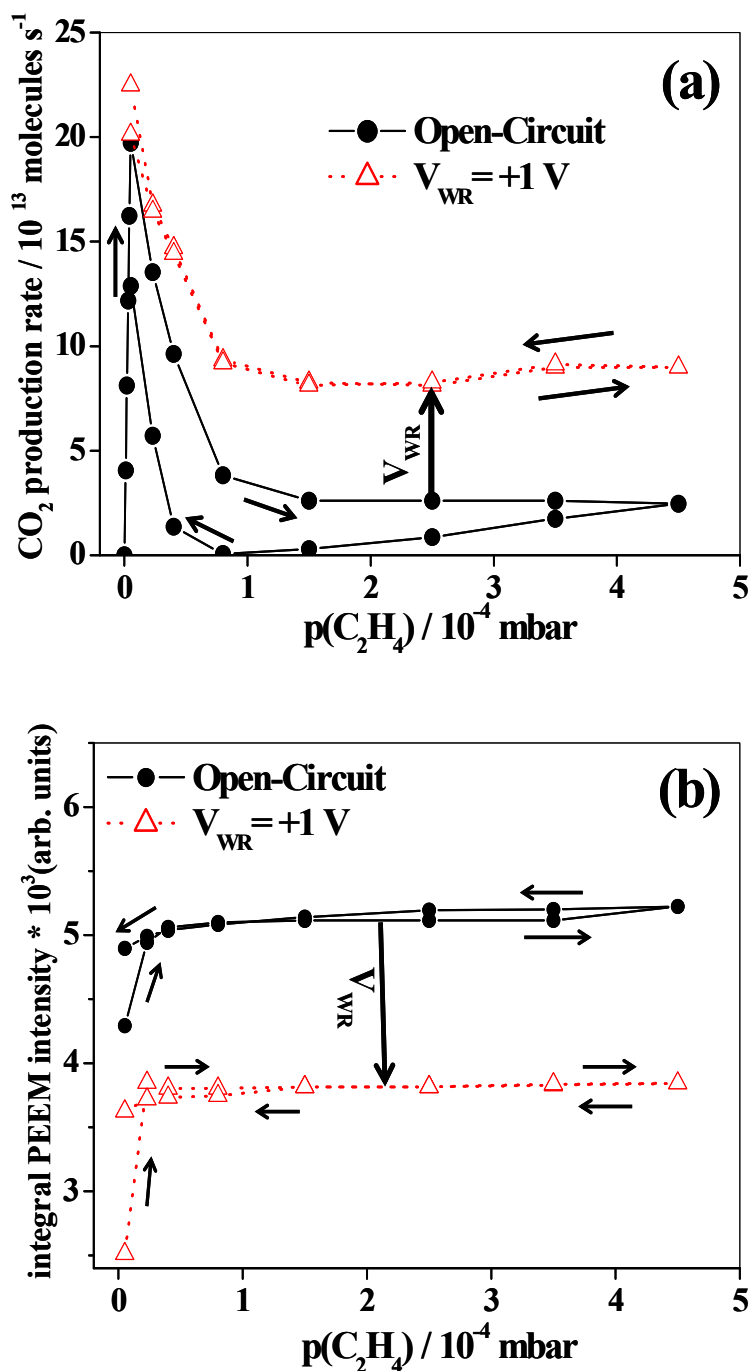


Figure 6.3: The effect of applying positive potential $V_{WR}=1$ V on the kinetics of ethylene oxidation and on the PEEM intensity is shown: (a) Reaction rates. The full black lines represent the open-circuit kinetics, i.e. the rate without applying an external voltage. The arrow indicates the rate increase during applying the electric potential with $p(C_2H_4)$ being kept constant. The dotted red lines display the reaction rate during cycling $p(C_2H_4)$ with the potential $V_{WR}=1$ V being kept fixed. (b) Variation of the integral PEEM intensity corresponding to the rate curves shown in (a). The digitized PEEM intensity was integrated over the whole PEEM image. Black lines represent open-circuit conditions, the dotted red lines the PEEM intensity during application of $V_{WR}=1$ V.

What has not been explained so far is why the active state which is reached through electrochemical promotion lies above the active branch of the unpromoted system as demonstrated by Fig. 6.3a. One possibility is that the electrochemical promotion leads to a more efficient reduction in carbon coverage than the transition to the active branch of the unpromoted bistable system. An alternative explanation is that electrochemical pumping either through structural or through chemical changes leads to a modified surface with enhanced catalytic activity. A number of observations strongly support the latter possibility. Firstly, as shown by Fig. 6.4 the high activity is only slightly reduced after switching off the applied electric potential (open circuit potential). It takes three complete oxidation/reduction cycles in O_2 and H_2 to restore the original catalytic activity (see Fig. 6.5). Secondly, the electrochemical promotion effect depends strongly on the reaction conditions as will be shown below by Figs. 6.6, 6.7 and 6.9.

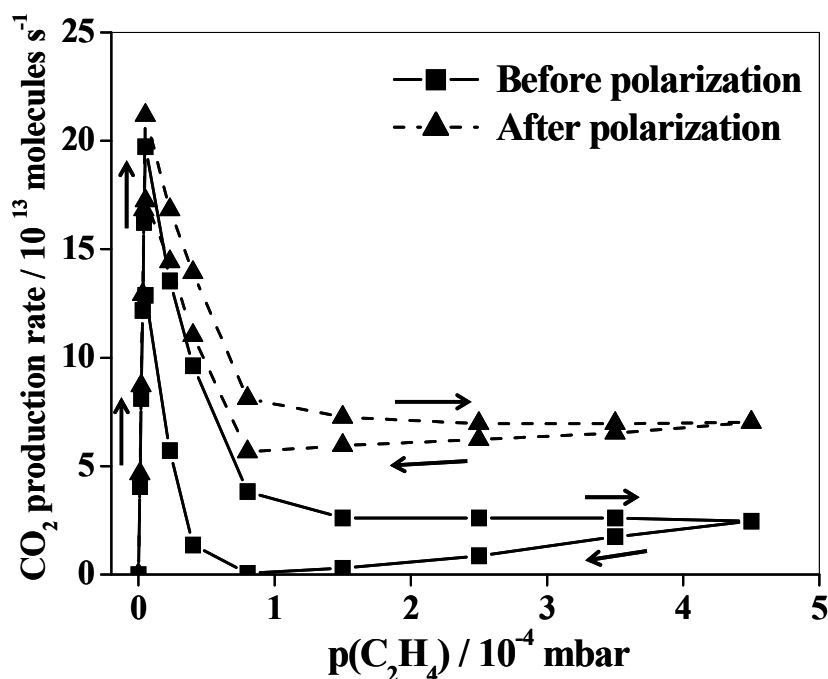


Figure 6.4: Increase in catalytic activity after anodic polarization on the Pt surface. All rate curves shown are recorded under open-circuit conditions at fixed $p(O_2) = 5 \times 10^{-5}$ mbar and $T = 623$ K. The full line display the reaction rate before anodic polarization and the dashed lines the reaction rate after anodic polarization with $V_{WR} = 1$ V. The polarization occurred in the activation experiment in Fig. 6.3.

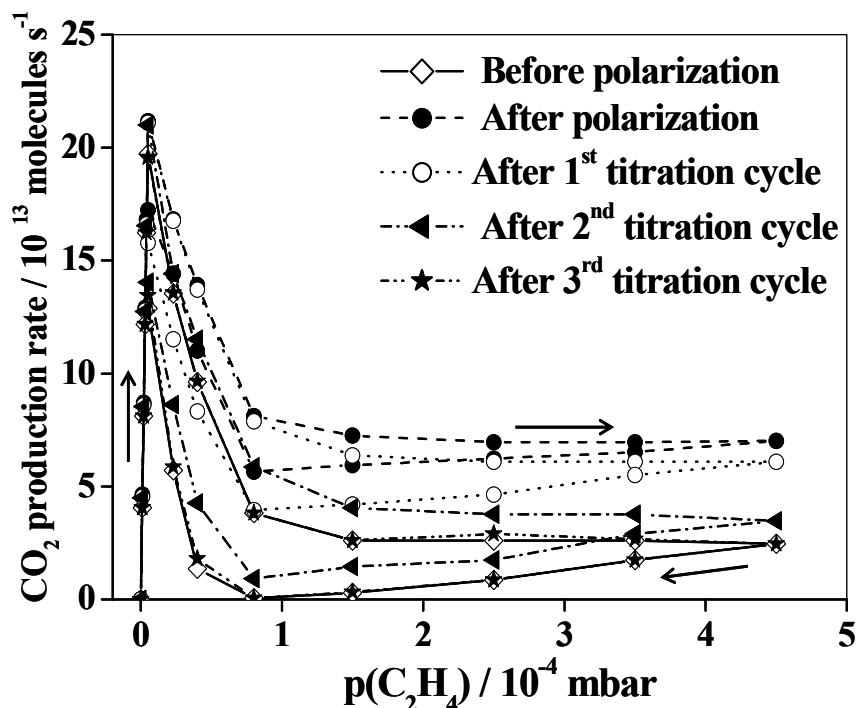


Figure 6.5: Oxidation/reduction cycles in O_2/H_2 to restore the original catalytic activity after anodic polarization on the Pt surface. All rate curves shown are recorded under open-circuit conditions at fixed $p(O_2)=5 \times 10^{-5}$ mbar and $T=623$ K. The full line display the reaction rate before anodic polarization and the dashed lines the reaction rate after anodic polarization with $V_{WR}=1$ V. The polarization occurred in the activation experiment in Fig. 6.3. The open circles, triangles and the stars display the rate after each O_2/H_2 titration cycle.

6.3 Dependence of the promotion effect on reaction conditions

The EPOC effect depends on the reaction conditions as demonstrated by Figs. 6.6, 6.7 and 6.9. As indicated by both figure the magnitude of the EPOC effect given by the lengths of the arrows.

6.3.1 Effect of applying potential starting from lower rate branch

Starting from the low rate branch at point A setting the working electrode to $V_{WR}=1$ V causes a transition to the dashed rate curve as shown in Fig. 6.6a. Within a few minutes the rate reaches point B on a new rate branch located above the upper rate

branch of the unpromoted system. With the potential still on no hysteresis is observed on this new branch upon cyclic variation of $p(\text{C}_2\text{H}_4)$.

As shown earlier with a graphitized dense Pt electrode on YSZ, the spillover oxygen reaching the surface through pores in the Pt layer spontaneously reacts with carbon forming CO and CO_2 thereby eating holes into the graphite layer [8]. The same hole-eating process will also take place during ethylene oxidation but, in addition, O_2 is now present in the gas phase. As spillover oxygen eats a hole into the CH_x layer now gaseous O_2 will adsorb into the uncovered Pt area, react with carbon thereby enlarging the hole. Due to this positive feedback the growth of the holes will obey autocatalytic kinetics, a process which one can denote as “ignition”. The term “ignition” here does not imply a temperature increase but just refers to the requirement that only a small perturbation suffices to dissolve a metastable, unreactive state of the system.

In agreement with this mechanistic picture an *in situ* XPS study showed that an EPOC effect only occurs if carbon is present on the surface. This hole-eating process can also be imaged by PEEM as demonstrated by the images in Fig. 6.7 showing the surface of a 200 nm thick Pt film (sample 5 in chapter 5) under reaction conditions before and after application of a potential of 1 V. Since chemisorbed oxygen increases the WF, this species is imaged as dark area in PEEM, and the CH_x layer appears as bright grey area [8, 20]. The surface is strongly inhomogeneous; only part of the carbon layer has been removed and replaced by oxygen.

Repeating the previous PEEM experiment with a smoother Pt film of a 600 nm thickness (sample 4 in chapter 5) only shows a homogeneous darkening of the surface upon applying a potential $V_{\text{WR}} = 1$ V as shown in Figs. 6.3b and 6.6b. Evidently the hole-eating process then takes place on a length scale below the resolution of about 1 μm . As indicated by Fig. 6.6b, also applying a positive potential $V_{\text{WR}} = 1$ V shifts the whole intensity curve to a lower value. The homogeneity of this transition depends on the sample preparation. With the smoother sample used here we can assume that the same mechanism holds but that the oxygen islands are below the resolution of the instrument thus giving the impression of a homogeneous transition. The PEEM data in Fig. 6.6b demonstrate that the magnitude of the shift during application of a positive potential remains nearly constant over the whole range over which $p(\text{C}_2\text{H}_4)$ is varied. This result is quite similar to Fig. 6.3b which has been explained in details there.

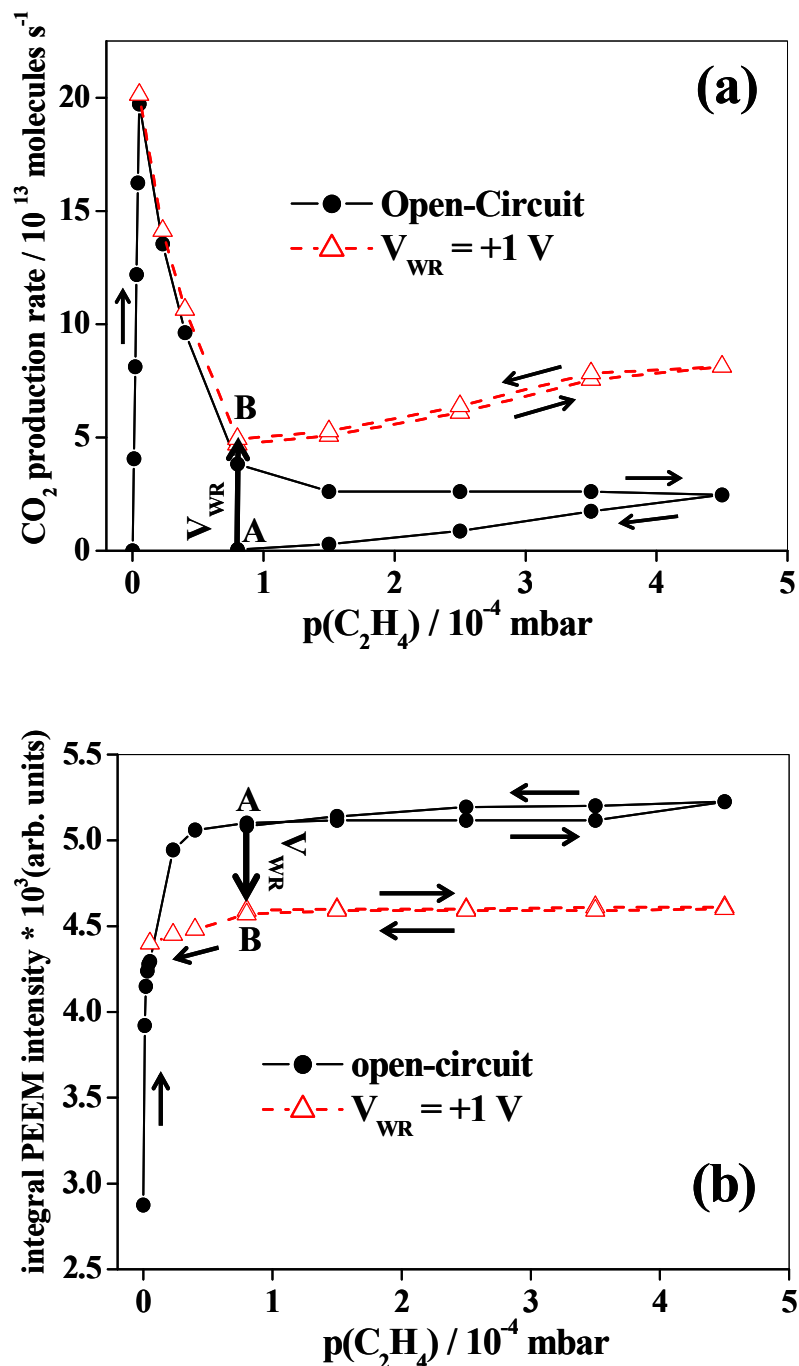


Figure 6.6: Electrochemical activation. The effect of applying positive potential $V_{WR} = 1$ V on the kinetics of ethylene oxidation and on the PEEM intensity is shown: (a) Reaction rates. The circles mark the hysteresis obtained upon cycling $p(\text{C}_2\text{H}_4)$ under open-circuit conditions. The AB arrow indicates the rate increase as an electric potential of 1 V is applied starting at point A with $p(\text{C}_2\text{H}_4)$ being kept constant. The triangles mark the reaction rate upon cycling $p(\text{C}_2\text{H}_4)$ with $V_{WR} = 1$ V. Reaction conditions: $T = 623$ K, $p(\text{O}_2) = 5 \times 10^{-5}$ mbar, waiting period for each data point 2 min. Thickness of Pt layer = 600 nm. (b) Variation of the integral PEEM intensity corresponding to the rate curves shown in (a). The digitized PEEM intensity was integrated over the whole PEEM image.

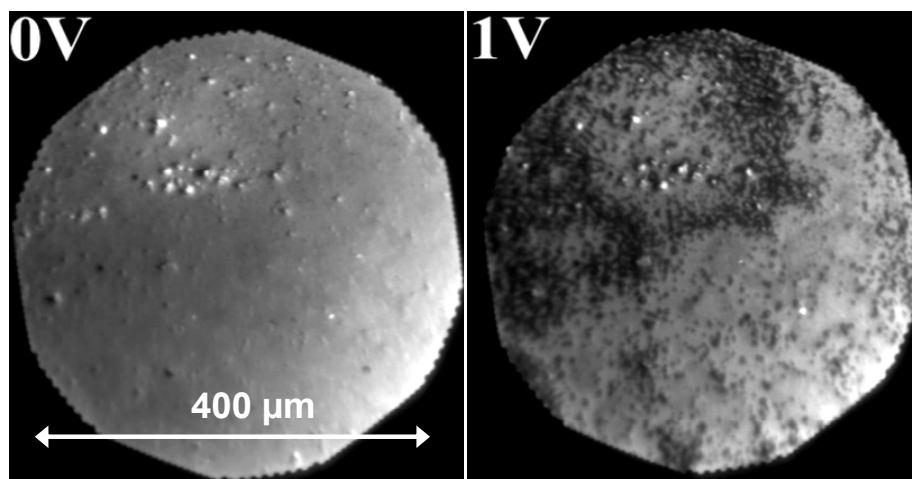
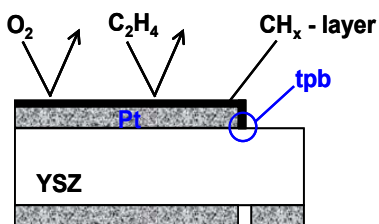


Figure 6.7. PEEM images showing the formation of oxygen islands (dark area) on the Pt surface as a result of electrochemical pumping under reaction conditions. Left image: open circuit conditions and right image: after applying $V_{WR} = 1$ V for 5 min. Reaction conditions: $T = 700$ K, $p(O_2) = 5 \times 10^{-5}$ mbar, $p(C_2H_4) = 8 \times 10^{-5}$ mbar. Thickness of Pt layer = 200 nm.

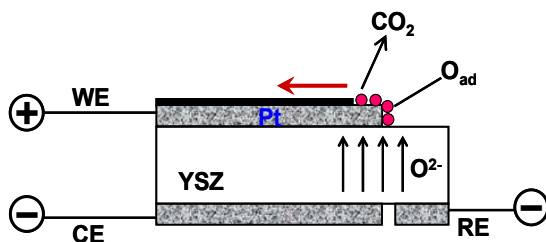
A schematic drawing for the sequence of the ignition process steps during application of anodic potential has been explained in Fig. 6.8. Firstly, the Pt surface is covered by a carbon layer which poisons the catalyst. In the second step setting the Pt WE at a positive potential leads to a spillover oxygen created by electrochemical pumping diffuses through pores in the Pt electrode (tpb) to the surface where it reacts with carbon to CO_2 . The spillover oxygen thus eats holes into the carbon overlayer through which oxygen from the gas phase can adsorb and react thereby enlarging the hole. With a larger hole more oxygen can adsorb, thus constituting a positive feedback between the size of the hole and the reactive removal of carbon. In other words, the electrochemical pumping causes an ignition from an unreactive carbon poisoned state of the surface to an active state with less carbon.

(I) poisoned state



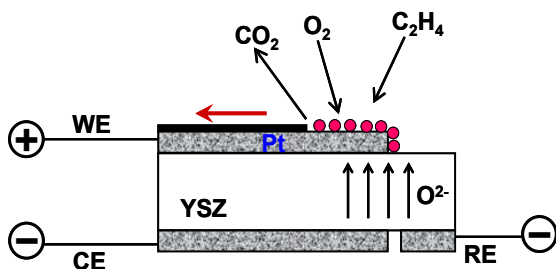
Open circuit

(II) hole eating



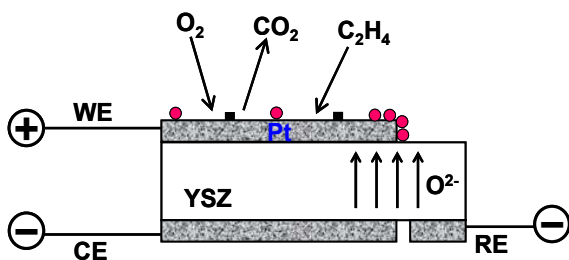
$V_{WR} = 1 \text{ V}$

(III) ignition



$V_{WR} = 1 \text{ V}$

(IV) reactive state



$V_{WR} = 1 \text{ V}$

Figure 6.8: Schematic representation of the ignition mechanism proposed for the electrochemical activation of catalytic ethylene oxidation on Pt/YSZ.

6.3.2 Effect of applying potential starting from upper rate branch

The EPOC effect depends strongly on the reaction conditions as demonstrated by Fig. 6.9. The open circuit experiment is the same as in Fig. 6.1 but now we apply the electrical potential at different points on the upper rate branch. In each polarization experiment, we start with a freshly prepared surface in order to rule out memory effects i.e. the catalyst treated with a complete oxidation/reduction cycles in O_2 and H_2 to restore the original catalytic activity after each measurements. As indicated by Fig. 6.9 setting the working electrode to $V_{WR} = 1$ V at point C instead of A causes a rate increase by a factor of 2.3 compared to the factor of 1.3 at point A. The time dependence of this electrochemical activation is displayed in Fig. 6.11 for the transition from G to H in Fig. 6.9b. The diagram shows how the rate increase is correlated with a decrease in PEEM intensity, i. e. a rising oxygen coverage. Intuitively one would expect that ignition becomes more difficult with rising $p(C_2H_4)$ because rising $p(C_2H_4)$ should lead to a denser CH_x -layer which should suppress activation of the poisoned state. What we observe in Fig. 6.9 is, however, just the opposite. If we chose point G instead of point A lying at higher $p(C_2H_4)$ applying the same potential leads to a much stronger increase in catalytic activity: point H is reached which belongs to the red rate curve and rate increase by a factor of 8 as presented in Fig. 6.10a for the rate ratio calculation. The EPOC effect given by the lengths of the arrows increases monotonically from left to right. Rather than changes in the adsorbate layer, a restructuring of the catalyst induced by the catalytic reaction and/or by the electric potential appears to play the dominant role. Support for the restructuring mechanism come from the observation that after electrochemical activation the enhanced catalytic activity persists or is only slightly reduced even if the applied potential is turned off as demonstrated in Fig. 6.4. It requires three complete oxidation/reduction cycles in O_2/H_2 to restore the initial state of the catalyst (see Fig. 6.5).

In short, the EPOC effect depends (i) on the reaction conditions and (ii) on the history of the sample.

A possible way to rationalize the dependence of the EPOC effect on the reaction conditions is to assume that the oxygen spillover localized around a pore in the Pt layer does not always lead to an ignition of the reaction but that, in addition, also favorable conditions in the carbonaceous layer surrounding the pore must be given. One would expect that ignition becomes more difficult the denser the carbonaceous layer grows. In

that case ignition should occur everywhere easily at low $p(\text{C}_2\text{H}_4)$ and be suppressed at many locations at high $p(\text{C}_2\text{H}_4)$. As shown by Fig 6.9 we observe just the opposite. The electrochemical promotion effect rises steeply with increasing $p(\text{C}_2\text{H}_4)$. One has to conclude that the dependence of the EPOC effect on the reaction conditions is rather difficult to explain with differences in the coverage and in the structure of the carbonaceous layer alone.

The fact that the enhanced activity is only slightly reduced after turning off the applied electric potential also supports this conclusion. Rather structural modifications of the Pt/YSZ catalyst caused by the electric potential in combination with an on-going reaction appear to yield a plausible explanation. In heterogeneous catalysis, it is well known that practically all catalysts are modified by a catalytic reaction with the extent reaching from microscopic structural modifications to real morphological changes [25,26]. These restructuring effects are typically associated with an activation or deactivation of the catalyst. Similar observations exist in electrochemistry where an enhanced or reduced performance of an electrochemical cell is observed after polarization for some time [27]. In both areas, very little is known about the detailed microscopic mechanisms of the restructuring process.

So far no *in-situ* studies of the EPOC effect have been conducted revealing any reaction- or potential-induced restructuring effects. In a detailed investigation of dense Pt electrodes on YSZ by Janek et al. morphological changes in the Pt layer were observed after pumping with a positive potential [27]. These morphological changes were caused by the mechanical pressure of gas bubbles evolving underneath the Pt layer. These effects were believed to be restricted to dense electrodes and therefore of little or no relevance to the porous Pt electrodes studied here.

Similar observations to the ones made here of a catalytic enhancement persisting after turning off the applied potential have been made in high pressure studies of the EPOC effect and summarized there under "permanent EPOC effect" [5,29,30]. In these studies the formation of a surface oxide has been proposed as possible explanation. *In situ* XPS measurements which were conducted up to 0.25 mbar did not reveal any sign of Pt oxide formation (see chapter 7). Reaction- or potential-induced restructuring of the Pt/YSZ catalyst remains therefore the most likely cause of the persisting high activity.

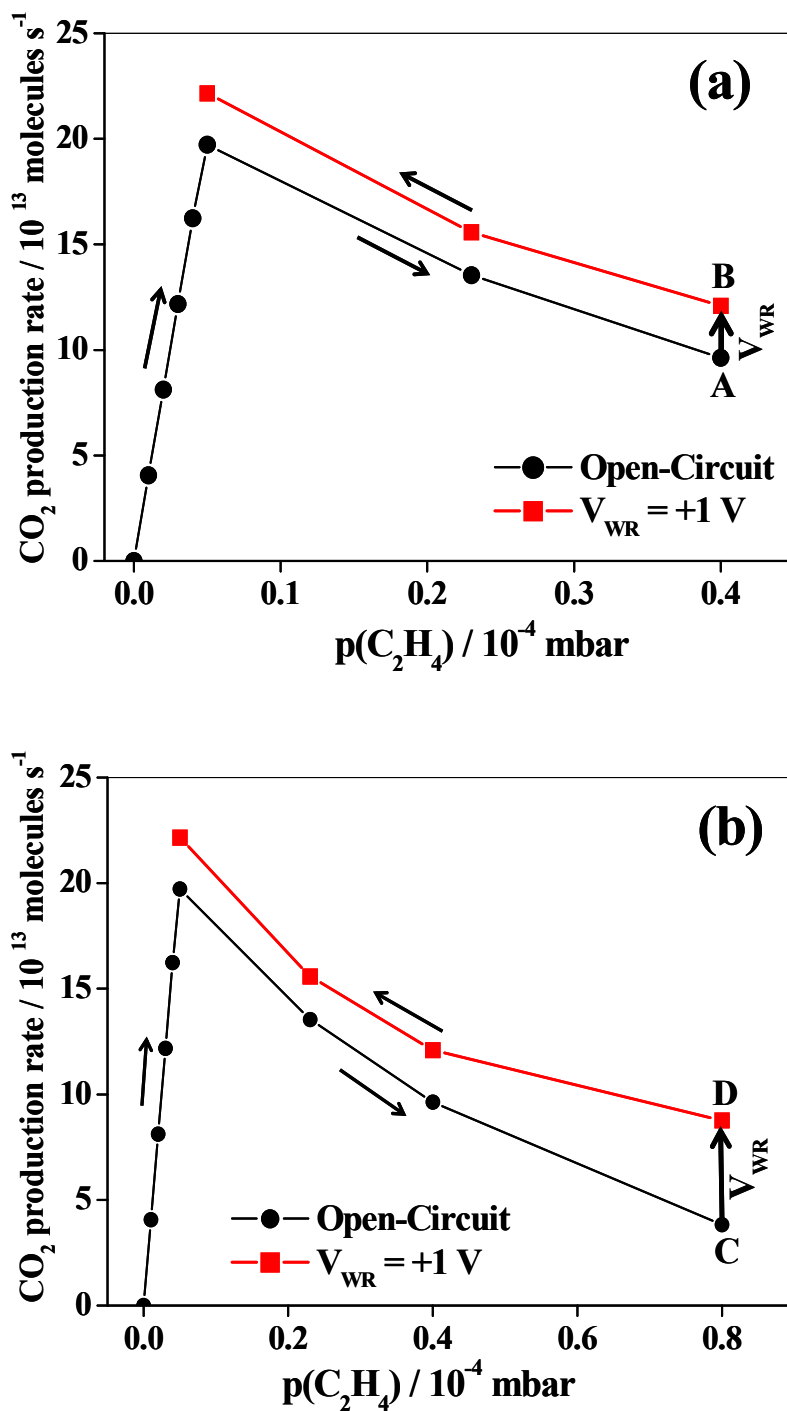


Figure 6.9.1: Dependence of electrochemical activation on the reaction conditions. The black lines represent the steady state reaction kinetics under OC conditions. The arrows denote the different degrees of electrochemical activation upon application of a potential $V_{\text{WR}} = 1$ V with $p(\text{C}_2\text{H}_4)$ being kept constant. Note that each arrow was measured with a freshly prepared surface starting from different points of the high rate branch. The red line is obtained by decreasing $p(\text{C}_2\text{H}_4)$ starting from point A and C with the electric potential still on. Reaction conditions: $T = 623$ K, $p(\text{O}_2) = 5 \times 10^{-5}$ mbar. Thickness of Pt layer = 600 nm.

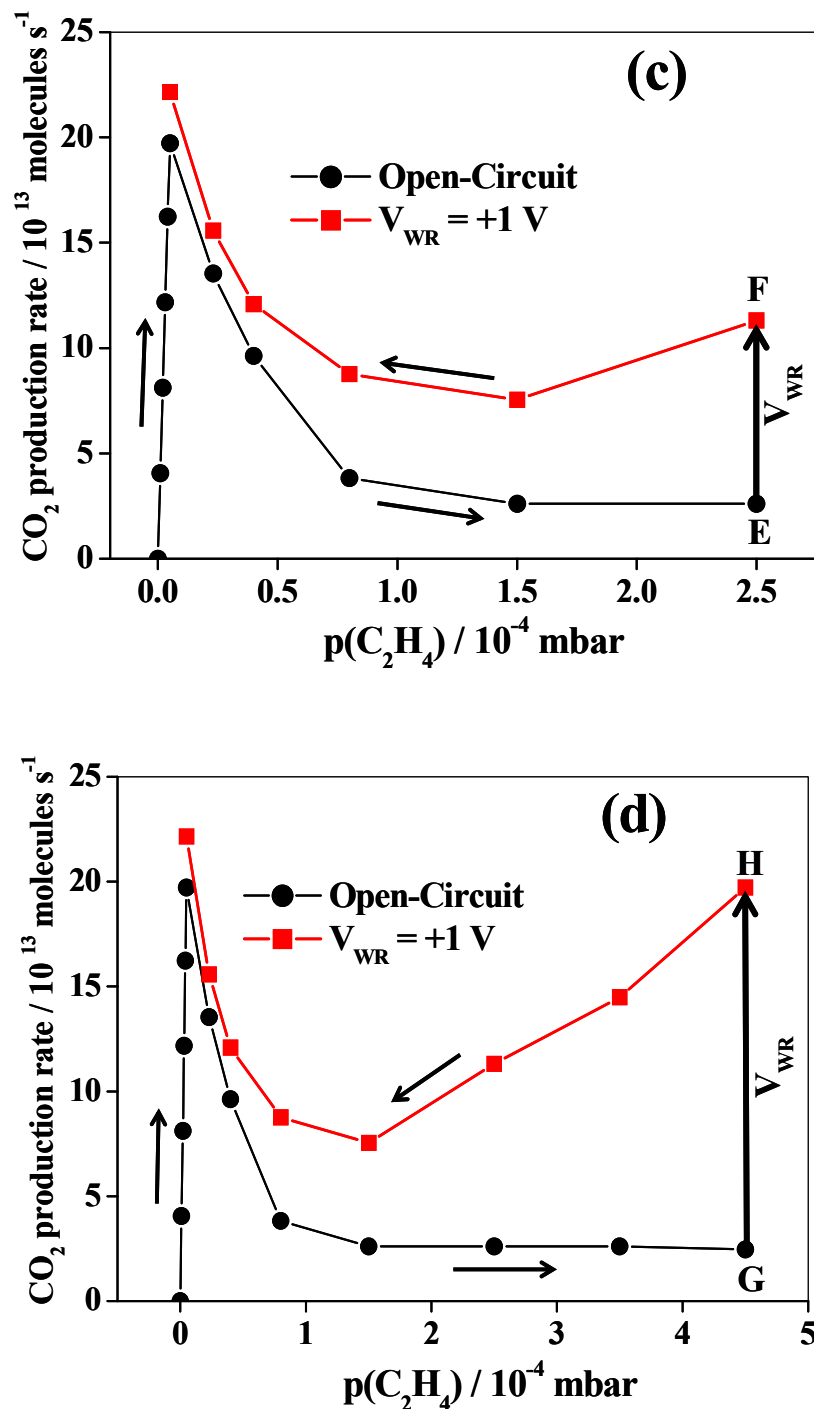


Figure 6.9.2: Dependence of electrochemical activation on the reaction conditions. The black lines represent the steady state reaction kinetics under OC conditions. The arrows denote the different degrees of electrochemical activation upon application of a potential $V_{\text{WR}} = 1$ V with $p(\text{C}_2\text{H}_4)$ being kept constant. Note that each arrow was measured with a freshly prepared surface starting from different points of the high rate branch. The red line is obtained by decreasing $p(\text{C}_2\text{H}_4)$ starting from point E and G with the electric potential still on. Reaction conditions: $T = 623$ K, $p(\text{O}_2) = 5 \times 10^{-5}$ mbar. Thickness of Pt layer = 600 nm.

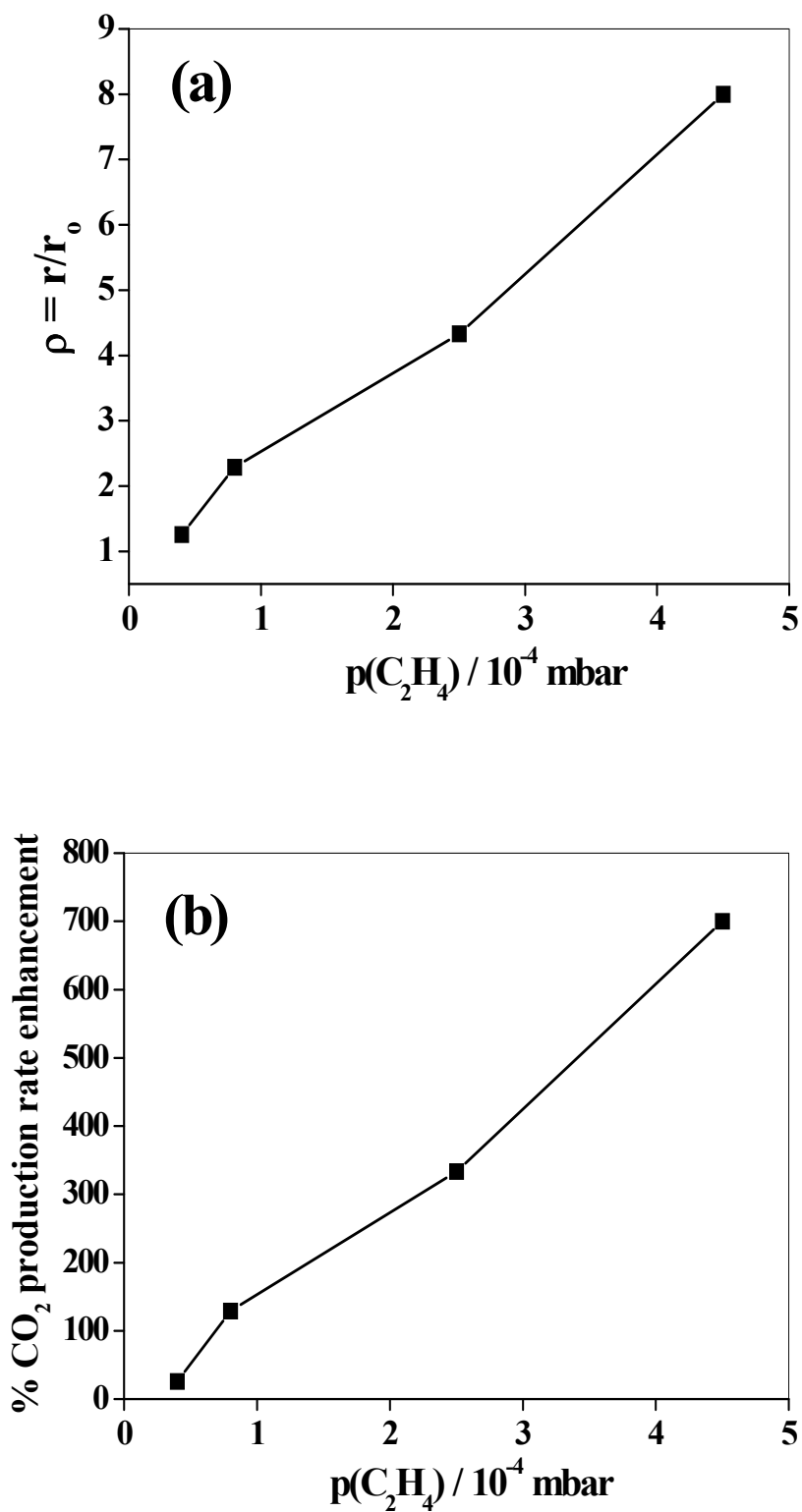


Figure 6.10: (a) Calculated rate enhancement ratio. (b) % CO_2 rate enhancement. Not all the data points were calculated from Fig. 6.9 corresponding to AB, CD, EF and GH transitions. Reaction conditions: $T = 623 \text{ K}$, $p(\text{O}_2) = 5 \times 10^{-5} \text{ mbar}$ and at fixed potential of 1V. Thickness of Pt layer = 600 nm.

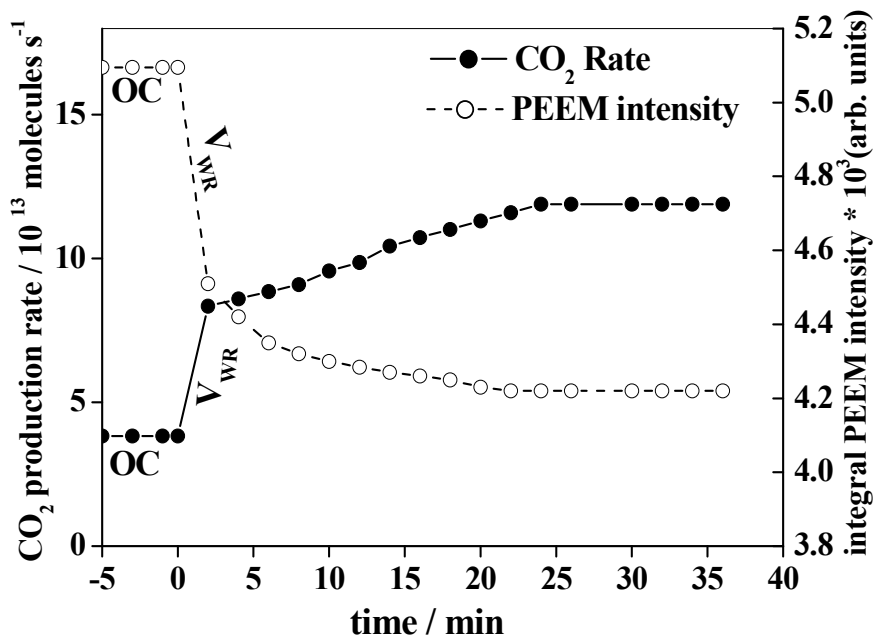


Figure 6.11: Evolution of the reaction rate and of the integral PEEM intensity during electrochemical pumping with $V_{WR} = 1$ V. The digitized PEEM intensity was integrated over the whole PEEM image. The diagram describes the transition marked in Fig. 6.9d by an arrow leading from G to H.

6.4 Catalyst potential variation (V_{WR})

6.4.1 Dependence on temperature

Figure 6.12 displays the dependence of the electrochemically induced rate increase on the applied potential for different temperatures. The rate first increases almost linearly with potential before increasing sharply between 0.5 V - 0.8 V followed by saturation beyond 1 V. At lower temperature saturation already sets in at lower potential, i. e. above 0.8 V at 568 K while at 723 K the rate curve flattens only beyond 1 V. With increasing voltage the electric current, that is the amount of transported oxygen ions will also grow exponentially following Arrhenius. A simple interpretation of the increase in saturation voltage with temperature would accordingly be that at higher temperature much more of the spillover oxygen is consumed by reaction and desorption so that a higher ionic current is required before saturation is reached.

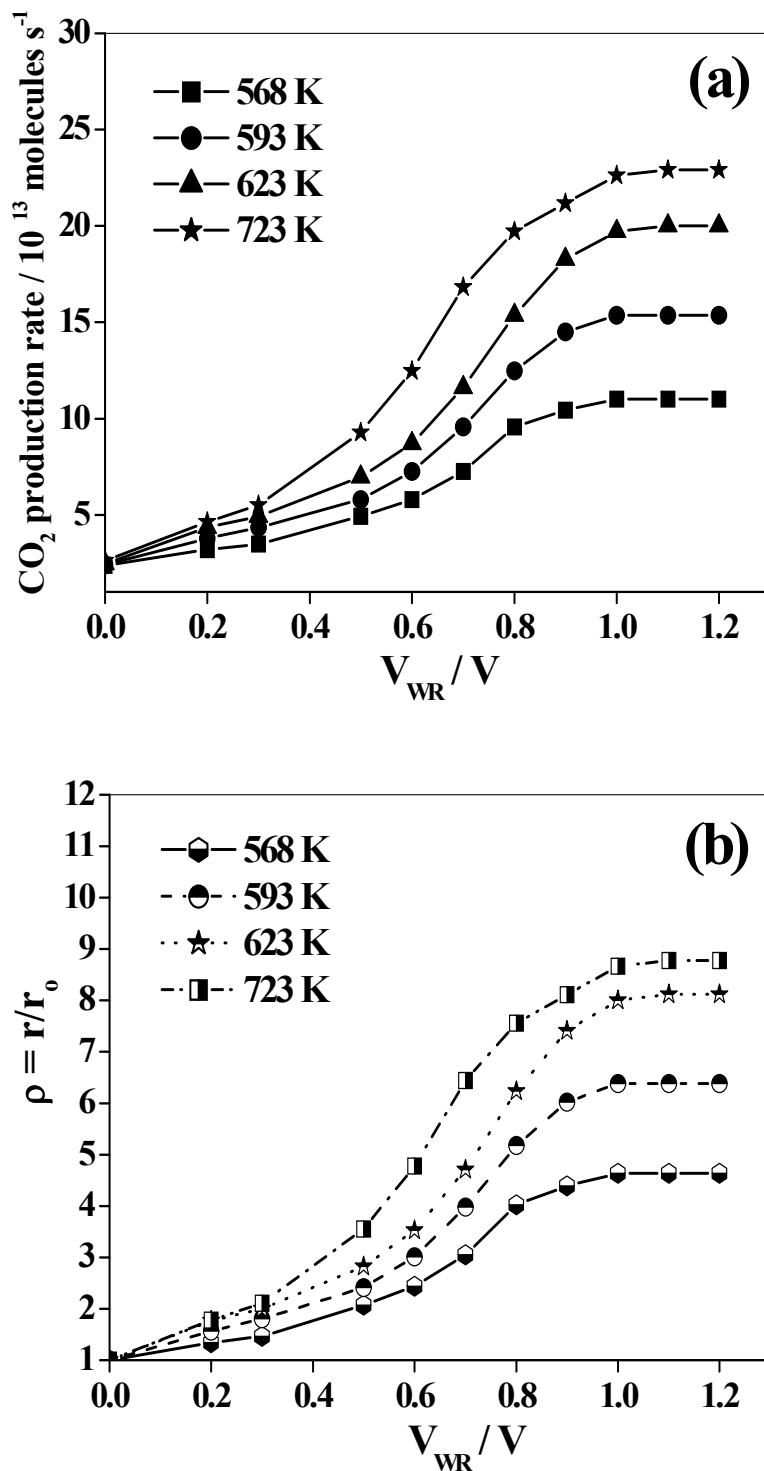


Figure 6.12. Dependence of electrochemical activation on the applied potential V_{WR} for varying temperatures with fixed $p(O_2) = 5 \times 10^{-5}$ mbar and a large excess of ethylene in the gas phase, i.e. $p(C_2H_4) = 4.5 \times 10^{-4}$ mbar. (a) Reaction rate and, (b) The corresponding calculated rate enhancement ratios.

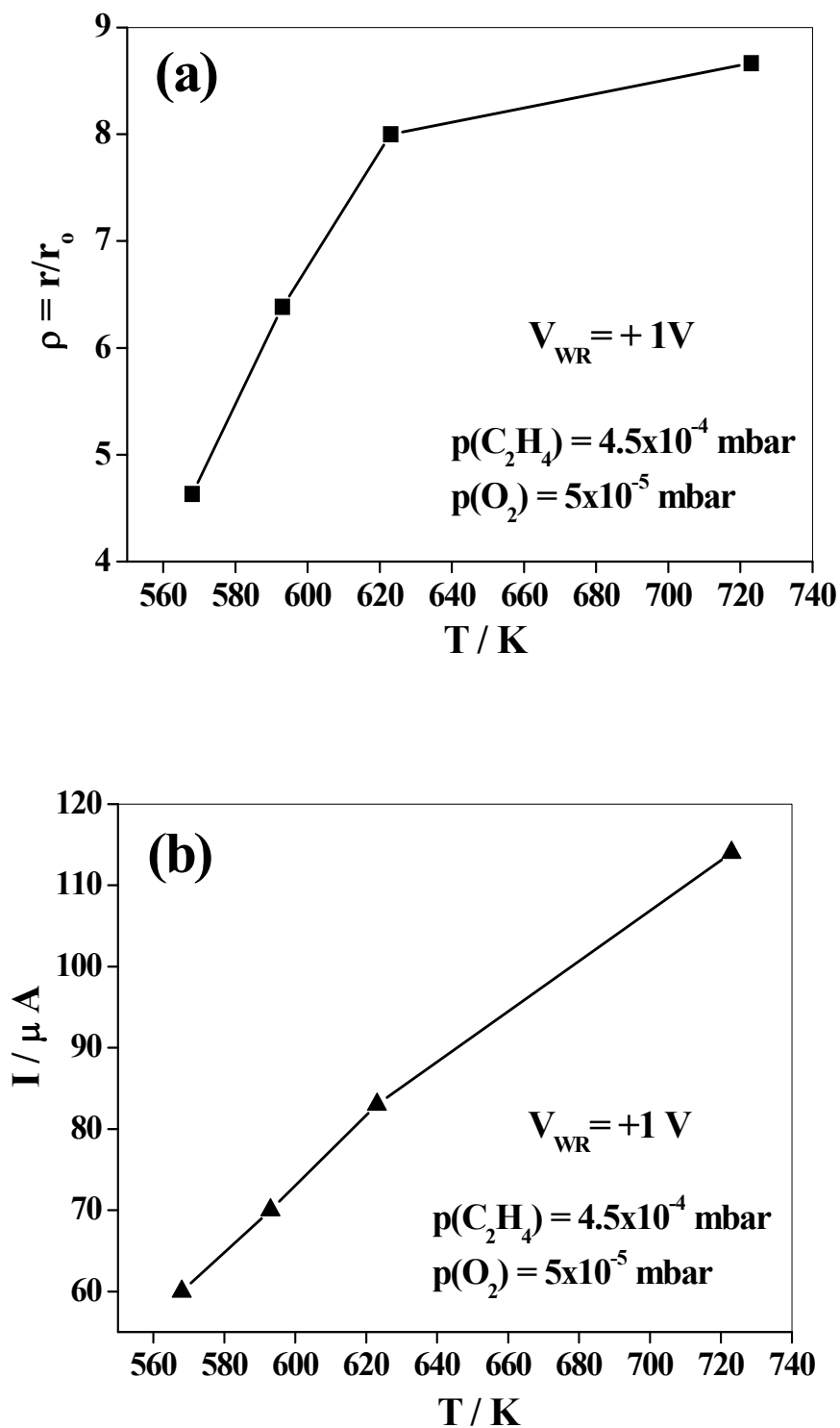


Figure 6.13. (a) Rate enhancement ratio (the data points taken from Fig. 6.12b). (b) Correlation between electrical current I (measured between counter and working electrode) and the temperatures. Experimental conditions: $p(\text{O}_2) = 5 \times 10^{-5}\text{ mbar}$, $p(\text{C}_2\text{H}_4) = 4.5 \times 10^{-4}\text{ mbar}$ and at fixed applied potential of 1 V . Thickness of Pt layer = 600 nm .

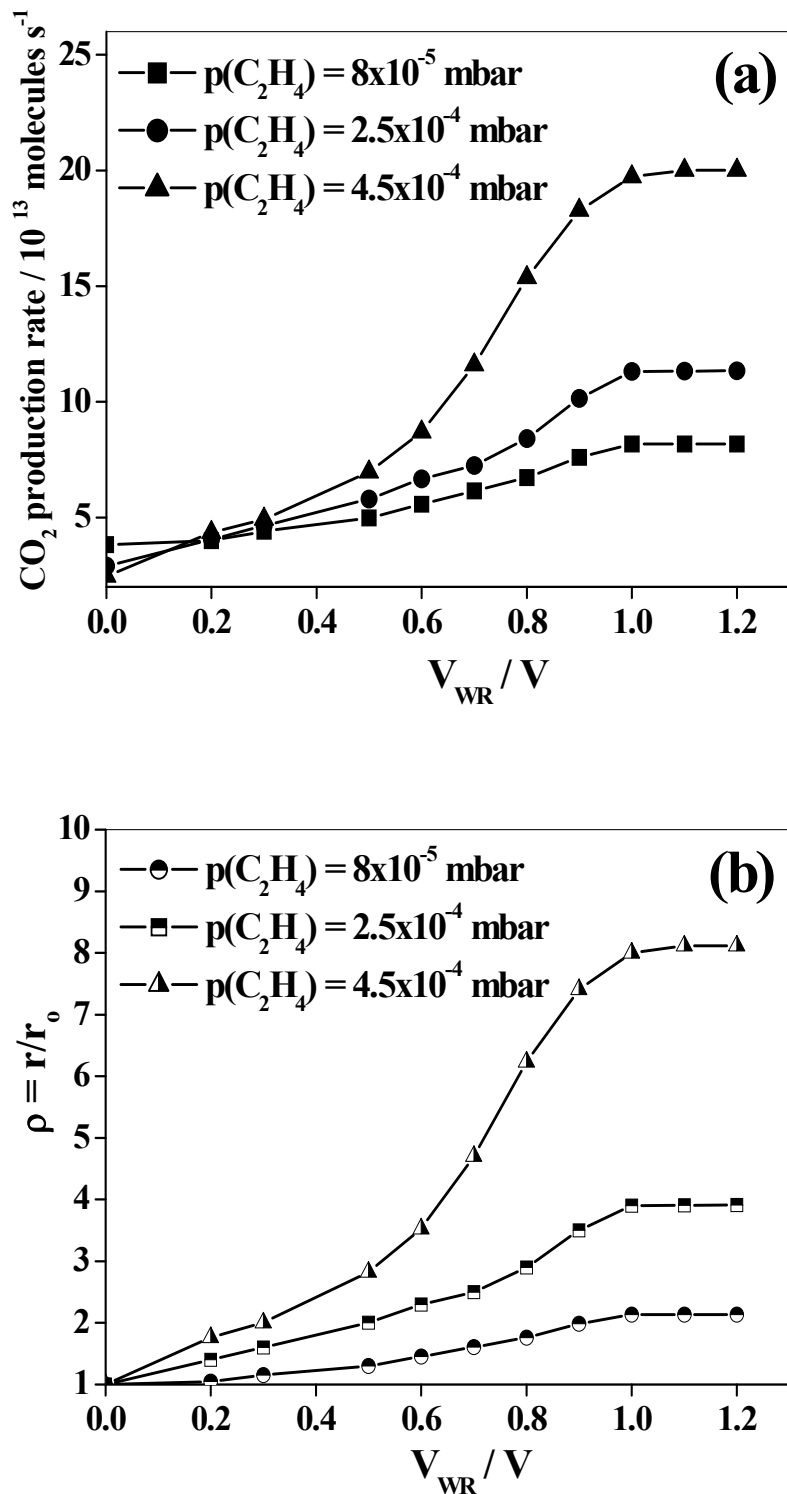


Figure 6.14. Effect of variation of the applied catalyst potential V_{WR} for different ethylene pressure. (a) Reaction rate. (b) The corresponding calculated rate enhancement ratio. Experimental conditions: $T = 623K$, $p(O_2) = 5 \times 10^{-5}$ mbar. Thickness of Pt layer = 600 nm.

The calculated rate enhancement ratio due to electrochemical pumping depends on the temperature. As shown in Fig. 6.13a the rate enhancement ratio, ρ , increases linearly with rising temperatures. At $T= 723$ K the rate enhancement ratio resulting from the electrochemical pumping is with $\rho= 8.67$ much higher than for $T= 568$ K with $\rho= 4.63$ for the same anodic potential of 1 V. In addition, the electrical current between working and counter electrode increases with rising temperature due to the decrease in the polarization resistance of the solid electrolyte as demonstrated by Fig. 6.13b. As shown by the plot the current increase only accounts for part of the rate growth while the rest has to be attributed to activities barriers in the catalytic process.

6.4.2 Dependence on ethylene partial pressure

Figure 6.14a shows effect of variation of the applied catalyst potential V_{WR} on the kinetics of CO_2 production for different ethylene partial pressures and constant $p(O_2)$. In a large excess of $p(C_2H_4)= 4.5 \times 10^{-4}$ mbar the rate enhancement due to the electrochemical pumping is much higher than at low $p(C_2H_4)$ as indicated by Fig. 6.14b. This dependence of the electrochemical promotion effect on the reaction conditions has been discussed in more details in section 6.3. As shown in Fig. 6.14a with a large excess of ethylene, the rate first increases almost linearly with the potential before it sharply rises between 0.5 V - 0.8 V followed by a saturation. We can attribute the sharp rise of the reaction rate to ignition of the reaction by spillover oxygen species. The absence of a vertical transition is explained with spatial inhomogeneities of the sample (see Fig. 6.7) causing a smoothening of the sharp transition.

6.5 Formation of bright spots in PEEM

If one applies a positive pumping voltage without any gases being introduced one observes in PEEM a rapid darkening of the surface as expected from electrochemically induced spillover of oxygen. After 4 min. bright spots on a dark background start to develop and grow in intensity as shown in Fig. 6.15a. These spots gain more intensity as time progresses. After switching off the applied potential the bright spots remain while the background slowly turns bright over a period of several hours due to the removal of spillover oxygen by clean-off reactions with gases in the residual atmosphere as

displayed in Fig. 6.15b. Exposure to hydrogen has no effect on the bright spots but during exposure to oxygen at $p(\text{O}_2) = 1 \times 10^{-5}$ mbar the intensity of the bright spots slowly fades away over a period of several (> 3) hours. When the electrochemical pumping is repeated the bright spots reappear again at exactly the same positions were they were seen initially. The bright spots were never observed under reaction conditions irrespective of the applied potential.

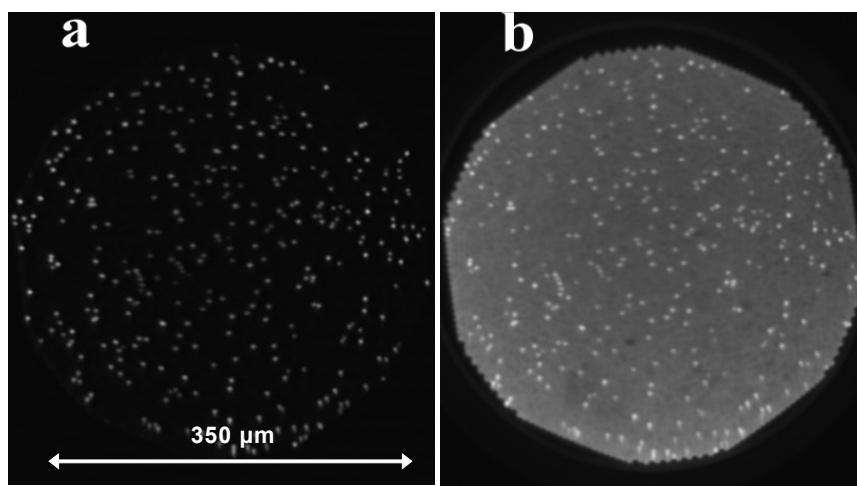


Figure 6.15: Formation of bright spots in PEEM during anodic polarization with $V_{\text{WR}} = 1$ V at $T = 623$ K and without any gases being introduced. The residual gas pressure is about 2×10^{-8} mbar. (a) PEEM image after 1000 s anodic polarization. (b) PEEM image after turning off the electric potential and keeping the sample in vacuum for one day at $T = 623$ K.

Since XPS measurements have shown that Pt electrodes on YSZ are contaminated with some SiO_x (x close to 2) it seemed close-lying to attribute the bright spots to this SiO_x contamination [7]. The SiO_x contaminations are, however, quite inert under mild reaction conditions and they should in any case not respond to exposure to oxygen. This clearly rules out SiO_x contaminations as explanation for the bright spots. A possible alkali contamination can also be ruled out because with the high mobility of alkali metals the bright spots would not form at the same position. On the other hand it is known that the Pt electrodes not completely cover the underlying zirconia substrate but some zirconia remains visible. Assuming that some metallic zirconium is formed by zirconia reduction the experimental observations would find a rather simple explanation. Metallic zirconia has a low work function and exposure to oxygen would reoxidize it slowly to

ZrO₂. Under reaction conditions it would not form because in the presence of reactive gases it would rapidly be oxidized. In previous experiments with a microstructured Pt/YSZ sample it had already been demonstrated that pumping with a negative potential of -1 V causes the formation of a bright reduction front in PEEM initiating the transformation of Zr⁴⁺ into Zr⁰ [31].

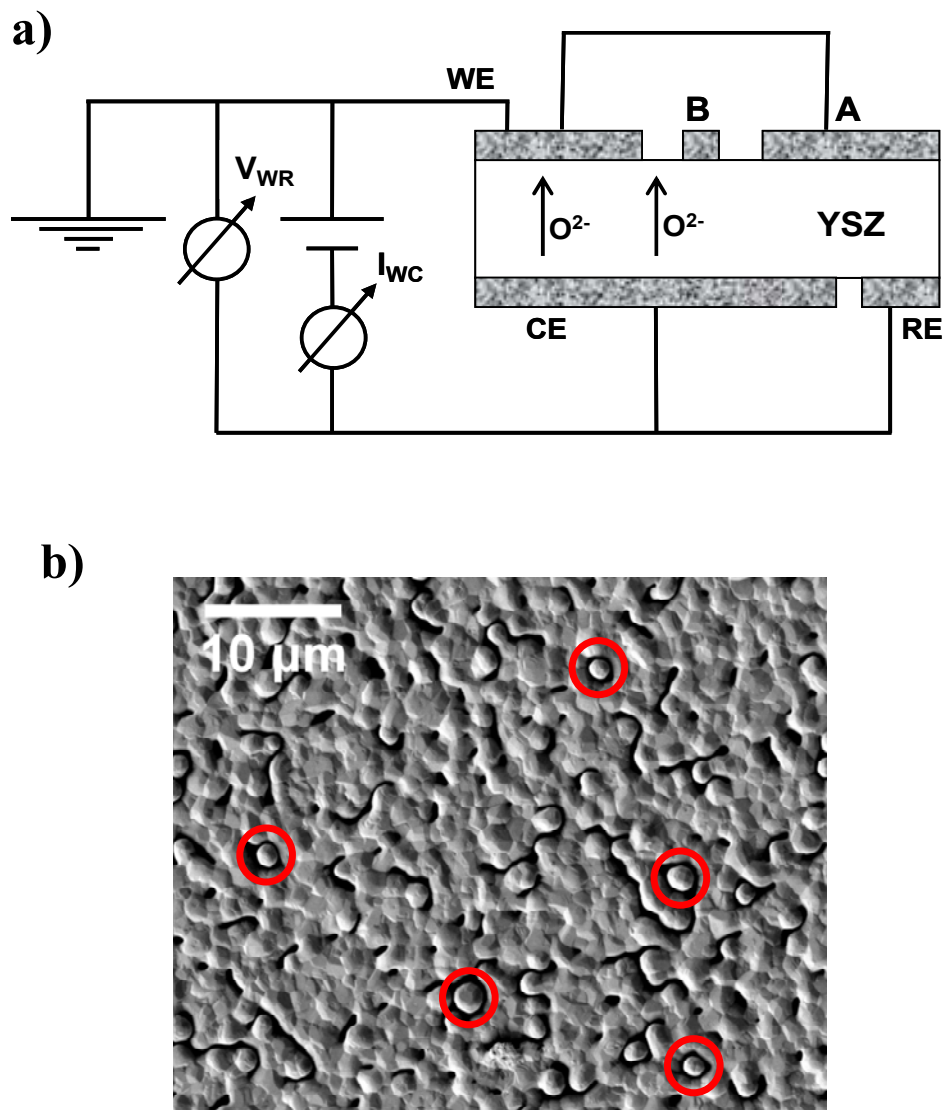


Figure 6.16: Zirconia reduction around isolated Pt islands. (a) Scheme showing electrically disconnected parts of the Pt working electrode. Region A is connected to ground potential while region B is disconnected and electrically floating. (b) SEM (scanning electron microscopy) micrograph of the Pt electrode prepared by sputtering. The Pt spots encircled are possible candidates for such electrically isolated Pt parts.

The problem which remains to be solved is to explain how a positive pumping voltage transporting oxygen to the working electrode can cause a reduction of zirconia. In order to find an answer we have to resort to the results of an earlier study of Pt/YSZ showing that not all parts of a porous Pt electrode are in electrical contact with each other [32]. If we assume that a similar situation also holds for the Pt electrode used here we have a situation schematically depicted in Fig. 6.16a. The free-floating parts of the metal electrode will be close to the potential of the counter electrode. That means they will be at negative and not at positive potential. Consequently these free-floating parts can cause a reduction of zirconia in their surroundings thus explaining the formation of bright spots in our experiment. The micrograph displayed in Fig. 6.16b demonstrates that such disconnected Pt islands are in fact likely to exist on the Pt layer.

6.6 High pressure XPS

Fig. 6.17a displays the the kinetics of ethylene oxidation on Pt/YSZ catalyst to CO_2 for varying $p(\text{C}_2\text{H}_4)/p(\text{O}_2)$ ratio under open circuit (OC) conditions and with an electric potential of 1 V applied. The experiment was conducted such that only the ratio of the two reactants was varied while the total pressure was always kept fixed at 0.2 mbar. Only at low $p(\text{C}_2\text{H}_4)/p(\text{O}_2)$ ratio the CO_2 production rate rises linearly with $p(\text{C}_2\text{H}_4)$ (similar to Fig. 6.1 under UHV conditions). Beyond the rate maximum the rate drops rapidly with rising $p(\text{C}_2\text{H}_4)/p(\text{O}_2)$ ratio. As demonstrated by Fig. 6.17b the drop in the rate of CO_2 production is due to formation of a carbonaceous CH_x - layer (see Fig. 6.2) which inhibits O_2 adsorption and therefore poisons the reaction. Now applying a potential of 1 V causes an increase in catalytic activity, but this effect occurs only beyond the rate maximum, i.e. in the carbon rich region. Before the rate maximum, i.e. in the carbon free region, the electric potential has no effect on the rate as demonstrated by Fig. 6.17a. One would expect that the increase of the CO_2 production rate with application of an electric potential is accompanied by a reduction on the carbon peak intensities, but what is found is that the carbon peak intensities are only slightly affected. Actually, this is not surprising because the electrocatalytic reaction takes place at the tpb, but what we are measured here is the outer surface of the catalyst. Therefore one expects only a small reduction of the carbon peak intensities via application of

electric potential because the oxygen spillover will not reach the outer surface of the porous Pt layer but will remain restricted to the vicinity of the tpb.

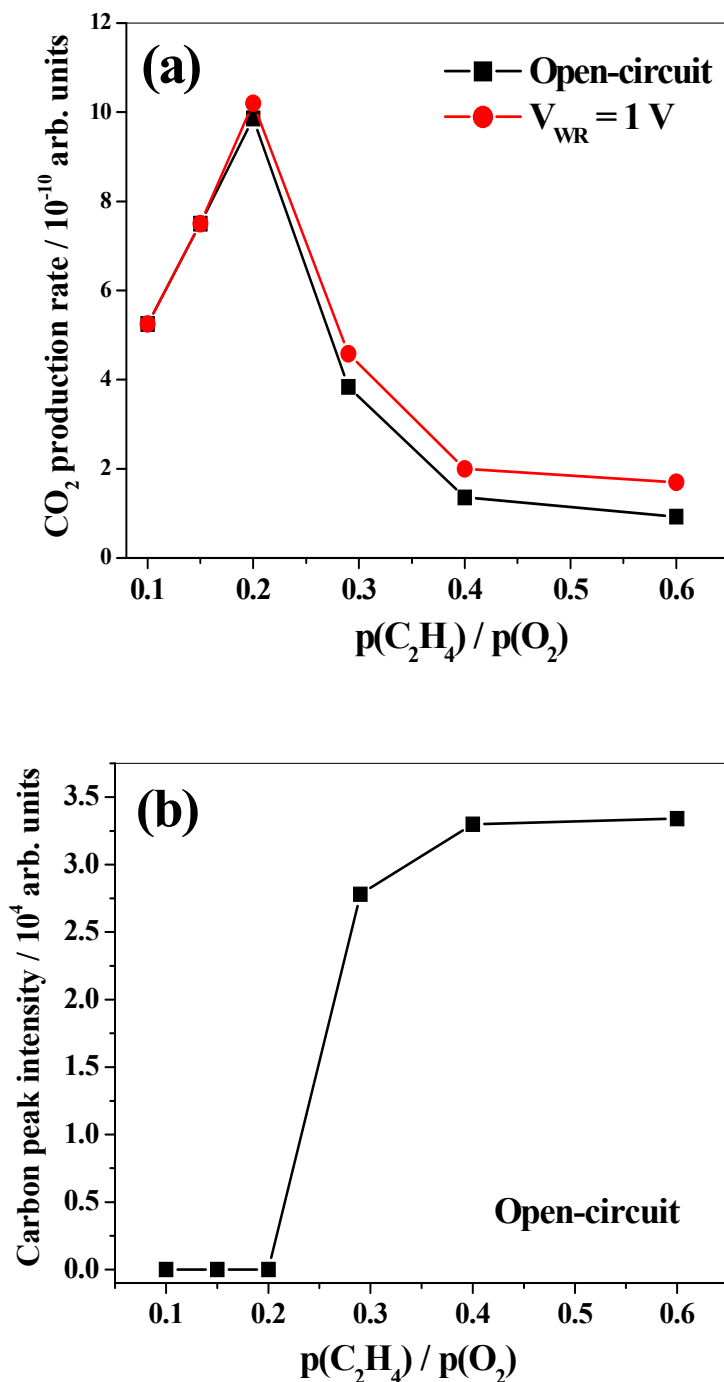


Figure 6.17: Kinetics of ethylene oxidation and electrochemical activation at Pt/YSZ catalyst under high pressure XPS. (a) Rate vs. $p(\text{C}_2\text{H}_4)/p(\text{O}_2)$ for OC conditions and with an applied electric potential of 1V. (b) Carbon signal C1s vs. $p(\text{C}_2\text{H}_4)/p(\text{O}_2)$ corresponding to the data presented in (a) for OC conditions. Experimental conditions: $T = 650$ K, $p(\text{total}) = 0.2$ mbar. Note that the sample used here is prepared by sputtering (sample 2 in chapter 5).

6.7 Discussion

(i) Concept of a special spillover species. Due to the huge Λ -factor of 3×10^5 the $C_2H_4 + O_2$ reaction on Pt/YSZ had a kind of paradigmatic role in reports on the EPOC effect [3-5,13]. Consequently, considerable theoretical efforts went into explaining the non-Faradaicity of such a reaction system. A theoretical concept developed for the O^{2-} -conducting system Pt/YSZ by Vayenas and co-workers were essentially based on the existence of two different oxygen species, regular chemisorbed oxygen and a special spillover species (more detail explained in section 2.1 in chapter 2). Vayenas and co-workers proposed a special spillover oxygen species, as a general concept, in order to explain the origin of the non-Faradaicity for all the reaction studied using cyclic voltametry (CV) and XPS [6,33,34]. However, the peak assigned in CV done by Vayenas et al. to the special spillover species was shown to be caused by Si contamination for other detailed investigations by Janek et al. [35].

Comparing this consistent but largely hypothetical concept with the experimental results of this study together with the results of earlier investigations one arrives at the following conclusions.

(ii) Identity of the oxygen spillover species. Using a microstructured Pt/YSZ sample XPS showed that the spillover species is identical to chemisorbed oxygen from the gas phase [7]. The same conclusion was also reached by Sobyenin et al. who studied the oxygen isotope exchange over Pt/YSZ catalysts and found no change in the Pt-O bond strength upon electrochemical polarization [16-18]. This result is in agreement with physical intuition because oxygen spilling over from the tpb onto the surface of the metal electrode the oxygen should lose its memory of where it came from originally.

Experiments with a differentially pumped XPS did not provide any evidence for a special oxygen spillover species in the system $C_2H_4 + O_2$ /Pt/YSZ up to a pressure of 0.2 mbar. The experimental evidence claimed in some reports for the existence of a special oxygen spillover species was shown to be based on artifacts and on a wrong interpretation of data.

(iii) Non-Faradaicity of EPOC. Since no valid evidence for a special oxygen spillover exists, the above cited concept to explain the non-Faradaicity of the reaction is purely hypothetical. In fact there is no need to invoke a special spillover species because

the non-Faradaicity can be explained in a much simpler way as follows. The hystereses in Figs. 6.3-6.6 can be described as a bistable system characterized by an active branch and an inactive branch in which the surface and hence the reaction is poisoned. As was shown the electrochemical induced spillover of oxygen can trigger the transition from the inactive branch to an active branch. Such an ignition process is, however, non-Faradaic because ignition requires only relatively small perturbation of the system while the large part of the oxygen required for combustion of ethylene comes from the gas phase. With ignition playing the dominant role the non-Faradaicity of the reaction can in principle even become infinitely large. If we take the transition from G to H in Fig. 6.9 as example, we calculate a Λ -factor of 2.4 from the electric current of 85 μA and the measured rate increase, Δr , using Eq. 4.20 in chapter 4.

The Λ -factor of 2.4 demonstrates that the electrochemically induced rate increase is non-Faradaic. This factor is far below the value of 3×10^5 reported in the literature for the high pressure experiments in a catalytic reactor [13]. Provided that one would manage to prepare a state of the surface in which the reaction would be nearly completely poisoned and only very small perturbation would suffice to ignite the reaction, then a very large Λ -factor would result. With the present experimental set-up in UHV in which also the backside of the sample and hot filaments contribute to the reaction rate, it is practically impossible to prepare such a state. In the type of reactor used in the high pressure experiments where a half-closed YSZ tube is employed such a state can evidently be prepared.

In practice, another aspect will play a big role in high pressure, however, the reaction will no longer be isothermal, a point which so far has been completely neglected in discussions of the non-Faradaicity of EPOC experiments. The comparison with catalytic CO oxidation on supported catalysts and 1 bar where T-excursions of more than 100 K have been reported upon ignition demonstrates that at least in the mbar range the reaction heat is no longer negligible [36]. For ethylene oxidation on supported Rh catalysts even temperature rises of more than 200 K have been found for reactant partial pressures < 100 mbar [37]. The thermal ignition which then takes place can accelerate the reaction dramatically via Arrhenius law thus potentially explaining some of the very high Λ -factors reported in the literatures. At the 10^{-2} – 10^{-1} mbar where the high-p EPOC experiments in ethylene oxidation have been conducted the effect of the reaction heat is probably at the borderline of becoming significant but the experimental set-up with only

a few μm thick metal layers on top of a ceramic material with bad thermal conductivity will certainly favor non-isothermal effects [38].

6.8 Conclusions

The electrochemical promotion of ethylene oxidation at Pt/YSZ catalysts has been studied in a UHV environment in a pressure range 10^{-6} - 10^{-4} mbar. A rate enhancement up to factor of 8 was observed and the rate increase was shown to be non-Faradaic. The kinetics of the system was shown to exhibit bistability caused by the inhibitory effect of a carbonaceous CH_x layer on oxygen adsorption. It was demonstrated that application of a positive potential can induce a transition from the inactive carbon poisoned state of the reaction to an active state. Mechanistically, the activation is attributed to electrochemically induced oxygen spillover eating holes into the carbonaceous layer. The EPOC effect depends on the reaction conditions and is linked to the presence of a carbonaceous layer on the Pt surface. Surprisingly, the EPOC effect increases strongly with rising $p(\text{C}_2\text{H}_4)$. This observation together with the persistence of the activation even after completely turning off the applied potential point towards restructuring of the Pt catalyst as cause for the remaining high activity. The non-Faradaicity of the reaction system can be explained as an ignition effect causing a transition from a poisoned state of the surface to an active state.

The ignition mechanism is based on autocatalysis and thus very similar to the chain reaction mechanism introduced by Sobyenin and coworkers [16-18]. Clearly there is no need to invoke a special oxygen spillover species in order to explain the non-Faradaicity observed in this reaction system. The ignition concept potentially applies to all reactions on Me/YSZ catalysts where an inhibitory adlayer can be removed by electrochemically generated oxygen spillover. Such systems are all catalytic reactions involving hydrocarbons but also catalytic CO oxidation on noble metals where a dense CO-adlayer can poison the reaction. It remains to be shown in the future that a number of the large Λ -factors reported in the literature can in fact be traced back to an ignition effect.

6.9 References

- [1] C. Wagner, *Adsorbed Atomic Species as Intermediates in Heterogeneous Catalysis*, Adv. Catal. 21 (1970) 323.
- [2] C. G. Vayenas, S. Bebelis, S. Ladas, Nature 343 (1990) 625.
- [3] C. G. Vayenas, S. Bebelis, I. V. Yentekakis, H. G. Lintz, Catal. Today 11 (1992) 303.
- [4] C.G. Vayenas, M.M. Jaksic, S.I. Bebelis, S.G. Nephytides, in: J.O.M. Bockris et al. (Eds.), *Modern Aspects of Electrochemistry*, 29, Plenum Press, New York, 1996, p. 57.
- [5] C. G. Vayenas, S. Bebelis, C. Pliangos, S. Brosda, D. Tsiplakides, *Electrochemical Activation of Catalysis: Promotion, Electrochemical Promotion, and Metal-Support Interactions*, Kluwer Academic / Plenum Publishers, New York, 2001.
- [6] S. Ladas, S. Kennou, S. Bebelis, C. G. Vayenas, J. Phys. Chem. 97 (1993) 8845.
- [7] B. Luerßen, S. Günther, H. Marbach,, M. Kiskinova, J. Janek, R. Imbihl, Chem. Phys. Lett. 316 (2000) 331.
- [8] B. Luerßen, E. Mutoro, H. Fischer, S. Günther, R. Imbihl, J. Janek, Angew. Chem. Int. Ed. 45 (2006) 1473.
- [9] M. Makri, C. G. Vayenas, S. Bebelis, K. H. Besocke, C. Cavalca, Surf. Sci. 369 (1996) 351.
- [10] R. M. Lambert, F. Williams, A. Palermo, M. S. Tikhov, Top. Catal. 13 (2000) 91.
- [11] O. A. Marina, I. V. Yentekakis, C. G. Vayenas, A. Palermo, R. M. Lambert, J. Catal. 166 (1997) 218.
- [12] C. G. Vayenas, S. Bebelis, S. Neophytides, J. Phys. Chem. 92 (1988) 5083.
- [13] S. Bebelis, C. G. Vayenas, J. Catal. 118 (1989) 125.
- [14] C. Koutsodontisa, A. Katsaounisa, J.C. Figueroab, C. Cavalcab, Carmo. J. Pereirab, C.G. Vayenas, Top. Catal. 38 (2006) 157.
- [15] E. I. Papaioannou, S. Souentie, F. M. Sapountzi, A. Hammad, D. Labou, S. Brosda, C. G. Vayenas, J. Appl. Electrochem. 40 (2010) 1859.
- [16] V.A. Sobyenin, V. I. Sobolev, V.D. Belyaev, O. A. Marina, Catal. Lett. 18 (1993) 153.
- [17] V.A. Sobyenin, V. I. Sobolev, V.D. Belyaev, A. K. Demin, O. A. Marina, React. Kinet. Catal. Lett. 47 (1992) 327.
- [18] V.A. Sobyenin, V.D. Belyaev, React. Kinet. Catal. Lett. 51 (1993) 373.
- [19] S. Günther, B. Kaulich, L. Gregoratti, M. Kiskinova, Prog. Surf. Sci. 70 (2002) 87.
- [20] M. E. Kordesch, W. Engel, G. John Lapeyre, E. Zeitler, A. M. Bradshaw, Appl. Phys. A 49 (1989) 399.
- [21] A.I. Boronin, V.I. Bukhtiyarov, R. Kvon, V.V. Chesnokov, R.A. Buyanov, Surf. Sci. 258 (1991) 289.
- [22] M. Salmeron, G. A. Somorjai, J. Phys. Chem 86 (1982) 341.
- [23] A. Kaloyannis, C. G. Vayenas, J. Catal. 182 (1999) 37.
- [24] In XPS the C 1s signal with 284.1 eV is about 0.5 eV lower than the C1s of graphite. The difference is attributed to incomplete carbon condensation, i. e. the presence of CH_x.
- [25] M. Flytzani-Stephanopoulos, L. D. Schmidt, Prog. Surf. Sci. 9 (1979) 83.
- [26] T. C. Wei, J. Phillips, Adv. Catal. 41 (1996) 359.

- [27] E. Mutoro, S. Günther, B. Luerßen, I. Valov, J. Janek, *Solid State Ionics* 179 (2008) 1835.
- [29] D. Tsiplakides, J. Nicole, C. G. Vayenas, C. Comninellis, *J. Electrochem. Soc.* 145 (1998) 905.
- [30] C. Falgairrette, A. Jaccoud, G. Foti, C. Comninellis, *J. Appl. Electrochem.* 38 (2008) 1075.
- [31] B. Luerßen, J. Janek and R. Imbihl, *Phys. Chem. Chem. Phys.* 4 (2001) 2673.
- [32] T. Neubrand, S. Günther, A. Fenske, R. Imbihl, *Phys. Chem. Chem. Phys.* 6 (2004) 3569.
- [33] C.G. Vayenas, A. Ioannides, S. Bebelis, *J. Catal.* 129 (1991) 67.
- [34] S. G. Neophytides, C. G. Vayenas, *J. Phys. Chem.* 99 (1995) 17063.
- [35] E. Mutoro, B. Luerssen, S. Guenther, J. Janek, *Solid State Ionics* 180 (2009) 1019.
- [36] J. Kellow, E. E. Wolf, *Chem. Eng. Sci.* 45 (1990) 2597; *Catalysis Today* 9 (1991) 47.
- [37] J. C. Kellow, Eduardo E. Wolf, *AIChE J.* 37 (1991) 1844.
- [38] In our own experiments with a thermocouple attached to the Pt WE, we could only detect a $\Delta T < 1$ K at 0.1 mbar upon ignition.

Chapter 7

In Situ X-ray Photoelectron Spectroscopy during Electrochemical Promotion of Ethylene Oxidation over a Bimetallic Pt-Ag/YSZ Catalyst at High Pressure

In previous studies for both separate systems, Pt/YSZ and Ag/YSZ the electrochemically induced oxygen spillover has been characterized by X-ray photoelectron spectroscopy (XPS) under low pressure conditions ($p < 10^{-4}$ mbar). In this chapter, we extended these studies for the first time up to 1 mbar using XPS at BESSY as in situ method to identify the relevant surface species during electrochemical promotion of ethylene oxidation over a bimetallic Pt-Ag/YSZ catalyst.

7. 1 Introduction

Most of the difficulties in coming to a clear mechanistic picture of the EPOC effect can be traced back to the well known pressure and material gap in heterogeneous catalysis. Nearly all of the EPOC studies have been conducted in the mbar to atmospheric pressure range with structurally and chemically badly defined catalysts. A small number of surface science type studies have been conducted but what is completely missing are high pressure studies characterizing the state of the catalyst with *in situ* techniques [1-3]. For this reason a differentially pumped X-ray photoelectron spectrometer was used with which *in situ* XPS experiments are feasible up to ≈ 1 mbar. The reaction system investigated is catalytic ethylene oxidation with O_2 on a bimetallic Pt-Ag/YSZ catalyst. In preceding studies the $C_2H_4 + O_2$ reaction on Pt/YSZ in an UHV environment ($p \approx 10^{-6} - 10^{-4}$ mbar) using PEEM as main method is investigated (see chapter 6). This reaction system played a kind of paradigmatic role in the EPOC studies because it exhibited the strongest non-Faradaic effect of all reaction systems investigated so far [4,5]. Ag is used as catalyst for the epoxidation of ethylene [6,7]. For both separate systems, Pt/YSZ and Ag/YSZ the electrochemically induced oxygen spillover has been characterized by XPS under low pressure conditions [8-10].

The electrocatalytic behavior of bimetallic electrodes was shown recently to exhibit quite favorable properties with respect to hydrazine oxidation where a non-Faradaic pathway indicating EPOC behavior was found [11]. The question addressed here is whether the presence of two metals leads to new unexpected results with respect to spillover and electrochemical promotion or whether the two metals just act independent of each other so that the resulting behavior is just a superposition of the known behavior of each of the two metals. As will be shown the two metals largely retain their individual properties in this electrochemical experiment.

In this study, the reaction system was investigated at 650 K keeping the total pressure fixed at 0.25 mbar and varying the ratio of the gases in the C_2H_4/O_2 mixture. The Pt-Ag/YSZ sample was heated from the backside through a 100-nm-thick SiC window with an infrared laser. The experimental were performed at the beamline U49/2-PGM1 at the synchrotron radiation facility BESSY in Berlin in a specially designed differentially pumped XPS system. More details have been explained in the experimental set up (see chapter 4). The spectral regions of Pt4f, Ag3d, O1s and C1s were recorded

under reaction condition. Blank experiments without the catalyst showed no catalytic contribution from SiC. For back ground subtraction of the reaction rate the experiments with the Pt-Ag/YSZ sample were repeated at room temperature. Under reaction conditions, the cell was operated as a continuous flow reactor. Gases were introduced via mass flow controllers. Reaction products were monitored with a differentially pumped QMS.

7. 2 Sample characterization

7. 2.1 Surface morphology

The morphology of the Pt/Ag WE after sintering in air for 3 h at 1123 K was investigated by scanning electron microscopy (SEM, JEOL JSM-6700F) and by surface profilometer (Veeco Dektak 6M stylus). As shown by Fig. 7.1a porous network film with a thickness in the order of a few μm was obtained (Fig. 7.1b).

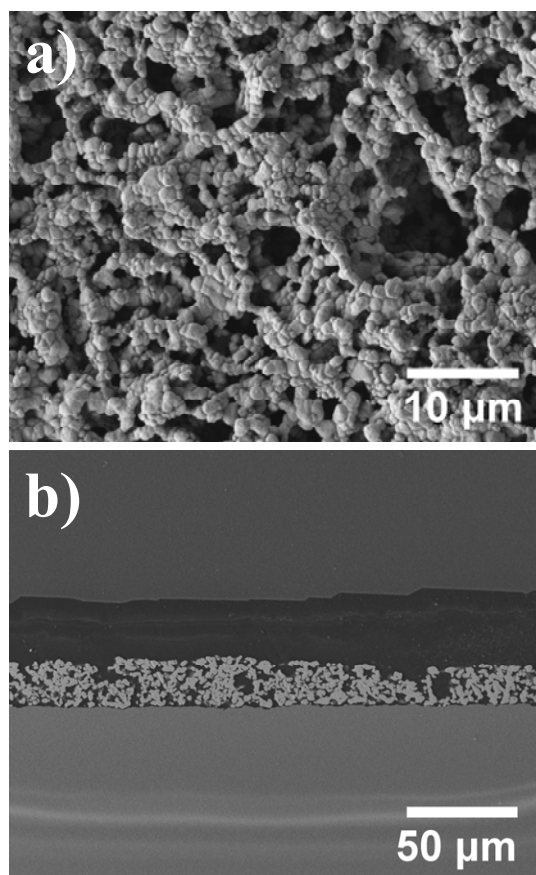


Figure 7.1: SEM micrograph of a Pt/Ag WE electrode on a YSZ (111) single crystal after annealing for 3 h in air at 1123 K. (a) Top view, and (b) Cross section.

7. 2. 2 XPS characterizations

7. 2.2.1 Survey spectrum

Prior to the experiments the Pt/Ag film was cleaned by repeated cycles of mild Ar^+ ion bombardment ($t= 20$ min, $E= 1.5$ keV, $p(\text{Ar})= 1 \times 10^{-4}$ mbar). After repeated cycles of cleaning and prior to starting quantification of the atomic composition, survey spectra were recorded with a wide binding energy window, as shown in Fig. 7.2. After recording the survey spectra, further analyses were performed within the narrow binding energy ranges of the atoms of interest (Pt4f, Ag3d, O1s and C1s). For each element one has at least one specific analytical region (in terms of electron binding energies). These binding energies give important information about the chemical composition as well as the state of the selected elements.

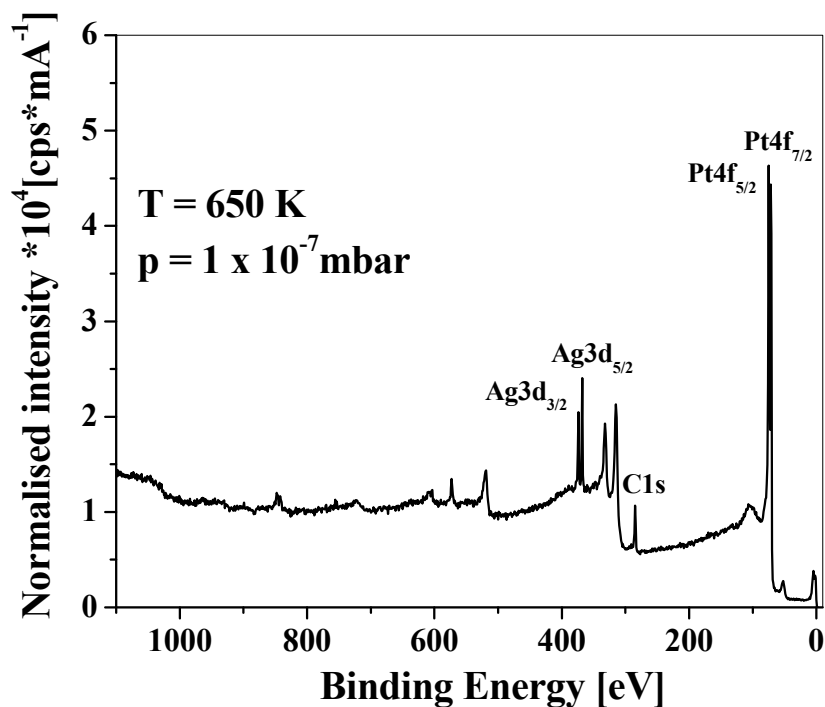


Figure 7.2: XPS survey spectrum for Pt/Ag catalyst deposited on YSZ (111) single crystal recorded prior to the EPOC/XPS experiments with a wide binding energy window and after several cycles of cleaning. The Pt/Ag WE surfaces were cleaned by repeated cycles of mild Ar^+ ion bombardment ($T \approx 400$ K, $E= 1.5$ keV, $p(\text{Ar})= 1 \times 10^{-4}$ mbar, and $t= 20$ min.).

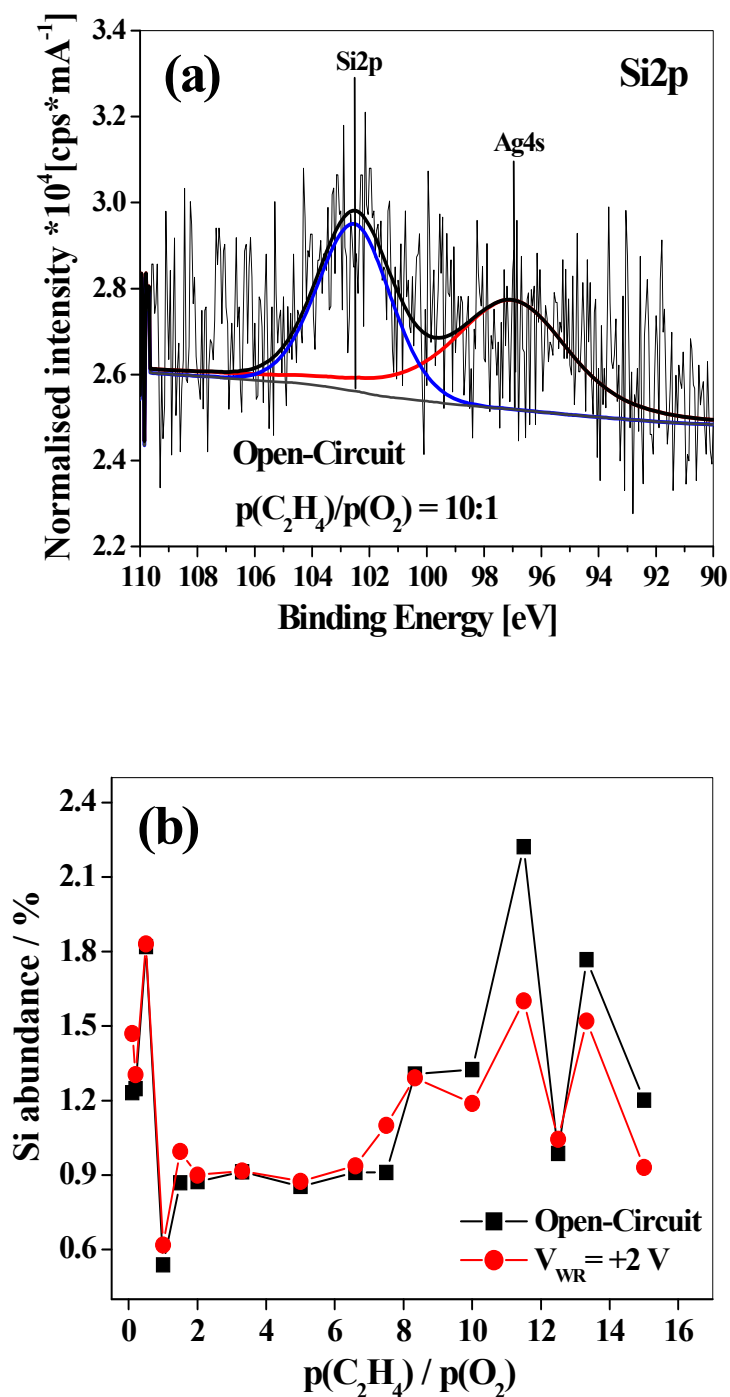


Figure 7.3: (a) Si2p spectrum under OC conditions for a $p(\text{C}_2\text{H}_4)/p(\text{O}_2) = 10:1$ ratio at 0.25 mbar and $T = 650$ K. (b) Variation of the Si concentration during the EPOC experiment displayed below in Fig 7. 6. The photoemission spectra indicated as only remaining contaminants Si after several cycles of cleaning and during variation of $p(\text{C}_2\text{H}_4)/p(\text{O}_2)$ ratios.

Since the XPS system was originally designed for the high pressure studies (10^{-7} -1 mbar), it was difficult to rule out the effect of contaminations especially Si during surface analysis. It was found that, after repeated cycles of cleaning the photoemission spectra indicated as only remaining contaminants Si ($\approx 2\%$) and oxygen as demonstrated by Fig. 7.3.

7. 2.2.2 Surface characterization

XP spectra of the bimetallic Pt/Ag working electrode under operating conditions i.e. under open circuit (OC) conditions and with an electric potential $V_{WR} = 2$ V applied are displayed in Figs. 7.4 and 7.5. At a ratio $p(C_2H_4)/p(O_2) = 10:1$ the surface is covered by a thick layer of carbonaceous CH_x species. The Pt4f spectrum in Fig. 7.4a displays besides the main component peak with a Pt4f_{7/2} signal at 71 eV which due to metallic Pt a second smaller component shifted by 0.90 eV to higher binding energy (BE). Since the shift of this higher-lying component is less than 1 eV it cannot be assigned to Pt oxide, but it may result from a local surface oxides e. g. at step edges or from the surface core level shift of Pt [12-17]. As indicated by Fig. 7.4c small shift of the Pt4f signal by 0.04 eV to lower BE is seen upon applying an electric potential. This shift is very small and could originate simply from an artifact, i. e. from some charging if not all parts of the WE electrode are in good electrical contact with each other.

In preceding studies similar observations to the ones made here of formation a bright spots on the PEEM images during application of a positive electric potential to the WE with respect to the RE for Pt/YSZ sample prepared by sputterin contains free floating parts. In these studies the free floating parts on the WE has been proposed as possible explanation for the formation of the bright spots on the PEEM images upon application of an electric potential to the WE (see chapter 6).

The corresponding Ag spectrum is reproduced in Fig. 7.5a. The Ag3d spectrum can be fitted with a single component but the BE of Ag3d_{5/2} of 367.71 eV is shifted by 0.59 eV to lower binding energy with respect to the BE of metallic Ag which lies at 368.3 eV. This shift is taken as evidence for alloy formation [18,19]. No changes in the BE of Ag3d are observed irrespective of whether an electric potential $V_{WR} = 2$ V is applied, or whether the gas phase composition is changed (see Fig. 7.5b).

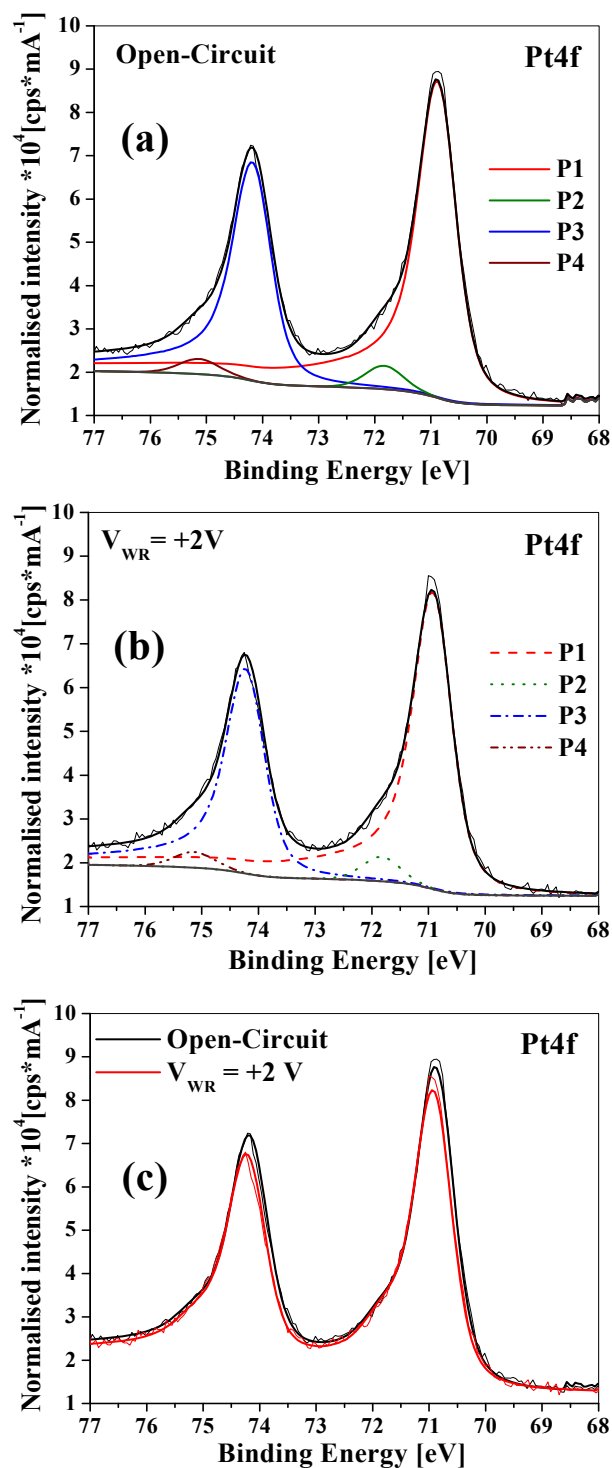


Figure 7.4: Pt4f photoelectron spectra characterizing Pt in the bimetallic Pt/Ag catalyst under reaction conditions. Experimental conditions: $p(\text{C}_2\text{H}_4)/p(\text{O}_2) = 10:1$, $T = 650 \text{ K}$, $p(\text{total}) = 0.25 \text{ mbar}$. (a) Pt4f spectrum under open circuit conditions. The different components for spectral fitting have the positions: P1= 70.90 eV, P2= 71.80 eV, P3= 74.20 eV and P4= 75.13 eV. (b) Pt4f spectrum under applied electric potential of 2V. (c) Comparison of the Pt4f spectra under OC conditions and with applied electric potential of 2V.

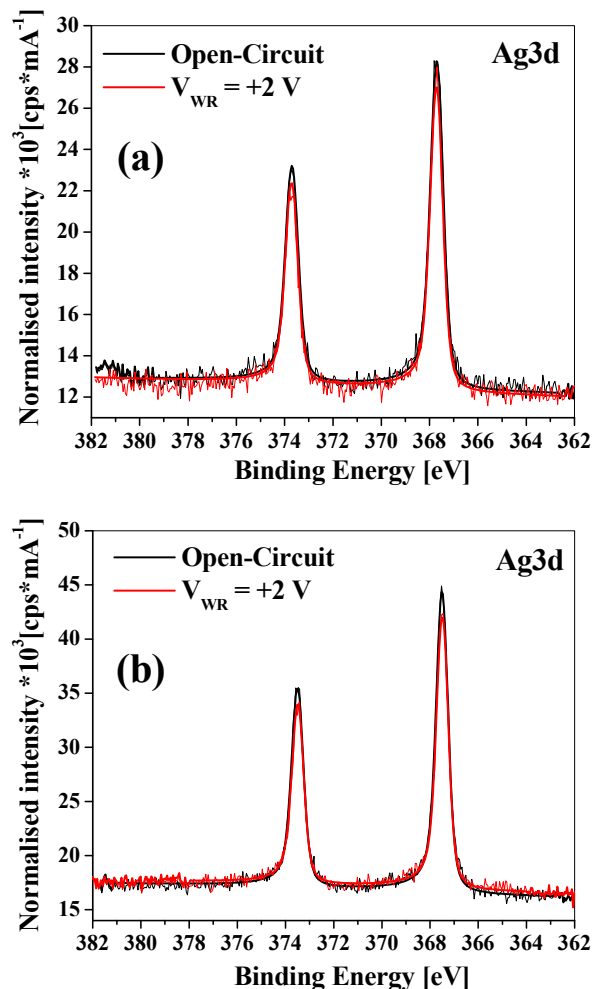


Figure 7.5: Ag3d photoelectron spectra characterizing Ag in the bimetallic Pt/Ag catalyst under reaction conditions at $T = 650$ K and $p(\text{total}) = 0.25$ mbar. A comparison of the Ag3d spectra under OC conditions and with applied electric potential of 2V under different $p(\text{C}_2\text{H}_4)/p(\text{O}_2)$ ratios. (a) $p(\text{C}_2\text{H}_4)/p(\text{O}_2) = 10:1$. (b) Ag3d spectrum with oxygen being in excess, i. e. $p(\text{C}_2\text{H}_4)/p(\text{O}_2) = 1:5$.

7.3 Reaction kinetics

7.3.1 Stationary kinetics

The catalytic reaction leads almost exclusively to CO₂ and H₂O according to Eqs. 2.2 and 2.3 in chapter 2.

Silver is a well known catalyst for epoxidation of ethylene yielding ethylene oxide as product [20]. Under our conditions we found no evidence for ethylene oxide as reaction product. Besides the main products CO₂ and H₂O only a small amount of H₂ ($\approx 2\%$ of the total QMS signal) was detected; CO may also be a potential product but the

CO signal at $m/e=28$ was hidden under the large main peak from ethylene. Figure 7.6 displays the kinetics of ethylene oxidation for varying $p(\text{C}_2\text{H}_4)/p(\text{O}_2)$ under open circuit (OC) conditions and with an electric potential of 2 V applied. The experiment was conducted such that only the ratio of the two reactants was varied while the total pressure was always kept fixed at 0.25 mbar. First, for a chosen partial pressure ratio the stationary CO_2 production under OC conditions was measured and then an electric potential was applied. For both cases the C1s, O1s, Pt4f and Ag3d regions were recorded with XPS (≈ 60 minutes per data point). Through measurements of the carbon signal (see below Fig. 7.9) it soon became evident that an accumulation of carbon on the surface takes place, i. e. measurements then no longer reflect a true stationary state of the system but a memory effect exists. In order to establish identical starting conditions therefore (starting from point IX in Fig. 7.9) the surface was exposed to pure O_2 at 0.25 mbar at $T=650$ K for several minutes prior to data taking.

The rate curves in Fig. 7.6a display the characteristic behavior with a reactive surface at low $p(\text{C}_2\text{H}_4)$ and a poisoned state at high $p(\text{C}_2\text{H}_4)$ which is well known from ethylene oxidation over Pt/YSZ (see chapter 6). At low $p(\text{C}_2\text{H}_4)$ and a correspondingly low carbon coverage ethylene molecules can adsorb and react uninhibitedly and the rate increases roughly linearly with $p(\text{C}_2\text{H}_4)$ (see Fig. 7.6b). Above a critical $p(\text{C}_2\text{H}_4)$ value a substantial carbon coverage builds up inhibiting O_2 adsorption and hence poisoning the catalytic surface. A relative maximum in the reaction rate marks this point. Beyond the rate maximum further increase of $p(\text{C}_2\text{H}_4)$ has a negative effect on the rate due to a growing carbon coverage as shown in Fig. 7.6. Applying a potential of 2 V causes an increase in catalytic activity, but this effect occurs only beyond the rate maximum. Before the rate maximum the electric potential has no effect on the rate as demonstrated by Fig. 7.6b. If one plots the relative rate increase versus the partial pressure ratio one obtains the graph displayed in Fig. 7.7a in which the relative rate increase grows roughly linearly with the $\text{C}_2\text{H}_4/\text{O}_2$ ratio. At a 10:1 ratio the electrochemically rate increase reaches 120%. If one looks into the absolute rate increase visible in Fig. 7.6a then this increase is nearly constant between the $\text{C}_2\text{H}_4/\text{O}_2$ ratios 2:1 and 10:1. The explanation for the different behavior of absolute and relative rate increase is simple. At high $p(\text{C}_2\text{H}_4)$ the rate curve in Fig. 7.6a reveals that the CO_2 production rate decays roughly with $1/p(\text{C}_2\text{H}_4)$. This results in an electrochemically induced relative rate increase which is first order in $p(\text{C}_2\text{H}_4)$.

Compared to previous studies of ethylene oxidation over Pt/YSZ with $V_{WR} = 2$ V a higher pumping voltage had to be applied in order to cause a comparable increase in the reaction rate. Typically, only 1 V was used there and even at 1 V potential the electrochemically induced rate increase was already in saturation (see chapter 6). A plot of the rate increase versus the applied potential in Fig. 7.7c reveals that at 1 V practically no effect is seen here. The explanation for the different behavior lies presumably in the reference electrode whose potential is not fixed by a gas atmosphere with constant composition but floats depending on gas composition and on the degree of oxidation/reduction of the zirconia at the reference electrode. In addition, the different preparation of the sample might play a role [21]. Here the WE was prepared by Pt paste whereas in the earlier experiments a sputtered electrode was used.

7.3.2 Kinetic instabilities

At ratios $p(\text{C}_2\text{H}_4)/p(\text{O}_2)$ larger than 10:1 kinetic instabilities occur and kinetic oscillations may develop as demonstrated by Fig. 7.8. Under OC conditions rate oscillations may evolve spontaneously as shown in Fig. 7.8a for a ratio $p(\text{C}_2\text{H}_4)/p(\text{O}_2) = 12.5:1$. They are irregular in amplitude and period with an average period around 20 s. From a noisy background sharp outbursts of the CO_2 signal occur after which the rate returns to the baseline. Applying an electric potential $V_{WR} = 2$ V causes the rate oscillations to vanish. After removing the applied voltage and establishing OC conditions the CO_2 rate returns to the original level and the rate oscillations reappear but now much more regular approaching harmonic oscillations with an average period around 10 s. At even larger $p(\text{C}_2\text{H}_4)/p(\text{O}_2)$ ratios a sequence complementary to the one depicted in Fig. 7.8a can be observed. As demonstrated by Fig. 7.8b for a ratio $p(\text{C}_2\text{H}_4)/p(\text{O}_2) = 15:1$ the rate is stationary under OC conditions but upon electrochemical pumping rate oscillations develop. The rate oscillations have been followed over a period of nearly two hours but during this time the character of the oscillations changes. While initially the rate jumps in an irregular way between an upper and a lower rate level, after 6300 s the rate remains mostly on the upper level with occasional spike-like excursions to the lower rate level. After reestablishing OC conditions the rate returns to the initial stationary level.

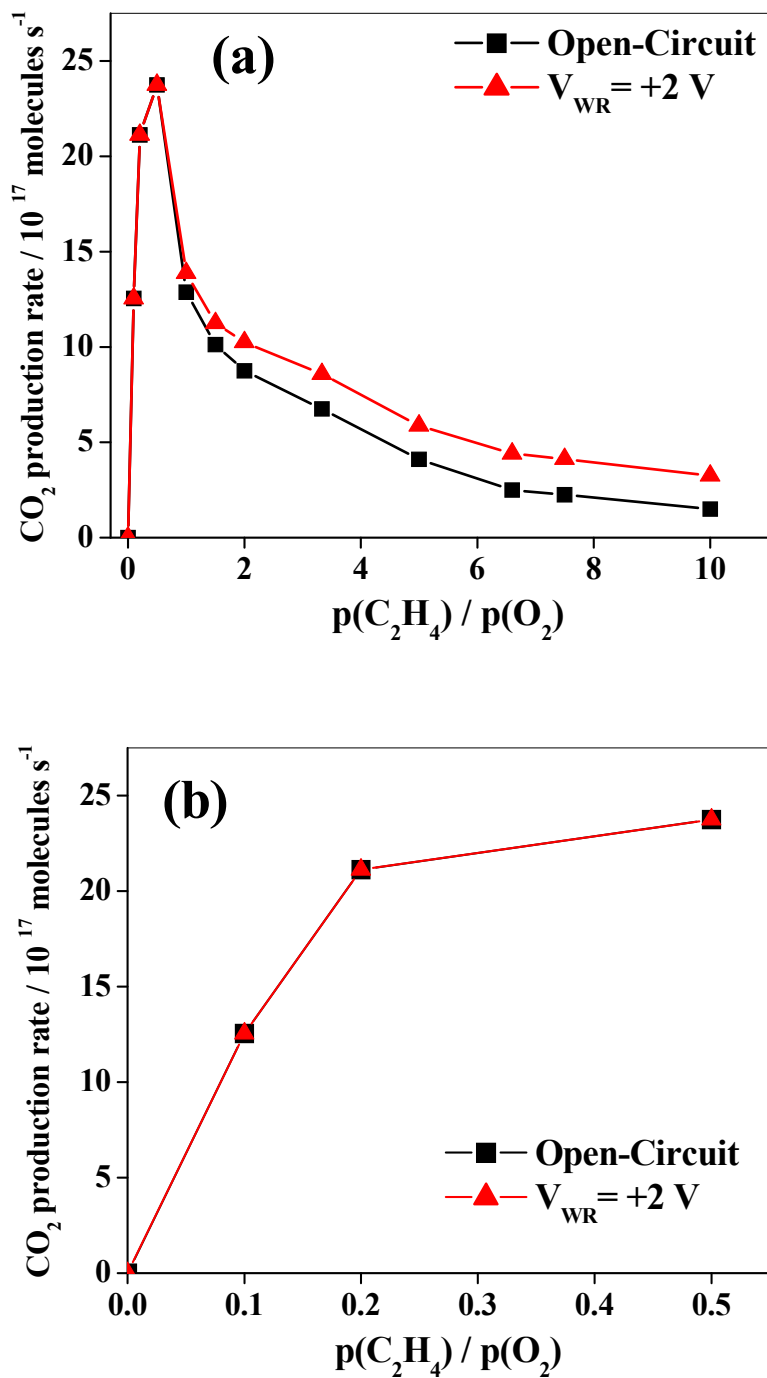


Figure 7.6: Kinetics of ethylene oxidation and electrochemical activation. Experimental conditions: T= 650 K, p(total)= 0.25 mbar. (a) Rate vs. p(C₂H₄)/p(O₂) for OC conditions and with an applied electric potential of 2V. (b) The plot represents an enlarged section of Fig. 7.6a showing the behavior of the rate from zero up to the rate maximum under OC conditions and with an applied electric potential of 2V.

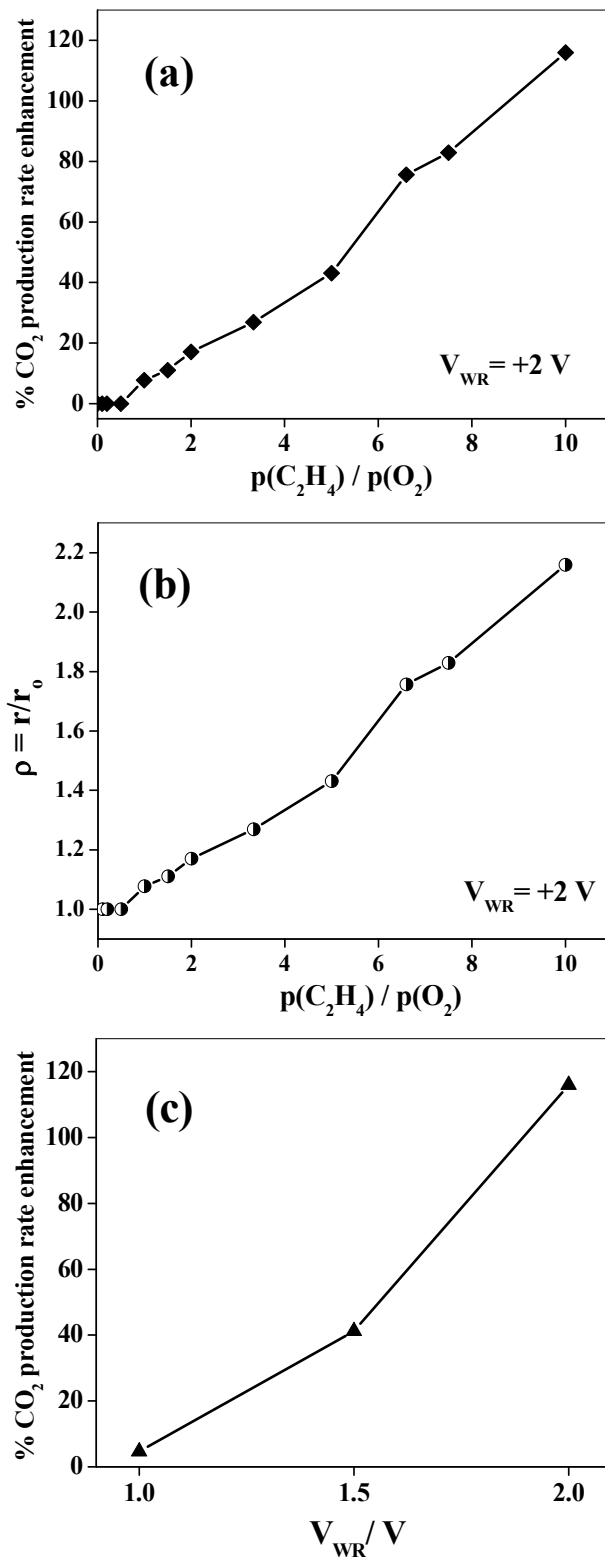


Figure 7.7: Effect of electrochemical activation on the kinetics: Experimental conditions: $T = 650 \text{ K}$, $p(\text{total}) = 0.25 \text{ mbar}$. (a) Relative electrochemically induced rate increase vs. $p(\text{C}_2\text{H}_4)/p(\text{O}_2)$, and (b) Rate enhancement ratio. The data points for (a) and (b) are taken from Fig. 7. 6. (c) Effect of variation of applied electric potential at ratio $p(\text{C}_2\text{H}_4)/p(\text{O}_2) = 10:1$.

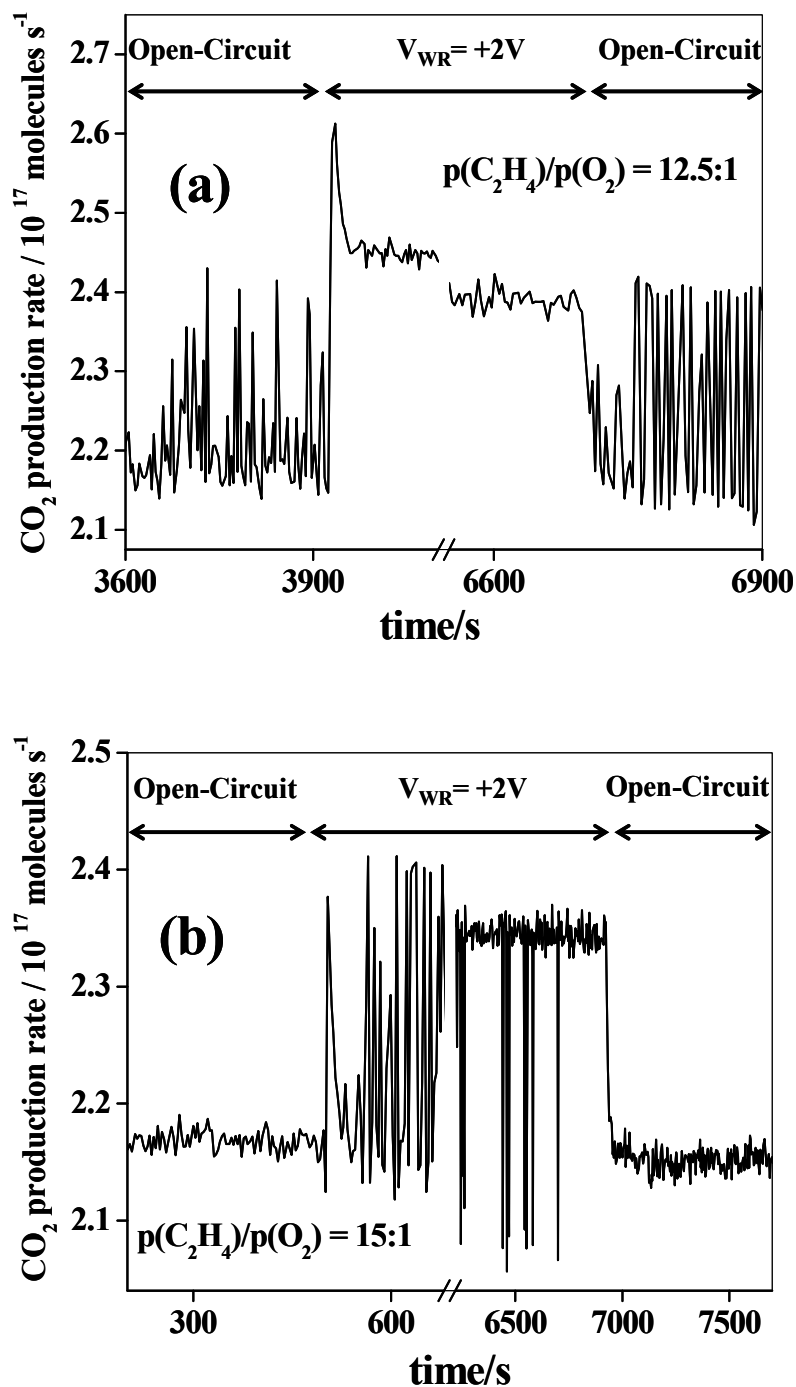


Figure 7.8: Kinetic oscillations in an EPOC experiment. Experimental conditions: $T = 650$ K, $p(\text{total}) = 0.25$ mbar. (a) Development of rate oscillations under OC conditions and suppression of the rate oscillations by an applied electric potential at ratio $p(\text{C}_2\text{H}_4)/p(\text{O}_2) = 12.5:1$. (b) Stationary reaction kinetics under OC conditions and appearance of rate oscillations during electrochemical pumping at ratio $p(\text{C}_2\text{H}_4)/p(\text{O}_2) = 15:1$.

7.4 Variation of the surface composition during EPOC

The variation of the C1s carbon signal during the EPOC experiment is shown in Fig. 7.9a. Under OC conditions some carbon is already present at very low $p(\text{C}_2\text{H}_4)$, i.e. before the rate maximum. With increasing $p(\text{C}_2\text{H}_4)$ the carbon signal rises rapidly and at the rate maximum the amount of carbon is already close to its maximum value. Upon further increasing $p(\text{C}_2\text{H}_4)$ the carbon signal remains roughly constant until a $\text{C}_2\text{H}_4/\text{O}_2$ ratio of 5 is reached and then starts to decrease by about 20 %. The variation of the Pt4f and of the Ag3d signals both normalized to C1s signal are displayed in Fig. 7.10. The dip we see in Fig. 7.9b in the carbon layer thickness around a ratio $p(\text{C}_2\text{H}_4)/p(\text{O}_2)= 1.5$ is an artifact caused by an oxygen treatment applied to remove residual carbon from the Pt surface. A dip also shows up in Fig. 7.10 for the same reason.

The fitted C1s spectra recorded at $\text{C}_2\text{H}_4/\text{O}_2$ ratios of 10:1, 5:1, 1:5 and 1:10, respectively, are reproduced in Figs. 7.11, 7.12, 7.13 and 7.14. The effect of the applied potential on the C1s line shape is demonstrated in Figs. 7.11b, 7.12b, 7.13bc and 7.14b. A comparison of the C1s spectra under OC conditions and with applied electric potential of 2V is demonstrated in Figs. 7.11c, 7.12c, 7.13c and 7.14c at $\text{C}_2\text{H}_4/\text{O}_2$ ratios of 10:1, 5:1, 1:5 and 1:10, respectively. As shown by Figs. 7.13 and 7.14 the C1s spectra recorded at low C_2H_4 partial pressure are well fitted with a main component centered at 284.3 eV (Doniach-Sunjic line shape, FWHM = 0.57 eV, asymmetric index 0.07). An additional component at 283.6 eV is present too in a very small amount. The spectra recorded at higher C_2H_4 partial pressure are in general broader as indicated by Figs. 7.11 and 7.12. The same fitting parameters were applied to fit all spectra independent of the $\text{C}_2\text{H}_4/\text{O}_2$ ratio. As demonstrated by Fig. 7.11a the XP C1s core level spectra, recorded at high $\text{C}_2\text{H}_4/\text{O}_2$ ratio i.e. $p(\text{C}_2\text{H}_4)/p(\text{O}_2)= 10:1$, have been deconvoluted into three surface contributions (C1- C3) plus a contribution from the gas phase (C4) centered at 283.6 eV, 284.3 eV, 284.75 eV and 286 eV, respectively.

In most cases applying an electric potential of 2 V has no influence on the number of the different fitted carbon species. In agreement with previous investigations, the main component C2 at 284.33 eV is assigned to sp^2 -bonded carbon [22,23]. Since this component represents a well ordered carbon structure it is less reactive toward oxidation and accordingly also persists in an excess of oxygen. Practically the same C1s BE of 284.3 eV was reported by Freyer et al. for thin graphitic layers produced by ethylene decomposition on Pt(111) [24].

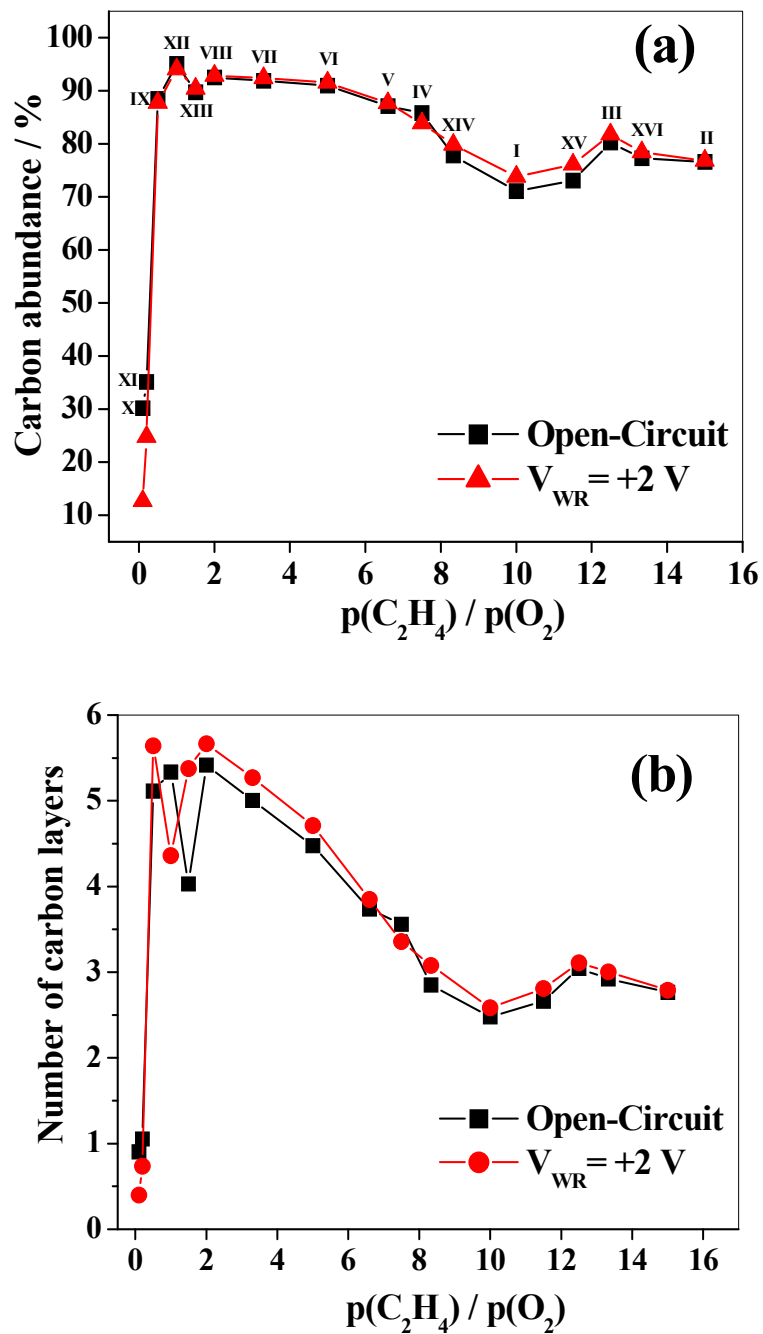


Figure 7.9: Variation of the carbon concentration during EPOC experiments. Experimental conditions: $T = 650 \text{ K}$, $p(\text{total}) = 0.25 \text{ mbar}$. (a) Carbon signal C1s vs. $p(\text{C}_2\text{H}_4) / p(\text{O}_2)$ for OC conditions and with an applied electric potential of 2V. The thin dotted lines represent the rate curves from Fig. 7.6. The roman numbers indicate the sequence in which the data points were taken. (b) Variation of the thickness of the carbonaceous layer vs $p(\text{C}_2\text{H}_4) / p(\text{O}_2)$ for OC conditions and with an applied electric potential of 2V during EPOC experiments.

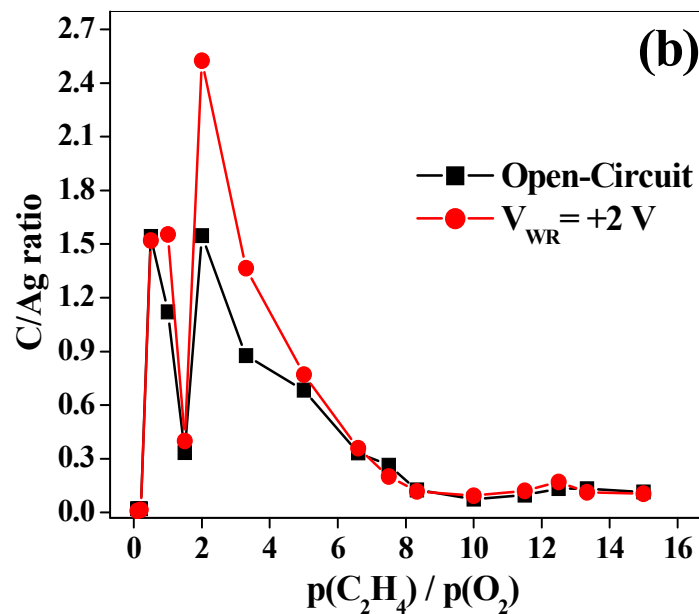
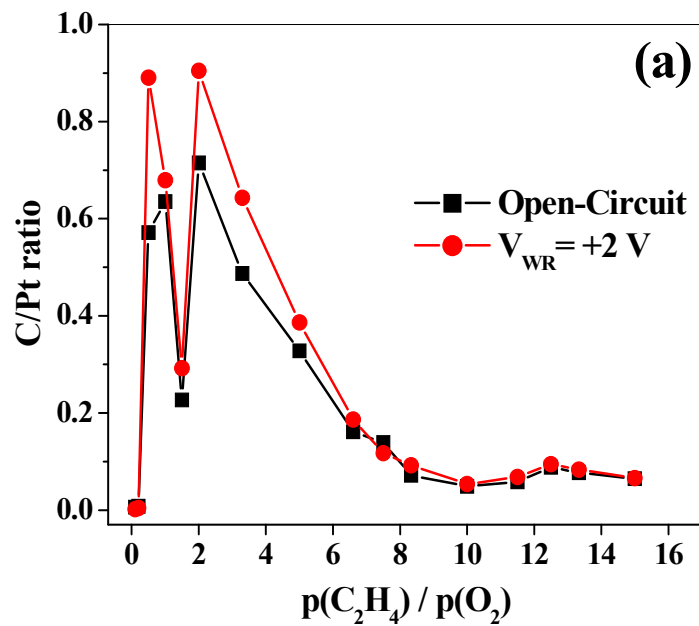


Figure 7.10: Variation of the C/Pt and the C/Ag ratio during the EPOC experiment displayed in Fig. 7.6. Experimental conditions: $T = 650 \text{ K}$, $p(\text{total}) = 0.25 \text{ mbar}$.

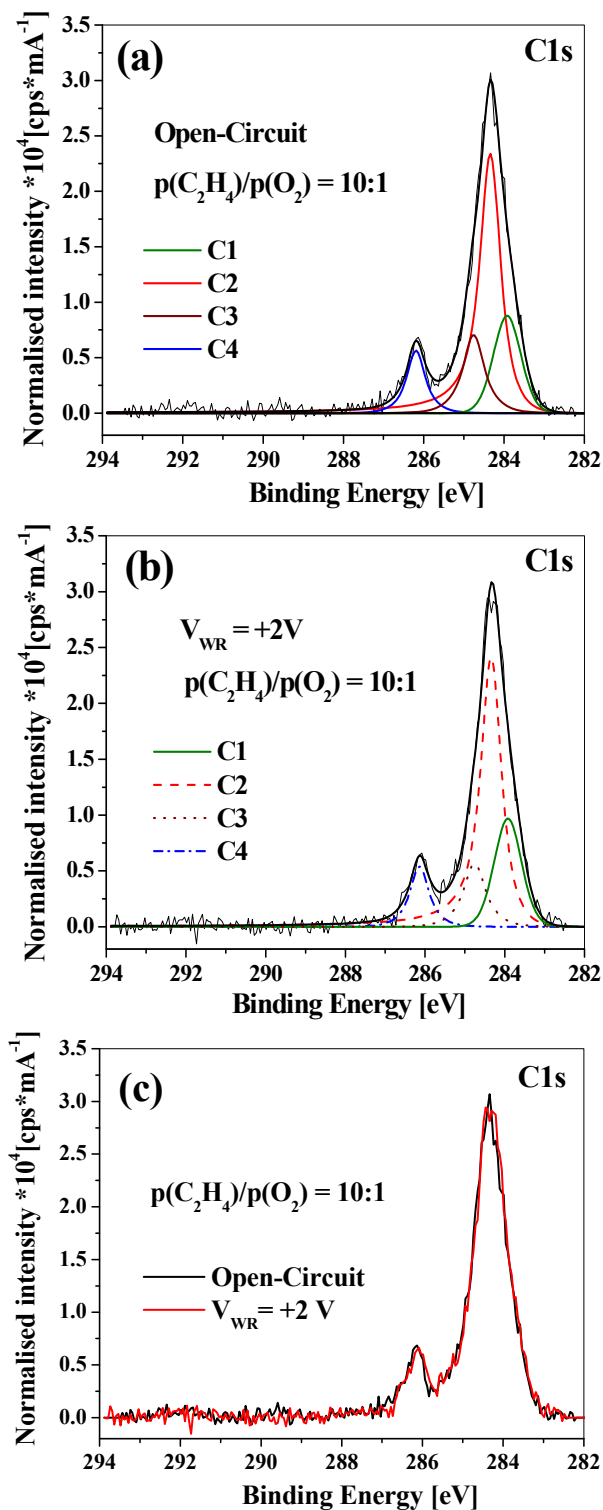


Figure 7.11: C1s photoelectron spectra showing the effect of electrochemical pumping. The spectra were all recorded under reaction conditions at p(C₂H₄)/p(O₂)= 10:1, T= 650 K, p(total)= 0.25 mbar. (a) Spectrum under OC conditions with the different contributions C1-4 indicated. (b) C1s spectra under application potential of 2V. (c) Comparison of the spectra under OC conditions and with applied electric potential of 2V for the same ratio.

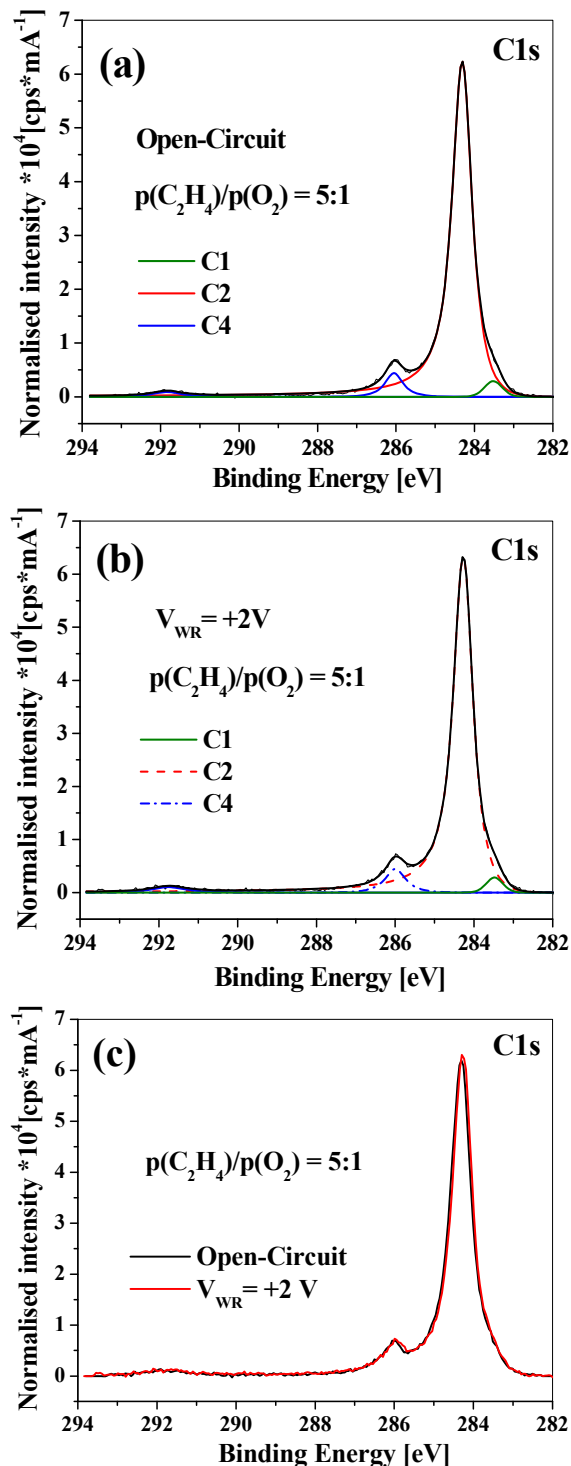


Figure 7.12: C1s photoelectron spectra showing the effect of electrochemical pumping. Experimental conditions: $p(\text{C}_2\text{H}_4)/p(\text{O}_2) = 5:1$, $T = 650 \text{ K}$, $p(\text{total}) = 0.25 \text{ mbar}$. (a) Spectrum under OC conditions with the different contributions C1, C2 and C4 indicated. (b) C1s spectra under application potential of 2V. (c) Comparison of the spectra under OC conditions and with applied electric potential of 2V. The highest on the carbon intensities value is not true but results from memory effect. i. e. large amount of carbon accumulated as shown in Fig. 7.9a

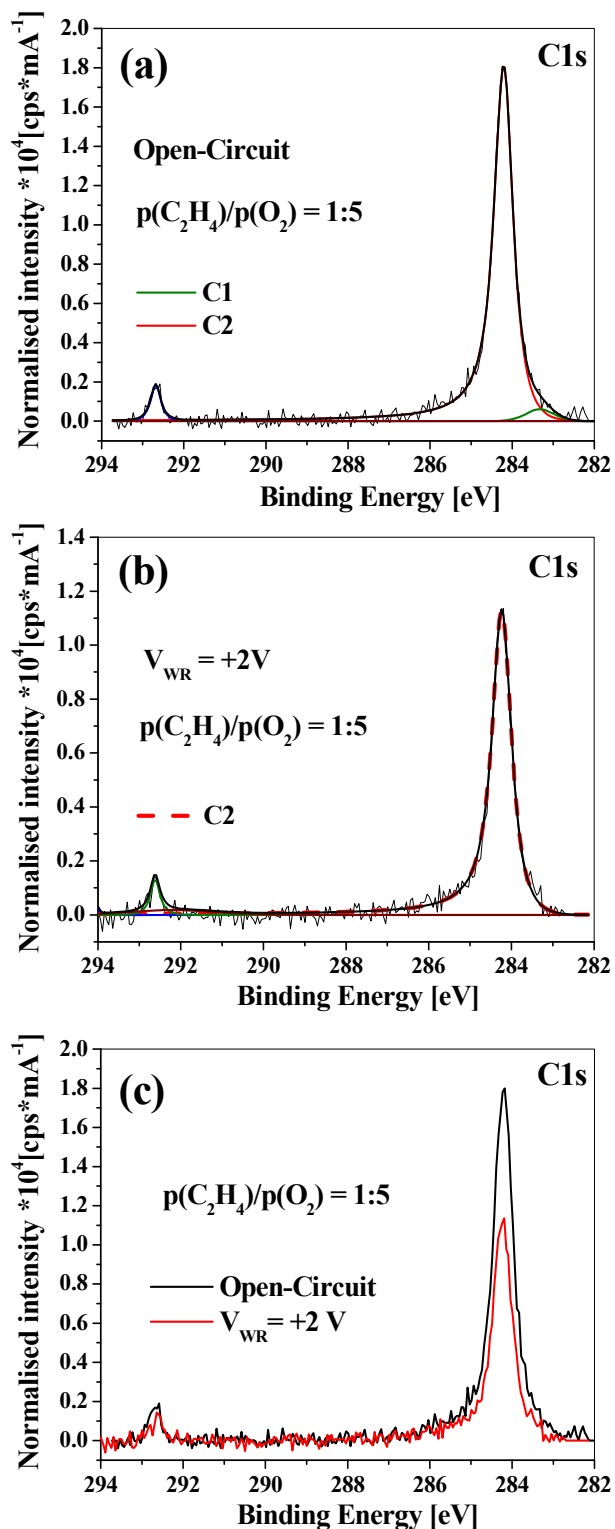


Figure 7.13: C1s photoelectron spectra showing the effect of electrochemical pumping. Experimental conditions: $p(\text{C}_2\text{H}_4)/p(\text{O}_2) = 1:5$, $T = 650 \text{ K}$, $p(\text{total}) = 0.25 \text{ mbar}$. (a) Spectrum under OC conditions with the different contributions C1 and C2 indicated. (b) C1s spectra under application potential of 2V. (c) Comparison of the spectra under OC conditions and with applied electric potential of 2V.

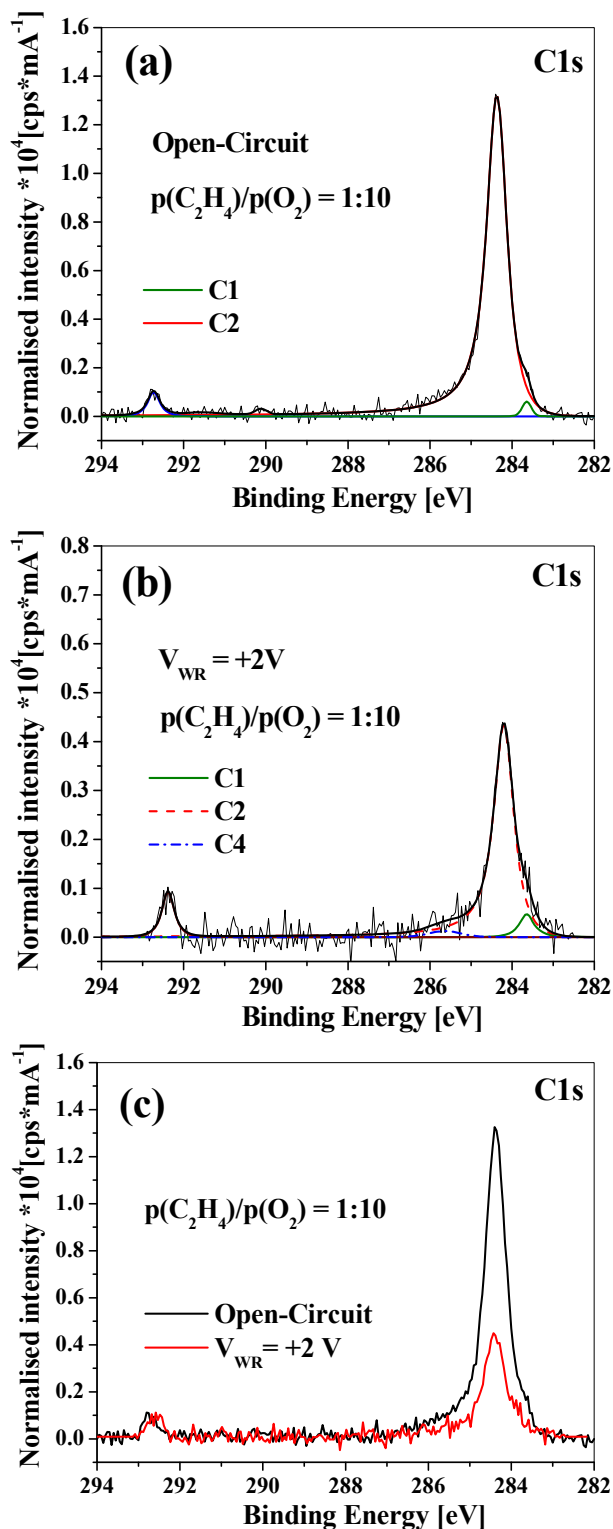


Figure 7.14: C1s photoelectron spectra showing the effect of electrochemical pumping. The spectra were all recorded under reaction conditions at $p(\text{C}_2\text{H}_4)/p(\text{O}_2) = 1:10$, $T = 650\text{ K}$, $p(\text{total}) = 0.25\text{ mbar}$. (a) Spectrum under OC conditions with the different contributions C1 and C2 indicated. (b) C1s spectra under application potential of 2V. (c) Comparison of the spectra under OC conditions and with applied electric potential of 2V for the same ratio.

On polycrystalline platinum (Pt black) a C1s BE of 284.6 eV was assigned to graphitic carbon whereas values of 284.1 and 284.4 eV were attributed to lower-dimensional condensation products of “chain” carbon and graphene, respectively [25]. According to numerous previous experiments at the ISSIS beam line the C3 component at 284.75 eV is assigned to more disordered C-C bonding [23]. A similar C1s BE energy was found by Paal on Pt and Pt-supported catalyst under ethylene atmosphere and interpreted there as hydrogenated carbon overlayer [26]. As shown by previous experiments at the ISSIS beamline the C1 component at 283.6 eV can be attributed to a carbidic species [23]. Rodriguez and co-workers attributed a C1s BE of 284.1 eV to lower-dimensional condensation products of “chain” carbon representing a precursor phase of the graphitic overlayer [25]. Here, at lower temperature, at 650 K, it is rather likely, that condensation to graphite is incomplete and some CH_x species are still present. The region around 284 eV might, for example, also contain an ethylidyne species because in an XPS study of Pt(111)/C₂H₄ a C1s BE of 284 eV was assigned to this species [27]. Gas phase ethylene is responsible for the C4 peak at 286.19 eV.

No changes in the BE of the C1s components are observed during application of potential of 2V. From the decrease of the Pt4f signal by about 90% (see Fig. 7.10a), relative to the carbon free surface it is evident that carbonaceous CH_x film has to be several layers thick. A rough estimate of the thickness can be made from the ratio of the C1s signal, I_C, to the Pt4f signal of the substrate, I_S, (see experimental setup in chapter 4) under the assumption that the Pt4f signal is exponentially damped by a thick carbon film with thickness, t. Expressing t in monolayers one obtains the plot in Fig. 7.9b.

As demonstrated by Fig. 7.9b the maximum carbon coverage is reached at the rate maximum with an average thickness of the carbonaceous film of about 5-6 monolayers (ML). The film thickness undergoes some variations beyond the rate maximum and starts to decrease continuously beyond a ratio p(C₂H₄)/p(O₂) of 3. Beyond a ratio of 10 the thickness increases again slightly but it has not been established whether this is a reproducible effect. At high p(C₂H₄) the data indicate a thickness of about 3 ML. Upon application of an electric potential we only observe a change in the carbon signal at low p(C₂H₄) i.e. before the rate maximum in the rate plot of Fig. 7.6a but not beyond the rate maximum with high p(C₂H₄) values as shown by Fig. 7.9. The C1s spectra reproduced in Figs. 7.11, 7.12, 7.13 and 7.14 illustrate a different behavior with respect to electrochemical pumping in different regions of the kinetics. With a large excess of

oxygen electrochemical pumping causes a drastic decrease of the carbon signal by $\approx 67\%$ at $p(\text{C}_2\text{H}_4)/p(\text{O}_2)= 1:10$ and by $\approx 37\%$ at $p(\text{C}_2\text{H}_4)/p(\text{O}_2)= 1:5$ (see Figs. 7.14c and 7.13c). In contrast, practically no effect has been observed in case of large excess of ethylene i.e. at ratio $p(\text{C}_2\text{H}_4)/p(\text{O}_2)= 10:1$ and $5:1$ as shown in Figs. 7.11c and 7.12c.

The reduction in the carbon signal is accompanied by an increase in the oxygen coverage. Fig. 7.15 shows the variation of the oxygen concentration during the EPOC experiment displayed in Fig. 7.6. The region where the oxygen concentration changes is also the region where electrochemical pumping causes a strong reduction of the carbon signal, and a substantial increase in oxygen coverage.

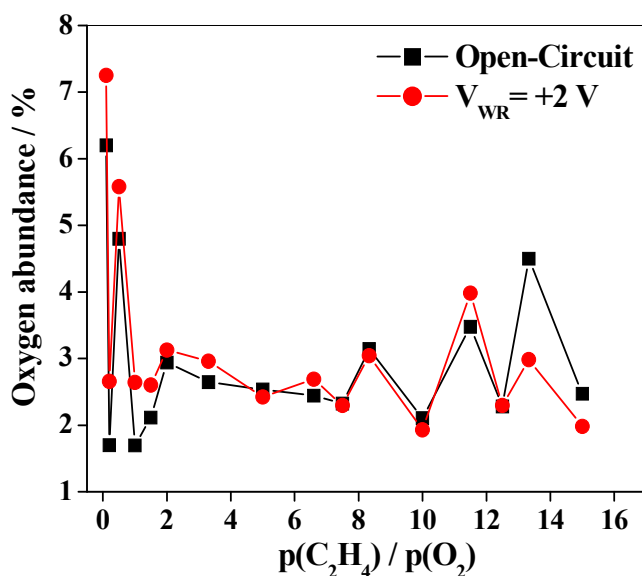


Figure 7.15: Variation of the oxygen concentration during EPOC experiments displayed in Fig. 7.6. Experimental conditions: $T= 650 \text{ K}$, $p(\text{total})= 0.25 \text{ mbar}$.

As mentioned before the reduction in the carbon signal is accompanied by an increase in the oxygen coverage as indicated by Fig. 7.16a showing the O1s region under OC conditions and during electrochemical pumping. We see that already prior to electrochemical pumping but with a large excess of oxygen ($p(\text{C}_2\text{H}_4)/p(\text{O}_2)= 1:5$), the dominant oxygen component is the one at 529.3 eV. Upon electrochemical pumping, it is this component which strongly grows by $\approx 60\%$. A close-lying BE at 529.6 eV has been found in an XPS study of Ag/YSZ and identified there as electrochemically induced oxygen spillover species [10]. A spillover oxygen species on Pt which is identical with chemisorbed oxygen on Pt should appear at 530.4 eV as demonstrated in a study with

a microstructured Pt/YSZ sample where the identity of electrochemically induced oxygen spillover was verified with XPS [8]. This contribution is missing here or quite small. Assuming that alloying has not strongly shifted the BE's we assign the 529.3 eV component to spillover oxygen on Ag sites. Evidently, we observe electrochemically induced oxygen spillover but we can only detect a spillover species over Ag sites and not over Pt sites. As indicated by Fig. 7.16a, growth of the 529.3 eV component due to electrochemical pumping is only detectable at low $p(\text{C}_2\text{H}_4)$, i. e. before the rate maximum in the rate curve of Fig. 7.6a.

Beyond the rate maximum only slight changes in the O1s spectrum occur upon electrochemical pumping as shown in Fig. 7.16b. The different adsorption states of oxygen on Ag have been studied quite in detail due to the importance of Ag as catalyst [28,29]. An oxygen state characterized by an O1s BE of 529.3 eV was found here for the spillover species onto Ag sites. This value is not far from the BE of 529.6 eV reported for the γ -species on Ag but it is more closely to the $\text{O}_{2\alpha}$ state reported recently with an O1s BE of 529.2 eV [29]. Therefore instead of assigning the spillover species to the highly stable γ -species formed on Ag in high temperature/high pressure (1 bar) O_2 treatments the peak is assigned to the $\text{O}_{2\alpha}$ state which develops on Ag foil and on Ag(110) already under milder conditions, i.e. at 0.25 mbar and with temperatures between 150 °C and 230 °C [29]. The presence of the $\text{O}_{2\alpha}$ state was found to be correlated with a shift of the Ag3d BE of 0.5 eV but in the EPOC experiments no such shift was found. The reason for this might be that the Ag3d already experienced a downward shift of 0.59 eV due to alloying with Pt (see section 7.2.2). Also in the Ag/YSZ study of Zipprich et al. the formation of the 529.6 eV oxygen spillover species upon electrochemical pumping was not correlated with any change in the Ag3d peak position [10]. Since this does not agree with findings for $\text{O}_{2\alpha}$ state the exact nature of the oxygen spillover species on Ag/YSZ still needs to be clarified.

Already with an excess of ethylene the O1s signal contains at least four species (O1-O4) as demonstrated by Figs. 7.17 and 7.18 which were recorded under open circuit conditions and with applied an electric potential of 2V with an excess of ethylene ($p(\text{C}_2\text{H}_4)/p(\text{O}_2)= 5:1$) and ($p(\text{C}_2\text{H}_4)/p(\text{O}_2)= 10:1$), respectively. The main component O3 at 531.77 eV is found typically on Pt catalysts under high pressure reaction conditions ($p > 10^{-3}$ mbar) [16]. It can be assigned to SiO_x with x being close to two. The SiO_2 is more or less inert but since Si accumulates this component reaches a substantial height in

the course of a high pressure study. The silicon abundance goes up to 2% at maximum (see Fig. 7.3). The O4 component at 533 eV originates from various oxygen containing carbon compounds [30]. The component O2 at 530.4 eV can be assigned to chemisorbed oxygen on Pt sites [8,17,31]. An additional oxygen component, O1, is seen at 529.3 eV, a BE characteristic for oxygen on Ag [10,28].

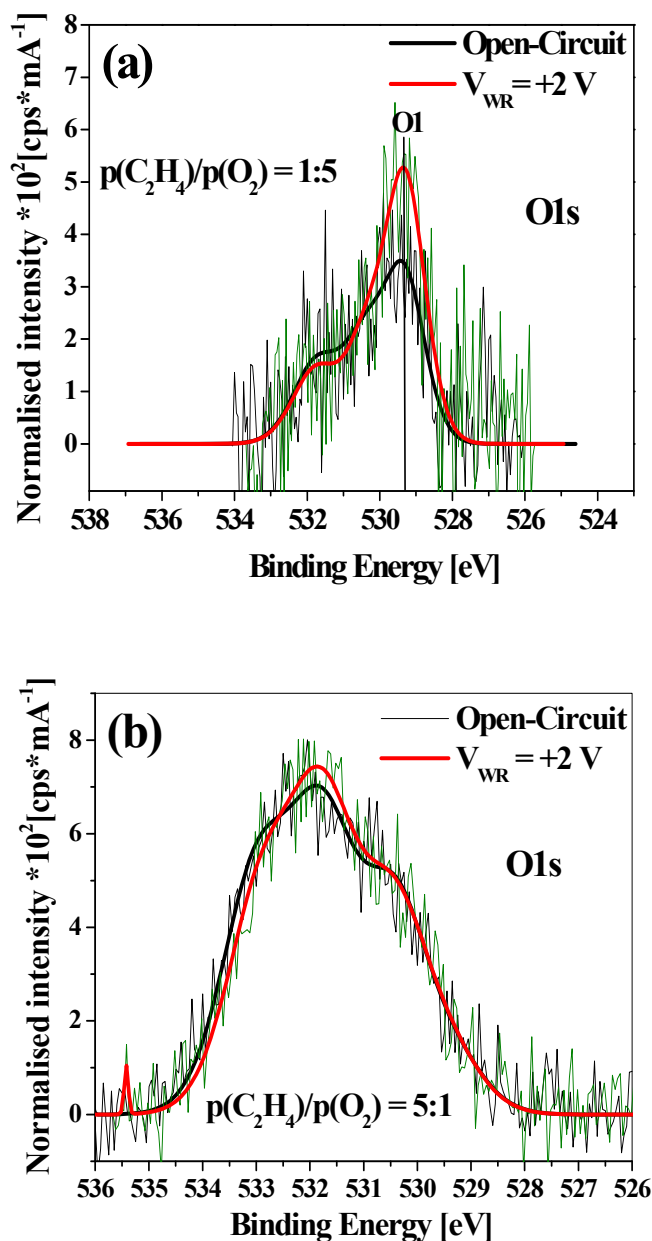


Figure 7.16: O1s photoelectron spectra showing the effect of electrochemical pumping. The spectra were all recorded under reaction conditions at $T = 650$ K and $p(\text{total}) = 0.25$ mbar. (a) Comparison of the spectra under OC conditions and with applied electric potential of 2V for a ratio $p(\text{C}_2\text{H}_4)/p(\text{O}_2) = 1:5$. (b) Same as in (a) but with ethylene being in excess, i. e. $p(\text{C}_2\text{H}_4)/p(\text{O}_2) = 5:1$.

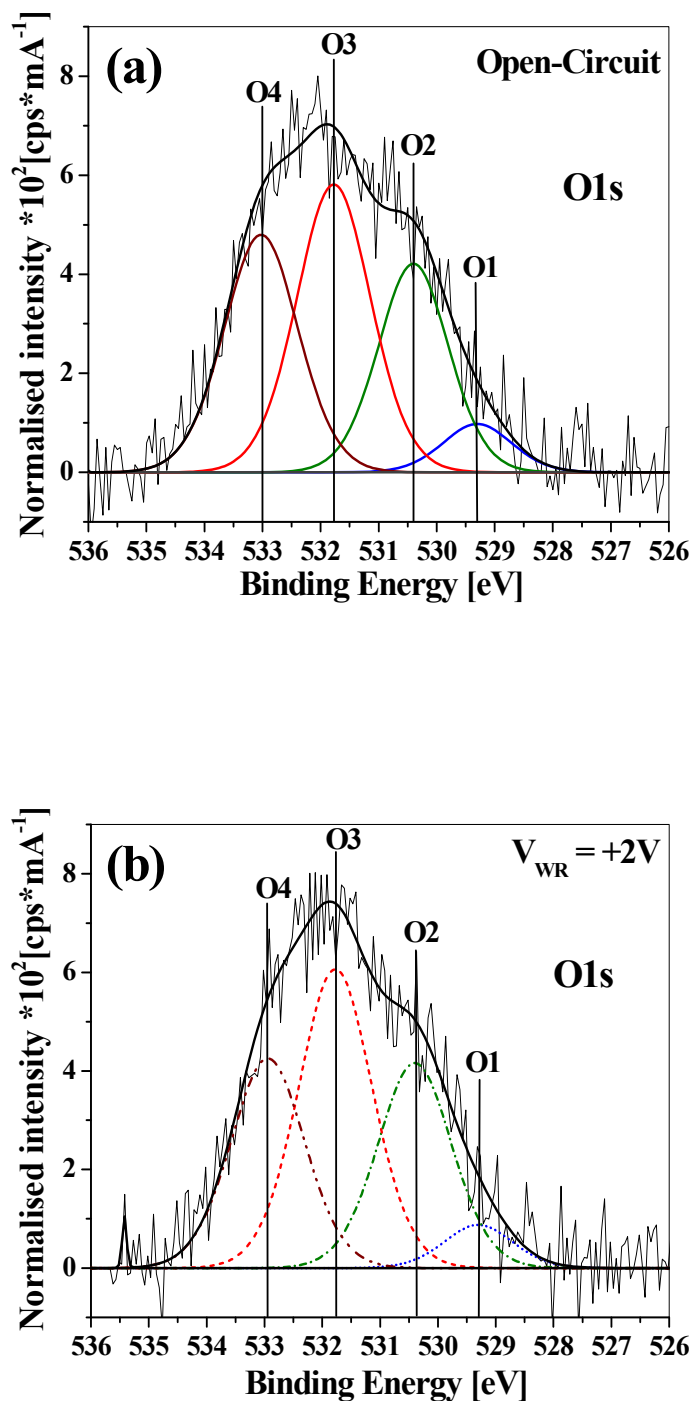


Figure 7.17: Deconvolution of the O1s spectrum under reaction conditions for ratio $p(\text{C}_2\text{H}_4)/p(\text{O}_2) = 5:1$. (a) Open circuit conditions. (b) Applied electric potential of 2V. The spectra were all recorded under reaction conditions at $T = 650 \text{ K}$ and $p(\text{total}) = 0.25 \text{ mbar}$.

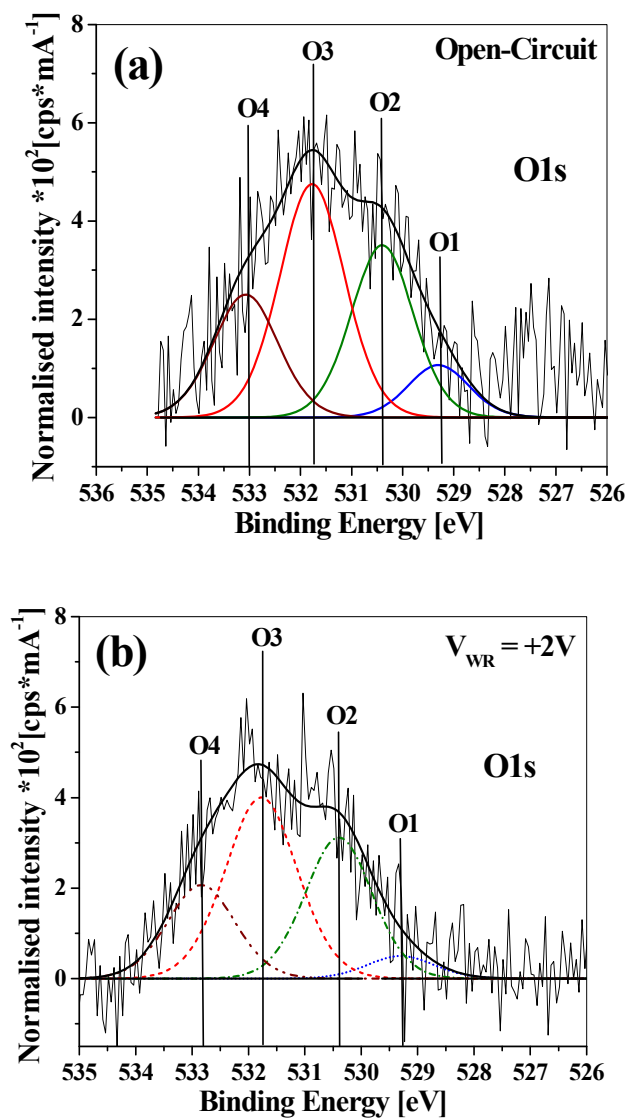


Figure 7.18: Deconvolution of the O1s spectrum under reaction conditions with ethylene in excess, i.e. $p(\text{C}_2\text{H}_4)/p(\text{O}_2) = 10:1$ under: (a) Open circuit conditions. (b) Applied electric potential of 2V. The spectra were all recorded under reaction conditions at $T = 650 \text{ K}$ and $p(\text{total}) = 0.25 \text{ mbar}$.

The variation of the Pt/Ag ratio during the EPOC experiments is depicted in Fig. 7.19. Beyond the rate maximum with an excess of ethylene the Pt/Ag ratio is around 1.5-1.7. Application of an electric potential in this region does not lead to significant changes in the Pt/Ag ratio in this region. However, left of the rate maximum in the first two data points Pt is enriched compared to the range where ethylene is in excess. Upon electrochemical pumping the enrichment of Pt is enhanced. The Pt/Ag ratio is equal 3.25 and 2.6 for $\text{C}_2\text{H}_4/\text{O}_2$ ratios of 1:10 and 1:5, respectively; upon electrochemical pumping the Pt/Ag ratio increases to 4.25 and 3.2 (see Fig. 7.19b). The region where the Pt/Ag

ratio changes is also the region where electrochemical pumping causes a strong reduction of the carbon signal and a substantial increase in oxygen coverage. A potential explanation for the Pt enrichment might therefore be that electrochemical pumping preferentially removes carbon from Pt sites. An alternative possibility is that the increase in oxygen coverage causes Pt to segregate to the surface. This possibility can be discarded because the O1s spectra indicate that the spillover oxygen binds to Ag and not to Pt sites.

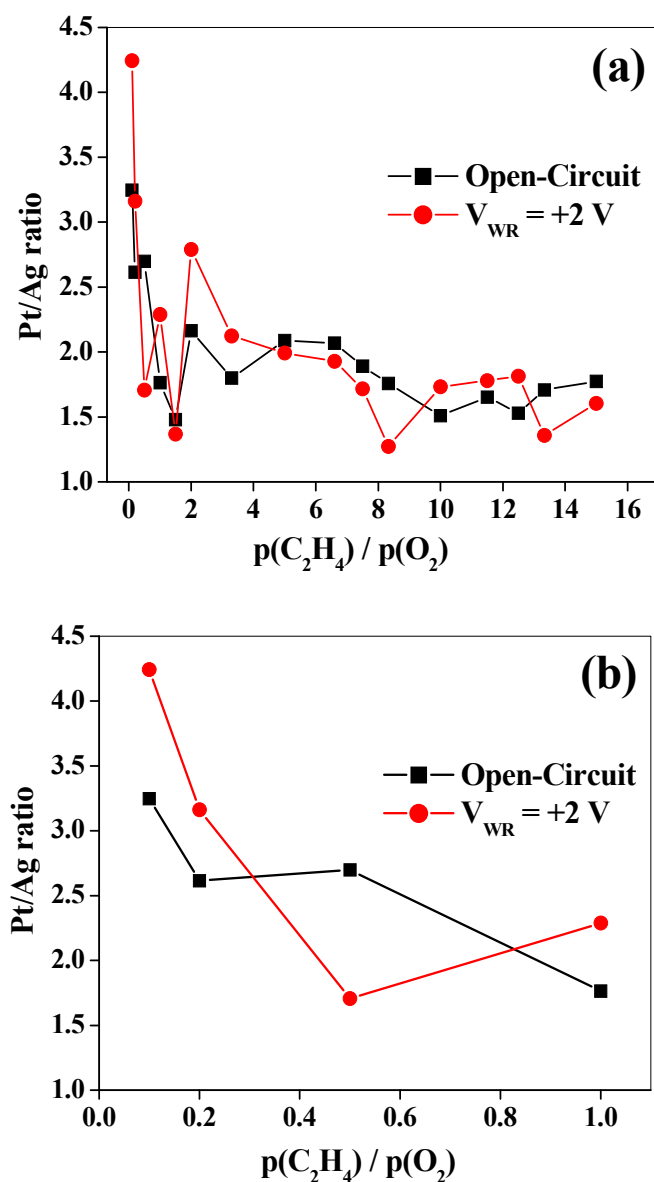


Figure 7.19: Variation of the Pt/Ag ratio during EPOC experiments displayed in Fig. 7.6. Experimental conditions: $T = 650 \text{ K}$, $p(\text{total}) = 0.25 \text{ mbar}$. (a) Pt/Ag ratio vs. $p(\text{C}_2\text{H}_4)/p(\text{O}_2)$ for OC conditions and with an applied electric potential of 2 V. (b) The drawing represents an enlarged section of Fig. 7.19a showing the effect of an applied electric potential on the first few data points.

As shown by Fig. 7.20 the variation of the Pt and the Ag concentrations during the EPOC experiment displayed in Fig. 7.6. The application of a potential before the rate maximum removes preferentially carbon from Pt sites i.e. the carbon observed before the rate maximum is attached to Ag sites. The different amount of carbon over Pt and Ag sites causes a different damping of the metal signal as $p(\text{C}_2\text{H}_4)/p(\text{O}_2)$ is varied.

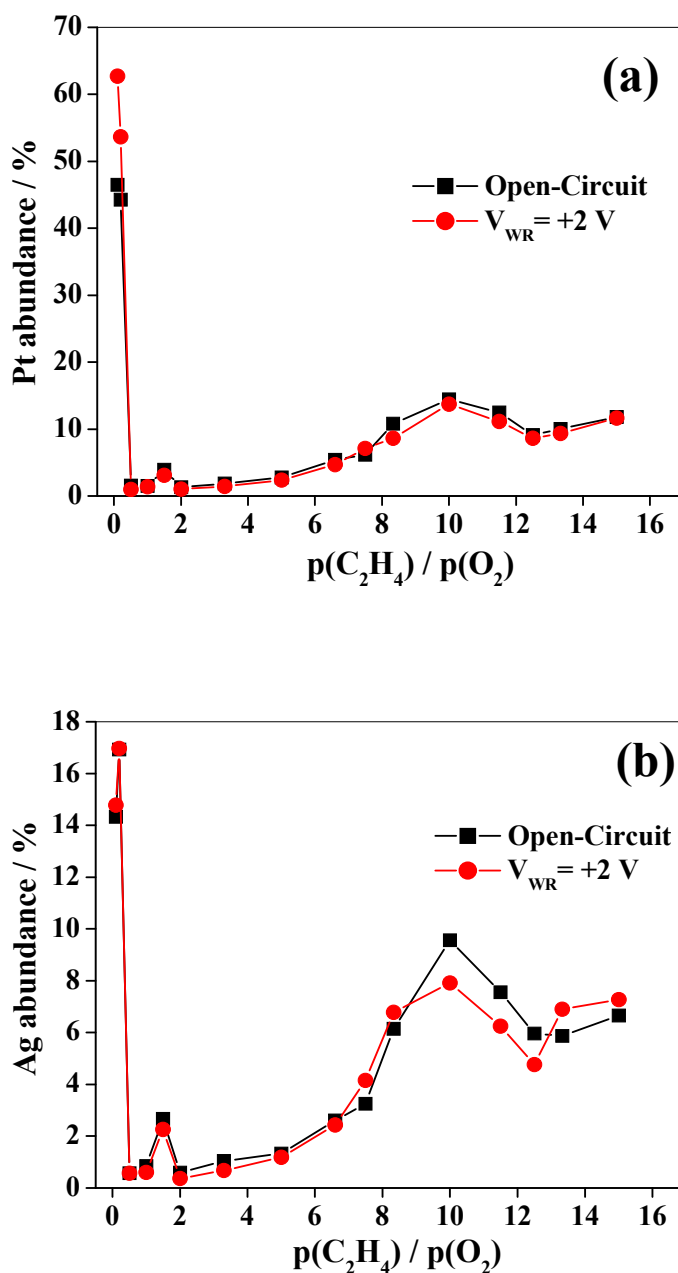


Figure 7.20: Variation of the Pt and the Ag concentrations during the EPOC experiment displayed in Fig. 7.6. Experimental conditions: $T = 650 \text{ K}$, $p(\text{total}) = 0.25 \text{ mbar}$.

7.5 Discussion

For explaining the EPOC effect in the $C_2H_4 + O_2$ reaction on Pt/YSZ the following mechanistic scheme based on ignition has been proposed (see chapter 6). The EPOC effect occurs only under conditions of ethylene excess so that a carbonaceous layer on Pt can build up which inhibits O_2 adsorption and hence poisons the catalyst. The effect of the electric potential is to generate oxygen spillover which eats holes into the carbon layer thus removing locally the inhibitory effect. Now O_2 adsorption from the gas phase can occur enlarging these holes via reaction fronts. Through partial removal of the carbonaceous layer the fronts initiate the transition from an unreactive to a reactive state of the surface. In this picture the role of spillover oxygen is just to ignite the reaction and consequently the EPOC effect is non-Faradaic.

With regard to the kinetics of the reaction (Fig. 7.6a) and the conditions for EPOC the picture for ethylene oxidation over Pt-Ag/YSZ is very much the same as for ethylene oxidation over Pt/YSZ (chapter 6). A closer look at the results of the *in situ* XPS measurements reveals, however, a number of observations which, at least at first sight, seems not to agree at all with the mechanism sketched above:

(i) In contrast to pure Pt electrodes we already find a substantial carbon coverage at low $p(C_2H_4)$ before the rate maximum is reached. Electrochemical pumping decreases the carbon signal but in contrast to what one expects, the partial removal of the carbonaceous layer has no effect on the rate.

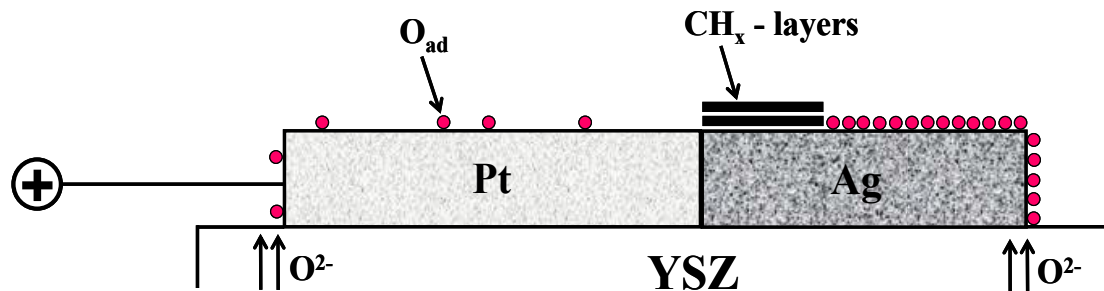
(ii) At high $p(C_2H_4)$ an EPOC effect is seen but again in contrast to what one expects the rate increase is not accompanied by a decrease of the carbon signal.

We can resolve the apparent contradictions between the observations in (i) and the proposed mechanism if we take into account that Ag is less reactive in the total oxidation of ethylene than Pt. If the Pt in the Pt-Ag/YSZ system behaves similar to Pt/YSZ, then the Pt should be carbon free at low $p(C_2H_4)$, and all the carbon should be concentrated on Ag sites. Since the Pt sites are the active sites, it is evident that a decrease of the carbon coverage on the Ag sites will have no consequences for the reaction rate. This mechanistic picture is schematically depicted in Fig. 7.21.

An alternative possibility would be that part of the carbonaceous layer becomes graphitic and thus electrically conducting [32,33]. This graphitic carbon if it grows at the tpb could therefore also act as an electrode thus potentially enforcing the electrochemical

promotion effect. Since this hypothesis found no experimental support it is pursued any further here.

(a) Oxygen in excess



(b) Ethylene in excess

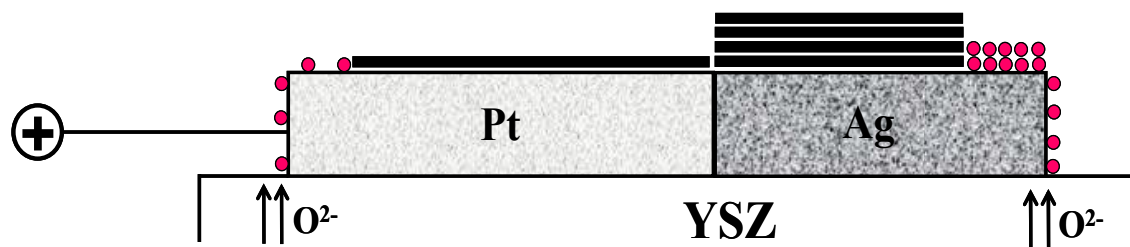


Figure 7.21: Scheme of the proposed electrochemical promotion mechanism of ethylene oxidation on bimetallic Pt/Ag electrodes on YSZ. It is assumed that the spillover oxygen over Pt is far more reactive than over Ag sites. (a) Promotion under conditions of oxygen being in excess, i.e. left of the rate maximum in reaction rate vs. $p(\text{C}_2\text{H}_4)/p(\text{O}_2)$ plot (Fig. 7.6a). (b) Promotion under conditions of ethylene being in excess, i. e. right of the rate maximum in reaction rate vs. $p(\text{C}_2\text{H}_4)/p(\text{O}_2)$ plot (Fig. 7.6a).

The fact that upon electrochemical pumping we see only strong growth of oxygen on Ag sites but not of oxygen on Pt sites does not mean that we have no oxygen spillover on Pt. What we measure is the stationary oxygen concentration. Therefore, if the spillover oxygen on Pt is much more reactive than spillover oxygen on Ag, we will consequently observe a high concentration of oxygen on Ag sites and a low concentration on Pt sites under reaction conditions. The different reactivities of the oxygen spillover species over Pt and Ag sites explains the O1s spectra made left of the rate maximum. At high $p(\text{C}_2\text{H}_4)$ electrochemical pumping does not lead to a detectable growth in oxygen coverage but again this probably just reflects the fact that with a large excess of ethylene the stationary concentration in reactive oxygen species will be very small (see Fig. 7.21).

The observation that the EPOC effect at high $p(\text{C}_2\text{H}_4)$ is not connected with a decrease of the carbon signal is in apparent contradiction to the mechanistic picture established for Pt/YSZ of a reaction front spreading out reactively removing carbon. The only valid conclusion from the experimental data can be that in our case there is no reaction front, but then the question is why no front develops? If we get back to the mechanistic picture of how a reaction front develops, then this is via spillover oxygen eating a hole into a carbon adlayer followed by oxygen adsorbing from the gas phase and reacting thus enlarging the hole. This mechanism works well if the carbonaceous film is not more than 1 ML thick but in our case the film is $\approx 5\text{-}6$ ML thick. Initiating a front under isothermal conditions will be quite difficult then.

A “non-Faradaic efficiency factor”, Λ , has been defined which according to the stoichiometry of ethylene combustion is obtained as $\Lambda = \Delta r / (I/6F)$ with Δr denoting the rate increase in CO_2 production and I representing the electric current flow between counter and working electrode [34,35]. Here for an ionic current $I = 5$ mA and with an effective pumping rate of 0.44 L/s one calculates from the measured QMS signal a Λ -factor of 2.18. The electrochemical promotion effect is therefore weakly non-Faradaic.

A Faradaic rate increase, i. e. $\Lambda = 1$, means that the electrochemically induced rate increase is entirely caused by spillover oxygen which reacts with the decomposition products of ethylene adsorption whereas gas phase oxygen plays no role. A value $\Lambda \approx 2$ indicates that both, oxygen from the gas phase and spillover oxygen, contribute about equally strong to the reaction rate. If, in a first approximation we neglect the gas phase

contribution the following picture of the EPOC process results. The three-phase-boundary is surrounded by a reaction zone whose spatial extension, r_z , is given by the diffusivity D_O of spillover oxygen and the lifetime τ of spillover oxygen according to $r_z = \sqrt{2D_O\tau}$. The lifetime of spillover oxygen is given by the impingement rate of ethylene multiplied with the reactive sticking coefficient; assuming $S_{\text{reac}} = 0.1$ about 10^4 monolayers adsorb per second resulting in a lifetime of the order of 10^{-4} s for spillover oxygen. With an oxygen diffusivity $D_O = 1.24 \times 10^{-5} \text{ cm}^2 \text{ s}^{-1}$ for 650 K one obtains a width of the reaction zone of $0.5 \text{ }\mu\text{m}$ [36]. Apparently the reaction zone is so small that it does not lead to a detectable change in the carbon signal. This reaction zone is located around the tpb but since we are using porous Pt electrodes this means that the tpb and therefore the reaction zone are not accessible to direct observation with XPS. Of course, in numerous experiments with porous Pt electrodes on YSZ spillover oxygen was measured. This means that the spillover oxygen originating at the tpb must have a sufficient mobility to reach the outer surface of the electrodes to be detected by surface analytical techniques such as XPS, PEEM or work function measurements with a Kelvin probe [8,9,35,37]. This requires a diffusion length of the order of micrometers and such conditions are given if the experiments are not conducted in a reacting environment. Under our conditions with a reaction limiting the life time of spillover oxygen the diffusion length is not sufficient to reach the outer surface of the electrode.

As one compares the EPOC effect found here with data in the literature for ethylene oxidation over Pt/YSZ one finds a quite different behavior. The highest Λ -factor of all EPOC systems investigated so far is reported with $\Lambda = 3 \times 10^5$ for ethylene oxidation over Pt/YSZ [4]. This investigation was carried out with reactants in the 10^{-2} mbar range and with helium as carrier gas at ≈ 1 bar. In a PEEM study of ethylene oxidation over Pt/YSZ conducted at 10^{-4} mbar a Λ -factor of 2.4 was obtained (see chapter 6). In the case of the atmospheric pressure study one can suspect that the huge Λ -factor is the result of thermal ignition as the reaction becomes non-isothermal.

One main motivation for this study has been the possibility that at high pressure an oxygen spillover species might develop which is different from chemisorbed oxygen. The existence of such a special spillover species has been postulated by Vayenas and co-workers in order to explain the non-Faradaic nature of the EPOC effect but so far no valid experimental proof exists [1,35]. Also here no indication for the existence of $O^{\delta-}$ species with δ close to 2 was found. According to the XPS study by Ladas et al. the O 1s

BE of this species should be located at 528.8 eV [38]. Following the "sacrificial promoter" concept of Vayenas this species should exhibit a reduced reactivity compared to regular chemisorbed oxygen. Therefore even in a reacting environment this species should reach a substantial concentration but no new component was found in the experimental data.

One could be tempted to summarize the results by stating that on the alloyed surface the two metallic constituents retain their individual behavior in the electrochemical promotion experiments. This would be problematic for several reasons. First of all, the XPS data alone do not allow us to directly separate the electrocatalytic contributions of the two metallic constituents. Nevertheless we could deduce a model from the measurements which consistently explained the available data. Following this model the Pt on the alloyed surface behaves like pure Pt electrodes in EPOC experiments conducted under the same conditions (see chapter 6). For Ag the case is more difficult. Firstly, no *in situ* XPS data are available for the EPOC behavior of Ag/YSZ at high pressure. Secondly, the shift of the Ag3d BE indicates alloying with Pt. Since we observe the formation of a several monolayers thick carbon layer on the Pt/Ag catalyst while on pure Pt, under the same conditions, the thickness of the carbon layer does not exceed one monolayer the effect of the Ag is evident. Whether this effect is due to alloying or whether this would also be observed on pure Ag is a question which remains to be solved in the future.

Kinetic oscillations occur in certain parameter range for a quite large number of heterogeneously catalyzed reactions comprising a pressure range from 10^{-9} mbar to atmospheric pressure [37]. In ethylene oxidation over Pt and Rh rate oscillations have been found in experiments conducted in the mbar – 1 bar range [38]. In EPOC experiments rate oscillations have been observed under galvanostatic control in catalytic CO oxidation over Pt/YSZ and in ethylene oxidation over Rh/YSZ [39-41]. Since the oscillations in catalytic CO oxidation occurred at the borderline of the stability range of Pt oxide a mechanism based on the periodic formation and reduction of Pt oxide has been suspected. In principle, numerous feedback mechanisms can potentially cause kinetic instabilities; without further experimental evidence, it is therefore of little use to speculate about possible oscillation mechanisms [37].

7. 6 Conclusions

The experiments presented here are the first EPOC experiments at high pressure (close to 1 mbar) in which the state of the surface was monitored *in situ* using XPS to identify the relevant surface species. An electrochemical promotion of ethylene oxidation over bimetallic Pt-Ag/YSZ catalysts has been found. The promotion effect is weakly non-Faradaic, i. e. spillover oxygen and oxygen from the gas phase contributes about equally strong to the reaction rate. As found in chapter 6 for ethylene oxidation over Pt/YSZ the promotion effect is linked to the presence of a carbonaceous CH_x layer inhibiting O₂ adsorption and hence poisoning the catalytic surface. An EPOC effect accordingly is only observed at high p(C₂H₄)/p(O₂) ratios. Under conditions under which we see an electrochemical promotion no effect of the pumping voltage on the carbon signal and on the oxygen signal can be detected. The absence of such an effect is attributed (i) to a rather thick carbonaceous film which comprises about 5-6 ML, and (ii) due to a relatively small reaction zone around the tpb. In contrast, at low p(C₂H₄) under conditions where no EPOC effect occurs electrochemical pumping leads to the appearance of an oxygen spillover species at 529.3 eV simultaneous with a decrease of the carbon signal. The spillover oxygen is assigned to oxygen on Ag sites which is less reactive than oxygen spillover over Pt sites species and therefore can be detected. Apparently, on the alloyed surface the two metallic constituents retain their individual behavior. An effect which has to be attributed to Ag is the formation of a several layers thick CH_x film. Under no conditions we observed any indication of a special spillover oxygen species (O^{δ-} with δ around 2) which has been postulated for Pt/YSZ [1,34,35].

7. 7 References

- [1] R. Imbihl, Prog. Surf. Sci. 85 (2010) 240.
- [2] I. V. Yentekakis, A. Palermo, N. C. Filkin, M. S. Tikhov, R. M. Lambert, J. Phys. Chem. B 101 (1997) 3759.
- [3] E. Mutoro, B. Luerssen, S. Guenther, J. Janek, Solid State Ion. 180 (2009)1019.
- [4] S. Bebelis, C. G. Vayenas, J. Catal. 118 (1989) 125.
- [5] E. Mutororo, C. Koutsodontis, B. Luerssen, S. Brosda, C.G. Vayenas, J. Janek, Appl. Catal., B 100 (2010) 328.

- [6] M. Stoukides, C. G. Vayenas, *J. Catal.* 70, 137 (1981); *ACS Symp. Ser.* 178, 181 (1982).
- [7] S. Bebelis, C. G. Vayenas, *J. Catal.* 138, 588 (1992).
- [8] B. Luerßen, S. Günther, H. Marbach, M. Kiskinova, J. Janek, R. Imbihl, *Chem. Phys. Lett.* 316 (2000) 331.
- [9] B. Luerßen, E. Mutoro, H. Fischer, S. Günther, R. Imbihl, J. Janek, *Angew. Chem. Int. Ed.* 45 (2006) 1473.
- [10] W. Zipprich, H. D. Wiemhöfer, U. Vöhrer, W. Göpel, *Ber. Bunsen.-Ges. Phys. Chem.* 99 (1995) 1406.
- [11] J. Sanabria-Chinchilla, K. Asazawa, T. Sakamoto, K. Yamada, H. Tanaka, P. Strasser, *J. Am. Chem. Soc.* 133 (2011) 5425.
- [12] F. Bensebaa, N. Patrito, Y. Le Page, P. L'Ecuyer, D. Wang, *J. Mater. Chem.* 14 (2004) 3378.
- [13] A. S. Arico, P. Creti, H. Kim, R. Mantegna, N. Giordano, V. Antonucci, *J. Electrochem. Soc.* 143 (1996) 3950.
- [14] Q. Li, K. Wang, S. Zhang, M. Zhang, J. Yang, Z. Jin, *J. Mol. Catal. A: Chem.* 258 (2006) 83.
- [15] A.M. Ruppert, T. Paryjczak, *Appl. Catal., A* 320 (2007) 80.
- [16] S. Günther, A. Scheibe, H. Bluhm, M. Hävecker, E. Kleimenov, A. Knop-Gericke, R. Schlögl, and R. Imbihl, *J. Phys. Chem. C* 112 (2008) 15382.
- [17] C.R. Parkinson, M. Walker, C.F. McConville, *Surf. Sci.* 545 (2003) 19.
- [18] J. B. Xu, T. S. Zhao, Z. X. Liang, *J. Phys. Chem. C* 112 (2008) 17362.
- [19] D. Zhao, Y-H. Wang, B. Yan, B-Q. Xu, *J. Phys. Chem. C* 113 (2009) 1242.
- [20] C. G. Freyschlag, R. J. Madix, *Mater. Today*, 14 (2011) 134.
- [21] C. Koutsodontisa, A. Katsaounisa, J.C. Figueroa, C. Cavalcab, Carmo. J. Pereirab, C.G. Vayenas, *Top. Catal.* 38 (2006) 157.
- [22] R. Larciprete, S. Lizzit, S. Botti, C. Cepek, A. Goldoni, *Phys. Rev. B* 66 (2002) 121402.
- [23] S. Hofmann, R. Blume, C. T. Wirth, M. Cantoro, R. Sharma, C. Ducati, M. Hävecker, S. Zafeiratos, P. Schnoerch, A. Oestereich, D. Teschner, M. Albrecht, A. Knop-Gericke, R. Schlögl, J. Robertson, *J. Phys. Chem. C* 113 (2009) 1648.
- [24] N. Freyer, G. Pirug, H. P. Bonzel, *Surf. Sci.* 126 (1983) 487.
- [25] N. M. Rodriguez, P. E. Anderson, A. Wootsch, U. Wild, R. Schlögl, Z. Paal, *J. Catal.* 197 (2001) 365.
- [26] Z. Paal, *J. Mol. Catal.* 94 (1994) 225.
- [27] T. Fuhrmann, M. Kinne, B. Tränkenschuh, C. Papp, J. F. Zhu, R. Denecke, H-P. Steinrück, *New J. Phys.* 7 (2005) 107.
- [28] V. I. Bukhtiyarov, A. Nizovskii, H. Bluhm, M. Hävecker, E. Kleimenov, A. Knop-Gericke, R. Schlögl, *J. Catal.* 238 (2006) 260.
- [29] T. C. R. Rocha, A. Oestereich, D. V. Demidov, M. Hävecker, S. Zafeiratos, G. Weinberg, V. I. Bukhtiyarov, A. Knop-Gericke, R. Schlögl, *Phys. Chem. Chem. Phys.* 14 (2012) 4554.
- [30] B. A. Sexton, A. E. Hughes, *Surf. Sci.* 140 (1984) 227.
- [31] C. Puglia, A. Nilsson, B. Hernnas, O. Karis, P. Bennich, N. Martensson, *Surf. Sci.* 342 (1995) 119.

- [32] S. Park, J. M. Vohs, R. J. Gorte, *Nature* 404 (2000) 265.
- [33] S. McIntosh, J. M. Vohs, R. J. Gorte, *J. Electroch. Soc.* 150 (2003) A470.
- [34] C.G. Vayenas, M.M. Jaksic, S.I. Bebelis, S.G. Nephytides, in: J.O.M. Bockris et al. (Eds.), *Modern Aspects of Electrochemistry*, 29, Plenum Press, New York, 1996, p. 57.
- [35] C. G. Vayenas, S. Bebelis, C. Pliangos, S. Brosda, D. Tsiplakides, *Electrochemical Activation of Catalysis: Promotion, Electrochemical Promotion, and Metal-Support Interactions*, Kluwer Academic / Plenum Publishers, New York, 2001.
- [36] E. Mutoro, C. Hellwig, B. Luerssen, S. Guenther, W. Bessler, J. Janek, *Phys. Chem. Chem. Phys.* 13 (2011) 12798.
- [37] C.G. Vayenas, S. Bebelis, S. Ladas, *Nature* 343 (1990) 625.
- [38] S. Ladas, S. Kennou, S. Bebelis, C. G. Vayenas, *J. Phys. Chem.* 97 (1993) 8845.
- [37] R. Imbihl, G. Ertl, *Chem. Rev.* 95 (1995) 697.
- [38] C. G. Vayenas, C. Georakis, J. Michaels, J. Tormo, A. Ioannides, S. Bebelis, *J. Catal.* 67 (1981) 348.
- [39] I. V. Yentekakis, C. G. Vayenas, *J. Catal.* 111 (1988) 170.
- [40] M. N. Tsampas, F. M. Sapoutzki, C. G. Vayenas, *Catal. Today* 146 (2009) 351.
- [41] E.A. Baranova, A. Thursfield, S. Brosda, G. Fo'ti, C. Comminellis, C.G. Vayenas, *Catal. Lett.* 150 (2005) 15.

Chapter 8

Summary

This chapter summarizes the important results coming out from this thesis.

In this study it was investigated how electrochemical pumping affects on the catalytic activity of Pt and Pt-Ag catalyst electrodes interfaced to a single crystal of yttrium stabilized zirconia (YSZ) during the $C_2H_4 + O_2$ reaction. The WE was brought onto the polished side of YSZ samples using two different ways of preparation: The first type was prepared by depositing Pt paste with a brush followed by annealing to 1123 K, and sintering at this temperature for 3 h in air. The second type of WE's was prepared by sputtering Pt onto the the YSZ samples at 300 K using a magnetron sputter technique in an inert atmosphere, followed by sintering at elevated temperatures up to 1123 K and 1373 K.

First of all, the WE electrodes were characterized by SEM, TEM, SAED, XRD, EDX, XPS, and by surface profilometry. As described in details in chapter 5 the as-sputtered samples show a compact amorphous Pt film covering uniformly the substrate. Upon annealing at 1123 K, gaps and pores at the interface develop leading to a partial dewetting of the Pt film. Increasing the annealing temperature to 1373 K transforms the polycrystalline Pt film into single crystalline grains exhibiting a (111) orientation towards the substrate.

After characterization of the WE electrodes the electrochemical promotion of ethylene oxidation to CO_2 and H_2O has been studied under UHV conditions, $p \approx 10^{-5} - 10^{-4}$ mbar range, with Pt/YSZ catalysts electrodes. PEEM was used as spatially resolving method. As explained in chapter 6 under open circuit conditions, i. e. without an external voltage applied the CO_2 production exhibits a pronounced hysteresis upon cyclic variation of $p(C_2H_4)$. XPS studies at BESSY conducted under high pressure up to 1 mbar, the hysteresis is caused by the build-up of a carbonaceous CH_x layer inhibiting O_2 adsorption and hence poisoning the reaction. The basic idea is that ethylene decomposition on Pt produces a carbonaceous CH_x film which inhibits O_2 adsorption and hence protects the carbonaceous layer against reactive removal by O_2 . However, in the presence of an excess of O_2 in the gas phase the CH_x layer is only metastable. Upon application of a positive potential spillover oxygen is created which eats holes in the CH_x layer. Now O_2 from the gas phase can adsorb reactively removing the carbonaceous layer. The electrochemical pumping in this concept just provides the ignition of the reaction:

The basic idea of the “ignition concept” is to explain the huge non-Faradaic effect, i.e. $\Lambda = 3 \times 10^5$, found in the electrochemical promotion of catalytic ethylene

oxidation and many other reaction systems exhibiting an EPOC effect without having to invoke the special oxygen spillover species postulated by Vayenas et al. In their “sacrificial promoter” mechanism besides regular chemisorbed oxygen a special oxygen spillover species should exist on Pt/YSZ with particular properties which differ from the properties of regular chemisorbed oxygen on Pt. With the ignition concept at least a plausible explanation can be suggested. For producing a large Λ -factor the optimum situation would be to start with a completely poisoned catalyst and then to ignite the reaction locally in a very small spot from where the excitation spreads out over the whole catalyst. Since the ignition consumes only a very small current the Λ -factor can be huge. Whether this recipe works depends on the heterogeneity of the sample, thickness of the carbon layer and on the preparation of the catalyst.

In situ XPS studies at BESSY under high pressure up to 1 mbar provided experimental support for the proposed mechanism for the EPOC effect during ethylene oxidation at pure Pt/YSZ catalyst. It was demonstrated that the electrochemical promotion is linked to presence of carbon on the electrode surface. No carbon has been detected left the rate maximum in a plot of reaction rate versus $p(\text{C}_2\text{H}_4)/p(\text{O}_2)$ and therefore no EPOC effect is observed in this region. Consequently right of the rate maximum, in the carbon rich region, an EPOC effect is seen.

Briefly, from UHV experiments in Hannover and high pressure XPS studies at BESSY in Berlin for $\text{C}_2\text{H}_4 + \text{O}_2/\text{Pt}/\text{YSZ}$ system, three important conclusions have been reached:

1. The CO_2 production rate exhibits a pronounced hysteresis upon cyclic variation of $p(\text{C}_2\text{H}_4)$ which can be attributed to different carbon coverages and hence different degrees of inhibition.
2. The electrochemical promotion is linked to the presence of carbon on the metal surface.
3. No special oxygen spillover species were detected under experimental conditions.

In chapter 7 the electrochemical promotion of the $\text{C}_2\text{H}_4 + \text{O}_2$ reaction over a bimetallic Pt/Ag catalyst (Pt:Ag ratio ≈ 1.5) interfaced to yttrium stabilized zirconia (YSZ) has been studied at 0.25 mbar and $T = 650$ K using X-ray photoelectron spectroscopy as *in situ* method. Applying a positive potential of 2V causes a relative rate increase in the CO_2 production up to 120%; the electrocatalytic promotion effect is

non-Faradaic ($\Lambda \approx 2$). An electrochemical promotion is found to occur only at high enough $p(\text{C}_2\text{H}_4)$ when a carbonaceous CH_x layers builds up inhibiting O_2 adsorption. The CH_x film is estimated to be about 5-6 layers thick. Only at low $p(\text{C}_2\text{H}_4)$ the application of an electric potential causes a decrease in the carbon signal associated with a growth of the $\text{O}1s$ signal at 529.3 eV. The latter species can be assigned to an electrochemically generated oxygen spillover species at Ag sites. The main effect of the addition of Ag is that much thicker carbon layers grow on the metal electrode as compared to pure Pt electrodes. Electrochemically the two metals retain their specific properties.

In summary, what should be demonstrated in this study is that it is unnecessary to construct a complicated mechanism with hypothetical surface species in order to explain the non-Faradaic nature of EPOC. There is a much simpler explanation which only relies on basic experimental facts and which should apply to numerous systems. It remains to be shown in future this ignition concept can also be verified for other systems.

Publications List

Publications included in this thesis

1. **A. Toghan**, R. Arrigo, A. Knop-Gericke, R. Imbihl: Ambient pressure X-ray photoelectron spectroscopy during electrochemical promotion of ethylene oxidation over a bimetallic Pt-Ag/YSZ catalyst, **Journal of Catalysis** **296** (2012) **99**.
2. **A. Toghan**, M. Khodari, F. Steinbach, R. Imbihl: *Microstructure of thin film platinum electrodes on yttrium stabilized zirconia prepared by sputter deposition*, **Thin Solid Films** **519** (2011) **8139**.
3. R. Imbihl, **A. Toghan**: *Comment to the Note by Vayenas and Vernoux on the Electrochemical Promotion of Ethylene Oxidation at a Pt/YSZ Catalyst*, **ChemPhysChem** **12** (2011) **1764**.
4. **A. Toghan**, L. M. Rösken, R. Imbihl: *Origin of Non-Faradayicity in Electrochemical Promotion of Catalytic Ethylene Oxidation*, **Physical Chemistry Chemical Physics** **12** (2010) **9811**.
5. **A. Toghan**, L. M. Rösken, R. Imbihl: *The electrochemical promotion of ethylene oxidation at Pt/YSZ catalyst*, **ChemPhysChem** **11** (2010) **1452**.

Publications not included in this thesis

6. M. M. Abou-Krishna, F. H. Assaf, **A. A. Toghan**: *Electrodeposition of Zn-Ni alloys from sulfate bath*, **Journal of Solid State Electrochemistry** **11** (2007) **244**.
7. M. Abou-Krishna, A. M. Zaky, **A. A. Toghan**: *Morphology, composition and corrosion properties of electrodeposited Zn-Ni alloys from sulphate electrolytes*, **Asian Journal of Biochemistry** **1** (2006) **84**.

Conferences contribution

1. **A. Toghan**, R. Arrigo, A. Knop-Gericke, R. Imbih: *In situ XPS studies during catalytic ethylene oxidation over a bimetallic Pt-Ag/YSZ catalyst electrode*, Electrochemistry Conference 2012: Fundamental and Engineering Needs for Sustainable Development, **2012**, München, Germany. **(Talk)**
2. **A. Toghan**, R. Arrigo, A. Knop-Gericke, R. Schlögl, R. Imbihl: *The electrochemical promotion of ethylene oxidation at bimetallic Pt-Ag/YSZ catalyst*, Deutsche Physikalische Gesellschaft Conference (DPG Spring Meeting), **2012**, Berlin, Germany. **(Talk)**
3. **A. Toghan**, M. Khodari, R. Imbihl: *Microstructure of thin film platinum electrodes on yttrium stabilized zirconia prepared by sputter deposition and their applications*, The 1st International Conference for Environmental Studies, **2012**, Qena-Luxor, Egypt. **(Poster)**
4. **A. Toghan**, L. Rösken, M. Hävecker, A. Knop-Gericke, R. Imbihl: *Pressure gap and electrode artefacts in the electrochemically induced oxygen spillover on Pt/YSZ electrodes*, Deutsche Physikalische Gesellschaft Conference (DPG Spring Meeting), **2011**, Dresden, Germany. **(Talk)**
5. **A. Toghan**, R. Imbihl: *Electrochemical promotion of catalytic ammonia oxidation at Pt/YSZ catalysts under low Pressure conditions*, Electrochemistry Conference 2010: From Microscopic Understanding to Global Impact, **2010**, Bochum, Germany. **(Poster)**
6. **A. Toghan**, L. Rösken, R. Imbihl: *Electrochemical promotion of catalytic ethylene oxidation on Pt/YSZ catalyst under low pressure conditions*, Deutsche Physikalische Gesellschaft Conference (DPG Spring Meeting), **2010**, Regensburg, Germany. **(Talk)**

7. **A. Toghhan**, L. Roesken, R. Imbihl: *Pressure gap in electrochemically induced oxygen spillover at Pt/YSZ electrodes*, Deutsche Physikalische Gesellschaft Conference (DPG Spring Meeting), **2009**, Dresden, Germany. **(Poster)**
8. **A. Toghhan**, M. Khodari, R. Imbihl: *Electrochemical promotion of catalytic CO oxidation on Pt/YSZ*, The 3rd International Conference on the "Recent Environmental Problems and Social Sharement", **2008**, Qena-Luxor, Egypt. **(Poster)**
9. **A. Toghhan**, R. Imbihl: *Ellipsometric study of the electrochemical promotion of catalytic CO oxidation with Pt/YSZ catalysts*, the 2nd International Conference on the "Electrochemical Promotion of Catalysis and its Applications" (EPOCAP), **2008**, Oléron, France. **(Poster)**
10. **A. Toghhan**, R. Imbihl: *Electrochemically controlled friction and catalysis on solid electrolytes*, The 2nd Training European Course on the "Basic and Application of Catalysis (Heterogeneous and Homogeneous)" (BACHH), **2008**, Ciudad Real, Spain. **(Talk)**
11. **A. Toghhan**, R. Imbihl: *Electrochemically controlled friction and catalysis on solid electrolytes*, the 1st International Conference on the "Origen of Electrochemical Promotion of Catalysis" (OREPOC), **2007**, Thessaloniki, Greece. **(Talk)**
12. M. M. Abou-krisa, F. H. Assaf, **A. A. Toghhan**: *Morpholgy, composition and corrosion properties of electrodeposition of zinc-nickel alloy from sulfate electrolytes; Electrodeposition of zinc-nickel alloy from sulfate baths; Cyclic voltammetric of zinc-nickel alloys in alkaline media*, The 4th International Conference on Electrochemistry and its Applications (ICE IV), **2004**, Aswan, Egypt. **(Posters)**

Curriculum Vitae

Personal data

Name: Arafat Ahmed Toghan Ahmed
Born March 18, 1978
Place of birth Qena, Egypt
Citizenship Egyptian

Academic degrees

2004 **M.Sc. in Chemistry** from Chemistry Department, Faculty of Science, South Valley University, Egypt
1999 **Bachelor of Science** (very good with honor) from Chemistry Department, Faculty of Science, South Valley University, Egypt

Awards

Juli 2010 - till now: Financial support from the German Research Foundation (DFG)
May 2008 - April 2010: Egyptian Ministry of Higher Education scholarship awards and financed for Ph. D. study in Germany
March 2009, January 2011, and January 2012: Visiting scientist in the Synchrotron Radiation at BESSY II, Helmholtz-Zentrum Berlin, Germany

Education stages

Since May 2008 **Doctoral student** at the group of Prof. Dr. Ronald Imbihl, Institute of Physical Chemistry and Electrochemistry, Leibniz Universität Hannover, Germany
2005-2008 **Assistant lecturer and research assistant** at Chemistry Department, Faculty of Science, South Valley University, Egypt
1999-2004 **Demonstrator** at Chemistry Department, Faculty of Science, South Valley University, Egypt
1996-1999 **Undergraduate student** at Faculty of Science, South Valley University, Egypt
1984 – 1995 **Primary, Preparatory and Secondary School**, Qena, Egypt

Erklärung zur Dissertation

Hierdurch erkläre ich, dass ich meine Dissertation selbständig verfasst und die benutzten Hilfsmittel und Quellen sowie gegebenenfalls die zu Hilfeleistungen herangezogenen Institutionen vollständig angegeben habe.

Die Dissertation wurde nicht schon als Masterarbeit, Diplomarbeit oder andere Prüfungsarbeit verwendet.